Springer Proceedings in Energy

Ahmet Yavuz Oral
Zehra Banu Bahsi Oral *Editors*

3rd International Congress on Energy Efficiency and Energy Related Materials (ENEFM2015)

Proceedings, Oludeniz, Turkey, 19–23 October 2015

Springer

Springer Proceedings in Energy

More information about this series at http://www.springer.com/series/13370

Ahmet Yavuz Oral · Zehra Banu Bahsi Oral
Editors

3rd International Congress on Energy Efficiency and Energy Related Materials (ENEFM2015)

Proceedings, Oludeniz, Turkey, 19–23 October 2015

Springer

Editors
Ahmet Yavuz Oral
Department of Materials Science and Engineering
Gebze Technical University
Gebze, Kocaeli
Turkey

Zehra Banu Bahsi Oral
Department of Environmental Engineering
Gebze Technical University
Gebze, Kocaeli
Turkey

ISSN 2352-2534 ISSN 2352-2542 (electronic)
Springer Proceedings in Energy
ISBN 978-3-319-45676-8 ISBN 978-3-319-45677-5 (eBook)
DOI 10.1007/978-3-319-45677-5

Library of Congress Control Number: 2016949603

Printed on acid-free paper

This Springer imprint is published by Springer Nature
The registered company is Springer International Publishing AG
The registered company address is: Gewerbestrasse 11, 6330 Cham, Switzerland

Organisation

Scientific Committee

Mohamed Bououdina, University of Bahrain, Kingdom of Bahrain
Cengiz Ozkan, University of California, Riverside, USA
Ali Mostafaeipour, Yazd University, Iran
Hussam (Sam) Jouhara, Brunel University London, UK
Mehmet Kanoğlu, Gaziantep University, Turkey
Andrés E. Sotelo Mieg, Universidad de Zaragoza, Spain
Manuela Sechilariu, Université de Technologie de Compiègne, France
Aishui Yu, Fudan University, P.R.C.
De Chen, Norwegian University of Science and Technology, Norway
Hui-Ming Cheng, Chinese Academy of Sciences, China
Xianmao Lu, National University of Singapore, Singapore
Zheng Bo, Zhejiang University, China
Meng Ni, The Hong Kong Polytechnic University, Hong Kong
Yong-yao Xia, Fudan University, P.R.C.
Haluk Beyenal, Washington State University, USA
Beddiaf Zaidi, Badji Mokhtar University, Algeria
Eugen Axinte, Gheorghe Asachi Tehnical University of Iasi, Romania
Biplab Paul, Linköping University, Sweden
Jyh-Chiang Jiang, NTUST, Taiwan
Liang-Yih Chen, NTUST, Taiwan
M.V. Sangaranarayanan, Indian Institute of Technology-Madras, India
Günther Benstetter, Deggendorf Institute of Technology, Germany
Chia-Jyi Liu, Natioal Changhua University of Education, Taiwan
Sangaraju Shanmugam, Daegu Gyeongbuk Institute of Science and Technology, South Korea
Aman Mahajan, Guru Nanak Dev University, India
Aline Rougier, CNRS, France
Ganpati Ramanath, Rensselaer Polytechnic Institute, USA
Seon Jeong Kim, Hanyang University, Republic of Korea

Organizing Committee

Ahmet Yavuz Oral, Gebze Technical University, Turkey
Zehra Banu Bahsi Oral, Gebze Technical University, Turkey
M. Alper Sahiner, Seton Hall University, USA
Ersin Kayahan, Kocaeli University, Turkey
Mehmet Sezer, Gebze Technical University, Turkey

Conference Organizing Company

Aig Turizm Seyahat Kongre ve Org. Tic. Ltd. Şti.

Atatürk Cad No:1 Tever Apt. D:11
Sahrayıcedid, Kadıkoy Istanbul, Turkey
+90 216 330 80 90
http://aigtur.com.tr/

Editorial

The 3rd International Congress on Energy Efficiency and Energy Related Materials (ENEFM2015) provided all scientists the opportunity to meet, present their work, discuss and mutually interact in order to enhance and promote their research work.

This volume, published by Springer, includes selected papers presented at this Congress, held in Oludeniz, Turkey, October 19–23, 2015.

On behalf of organizing committee we would like to thank all the participants, plenary and invited speakers for their valuable contribution.

We would also like to thank AIGTUR for their support in the organization of the Congress as well as the publishers for the quality of this edition.

Gebze, Turkey

Ahmet Yavuz Oral
Zehra Banu Bahsi Oral

Contents

Contributors

Noureddine Abdelbaki University Akli Mohand Oulhadj, Bouira, Algeria

Sobhy M. Abdelkader Electrical Engineering Department, Mansoura University, Mansoura, Egypt

Abubakar Abdulkarim Department of Electrical and Electronics Engineering, University of Ilorin, Ilorin, Nigeria

Yassine Agguine Laboratoire de Chimie Bioorganique et Macromoléculaire (LCBM) Faculté des Sciences et Techniques, Université Cadi Ayyad, Guéliz, Marrakech, Morocco

Hedjaj Ahmed Faculty of Hydrocarbons and Chemistry Independence Street, Laboratory of Petroleum Equipments Reliability and Materials, University Mohamed Bougara, Boumerdes, Algeria

A. Babich National Research University of Electronic Technology, Zelenograd, Moscow, Russia

Anguel Baltov Institute of Mechanics, Bulgarian Academy of Sciences, Sofia, Bulgaria

Takayuki Ban Department of Chemistry and Biomolecular Science, Gifu University, Gifu, Japan

A. Baranchikov Kurnakov Institute of General and Inorganic Chemistry of the Russian Academy of Sciences, Moscow, Russia

Lallia Belkacem Faculty of Hydrocarbons and Chemistry Independence Street, Laboratory of Petroleum Equipments Reliability and Materials, University Mohamed Bougara, Boumerdes, Algeria

Kahina Bentaleb Unité Matériaux et Transformations – UMET (UMR CNRS N° 8207) Bâtiment C6, Université Lille 1 - Sciences et Technologies, Villeneuve d'Ascq Cedex, France; Laboratoire Physico-Chimie des Matériaux-Catalyse et

Environnement, Université des Sciences et de la Technologie d'Oran – Mohamed Boudiaf « USTO », Oran, Algeria

Mourad Bettayeb Faculty of Hydrocarbons and Chemistry Independence Street, Laboratory of Petroleum Equipments Reliability and Materials, University Mohamed Bougara, Boumerdes, Algeria

Kanhu Charan Bhuyan ECE Department, National Institute of Technology, Rourkela, India

Elahmoun Bouali Faculty of Hydrocarbons and Chemistry Independence Street, Laboratory of Petroleum Equipments Reliability and Materials, University Mohamed Bougara, Boumerdes, Algeria

Zohra Bouberka Unité Matériaux et Transformations – UMET (UMR CNRS N° 8207) Bâtiment C6, Université Lille 1 - Sciences et Technologies, Villeneuve d'Ascq Cedex, France; Laboratoire Physico-Chimie des Matériaux-Catalyse et Environnement, Université des Sciences et de la Technologie d'Oran – Mohamed Boudiaf « USTO », Oran, Algeria

Amel Boufrioua Electronics Department, Technological Sciences Faculty, University of Mentouri brothers Constantine, Constantine, Algeria

Kamel Bourai Centre de Développement Des Technologies Avancée (CDTA), Alger, Algeria

Th. Boutsika National Center for Scientific Research DEMOKRITOS, Institute of Nuclear and Radiological Sciences and Technology, Energy and Safety, Aghia Paraskevi, Attiki, Greece

Pınar Acar Bozkurt Department of Chemistry, Science Faculty, Ankara University, Ankara, Turkey

Razvan Buhosu Integrated Energy Conversion Power Systems and Advanced Control of the Complex Processes Research Centre, Dunarea de Jos University of Galati, Galati, Romania

Muammer Canel Department of Chemistry, Science Faculty, Ankara University, Ankara, Turkey

F. Capelli Department of Electrical Engineering, Universitat Politècnica de Catalunya, Terrassa, Spain; SBI Connectors Spain SLU, Sant Esteve Sesrovires, Spain

Daniel Champier Université Pau & Pays Adour, SIAME, Pau, France

Kheira Chinoune Laboratoire Physico-Chimie des Matériaux-Catalyse et Environnement, Université des Sciences et de la Technologie d'Oran «USTO», Oran, Algeria

Paul Cizmas Department of Aerospace Engineering, Texas A&M University, College Station, TX, USA

Joseph Coleman Mobile and Marine Research Centre, University of Limerick, Limerick, Ireland

Sterian Danaila Elie Carafoli Department of Aerospace Sciences, University Politehnica of Bucharest, Bucharest, Romania

Abdelkader Djelloul Centre de Recherche En Technologie Des Semi-Conducteurs Pour L'Energétique 'CRTSE', Alger, Algeria

Mahdi Ebrahimi Salari Mobile and Marine Research Centre, University of Limerick, Limerick, Ireland

Said Eddarir Laboratoire de Chimie Bioorganique et Macromoléculaire (LCBM) Faculté des Sciences et Techniques, Université Cadi Ayyad, Guéliz, Marrakech, Morocco

Georg Frey Chair of Automation and Energy Systems, Saarland University, Saarbrücken, Germany

Mohamed Gaceb Faculty of Hydrocarbons and Chemistry Independence Street, Laboratory of Petroleum Equipments Reliability and Materials, University Mohamed Bougara, Boumerdes, Algeria

Marian Gaiceanu Integrated Energy Conversion Power Systems and Advanced Control of the Complex Processes Research Centre, Dunarea de Jos University of Galati, Galati, Romania

Yosr E.E.D. Gamal National Institute of Laser Enhanced Sciences, Cairo University, El-Giza, Egypt

Chenlong Gao Department of Materials Science and Metallurgy, University of Cambridge, Cambridge, UK

B.A. Glowacki Department of Materials Science and Metallurgy, University of Cambridge, Cambridge, UK; Department of Physics and Energy, University of Limerick, Plassey, Ireland; Institute of Power Engineering, Warsaw, Poland

Dmitry G. Gromov National Research University of Electronic Technology, Zelenograd, Moscow, Russia

Abdelkader Guenda Centre de Recherche En Technologie Des Semi-Conducteurs Pour L'Energétique 'CRTSE', Alger, Algeria

Krzysztof Górecki Department of Marine Electronics, Gdynia Maritime University, Gdynia, Poland

Paweł Górecki Department of Marine Electronics, Gdynia Maritime University, Gdynia, Poland

Sławomir Halbryt SESCOM S.A., Gdańsk, Poland

Kholoud A. Hamam Department of Physics, Faculty of Science, King Abdulaziz University, Jeddah, Saudi Arabia

Uğur Hayta Department of Chemistry, Science Faculty, Ankara University, Ankara, Turkey

S. Hopkins Department of Materials Science and Metallurgy, University of Cambridge, Cambridge, UK

Elias Houstis IRETETH/CERTH and University of Thessaly, Volos, Greece

A. Ikonomopoulos National Center for Scientific Research DEMOKRITOS, Institute of Nuclear and Radiological Sciences and Technology, Energy and Safety, Aghia Paraskevi, Attiki, Greece

Yuki Ishikawa Department of Electrical and Electronic Engineering, Ibaraki University, Hitachi, Japan

Dragos Isvoranu Elie Carafoli Department of Aerospace Sciences, University Politehnica of Bucharest, Bucharest, Romania

Anatol Jaworek Centre of Hydrodynamics, Institute of Fluid-Flow Machinery Polish Academy of Sciences, Gdańsk, Poland

Naoto Kakimoto Department of Electrical and Electronic Engineering, Ibaraki University, Hitachi, Japan

Tolga Kara Faculty of Engineering and Natural Sciences, Istanbul Bilgi University, Istanbul, Turkey

I.S. Karavaev National Research University of Electronic Technology, Zelenograd, Moscow, Russia

Elena P. Kirilenko National Research University of Electronic Technology, Zelenograd, Moscow, Russia

Takumi Kishita Department of Electrical, Electronic and Computer Engineering, Gifu University, Gifu, Japan

Ya S. Kozhevnikov National Research University of Electronic Technology, Zelenograd, Moscow, Russia

S. Kozyukhin Kurnakov Institute of General and Inorganic Chemistry of the Russian Academy of Sciences, Moscow, Russia

Ewa Krac Department of Marine Electronics, Gdynia Maritime University, Gdynia, Poland

M. Krauz Ceramic Department CEREL, Institute of Power Engineering, Warsaw, Poland

Alicja K. Krella Centre of Hydrodynamics, Institute of Fluid-Flow Machinery Polish Academy of Sciences, Gdańsk, Poland

Andrzej Krupa Centre of Hydrodynamics, Institute of Fluid-Flow Machinery Polish Academy of Sciences, Gdańsk, Poland

R.V. Kumar Department of Materials Science and Metallurgy, University of Cambridge, Cambridge, UK

Tetsuji Kume Department of Electrical, Electronic and Computer Engineering, Gifu University, Gifu, Japan

S. Lalaouna SBI Connectors Spain SLU, Sant Esteve Sesrovires, Spain

P. Lazarenko National Research University of Electronic Technology, Zelenograd, Moscow, Russia

H.J. Lee Plasma Physics Lab, Department of Nuclear and Energy Engineering, Institute for Nuclear Science and Technology, Jeju National University, Jeju, South Korea

Constantin Leventiu Elie Carafoli Department of Aerospace Sciences, University Politehnica of Bucharest, Bucharest, Romania

K.A. Lyakhov Plasma Physics Lab, Department of Nuclear and Energy Engineering, Institute for Nuclear Science and Technology, Jeju National University, Jeju, South Korea

Kamalakanta Mahapatra ECE Department, National Institute of Technology, Rourkela, India

Linda Mahiou Centre de Recherche En Technologie Des Semi-Conducteurs Pour L'Energétique 'CRTSE', Alger, Algeria

Ulrich Maschke Unité Matériaux et Transformations—UMET (UMR CNRS N° 8207), Bâtiment C6, Université Lille 1—Sciences et Technologies, Villeneuve d'Ascq Cedex, France

Mourad Mebarki Centre de Recherche En Technologie Des Semi-Conducteurs Pour L'Energétique 'CRTSE', Alger, Algeria

Samir Meziani Centre de Recherche En Technologie Des Semi-Conducteurs Pour L'Energétique 'CRTSE', Alger, Algeria

D. John Morrow EPIC School of Electronics, Electrical Engineering and Computer Science, The QUB, Belfast, UK

Abderrahmane Moussi Centre de Recherche En Technologie Des Semi-Conducteurs Pour L'Energétique 'CRTSE', Alger, Algeria

M. Mumtaz Materials Research Laboratory, Department of Physics FBAS, International Islamic University (IIU), Islamabad, Pakistan

Abdelouahab Nadim Unité Matériaux et Transformations – UMET (UMR CNRS N°8207) Bâtiment C6, Université Lille 1 - Sciences et Technologies, Villeneuve d'Ascq Cedex, France; Laboratoire de Chimie Bioorganique et Macromoléculaire (LCBM) Faculté des Sciences et Techniques, Université Cadi Ayyad, Guéliz, Marrakech, Morocco

Antonia Nasiakou IRETETH/CERTH and University of Thessaly, Volos, Greece

Marco Nesarajah Chair of Automation and Energy Systems, Saarland University, Saarbrücken, Germany

Cristian Nichita University of Le Havre, Le Havre Cedex, France

Gergana Nikolova Institute of Mechanics, Bulgarian Academy of Sciences, Sofia, Bulgaria

Masaki Nomura Environmental and Renewable Energy Systems Division, Graduate School of Engineering, Gifu University, Gifu, Japan

Shuichi Nonomura Environmental and Renewable Energy Systems Division, Graduate School of Engineering, Gifu University, Gifu, Japan

Abdelkader Noukaz Centre de Développement Des Technologies Avancée (CDTA), Alger, Algeria

Suguru Odakura Department of Electrical and Electronic Engineering, Ibaraki University, Hitachi, Japan

Fumitaka Ohashi Environmental and Renewable Energy Systems Division, Graduate School of Engineering, Gifu University, Gifu, Japan

Muammer Ozbek Faculty of Engineering and Natural Sciences, Istanbul Bilgi University, Istanbul, Turkey

J.-R. Riba Department of Electrical Engineering, Universitat Politècnica de Catalunya, Terrassa, Spain

A. Rodriguez SBI Connectors Spain SLU, Sant Esteve Sesrovires, Spain

Maxim S. Rogachev National Research University of Electronic Technology, Zelenograd, Moscow, Russia

V.M. Rykov National Research University of Electronic Technology, Zelenograd, Moscow, Russia

Manuela Sechilariu Sorbonne University, Université de Technologie de Compiègne, Compiègne, France

Ahmad Syahiman Mohd Shah Department of Electrical and Electronic Engineering, Ibaraki University, Hitachi, Japan

A. Sherchenkov National Research University of Electronic Technology, Zelenograd, Moscow, Russia

M. Yu Shtern National Research University of Electronic Technology, Zelenograd, Moscow, Russia

Yury I. Shtern National Research University of Electronic Technology, Zelenograd, Moscow, Russia

A. Shuliatyev National Research University of Electronic Technology, Zelenograd, Moscow, Russia

Alexey S. Shulyat'ev National Research University of Electronic Technology, Zelenograd, Moscow, Russia

G. Sideratos National Center for Scientific Research DEMOKRITOS, Institute of Nuclear and Radiological Sciences and Technology, Energy and Safety, Aghia Paraskevi, Attiki, Greece

Sedat Sisbot Engineering Faculty Electrical Engineering Department, Izmir University, İzmir, Turkey

Arkadiusz T. Sobczyk Centre of Hydrodynamics, Institute of Fluid-Flow Machinery Polish Academy of Sciences, Gdańsk, Poland

Sorin Statescu Galfinband SA, Galati, Romania

Hiroki Takahashi Department of Electrical and Electronic Engineering, Ibaraki University, Hitachi, Japan

S. Timoshenkov National Research University of Electronic Technology, Zelenograd, Moscow, Russia

Daniel Toal Mobile and Marine Research Centre, University of Limerick, Limerick, Ireland

R.I. Tomov Department of Materials Science and Metallurgy, University of Cambridge, Cambridge, UK

Nesrine Touaa Laboratoire Physico-Chimie des Matériaux-Catalyse et Environnement, Université des Sciences et de la Technologie d'Oran «USTO», Oran, Algeria

Alexey Yu. Trifonov Scientific Research Institute of Physical Problems Named After F.V.Lukin, Moscow, Russia

K.M. Murat Tunc Faculty of Engineering and Natural Sciences, Istanbul Bilgi University, Istanbul, Turkey

Koki Uehara Environmental and Renewable Energy Systems Division, Graduate School of Engineering, Gifu University, Gifu, Japan

Zahir Usman Materials Research Laboratory, Department of Physics FBAS, International Islamic University (IIU), Islamabad, Pakistan

Manolis Vavalis IRETETH/CERTH and University of Thessaly, Volos, Greece

Mitsuo Yamaga Department of Electrical, Electronic and Computer Engineering, Gifu University, Gifu, Japan

Ana Yanakieva Institute of Mechanics, Bulgarian Academy of Sciences, Sofia, Bulgaria

Hasan Yazicioglu Department of Wind Energy, Technical University of Denmark, Kongens Lyngby, Denmark

Janusz Zarębski Department of Marine Electronics, Gdynia Maritime University, Gdynia, Poland

Dimitris Zimeris IRETETH/CERTH and University of Thessaly, Volos, Greece

Part I
General Issues

Urban DC Microgrids for Advanced Local Energy Management with Smart Grid Communication

Manuela Sechilariu

Abstract This paper presents an urban DC microgrid aiming an optimal energy management and taking into account messages from the smart grid. Concerning ancillary services, a microgrid controller is proposed to interact with the smart grid; it provides voltage control, power balancing, load shedding, and takes into account the system imposed constraints. Experimental results prove the technical feasibility of the urban DC microgrid. The study limits concern mainly the forecasting uncertainties and the real-time optimization.

Keywords Microgrid · Power optimization · Energy management · Smart grid

1 Introduction

The distributed energy generation shows a very rapid growth and reveals an increasing complexity for grid's managers due mainly to prosumer sites, i.e. producer and consumer sites.

The intermittent nature of renewable energy sources, e.g. photovoltaic (PV) generator, remains an issue for their integration into the public grid resulting in: fluctuations of voltage and/or frequency, harmonic pollution, difficulty for load management. This leads to new methods for power balancing between production and consumption [1].

Urban areas have great potential for intensive development of PV sources. To increase their integration level and obtain a robust power grid, the smart grid could solve problems of peak consumption, optimal energy management, and demand response. The smart grid is being designed primarily to exchange information on grid needs and availability, help balancing power, avoid undesirable injection, and

M. Sechilariu (✉)
Sorbonne University, Université de Technologie de Compiègne,
EA 7248 AVENUES Rue Roger Couttolenc CS 60319,
60203 Compiègne, France
e-mail: manuela.sechilariu@utc.fr

A.Y. Oral and Z.B. Bahsi Oral (eds.), *3rd International Congress on Energy Efficiency and Energy Related Materials (ENEFM2015)*, Springer Proceedings in Energy, DOI 10.1007/978-3-319-45677-5_1

perform peak shaving [2]. Concerning ancillary services (power grid technical regulations), for a better decentralization of the production, microgrids play an important role. A microgrid includes a multi-source system consisting of renewable and traditional energy sources, storage systems, and adjustable loads. A microgrid controller interacts with the smart grid; it provides voltage control, power balancing, load sharing or load shedding, and takes into account the constraints of the public grid provided by smart grid communication [1, 2].

In this context, at urban scale, the proposed system is a building-integrated DC microgrid, which provides a solution for the self-supply of buildings, electric vehicles, and grid-interaction control [3–5]. The microgrid controller is designed and developed like an intelligent energy management system that optimizes power transfer, adapts to conditions imposed by the public grid through the smart grid bus communication, and takes into account the various constraints in order to minimize the energy consumption from the public grid and to make full use of local production [6]. The interface between the smart grid and the proposed microgrid offers strategies which ensure, at the same time, local power balancing, local power flow optimization and response to grid issues such as peak shaving and avoiding undesired injections. The microgrid is proposed with DC bus link for an efficiently integration of other renewable sources and storage, for absence of phase synchronization, and because only the voltage must be stabilized. In addition, considering the DC bus and a DC load directly connected, the overall performance is improved by removing multiple energy conversions [5]. Indeed, a DC network building distribution may use the existing cables with the same power transfer as in AC distribution [7]. The DC bus can supply directly many building appliances (lighting, ventilation, electronic office equipment) as well as an electric vehicle.

The main scientific issue is the difficulty of global optimization due to the risk of mismatch between production/consumption predictions and real time operating conditions, on the one hand, and the need to take into account the constraints imposed by the public grid, on the other hand.

This paper presents the urban DC microgrid in Sect. 2 and the power management and optimization following the proposed microgrid controller in Sect. 3. A grid-connected DC microgrid, for which experimental results are given, is described in Sect. 4. Conclusions and furthers works are given in Sect. 5.

2 Urban DC Microgrid

The concept of smart grid appears and leads to microgrids for prosumer sites in order to reduce losses and peak energy demand, and also to play a role in local regulation, through the data communication. In urban areas, at the local level, the microgrid may be integrated to the building prosumer and connected to public grid by an adapted controller. At urban scale there are several building-integrated microgrids and parts of traditional public grid, all connected to the grid by a point of common coupling [2]. Intelligent switches are used to allow connection and

islanding. Furthermore, a communication network is added, i.e. communication bus, whose routers are dedicated to direct messages following energy management priorities or special areas. Some dedicated controller interfaces generate and receive messages. The urban DC microgrid developed below is building-integrated and connected to the smart grid as described above.

3 Power Management and Optimization

The microgrid controller must provide the interface between the public grid and the loads (e.g. buildings, electric vehicles), aiming an optimal power management.

Figure 1 illustrates the power management interface principle based on the main data which have to be exchanged between the microgrid and the public grid. Thus, the microgrid controller must take into account information about the public grid availability and dynamic pricing, inform the smart grid on injection intentions and power demand, meet the demand of the end-user with respect to all physical and technical constraints, and operate with the best energy cost for the public grid and for the end-user. To meet these objectives as well as other actions described in Fig. 1 (forecasting, smart metering, monitoring…) a specific interface associated with the urban microgrid was designed as proposed thereafter.

The developed microgrid controller presented in Fig. 2 is a multilayer and multiscale design able to provide flexibility with respect to the necessary algorithms [6]. There are four functional layers whose response times range from days to less than a second. Human-machine interface allows taking into account the end-user options as predefined operating mode, or building critical loads, or load shedding limit, or other specific criteria. Prediction layer takes into account the end-user option, several forecast data (building operating mode, grid time-of-use, and weather), and aims to calculate two powers related to: renewable energy production prediction and energy demand prediction. These two powers are given as inputs for the energy management layer which is the most important intelligent layer. The energy costs optimization is calculated in this layer and is mainly based on the previously calculated predictions and the system constraints such as dynamic pricing, peak consumption, public grid vulnerabilities, and storage capacity. The

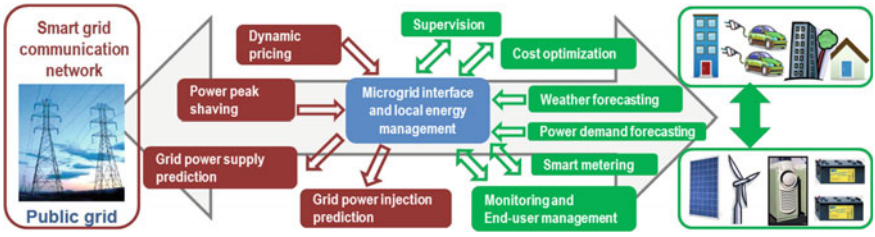

Fig. 1 Power management interface principle

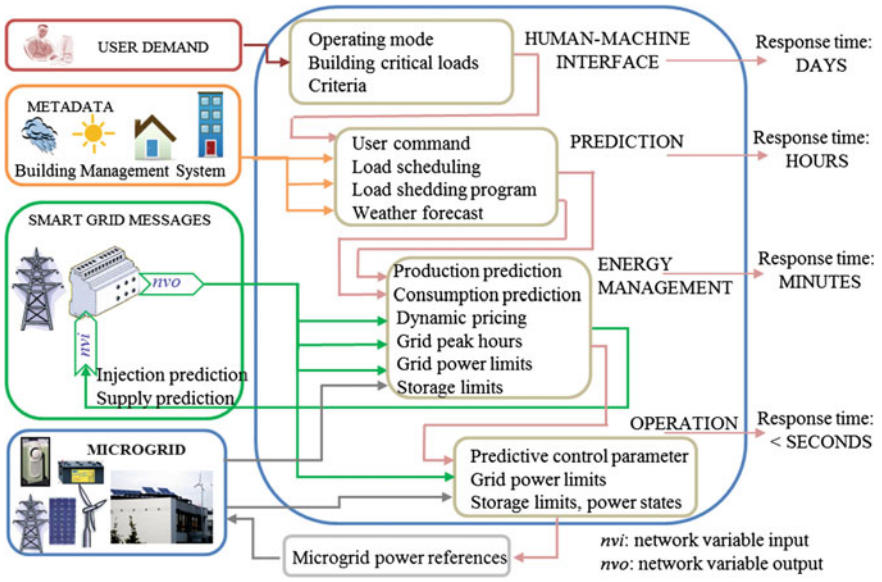

Fig. 2 Microgrid controller

optimization is solved by mixed integer linear programming and the solver could be CPLEX [8]. The obtained results are the optimal power evolution of each source for which the total cost is the minimum for the considered time duration. These powers cannot easily be implemented in real-time control. The solution is to translate the power flows into a single interface parameter for power balancing control, which is the predictive control parameter, one of the outputs of this layer. The second output concerns the predictions to be transmitted to smart grid (injection and supply). The predictive control parameter is applied in the operational layer, which algorithm controls the power balancing in the microgrid system.

The algorithm provides real-time references of the system powers and the coefficient of possible load shedding.

For urban microgrids several operating strategies are developed based on sources that make up the microgrid (PV sources and wind turbine, storage, public grid connection, micro-turbine or bio-diesel generator) and loads (buildings electric loads and electric vehicles charging stations). Figure 3 presents the main possible strategies. Renewable energies supply the building and charge the electric vehicles. The renewable excess energy could be stored and/or injected into the grid. The grid, if available, is used only as back-up for the building and the electric vehicles. The micro-turbine operates only if the grid is not available. The electric vehicles, if required for stringent situations, can supply the building and/or provide energy to the grid. The messages received from the smart grid command the microgrid operating mode aiming compliance the actual availability of the grid.

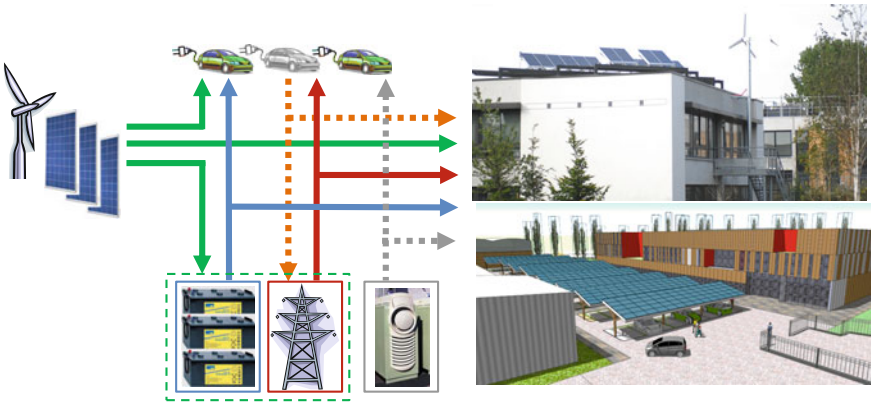

Fig. 3 Energy management strategies for urban DC microgrid

4 Building-Integrated DC Microgrid for Grid-Connected Mode

The DC microgrid given in Fig. 4 consists of physical power system and its controller as presented above. The power system includes a DC load and sources which are connected on the DC bus through their dedicated converters, while the DC load demands power directly from the DC bus.

The power balancing control principle and constraints are presented following the power flow schema shown in Fig. 5 [6]. The proposed strategy is to operate with the minimum energy cost for the considered period. Within the given limits, the public grid can supply or absorb energy to or from the microgrid. The same applies to the storage, charge or discharge operating mode. The DC load can demand power up to its maximum power, but limited power can be a load shedding result. For the PV array (PVA), two controls are implemented: a maximum power

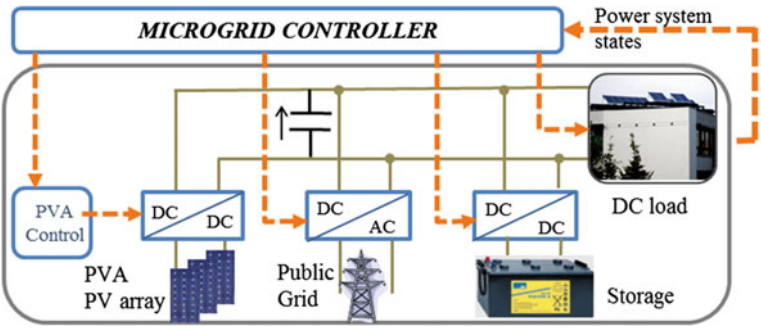

Fig. 4 DC microgrid building-integrated for grid-connected mode

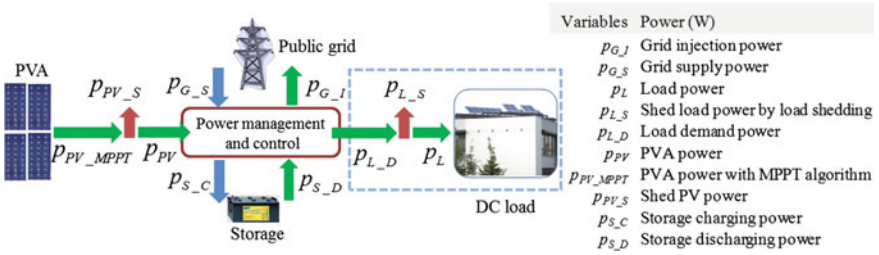

Fig. 5 Control principle and constraints following the power flow schema

point tracking (MPPT) control to extract the maximum power and a limited control to extract a limited power to meet power balancing for some stringent situations. The power balancing shows that the adjustment variables are the public grid and storage, within their physical and functional limitations. The predictive control parameter decides the contribution of these two sources, grid and storage. This control parameter must be the image of the power flow optimized in energy costs. The energy cost optimization take into account the day-ahead forecasting of the PVA production as well as the load power demand. Combined with this robust power balance strategy, the energy cost optimization is formulated as minimization of the total energy cost with respect to system physical constraints and imposed limits. To minimize the energy cost, energy tariffs are imposed as follow. The storage can be used as often as possible; an arbitrary but lowest tariff is given. In order to avoid the two operations, very penalizing energy tariff is proposed for PVA power limiting and load shedding. Public grid tariff is suggested to be lower than the PVA or load shedding tariff. There are two grid tariffs: peak hours and normal hours. The end-user can accept certain amount of load shedding.

Following the experimental platform given in [5, 6], three tests were done in 2013 for three different meteorological profiles. For each profile, Table 1 presents the obtained total energy costs for ten hours: C1 as optimum cost following power predictions, C2 as actual cost (experiment), and C3 as optimum cost for real conditions calculated after operation. One notes that C2 is close to C3.

Table 1 Energy total cost

Case	Total energy cost (€)		
	August 21	August 9	July 30
C1	−0.777	−0.149	0.386
C2	0.225	0.929	3.219
C3	−0.247	0.357	2.165

5 Conclusions

The DC microgrid optimizes energy cost and offers good predictive management. It is a reconfigurable control, easy to implement, and uncertainties do not affect the control; however the energy cost becomes suboptimal.

References

1. Hatziargyriou, N.: Microgrids: architectures and control. Wiley–IEEE, New York (2014). doi:10.1002/9781118720677.fmatter
2. Wang, B.C., Sechilariu, M., Locment, F.: Intelligent DC microgrid with smart grid communications: control strategy consideration and design. IEEE T Smart Grid **3**(4), 2148–2156 (2012). doi:10.1109/TSG.2012.2217764
3. Sechilariu, M., Wang, B.C., Locment, F.: Building integrated photovoltaic system with energy storage and smart grid communication. IEEE T Ind. Electron. **60**, 1607–1618 (2013). doi:10.1109/TIE.2012.2222852
4. Locment, F., Sechilariu, M.: Modeling and simulation of DC microgrids for electric vehicle charging stations. Energies **8**, 4335–4356 (2015). doi:10.3390/en8054335
5. Sechilariu, M., Locment, F., Wang, B.C.: Photovoltaic electricity for sustainable building. Efficiency and energy cost reduction for isolated DC microgrid. Energies **8**, 7945–7967 (2015). doi:10.3390/en8087945
6. Sechilariu, M., Wang, B.C., Locment, F., Jouglet, A.: DC microgrid power flow optimization by multi-layer supervision control. Design and experimental validation. Energ. Convers. Manage **82**, 1–10 (2014). doi:10.1016/j.enconman.2014.03.010
7. Patterson, B.T.: DC, come home: DC microgrids and the birth of the "enernet". IEEE Power Energy M **10**(6), 60–69 (2012). doi:10.1109/MPE.2012.2212610
8. IBM: ILOG CPLEX optimizer. http://ibm.com (2012). Accessed 10 Oct 2015

Proper Orthogonal Decomposition Applied to a Turbine Stage with In-Situ Combustion

Dragos Isvoranu, Sterian Danaila, Paul Cizmas and Constantin Leventiu

Abstract The paper presents a POD analysis of the numerical simulation results obtained from the numerical simulation of transport phenomena in a one-stage turbine-combustor (i.e. a turbine stage with in situ combustion). The motivation of this research is to investigate the new fuel injection concept that consists of a perforated pipe placed at mid-pitch in the stator row passage and different axial positions. The main goal of this simulation is to assess the stability of the in situ combustion with respect to the unsteadiness induced by the rotor-stator interaction. To identify the sources of instability for this complex flow, the proper orthogonal decomposition technique is used to analyze the natural patterns and couplings between various modes of pressure, temperature, velocity and chemical production rate distributions.

Keywords Turbine combustor · POD · Natural patterns

1 Introduction

This in situ reheat takes place in a turbine-combustor, that is, a turbine where fuel is injected and combusted, in addition to the combustion that takes place in the main combustor. For the same power produced, in situ reheat allows the decrease of the thermal load in the main combustor, therefore reducing the maximum temperature of the cycle and the temperature variation throughout the combustion process. Decreasing the combustor temperature reduces the NOx and unburned hydrocarbon emissions and also diminishes the need for costly combustor materials and thermal barrier coatings on the combustor liner, enabling a more resource efficient

D. Isvoranu (✉) · S. Danaila · C. Leventiu
Elie Carafoli Department of Aerospace Sciences, University Politehnica of Bucharest, Bucharest, Romania
e-mail: ddisvoranu@gmail.com

P. Cizmas
Department of Aerospace Engineering, Texas A&M University, College Station, TX, USA

A.Y. Oral and Z.B. Bahsi Oral (eds.), *3rd International Congress on Energy Efficiency and Energy Related Materials (ENEFM2015)*, Springer Proceedings in Energy, DOI 10.1007/978-3-319-45677-5_2

manufacturing. A performance cycle analysis for this type of GTE included in [1] showed that for high speed transportation (above Mach 2.2) the turbine burner has the best fuel economy. To our best knowledge, besides pioneering works referenced in [2–4], one of the most interesting publicly released research in this domain dates back in 2009 and belongs to a group of researchers at University of California at Irving [5].

2 Proper Orthogonal Decomposition

The Proper Orthogonal Decomposition (POD) is a method that reconstructs a set of data from its projection on an optimal basis. Besides using an optimal basis for reconstructing data, POD does not use any prior knowledge of the data set. Because it is dependent only on the basis of data, POD is also used in natural patterns analysis of the flow field.

To rebuild the dynamic behavior of a system, POD breaks down data into two parts: a time dependent part, that generates the amplitude coefficients $a_k(t)$ and a spatial coordinates dependent part that yields an orthonormal functional basis $\psi_k(\mathbf{x})$. The reconstructed model reads:

$$u(\mathbf{x}, t) = \sum_{k=1}^{M} a_k(t) \cdot \psi_k(\mathbf{x}) \tag{1}$$

where M is the number of data snapshots. The reconstruction dataset error is:

$$\varepsilon(\mathbf{x}, t) = u(\mathbf{x}, t) - \sum_{k=1}^{M} a_k(t) \cdot \psi_k(\mathbf{x}) \tag{2}$$

The functional basis on which this set is reconstructed is optimal as the average of the squared error is minimized for any number $m \leq M$ of base functions from all possible sets of orthogonal functions.

In the field of fluid mechanics, two main approaches have been used: the first one, the classical, continuous POD was promoted by Lumley [6]; the second one, is based on the so called snapshot approach and originates in the works of Sirovitch [7].

Herein, the discrete POD-snapshot approach is used. We start form a set of M snapshots obtained from the numerical simulation of the given model. The simulation can be performed either with a commercial or in-house code. The sampling rate must comply with Nyquist-Shannon [8] criterion used for signal reconstruction. The construction of the correlation matrix is done as follows, either for a vector valued or scalar valued function. Assuming that the quantity of interest is denoted by u, first we have to arrange all its values for a certain snapshot in a vector with dimension N (N could be very large depending on the discretized

model). Then, for each following snapshot, we proceed identically in order to build the next $N \times M$ matrix:

$$W_C = \begin{bmatrix} u(\mathbf{x}_1, t_1) & u(\mathbf{x}_1, t_2) & \cdots & u(\mathbf{x}_1, t_M) \\ u(\mathbf{x}_2, t_1) & u(\mathbf{x}_2, t_2) & \cdots & u(\mathbf{x}_2, t_M) \\ \vdots & \vdots & \cdots & \vdots \\ u(\mathbf{x}_N, t_1) & u(\mathbf{x}_N, t_2) & \cdots & u(\mathbf{x}_N, t_M) \end{bmatrix} \tag{3}$$

The correlation matrix is then built as $C_{M\times M} = W_C^T \cdot W_C$. The previous square matrix is positive definite, hence it yields positive, real eigenvalues λ_k and the associated eigenvectors ϕ_k that are rearranged in a matrix Φ from the most energetic to the least energetic content (eigenvalues in decreasing order). The eigenmodes with only spatial dependence ψ_k are obtained as:

$$\Psi_{N\times M} = (W_{N\times M} \cdot \Phi_{M\times M}) \cdot L_{M\times M} \tag{4}$$

where $L_{M\times M}$ is a diagonal square matrix with elements $1/\sqrt{\lambda_k}$ arranged in descending order. The reconstruction of $\tilde{u}(\mathbf{x}, t)$ based on $m < M$ modes follows the equation:

$$\tilde{u}(\mathbf{x}, t) = \sum_{k=1}^{m} \sqrt{\lambda_k}\phi_k(t)\psi_k(\mathbf{x}) = \sum_{k=1}^{m} a_k(t)\psi_k(\mathbf{x}) \tag{5}$$

Considering the flow variables of interest, ROM models (Eq. 5) can be devised for each one of them.

3 Results

The simulation performed for the turbine combustor [9] offered the requested snapshots with a sampling rate of 10 snapshots per cycle. Here, a cycle is defined as the time requested for the rotor to travel a distance equal to the stator pitch length at mid span. First 41 out of 200 snapshots were analyzed. The configuration space contains density, absolute pressure, velocity components in stationary frame, temperature, static entropy, Mach number and the reaction rates for methane and carbon mono-oxide oxidation. Applying the procedures described by Eqs. (3)–(5) we obtained the specific eigenspectra. Figure 1 illustrates these spectra for temperature and methane decomposition reaction.

The most outstanding feature of the eigenspectra for the specified configuration space is the similarity of the eigenvalue modal distributions among all flow variables except for the two reaction rates. The “energy” spectrum for the methane oxidation rate needs at least 20 modes to cover 95 % of the total energy content, while for the rest of the variables 1 mode is sufficient. Five modes are needed for

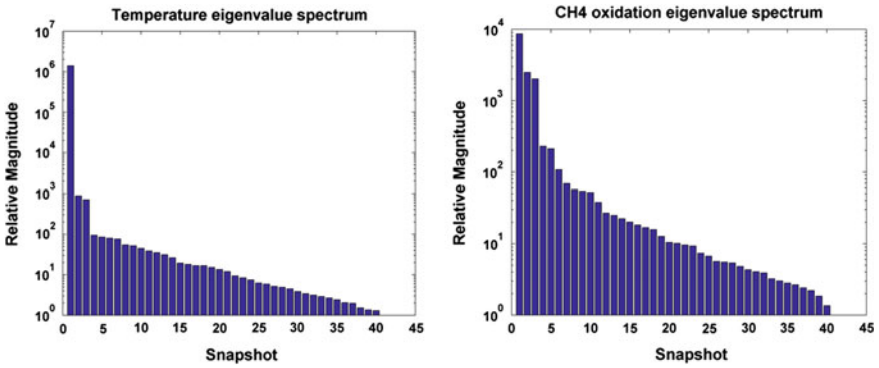

Fig. 1 Temperature (*left*) and CH_4 oxidation rate (*right*) eigenspectrum

CO oxidation rate. The same observation becomes apparent from the normalized RMSE of the reconstructed snapshots displayed in Fig. 2.

The normalized error is reduced by more than 50 % for all variables in the configuration space when incresing the number of modes from 5 to 20. However, the error is unacceptable for CH_4 oxidation rate and still too large for CO oxidation rate. The natural patterns of the reactive flow are associated with the eigenmodes ψ_k distributions. It was confirmed that first mode distributions are similar to the first snapshot variables distributions, excepting the scale. As expected, the reaction rates and temperature modes are well coupled up until the third mode (Fig. 3) even if the nodes and antinodes switch places along the rotor-stator interface. Beyond third mode, these correlations are lost for CH_4 reaction rate but remain visible for CO reaction rate and temperature up to fifth mode.

The next acoustic modes bring new correlations between absolute pressure and CO reaction rate along the rotor-stator interface which are apparent from Fig. 4.

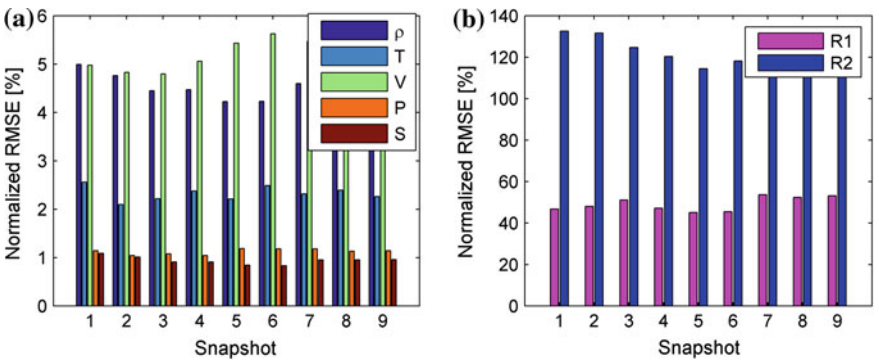

Fig. 2 Accuracy for the first nine reconstructed snapshots for 5 modes reconstruction; **a** flow variables; **b** reaction rates

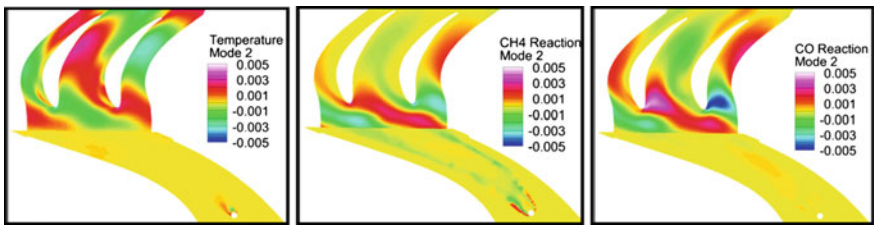

Fig. 3 Temperature and reaction rates correlations on the second mode

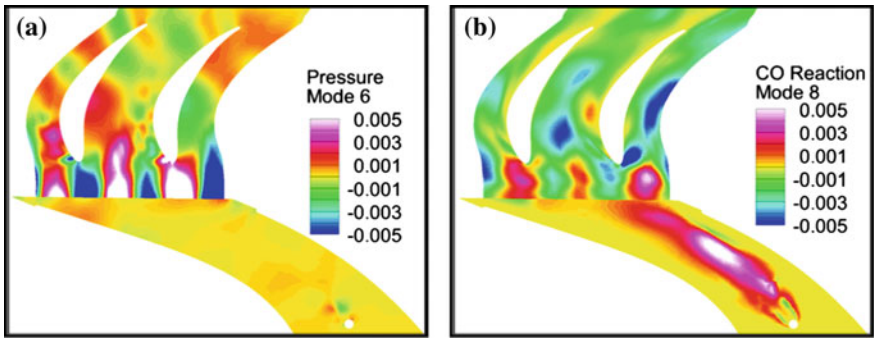

Fig. 4 Acoustic correlations between pressure (**a**) and CO reaction rate (**b**)

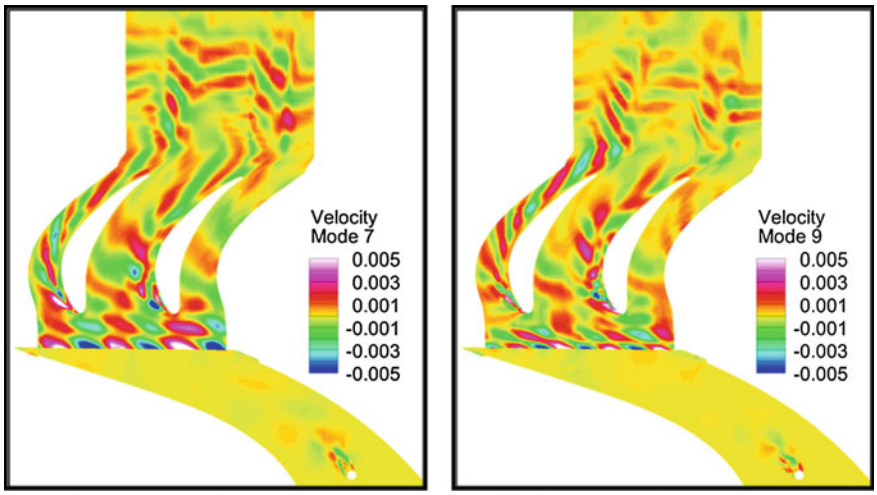

Fig. 5 Velocity odd-even decoupling in the wake of the injection pipe for modes 7 and 9

Odd-even decoupling and oscillations are characteristics emerging from higher acoustic modes for pressure and velocity, especially in the wake of the injection pipe, as depicted in Figs. 4a and 5.

4 Conclusions

In this study we explored the possibility of using the POD method for obtaining information on the natural patterns of various transport quantities that define the gas expansion in a turbine-combustor. The paper presented the methodology proposed for developing this reduced-order model. The numerical investigation of the energy spectra showed a large disparity between the numbers of modes needed for reconstructing flow variables compared to the variables describing the chemical species. While using the Westbrook-Dryer mechanism [10], the reconstruction of CH_4 oxidation rate required the largest number of modes. To improve the accuracy of the reduced-order model, we identified the following options: (1) using a higher frequency for sampling the full-order model (FOM), (2) using smaller time steps in the FOM/ROM numerical simulations, and (3) revisiting the reaction mechanism and finding better reaction rate coefficients.

Acknowledgments This research was funded by the Joint Applied Research Project PN-II-PT-PCCA-2013-4, with the support of ANCS, CNDI—UEFISCDI, contract no. 286/2014.

References

1. Sirignano, W.A., Liu, F.: Performance increases for gas-turbines engines through combustion inside the turbine. J. Propul. Power **15**(1), 111–118 (1999). doi:10.2514/2.5398
2. Isvoranu, D., Cizmas, P.G.A.: Numerical simulation of combustion and rotor-stator interaction in a turbine combustor. Int. J. Rotating Mach. **9**(5), 363–374 (2003). doi:10.1155/S1023621X03000344
3. Chambers, S., Flitan, H., Cizmas, P., Bachovchin, D., Lippert, T., Little, D.: The influence of in situ reheat on turbine-combustor performance. J. Eng. Gas Turbines Power, **128**(7), 560–572 (2006). doi:10.1115/GT2004-54071
4. Bachovchin, D., Lippert, T., Newby, R.A., Cizmas, P.G.A.: Gas turbine reheat using in situ combustion. https://www.etde.org/etdeweb/servlets/purl/827534-LNef4Y/native/827534.pdf (2004). Accessed 21 Dec 2006
5. Sirignano, W.A., Dunn-Rankine, D., Liu, F., Colcord, B., Puranam, S.: Turbine burners: turbulent combustion of liquid fuels. Final Report www.dtic.mil/cgi-bin/GetTRDoc?AD=ADA513881 (2009). Accessed 30 Aug 2013
6. Lumley, J.: Stochastic Tools in Turbulence. Academic Press (1970)
7. Sirovich, L.: Turbulence and the dynamics of coherent structures, parts I-III. Q. Appl. Math. **45**, 561–590 (1987)
8. Jerri, A.J.: The Shannon sampling theorem—its various extensions and applications: a tutorial review. Proc. IEEE **65**(11), 1565–1596 (1977). doi:10.1109/PROC.1977.10771

9. Danaila, S., Isvoranu, D., Leventiu, C.: Preliminary simulation of a 3D turbine stage with in situ combustion. Appl. Mech. Mater. **772**, 103–107 (2015). doi:10.4028/www.scientific.net/AMM.772.103
10. Westbrook, C.K., Dryer, F.L.: Simplified reaction mechanisms for the oxidation of hydrocarbon fuels in flames. Combust. Sci. Technol. **27**, 31–43 (1981). doi:10.1080/00102208108946970

Strategies of Maximizing the Benefits of Storage and Diesel Generator for Standalone Microgrid

Abubakar Abdulkarim, Sobhy M. Abdelkader and D. John Morrow

Abstract This paper proposed methods of maximizing the benefits of storage and diesel generator connected to a standalone microgrid. The analysis is based on the effects of site and size factors on the number of times diesel generator starts. Markov technique has been used for the analysis of the output powers of the WECS and SECS. The proposed method has been tested by increasing the rated power of the WECS and SECS by 25, 50, 75 and 100 %. The results have shown a decreased in the number of times a diesel generator starts by 2, 7, 9 and 9 % for WECS. Similarly, SECS decreased same by 4, 8, 11, and 13 %. Also, study of wind generator parameter at different cut-in-speeds levels, including 2, 2.5, 3.5 and 4 m/s reduced the number of times a diesel generator start by 122, 147, 116 and 134. In addition, the influences of storage and weather on the availability of system have also been investigated using Variable Boolean Logic Driven Markov process. In this case, the results have shown adding storage system; increased the microgrid availability by 0.058. In the same way, neglecting weather factor overestimate the system availability by 0.0104. Also, increasing the rated power of the WECS is the best way of maximizing the BCR of the system.

Keywords Microgrid · Availability · Wind · PV · Diesel generator · Battery

A. Abdulkarim (✉)
Department of Electrical and Electronics Engineering, University of Ilorin, Pmb 1515, Ilorin, Nigeria
e-mail: abkzarewa@yahoo.com

S.M. Abdelkader
Electrical Engineering Department, Mansoura University, Mansoura 35516, Egypt
e-mail: sobhy_abdelkader@yahoo.com

D.J. Morrow
EPIC, School of Electronics, Electrical Engineering and Computer Science, The QUB, Belfast, UK
e-mail: dj.morrow@ee.qub.ac.uk

A.Y. Oral and Z.B. Bahsi Oral (eds.), *3rd International Congress on Energy Efficiency and Energy Related Materials (ENEFM2015)*, Springer Proceedings in Energy, DOI 10.1007/978-3-319-45677-5_3

1 Introduction

Isolated loads and communities are left behind the schemes of things in the area of energy utilization. Global figure has shown that about 1.5 billion people are known to have no access to the electricity. Therefore, these people are forced to use fuel for their daily energy needs and relied on the use of diesel generator.

Adding renewable energy resources such as wind and solar to an existing diesel generator may affect the characteristics of the systems such as reliability, carbon emission and the cost of the energy. In some cases due to the variability of the output powers of the renewable energy resources, there is need to add a storage system. In this arrangement the diesel generator operates only when the renewable energy and storage cannot meet the demand. Therefore, the economic benefit of the system is expected to improve. This necessitated the need to investigate the strategies that will decrease the number of times a diesel generator start. Adding storage into the hybrid microgrid system may to affect the availability of the network. In the same way there is need to analyse the improvement in the system availability. This will be the basis for comparing the availability of operating the microgrid in the presence and absence of storage system.

2 Output Power of the Renewable Energy System

Renewable energy potential of Belfast, United Kingdom is used in the analysis. The hourly output power of the wind energy conversion system (WECS) and solar energy conversion system (SECS) are combined to determine the hourly renewable output power of the microgrid. It is assumed that modelling this way takes hourly fluctuations of both WECS and SECS into consideration. WECS output power is a function of the three wind speed, these results in different design alternatives [1]. The power output of wind energy conversion system is determined using Eq. 1.

$$P(v) = \begin{array}{cc} P_r \cdot \frac{V_i - V_{ci}}{V_r - V_{ci}} & V_{ci} < V < V_r \\ P_r & V_r \leq V < V_{co} \\ 0 & V \leq V_{ci} \text{ or } V \geq V_{co} \end{array} \quad (1)$$

On the other hand, the output power of the SECS can be determined from different mathematical models. The model used in the determination of the output power of the SECS is expressed in Eq. 2.

$$P_{SEC} = \eta_g A_m N_{PV} G_t \quad (2)$$

where, P_r: rated power of WECS, V_i, V_{ci}, V_r and V_{co}: wind, cut-in, rated and cut-out speed respectively. G_t is the solar radiation of the operating point (w/m^2), η_g is the instantaneous PV generator efficiency, A_m is the area of a single module used in the

analysis (m^2) and N_{PV} is the number of module. The module efficiency can be determined based on the mathematical model defined in [1]. The total hourly output power of the renewable energy side of the proposed system is used to derive the renewable energy power classes. This includes minimum power (Pmin), maximum power (Pmax) and the mean power of the system as described in [2]. By modelling this way, it is possible to determine the transition rates between power classes of the site.

3 Markovian Model

In order to analyse the hybrid microgrid using Markov process, a Markov model has been developed. The model is assumed to consist of the output powers of the two renewable energy resources. It is assumed that each state correspond to a class with corresponding output power levels of the state. The mathematical expressions of these variables are described in [2]. Repeating the load demand for a period of one year shows the need for a storage and diesel generator. These have been added to the system by proposing an algorithm that is not shown here. However, after incorporation of the storage and a diesel generator, the influences of these units on the system response have been observed. The new power profile and table were obtained. On the other hand, the solution of the model is shown in Table 1. Total annual energy need by the system is determined using Eq. 3.

$$E_{Li} = 24 \cdot 365 \cdot \sum_{i=1}^{N} P_{Li} \cdot T_{Li} \tag{3}$$

where, P_{Li} and T_{Li} represents the demand and the duration of each interval.

Table 1 Steady state solution

Power class	Steady state probability	Duration (h) Mr.	Frequency (Event/h) fr
P0	0.1515	1.6464	0.0920
P1	0.0842	1.3692	0.0615
P2	0.0162	1.2137	0.0134
P3	0.0901	1.1418	0.0789
P4	0.1140	1.1100	0.1027
P5	0.0903	1.0632	0.0849
P6	0.0523	1.0481	0.0499
P7	0.0872	1.0092	0.0864
P8	0.1570	1.0000	0.1570
P9	0.0693	1.0000	0.0693
P10	0.0879	1.0000	0.0879

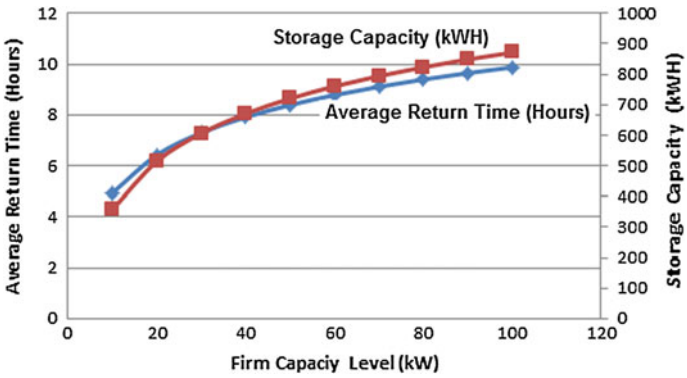

Fig. 1 Average return time and storage capacity at different firm levels

4 Economics Benefits of the Storage

It has already been established that the output power of the renewable energy depends on the failure and repair rate of the WECS and SECS. Therefore, a model that takes the failure rate and repair rates into considering is proposed. The modification introduced in this paper is the assumption on the determination of the failure and repair rates of the system. The proposed procedure determined the failure and the repair rates using the series parallel theorems of reliability algebra. Modelling this way enables the use Markov theorem for the determination of the capacity of the storage system such that it has economic value. The output powers of the renewable energy sources are represented by the 3–state Markov model [3]. The aim is to determine the storage capacity that could be used for the maximum net saving. System average return time and capacity Q as a function of firm capacity is shown in Fig. 1. Similarly, the total annual cost and the system savings as a function of storage capacity is also presented in Fig. 2. In the same way, the system BCR and total savings at different storage capacity are related in Fig. 3. The sensitivity analyses of the rated power of the WECS and SECS have shown that BCR of the proposed systems is more sensitive to the rated power of WECS. In addition, the results have shown a decreased in the BCR of the system with increased in the rated power of the WECS and the SECS. Also the system saving is not sensitive to the rated power of the WECS and SECS.

5 Benefits of Storage on the System Availability

System availability is one of the problems against the utilizations of renewable energy resources. Therefore, this section proposed another approach to investigate this factor. The proposed method combined Markov process and Fault tree. This

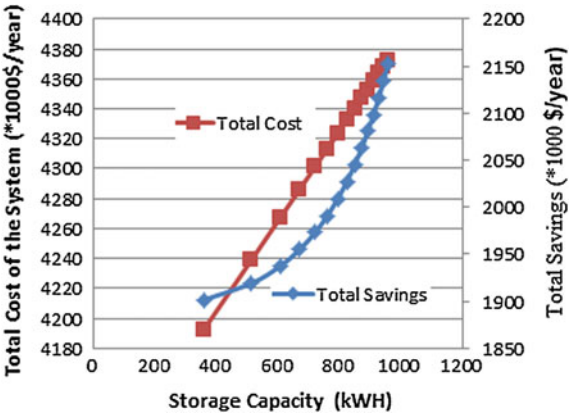

Fig. 2 Total cost of the system and savings as a function of storage capacity

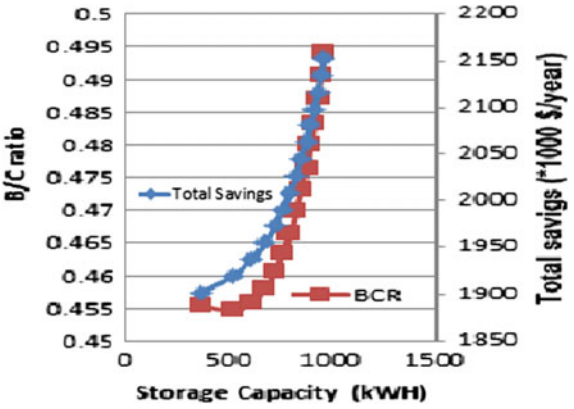

Fig. 3 BCR and annual savings against storage capacity

approach is called variable Logic Driven Markov Process (BDMP) [4]. BDMP is proposed because it uses state transition rate instead of state probabilities. Application of the proposed procedure is tested on a standalone microgrid. It is initially assumed that the system consists of diesel generator. Therefore the availability of the system is the availability of the diesel generator. Adding WECS and SECS to the diesel generator leads to a different availability of the system. Availability model of the hybrid system is presented in the form of the state space model shown in Eq. 4. Solution of the model shows that the availability of the microgrid is 0.9170. Integration of the storage result into a more complex state space model that is not shown here and the availability of the microgrid is 0.9735.

$$\begin{bmatrix} \dot{p}_o(t) \\ \dot{p}_1(t) \\ \dot{p}_2(t) \\ \dot{p}_3(t) \\ \dot{p}_4(t) \\ \dot{p}_5(t) \end{bmatrix} = \begin{bmatrix} -(\lambda_T + \lambda_{DG}) & \mu_R & \mu_T & 0 & 0 & 0 \\ \lambda_{DG} & -(\lambda_T + \lambda_{DG} + \mu_R) & 0 & \mu_T & \mu_{DG} & 0 \\ \lambda_T & 0 & -(\lambda_R + \mu_T) & \mu_R & 0 & 0 \\ 0 & \lambda_T & \lambda_R & -(\lambda_{DG} + \mu_R + \mu_R) & 0 & \mu_{DG} \\ 0 & \lambda_{DG} & 0 & \lambda_{DG} & -(\lambda_T + \mu_{DG}) & \lambda_T \\ 0 & 0 & 0 & 0 & \lambda_T & -(\mu_{DG} + \mu_T) \end{bmatrix} \times \begin{bmatrix} p_o(t) \\ p_1(t) \\ p_2(t) \\ p_3(t) \\ p_4(t) \\ p_5(t) \end{bmatrix} \tag{4}$$

6 Effects of Size Factors on the Diesel Generator

This section studies the effects of the size factors on the operation of diesel generator. The effects have come down to the rated power of the WECS and SECS. The aim of this section is achieved by analysing the number of times a diesel generator starts. Different simulations have been carried out including the base case in which the actual renewable energy potentials of the area are used. Follow by cases II, III, IV and V for 25, 50, 75 and 100 % increase in the rated power of the WECS and SECS. The result of this analysis is shown in Fig. 4. The results have shown a

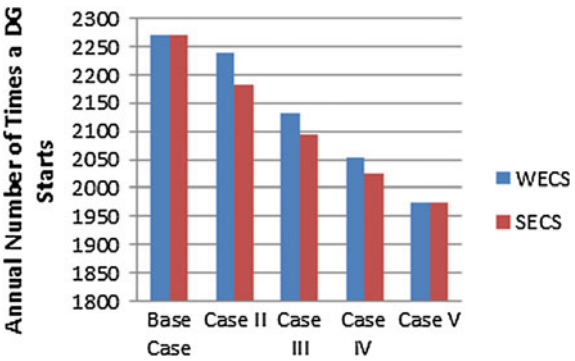

Fig. 4 Number of diesel generator starts VS rated power

decreased in the number of times a diesel generator starts by 2, 7, 9 and 9 % for WECS. Similarly, SECS decreased same by 4, 8, 11, and 13 %.

7 Effects of Site Factors on the Diesel Generator

Another factor in the analysis of hybrid microgrid is the cut-in-speed of the wind turbine generator. Variations of cut-in speed with the number times a diesel generator start is investigated. Therefore, in order to achieve this aim, the cut-in speed of the wind turbine is varies at different levels. The levels include 2.0, 2.5, 3.0, 3.5 and 4.0 m/s. The numbers of times diesel generator starts are 112, 147, 116 and 134 respectively. Hence it can be seen that the best system benefit is obtained when the cut-in speed is 2.5 m/s. The cut-in-speed affects the number of times diesel generator starts.

8 Conclusion

The paper has shown that it is possible to determine the storage capacity required for the maximum benefit of storage connected to standalone microgrid. The best way of maximizing the benefit of the proposed microgrid is by increasing the rated power or decrease the capital cost of the WECS. System availability increased by 5.8 % when a storage system is added compared to operating the system without storage system. In the same way, the percentage number of times a diesel generator start is more sensitive to the rated power of SECS. Finally, for realistic planning, the papers show that the cut-in speed of wind turbine has a great influence on the number of times a diesel generator start. Further works can be on the impacts of different hybrid energy technology on the availability of the proposed system.

References

1. Tafreshi, S., Zamani, H., Ezzati, S., Vahedi, H.: Optimal unit sizing of distributed energy resources in microgrid using genetic algorithm. 18th Iranian conference on electrical engineering (ICEE), Isfahan, Iran (2010). doi:10.1109/IRANIANCEE.2010.5506961
2. Manco, T., Testa, A.: A Markovian approach to model power availability of a wind turbine. Power tech, IEEE, Lausanne (2007). doi:10.1109/PCT.2007.4538496
3. Abdelkader, S.: Analysis of wind energy conversion system based on Markov state model. Renewable power generation conference (RPG 2013), 2nd IET, Beijing (2013). doi:10.1049/cp.2013.1786
4. Bouissou, M., Bon, J.: Boolen logic driven Markov processs: a powerful new formalism for specifying and solving very large Markov models. Reliab. Eng. Syst. Saf. **82**(2), 149–163 (2003). doi:10.1016/S0951-8320(03)00143-1

Optimal Control of the DC Motors with Feedforward Compensation of the Load Torque

Marian Gaiceanu

Abstract The goal of the electrical drives is to control the mechanical load in accordance with the process requirements. The mechanical load is characterized by load torque and moment of inertia. Considering that the moment of inertia is reduced to the rotor of the electrical machine, optimal control of the DC motor with feedforward load torque compensation is proposed in this paper. In order to find the feedback component of the electrical drive system (EDS), Algebraic Riccati Equation (ARE) is solved. By adding a load torque dependent component to the DC armature voltage control, the mechanical load action is compensated. The compensator will lead to an increased voltage control such that the influence of the load torque will be eliminated. The numerical results of the EDS are shown. The method can be applied to electrical vehicles in order to compensate in real time the large variations of the load torque.

1 Introduction

The electric drives are widespread in the world. More than 60 % of the consumed energy is distributed in the electric drives area. The conventional control does not include the energy reduction aspects during dynamic regimes (starting, stopping or reversing). A small reduction of the consumed energy would have a great impact both on energy market and greenhouse gases emissions. Therefore, the insertion of the optimal control should become a necessity to all power converters manufactures. The objective of the paper is to underlines the advantages of using the applied optimal control theory into the electric drive systems, to propose implementation topologies, to improve the obtained solution, and to choose the adequate one for real time control [1]. The standard design methodology of the linear quadratic

M. Gaiceanu (✉)
Integrated Energy Conversion Power Systems and Advanced Control of the Complex Processes Research Centre, Dunarea de Jos University of Galati, 47 Domneasca Street, Galati, Romania
e-mail: marian.gaiceanu@ugal.ro

A.Y. Oral and Z.B. Bahsi Oral (eds.), *3rd International Congress on Energy Efficiency and Energy Related Materials (ENEFM2015)*, Springer Proceedings in Energy, DOI 10.1007/978-3-319-45677-5_4

controllers does not includes the issue of load disturbances. By using the numerical simulation, the advantages of this study will be shown.

2 Problem Formulation of the Optimal Control

The considered objectives of the optimal control are: to minimize the performance index by determining a control that minimizes losses in the rotor circuit and to maintain the state variables into the admissible limits while supporting the disturbances. The above mentioned objectives, for DC electric drive system, can be integrated into quadratic cost functional. Therefore, the energy model will be incorporated into the performance index. Taking into account the dynamic regimes, the mathematical model of the DC drive the operating at the constant flux is as follows:

$$\overset{\circ}{\mathbf{x}}(t) = \mathbf{A}\mathbf{x}(t) + \mathbf{B}\mathbf{u}(t) + \mathbf{G}\mathbf{w}(t), \tag{1}$$

in which: **A**—the system matrix, **B**—the control vector, **G**—the load vector, the state vector $\mathbf{x}(t) = \begin{bmatrix} \omega(t) \\ i_A(t) \end{bmatrix}$ is composed by the angular velocity and the armature current $i_A(t)$; the control $\mathbf{u}(t) = [u_R(t)]$ consists of the armature voltage, and $\mathbf{w}(t) = [m_s(t)]$ is the load torque disturbance.

2.1 The Initial Conditions

Taking into account a starting process of the DC drive, the initial conditions are as follows:

$$\mathbf{x}(0) = \begin{bmatrix} \omega(0) \\ i_A(0) \end{bmatrix} = \begin{bmatrix} 0 \\ 0 \end{bmatrix}. \tag{2}$$

2.2 The Final Conditions

The types of the LQ optimal problems are classified according to the imposed final conditions [1].

If the final time t_1 is specified and the desired final state is free (the final value of the armature current cannot be known, the value of it depends on the load level; therefore the final current state value is set to 0):

$$\mathbf{x}_1 = \begin{bmatrix} \omega_1 \\ 0 \end{bmatrix}, \tag{3}$$

the optimal problem is namely with *fixed final time, and free state* or with *finite horizon*.

In this case, the quadratic cost performance is defined as:

$$J_1[\mathbf{u}(t)] = \frac{1}{2}\left\langle [\mathbf{x}(t_1) - \mathbf{x}_1]^T, \mathbf{S}[\mathbf{x}(t_1) - \mathbf{x}_1] \right\rangle + \frac{1}{2}\int_0^{t_1} \left[\left\langle \mathbf{x}^{\mathbf{T}}(t), \mathbf{Q}\mathbf{x}(t) \right\rangle + \left\langle \mathbf{u}^{\mathbf{T}}(t), \mathbf{R}\mathbf{u}(t) \right\rangle\right] \mathrm{d}t, \quad (4)$$

in which **S**, **Q** and **R** are the weighting matrices and have the constant values. Additionally, **S**, **Q** are positive semi definite, and $\mathbf{R} > 0$ is positive definite.

If the final time is not finite, and the final state is not specified, the optimal problem is with no specified time, free state or with *infinite horizon*.

The adopted quadratic performance index is as:

$$J_2(\mathbf{u}) = \frac{1}{2}\int_0^{\infty} [\mathbf{x}^{\mathbf{T}}(\mathbf{t})\mathbf{Q}\mathbf{x}(\mathbf{t}) + \mathbf{u}^{\mathbf{T}}(\mathbf{t})\mathbf{R}\mathbf{u}(\mathbf{t})]dt. \quad (5)$$

The optimal control problems consist of finding a solution that transfer the system (1) from the initial conditions to the final conditions by minimizing the performance index (J_1 or J_2), i.e. one or more energetic components of the DC drive system.

2.3 Solution of the Optimal Control Problems

The DC drive system is completely controllable and observable, and by choosing the weighting matrices as above, the solution exists and is unique. The linear quadratic control is based on the solution delivered by Matrix Riccati Differential Equation in case of using J_1 performance index or by Algebraic Riccati Equation in case of using J_2 performance index.

The optimal control could be find by introducing the adequate Hamiltonian function:

$$\begin{aligned} H[\mathbf{x}(t), \mathbf{u}(t), \mathbf{y}(t)] = \frac{1}{2}\left[\left\langle \mathbf{x}^{\mathbf{T}}(t), \mathbf{Q}\mathbf{x} \right\rangle + \left\langle \mathbf{u}^{\mathbf{T}}(t), \mathbf{R}\mathbf{u}(t) \right\rangle\right] \\ + \left\langle \mathbf{p}^{\mathbf{T}}(t), [\mathbf{A}\mathbf{x}(t) + \mathbf{B}\mathbf{u}(t) + \mathbf{G}\mathbf{w}(t)] \right\rangle \end{aligned} \quad (6)$$

in which the $\mathbf{p}^{\mathbf{T}}$ is the transpose of the co-state vector.

By cancelling the first order derivative of the Hamiltonian respect to u, the general optimal solution is provided as:

$$\mathbf{u}^*(t) = -\mathbf{R}^{-1}\mathbf{B}^{\mathbf{T}}\mathbf{p}(t). \tag{7}$$

In case of using $J_1(\mathbf{u})$ performance criterion, the non-recursive (without overshoot and good robustness to load variation) solution could be obtained:

$$\mathbf{u}^*(t) = -\mathbf{R}^{-1}\mathbf{B}^{\mathbf{T}}\mathbf{P}(t_1 - t)\mathbf{x}(t) + \mathbf{R}^{-1}\mathbf{B}^{\mathbf{T}}\mathbf{K_1}(t_1 - t)\mathbf{x_1} + \mathbf{R}^{-1}\mathbf{B}^{\mathbf{T}}\mathbf{K_2}(t_1 - t)\mathbf{w}(t). \tag{8}$$

In case of using $J_2(\mathbf{u})$ performance criterion, the recursive state feedback solution (LQR) is provided:

$$u^*(t) = -\frac{1}{r}[1 \quad 0]\begin{bmatrix} k_{11} & k_{12} \\ k_{21} & k_{22} \end{bmatrix}\begin{bmatrix} x_1 \\ x_2 \end{bmatrix}, \tag{9}$$

the parameters being the choosing value of the weighting matrix R, and from the ARE solution.

The authors added the tracking component [2] of the imposed reference in order to obtain a zero steady state error,

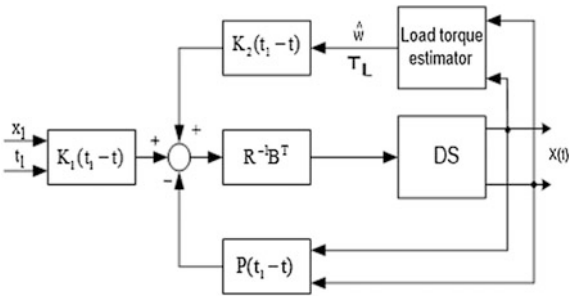

Fig. 1 Multivariable optimal control based on MRDE nonrecursive solution

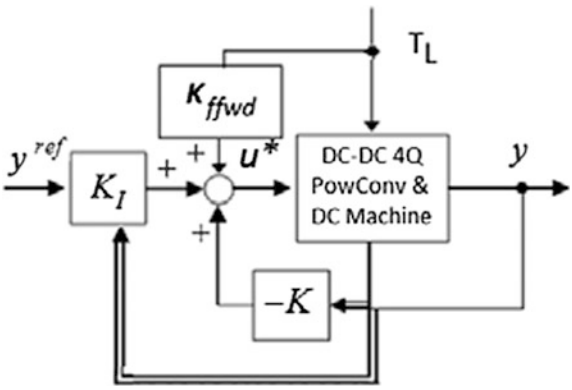

Fig. 2 Multivariable optimal control based on ARE solution

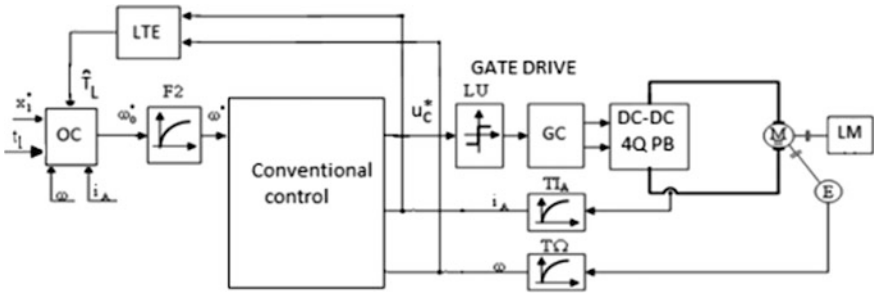

Fig. 3 Implementation of the MRDE solution

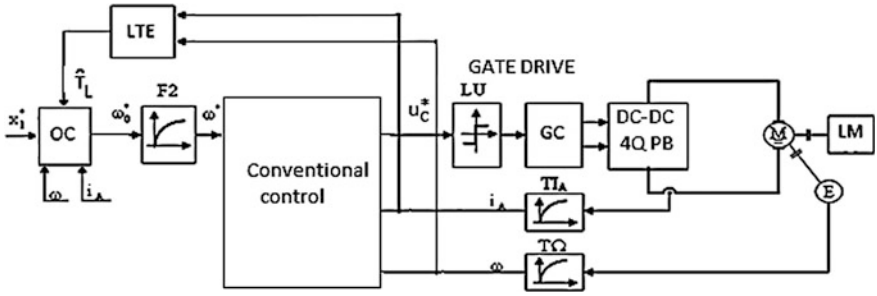

Fig. 4 Implementation of the ARE solution

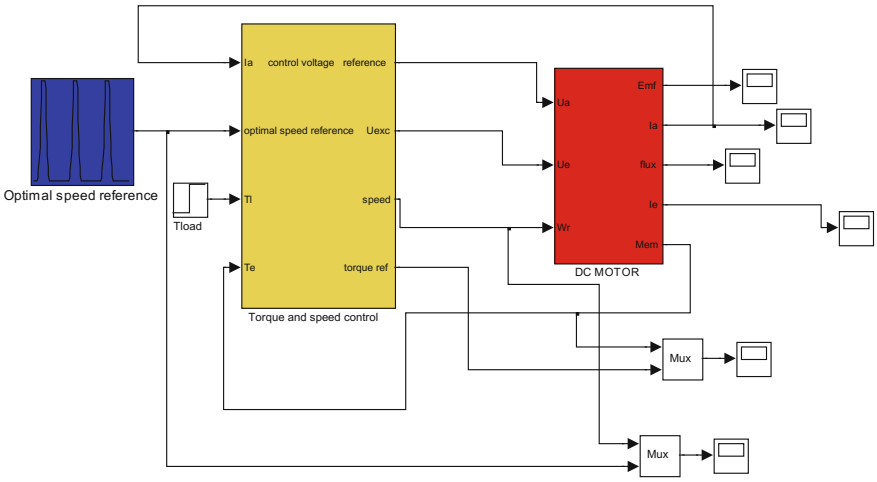

Fig. 5 Maltab-Simulink multivariable optimal control based on MRDE nonrecursive solution

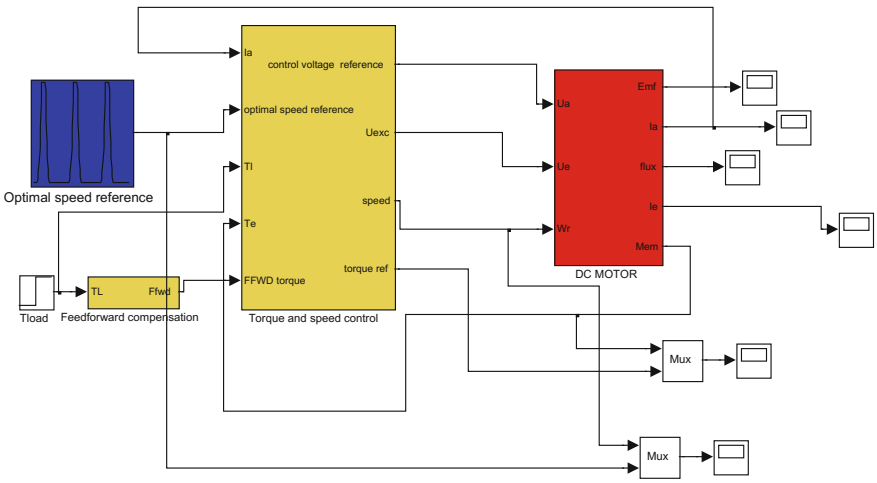

Fig. 6 The proposed feedforward load torque control combined with ARE solution

$$K_I = -\left[C(A+BK)^{-1}B\right]^{-1} \tag{10}$$

where the state feedback, **K**, is the ARE solution and the load feedforward compensation component, respectively:

$$K_{ffwd} = \frac{R_a}{(k\Phi)k_d}, \tag{11}$$

k_d—the gain of the DC-DC power converter.

Topologies of the optimal drive systems are shown in the following Figs. (1, 2, 3 and 4):

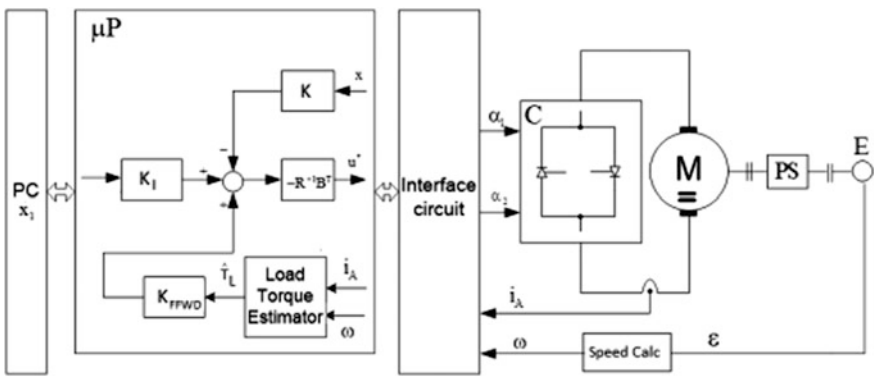

Fig. 7 Implementation of the ARE solution

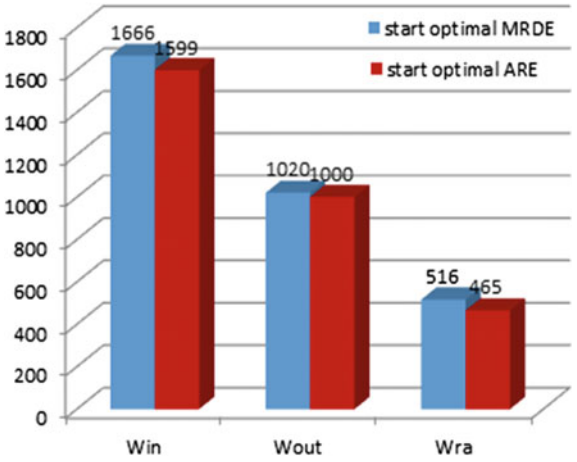

Fig. 8 ARE optimal solution: 4 % energy reduction of the drive system comparative with optimal MRDE solution

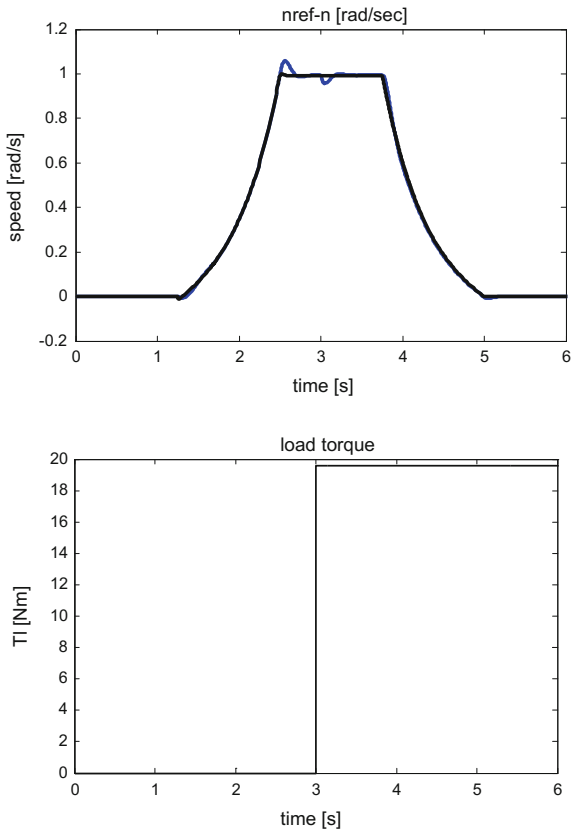

Fig. 9 Speed response under the load torque of the multivariable optimal control based on MRDE nonrecursive solution

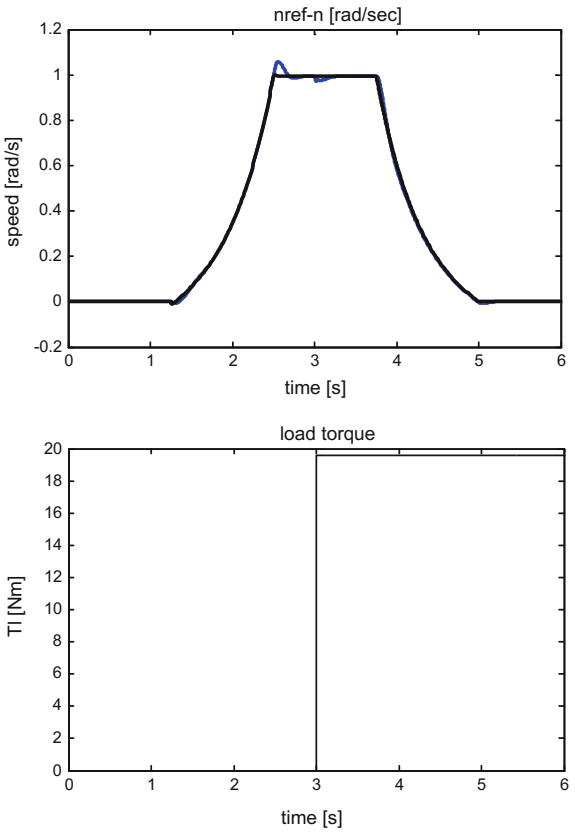

Fig. 10 Speed response under the load torque of the multivariable optimal control based on ARE solution with feedforward torque component

Simulink implementation of the MRDE (Fig. 5) **and ARE** (Fig. 6) **solutions**

DC Motor data: rated power P_N = 4.75 kW, rated speed n_n = 1750 rpm, the maximum speed at flux weakening n_{max} = 4150 rpm, rated voltage U_{AN} = 420 V, U_{EN} = 220 V, T_L = 25 Nm, R_A = 4.53 Ω, R_E = 220 Ω, L_A = 17.5 mH, L_E = 44 H, J = 0.026 kgm^2, k = 1818, Fv = 0.002. Multivariable optimal control based on MRDE nonrecursive solution (Figs. 1 and 3), and on ARE solution (Figs. 2 and 4) are implemented in Maltab-Simulink (Fig. 5 and 6).

In the Fig. 7, the implementation method of the ARE solution is shown. The 4 % energy reduction is obtained (Fig. 8).

The comparative speed response for both optimal control solutions under the rated load torque is shown in Fig. 9 (MRDE), and Fig. 10 (ARE).

3 Conclusions

In this paper the new type of the complete optimal control is shown. Compared to the other optimal control solutions, the real-time implementation of the obtained optimal drive system requires low digital power resources. The solution contains three components: the forcing component, the feedback and has in view the minimization of the expended energy in the rotor windings, and the feed forward torque compensation. The proposed torque compensation method conducts to the energy saving (Fig. 8).

Acknowledgment This work was supported by a grant of the Romanian National Authority for Scientific Research, CNDI—UEFISCDI, project number PN-II-PT-PCCA-2011-3.2-1680.

References

1. Sheta, M.A., Agarwal, V., Nataraj, P.S.V.: A new energy optimal control scheme for a separately excited DC motor based incremental motion drive. Int. J. Autom. Comput. **6**(3), 267 (2009)
2. Morzhov, A.V., Faldin, N.V.: Synthesis of time-optimal tracking DC electric drive with limitation on consumed power. J. Comput. Syst. Sci. Int. **50**(2), 205–219 (2011)

Photovoltaic Power Conversion System as a Reserve Power Source to a Modern Elevator

Marian Gaiceanu, Cristian Nichita and Sorin Statescu

Abstract The main objective of this paper is to integrate a green source in the safety system of a modern elevator. In order to drive the elevator with 480 kg maximum load 1 kW induction motor is chosen. The sunlight through photovoltaic panels is converted into electricity. To ensure a continuous energy, an energy storage system is inserted in the power conversion system. The extracted energy is maximized by using the maximum power point tracking methods. A comparative analysis of these methods is presented. In order to size the necessary photovoltaic panels the potential of the local solar power is taken into account, i.e. the solar potential of Galati city, located in south-eastern region of Romania. In order to ensure a constant voltage the DC-DC power converter is inserted. The constant DC link voltage is used by the power inverter in order to supply the induction machine. The obtained numerical results confirm the feasibility of the solution.

M. Gaiceanu (✉)
Integrated Energy Conversion Power Systems and Advanced Control of the Complex Processes Research Centre, Dunarea de Jos University of Galati, 47 Domneasca Street, Galati, Romania
e-mail: marian.gaiceanu@ugal.ro

C. Nichita
University of Le Havre, 25 Rue Philippe Lebon, 76058 Le Havre Cedex, France
e-mail: nichita@univ-lehavre.fr

S. Statescu
Galfinband SA, Smardan 2A Street, Galati, Romania
e-mail: office@galfinband.ro

A.Y. Oral and Z.B. Bahsi Oral (eds.), *3rd International Congress on Energy Efficiency and Energy Related Materials (ENEFM2015)*, Springer Proceedings in Energy, DOI 10.1007/978-3-319-45677-5_5

1 Introduction

Electric drives cover a wide range of power (from 0.1 kW to 100 MW) and speed (100 to 50,000 rev/min) and are necessary in all industry types. In this respect they are obviously the most important way of practical application in industry, modern achievements of the electrical and electronics engineering. On the other hand, rapid development of industries like power electronics, electronic computers and microprocessors recently greatly boosted the development of industrial electric drives. Electric elevators use electric energy to drive and control. Both during the movement and stopping, the elevators must ensure the protection of persons. In order to design a back-up power system for a regenerative elevator the photovoltaic (PV) renewable energy source has been taken into account. The back-up power system consists of an adequate PV module adapted to the local city solar potential, Galati, from south-eastern region of Romania, Eastern Europe, a battery being capable to deliver the appropriate power to the elevator by means of three-phase power inverter and induction motor. Therefore, the grid-connected with battery PV power system is necessary. Taking into consideration the adopted emergence solution into a commercial building, the power quality delivered into grid is an important issue of the power system. The recovered energy during braking or elevator downward is delivered into the network at high quality power factor. In order to demonstrate the feasibility of the solution, the simulation results are provided.

2 The Dynamic Sizing of the Electric Motor and PV Potential (Galati, Romania)

Taking into account the imposed speed cycle (Fig. 1) for the elevator system, the necessary power of the induction machine (im) has been dynamically designed, therefore the mechanical power and the necessary load torque for the induction machine have been found (Fig. 2).

Taking into account the existing topologies of the PV solar energy system, the monthly average electricity production for an elevator system situated at South-Eastern region of Romania (Fig. 3) is presented in Fig. 4.

Taking into consideration the total energy required to support a voltage outage of 288 min per day a back-up system has been designed.

3 The Topology of the Elevator IM Drive System

The required energy is necessary in order to extract safely the personnel from the elevator cabin and to assure the operating conditions of the elevator drive system during the voltage outage. The back-up system consists of both PV panel of

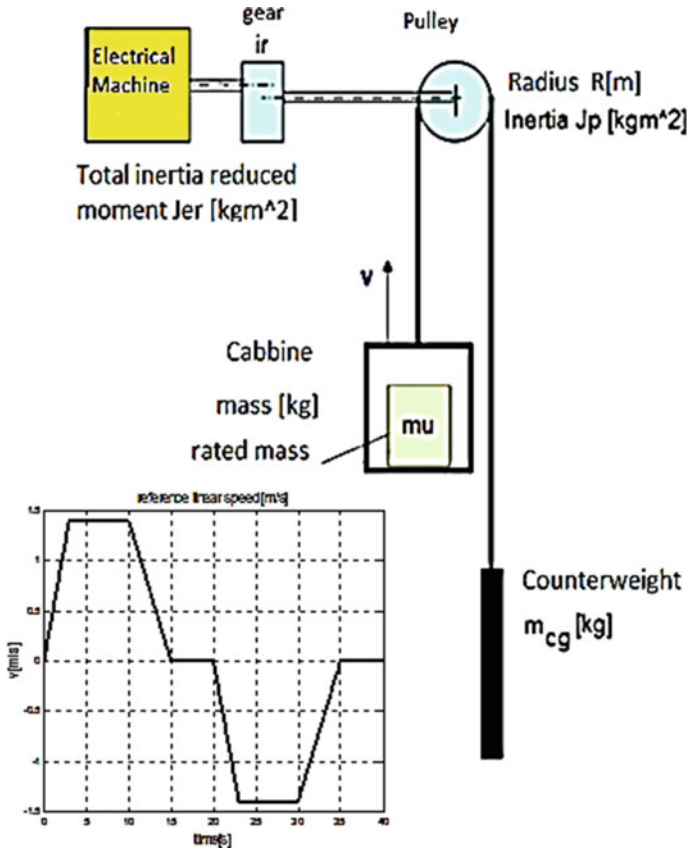

Fig. 1 The topology of the elevator load system and the speed cycle

1000 W and a battery pack acting as energy buffer. The role of the battery is to provide the required energy, to smooth the voltage, and to maintain a constant value of it. Therefore, a unidirectional DC-DC power converter is necessary. The PV control has in view the extraction of the maximum energy from the cells system by using Perturbe and Observe algorithm, and to regulate the dc output voltage. Both energy sources are connected to the dc link of the three-phase power inverter through the charge controller. The excedentary energy from the PV panel is used to recharge the battery pack. Therefore, bidirectional dc-dc power converter is used. The feasibility of the proposed solution is shown in this paper, and validated through numerical results by using block diagram shown in Fig. 5.

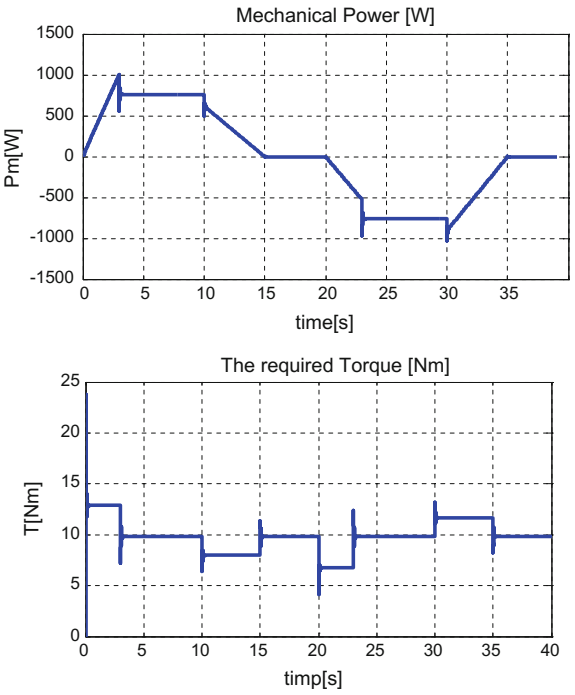

Fig. 2 Dynamical results of the motor sizing (mechanical power and the torque)

4 The Mathematical Model of the AC-AC Power Converter

4.1 Mathematical Model of the AC-DC Active Rectifier

The power converter is formed by AC-DC active rectifier and DC-AC power inverter. The above mentioned decoupled power structure is connected through a common dc-link. The AC-DC active rectifier is described by the grid voltage vector equation [2]:

$$\overrightarrow{E} = L \cdot \frac{d\overrightarrow{I}}{dt} + \overrightarrow{V} \tag{1}$$

in which the grid supply voltage vector is denoted by, the main inductance by L, the line current vector by I, and the input voltage vector of the active rectifier by V; and the dc-link voltage equation [3]:

$$\frac{dV_{dc}}{dt} = \frac{3}{2} \cdot \frac{V_D \cdot I_D + V_Q \cdot I_Q}{C \cdot V_{dc}} - \frac{I_{outdc}}{C}, \tag{2}$$

where the grid voltage components E_Q and E_D, line current components I_D and I_Q.

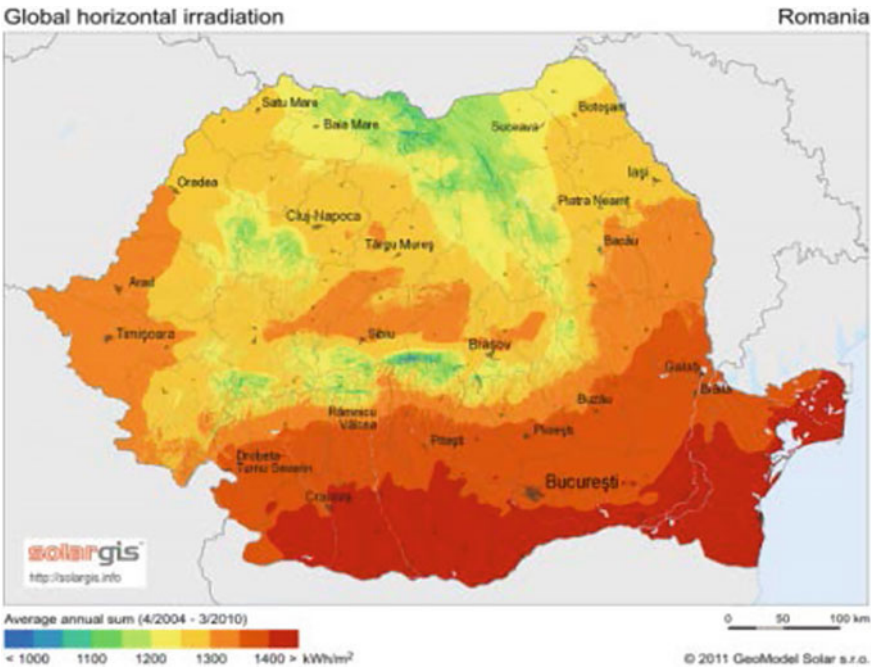

Fig. 3 Global horizontal irradiation-Romania [1]

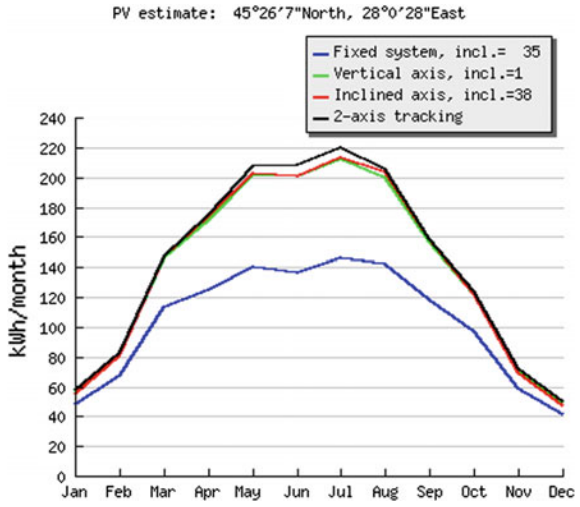

Fig. 4 The monthly average electricity production for different PV topologies [1]

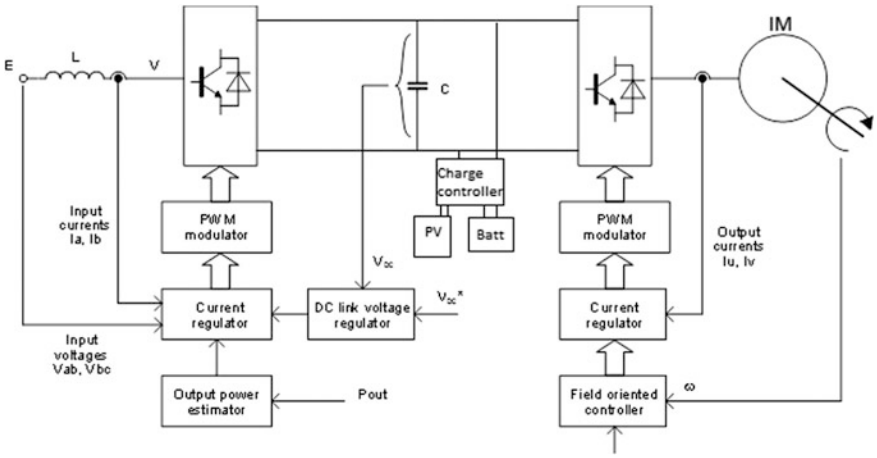

Fig. 5 Block diagram of the complete control system of the quasi sinusoidal AC-AC converter

4.2 *Mathematical Model of the Three-Phase Induction Machine*

The mathematical model of the vector controlled three-phase squirrel cage induction machine is based on the stator voltage equations, magnetizing current equation and the mechanical motion equation [4]:

$$\begin{aligned}
&\sigma T_s \frac{di_{ds}}{dt} + i_{ds} = \frac{v_{ds}}{R_s} - (1-\sigma)T_s \frac{di_{mR}}{dt} + \sigma T_s \omega_e i_{qs} \\
&\sigma T_s \frac{di_{qs}}{dt} + i_{qs} = \frac{v_{qs}}{R_s} - (1-\sigma)T_s \omega_e i_{mR} - \sigma T_s \omega_e i_{ds} \\
&\frac{di_{mR}}{dt} = \frac{1}{T_r}(-i_{mR} + L_m i_{ds}) \\
&J\frac{d\omega_r}{dt} = k_T i_{mR} i_{qs} - T_L, \quad K_T = \frac{2}{3}(1-\sigma)L_s \\
&\omega_e = \omega_r + \omega_{sl}, \quad \omega_{sl} = \frac{R_r}{L_m}\frac{i_{qs}}{i_{mR}}
\end{aligned} \quad , \qquad (3)$$

where: R_s—phase stator resistance; ω_e—magnetic field synchronous speed; ω_r—rotor angular speed; ω_{sl}—slip angular speed; i_{ds} (i_{qs}) d-axis (q-axis)—stator current; v_{ds}^* (v_{qs}^*) d-axis (q-axis)—stator voltage commands; L_s (L_r)—the stator (rotor) inductance; L_m—the mutual inductance; $T_s = L_s/R_s$ the time constant of the stator circuit; σ—the total leakage factor; T_L—the total load torque; $T_r = L_r/R_r$ the time constant of the rotor circuit; K_T—torque constant, J—the moment of inertia; p—the number of poles pairs.

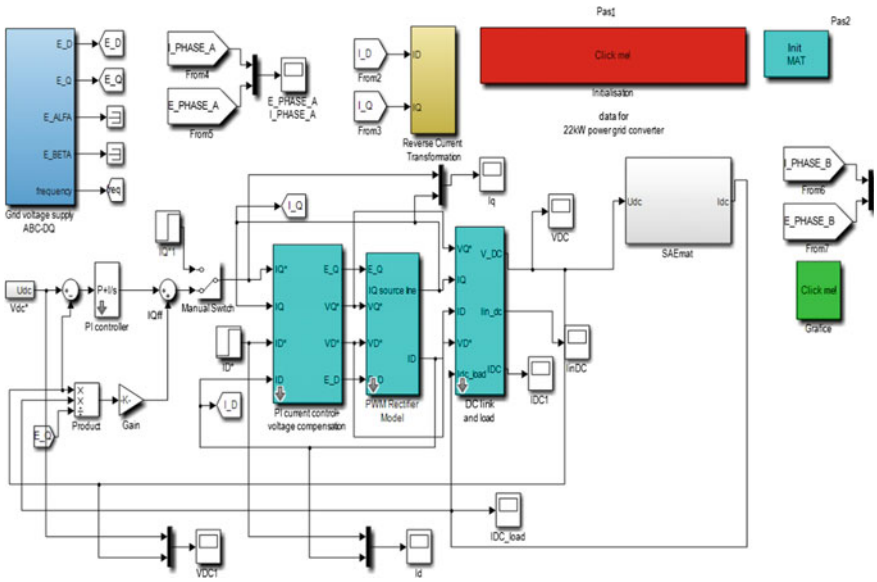

Fig. 6 Simulink model of the ac-ac power converter with PV back-up power system

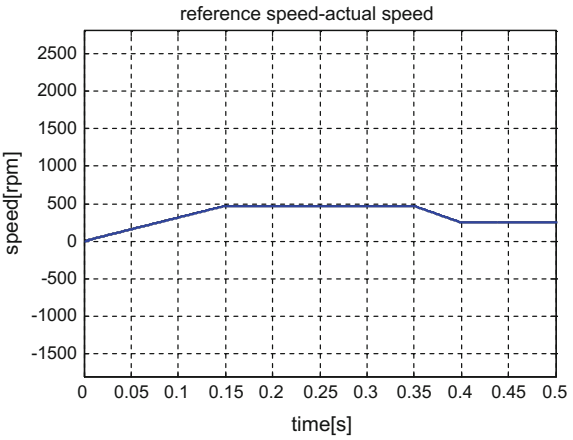

Fig. 7 Comparison between speed reference and the feedback speed

5 Simulation Results

In order to show the feasibility of the proposed solution the entire system control [5] has been developed in Matlab-Simulink (Fig. 6) for an active power rectifier of S_n = 22 kVA rated apparent power with the following parameters: line inductance R_{in} = 0.001 Ω, Li_n = 2.1 mH, dc-link capacitor of C = 1565 μF, the rated data for the induction machine P_n = 1 kW, n_N = 2000 rpm, T_L = 12 Nm. Taking into

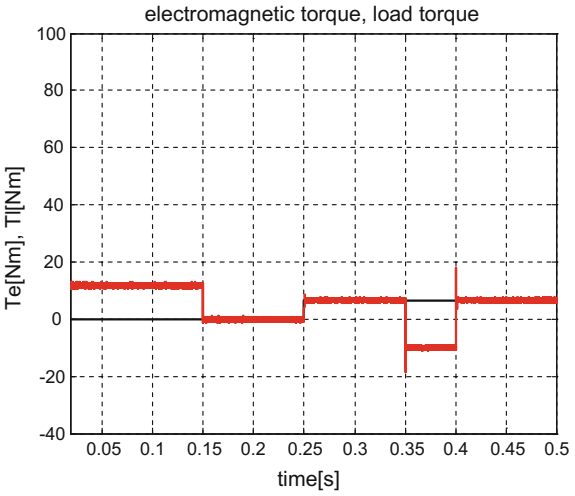

Fig. 8 Electromagnetic torque and load torque comparison

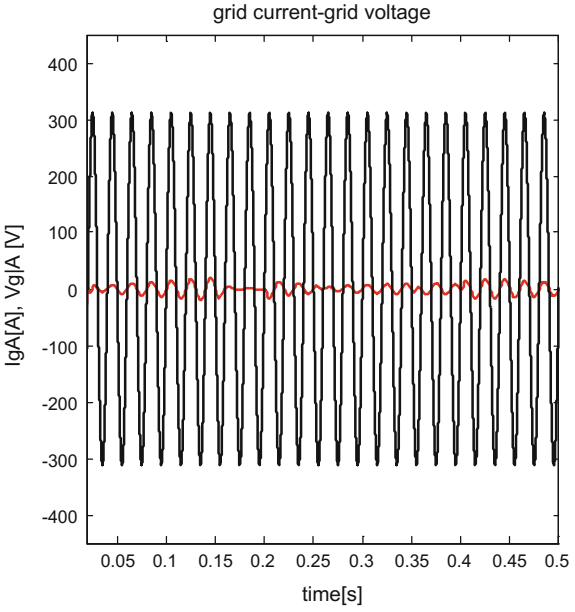

Fig. 9 Unity power factor in any operating conditions

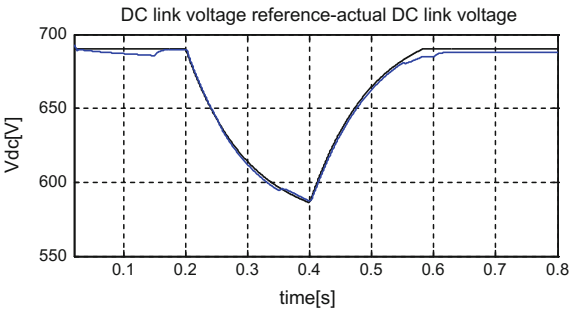

Fig. 10 DC link voltage, VDC (V)

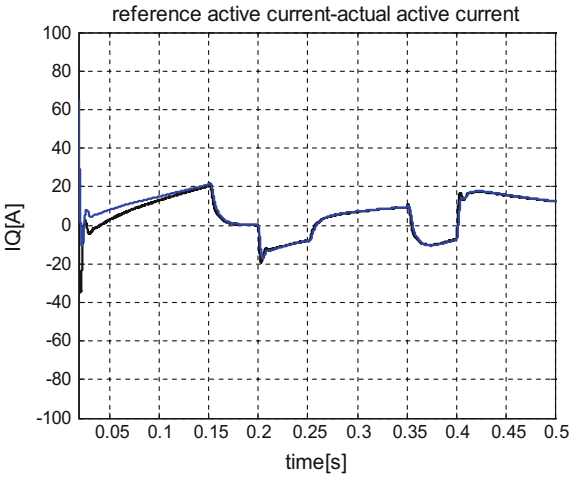

Fig. 11 Active current controller: the reference and the feedback

consideration the daily energy usage (Wh) and the elevator as load in order to assure a 288 min autonomy in case of voltage outage, and considering a 50 % battery discharge rate 1380 Wh battery bank capacity has been resulted. By knowing the system voltage, 4 series batteries have been specified for the actual requirements. The MK 8A27DT-DEKA 12V 92Ah AGM battery has been chosen. The adequate numerical simulation results when the electric network is suddenly interrupted and the back-up system becomes active are presented in Figs. 7, 8, 9, 10 and 11.

The numerical results show the efficacity of the entire control: the speed controller (Fig. 7), validation of the mechanical side of the IM drive (Fig. 8), unity power tfactor operation (Fig. 9), DC link voltage controller (Fig. 10), and the active current controller for the active power rectifier (Fig. 11). At $t = 0.2$ s a voltage outage has been considered (Fig. 10), the numerical results proving the accuracy of the back-up system design stage.

6 Conclusions

The authors of this paper proposed a modern power system for electric elevator, capable to sustain the operating conditions during voltage outage. Moreover, the proposed control assures the unity power factor operation and the regenerating capability of the entire elevator system (Fig. 9). By introducing both PV panels and battery bank an adequate autonomy of the elevator drive system has been assured. The numerical results confirm the accuracy of using the design, modelling, control and implementation concepts.

Acknowledgments This work was supported by a grant of the Romanian National Authority for Scientific Research, CNDI—UEFISCDI, project number PN-II-PT-PCCA-2011-3.2-1680.

References

1. http://re.jrc.ec.europa.eu/pvgis/apps4/PVcalc.php
2. Kazmierkowski, M., Krishnan, R., Blaabjerg, F.: Control in power electronics. Academic Press, An imprint of Elsevier Science (2002)
3. Uhrin, R., Profumo, F.: Stand alone AC/DC converter for multiple inverter applications. In: Power Electronics Specialists Conference. PESC'96 Record, 27th Annual IEEE, vol. 1, pp. 120–126, 23–27 June 1996
4. Leonhard, W.: Control of electrical drives. Springer, Berlin (1996)
5. Bajracharya, C., Molinas, M., Suul, J.A., Undeland, T.M.: Understanding of tuning techniques of converter controllers for VSC-HVDC NORPIE/2008. Nordic Workshop on Power and Industrial Electronics, CD, pp. 1-8, 9–11 June 2008

Urban Cycle Simulator for Electric Vehicles Applications

Marian Gaiceanu, Razvan Buhosu and Sorin Statescu

Abstract The paper aims to accomplish a standardized simulator for urban cycle of an electric vehicle. The electric vehicle is supplied by two power sources: a fuel cell and a battery. Each source is connected in series with one three-phase inverter to a separate DC-DC converter in order to stabilize the voltage. Each of the two 3-phase inverters feeds alternatively the stator of an asynchronous machine with six phases. Field oriented vector control is involved; the obtained numerical results emphasize the quality of the strategy, and of the chosen architecture.

1 Introduction

The paper has in view an analysis of the different Electric Vehicle (EV) topologies based on fuel cells technology. The Proton Exchange Membrane Fuel Cells (PEMFC) are well fitted to the EV traction due to the high speed response, high efficiency, reduced impact on environment [1]. The main disadvantages of the fuel cells are the lack of the hydrogen supply infrastructure, the required safety level of the EV, and the high cost [2, 3].

Three EV propulsion architectures are proposed: Fuel cells as a reserve power source; Load Following Fuel Cells, and Integrated EV with double power supply. In order to provide an accurate simulator, the energetic mathematical model of each

M. Gaiceanu (✉) · R. Buhosu
Integrated Energy Conversion Power Systems and Advanced Control of the Complex Processes Research Centre, Dunarea de Jos University of Galati, 47 Domneasca Street, Galati, Romania
e-mail: marian.gaiceanu@ugal.ro

R. Buhosu
e-mail: razvan.buhosu@ugal.ro

S. Statescu
S.C. Galfinband SA, 2A Smardan, 800701 Galati, Romania
e-mail: office@galfinband.ro

A.Y. Oral and Z.B. Bahsi Oral (eds.), *3rd International Congress on Energy Efficiency and Energy Related Materials (ENEFM2015)*, Springer Proceedings in Energy, DOI 10.1007/978-3-319-45677-5_6

configuration type has been developed. Different speed cycles have been applied on each architecture type. The analysis of the obtained results reveals the accuracy of the proposed EV simulators [4, 5].

2 The Topologies of the Proposed Fuel Cell Electric Vehicle

In order to validate the Urban (UDC), Extra-Urban (EUDC) and New European Driving (NEDC) Cycles simulators three topologies of the fuel cell Electric Vehicles have been proposed. Taking into consideration that the UDC is the most energy consuming drive cycle, the vehicle autonomy could be critical. Therefore, this study will focus on the finding an efficient topology by using the fuel cells (FC). In the first topology the FC acts as a reserve power source (Fig. 1). The second topology is designed as Load Follower (Fig. 2) [6], and the third as Load Sharing (Fig. 3) [6].

2.1 The Energetic Mathematical Models of the Proposed EV Architectures

Taking into account the above mentioned topologies, the energetic model of each component has been deducted. Choosing a type of architecture or another is performed depending on the vehicle mission for cycles adapted to the type of road. The first vehicle architecture is designed for urban cycle (Fig. 4). The number of sources must be able to provide quick response to vehicle acceleration, but above all to

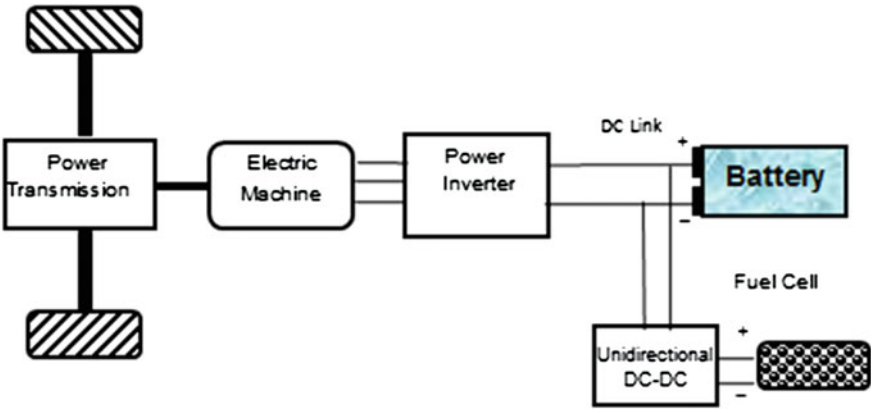

Fig. 1 EV 1st topology with FC as a reserve power source

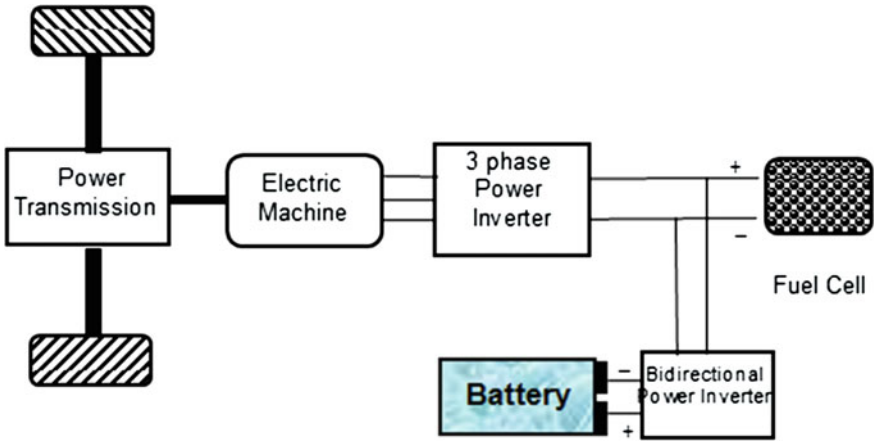

Fig. 2 Load follower EV 2nd topology

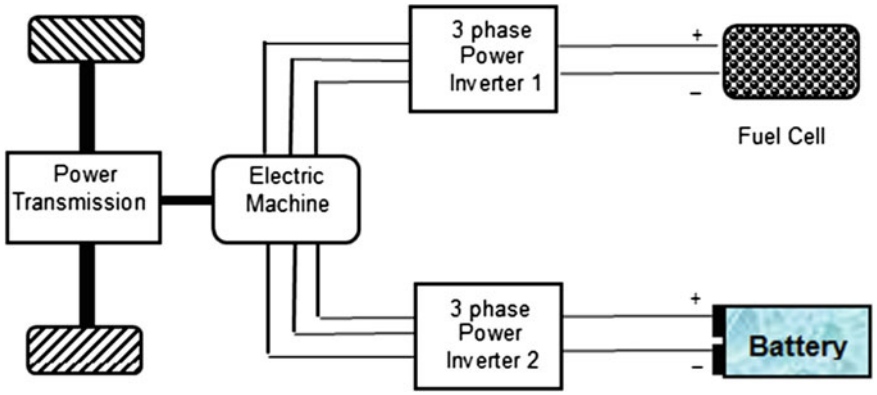

Fig. 3 Integrated EV with double power supply: load sharing

ensure the autonomy of everyday, autonomy that is not provided solely by the batteries. Indeed, the fuel cell during an urban cycle will provide the energy needed during steady state regime (constant speed).

Therefore, the battery will provide the power required to load transient load changes related (braking, starting, reversing). For the second topology (Fig. 5), the fuel cell system operates as load follower. This topology is consistent when sizing the power output of the fuel cell close to the maximum power required by the vehicle during traction. Batteries should operate only when the load demands are greater than the maximum output power of the fuel cells. The last proposed topology (Fig. 6) adopts a dual motor traction with double three-phase windings, consisting of two equal windings supplied from the fuel cell and battery by means of two separate power inverters. During traction both power supply devices are

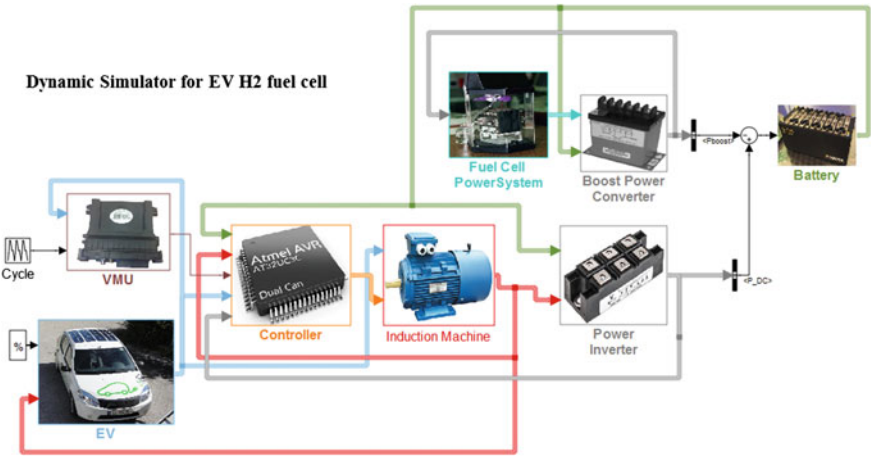

Fig. 4 EV simulator for the 1st topology

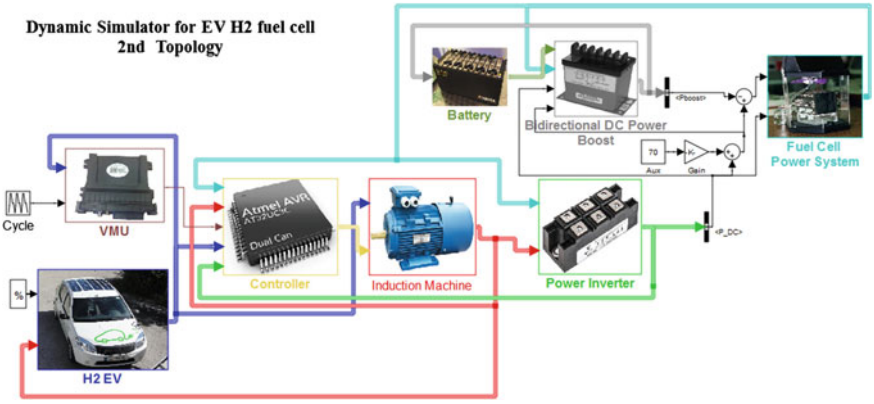

Fig. 5 EV simulator for the 2nd topology

involved: 50 % Load Sharing, and Load Follower. The recovered energy during braking process is sent to the battery through the bidirectional DC-DC power converter.

2.2 *Comparative Results*

In order to obtain an accurate simulators, three Matlab-Simulink energetic models are implemented. In Fig. 7, 8, 9, 10 and 11, the comparisons between the experimental data and the data obtained from the third simulator (Fig. 6) are shown.

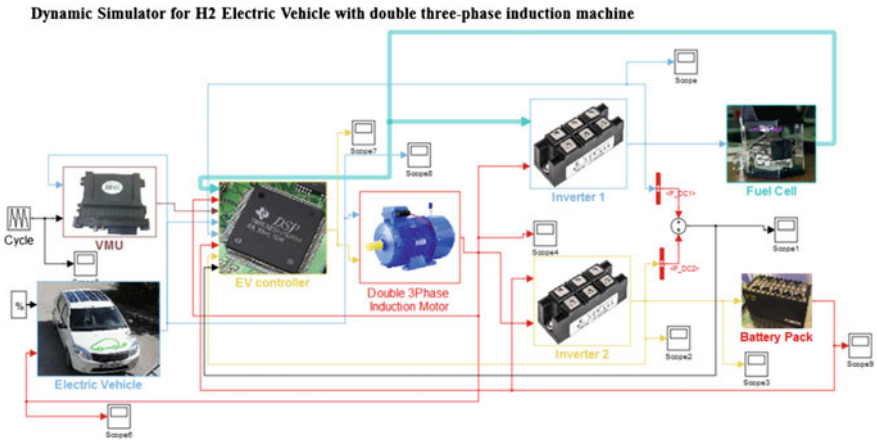

Fig. 6 EV simulator for the 3rd topology

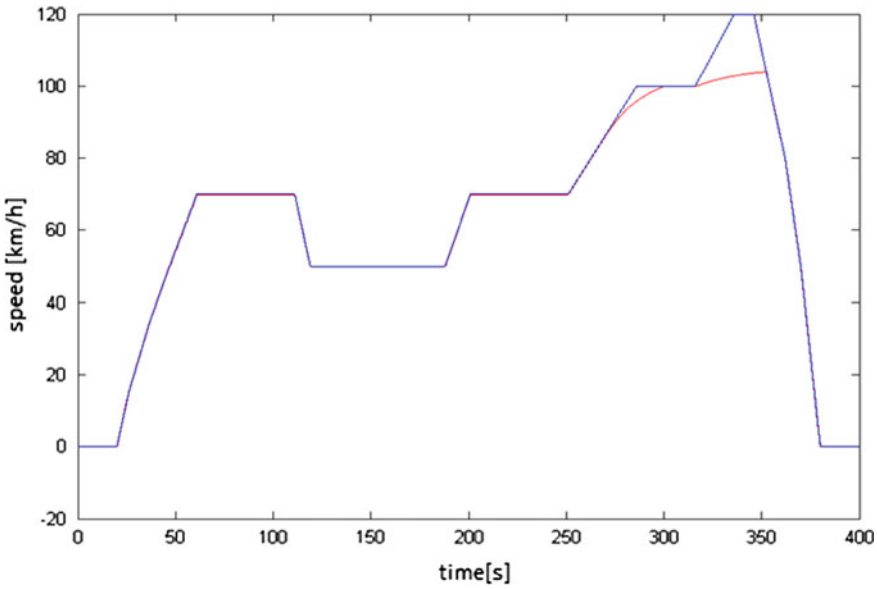

Fig. 7 The speed driving cycle

From Figs. 7, 8, 9, 10 and 11 it could be noticed that only a little mismatch exists between the real battery voltage and the simulated one. The explanations is that temperature has a strong influence on battery parameters. The model is considered to have set values obtained from the experimental measurements at 25 °C

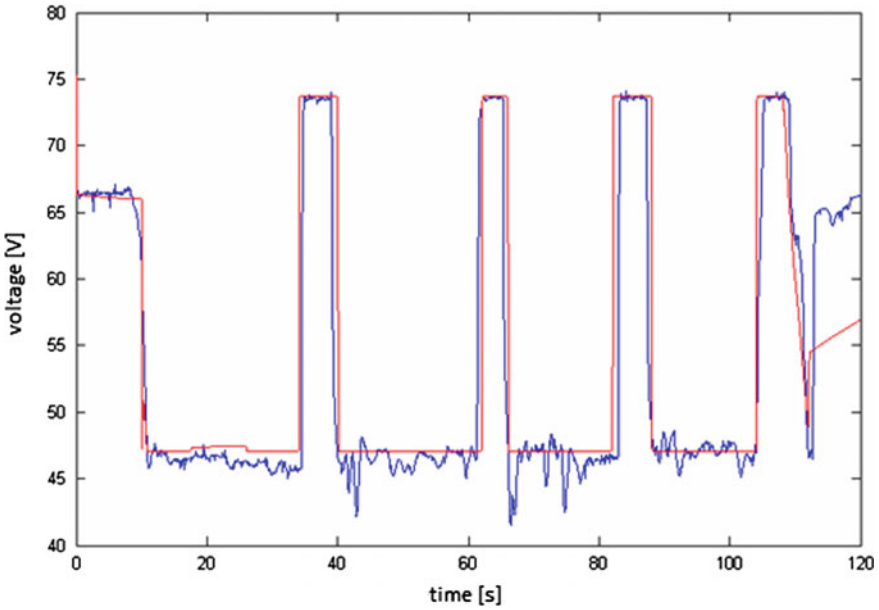

Fig. 8 Fuel cell voltage (V)

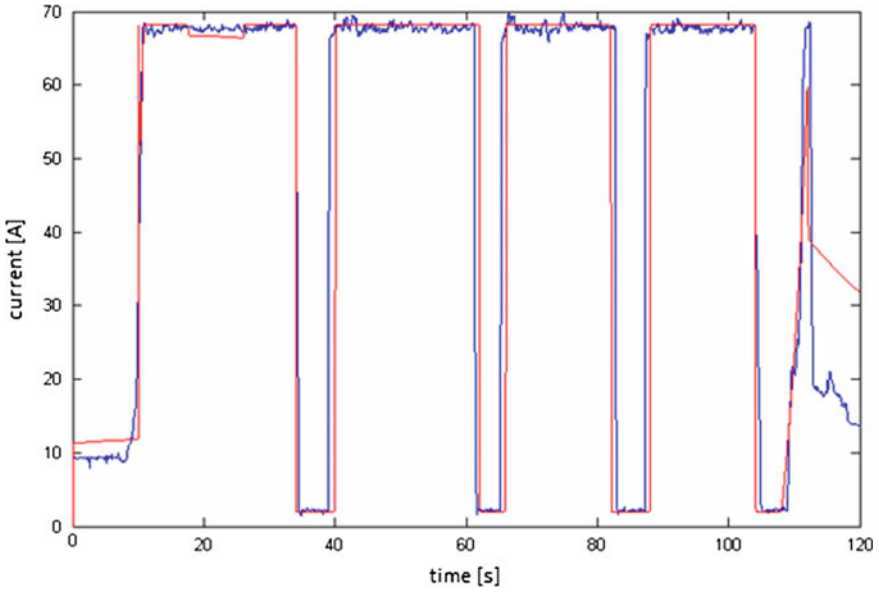

Fig. 9 Fuel cell current (A)

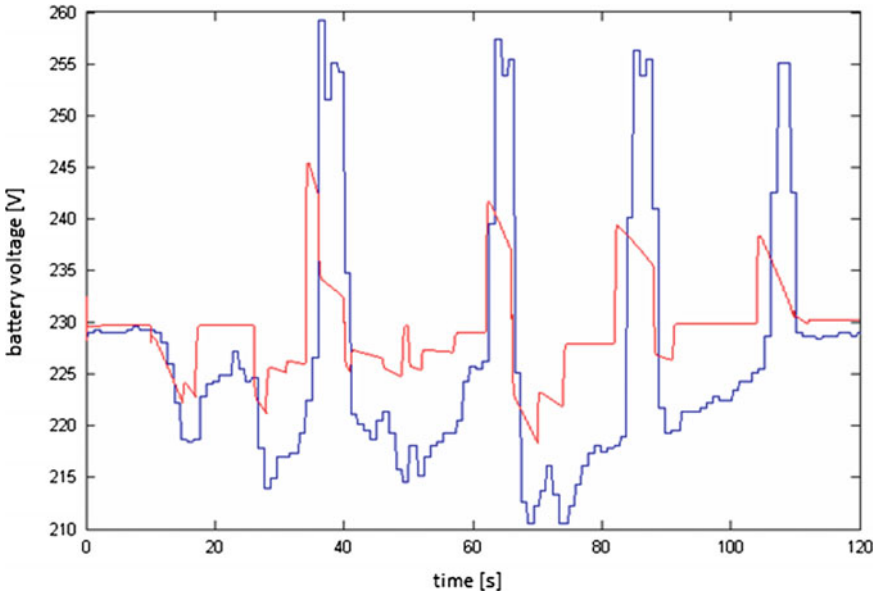

Fig. 10 Battery voltage (V)

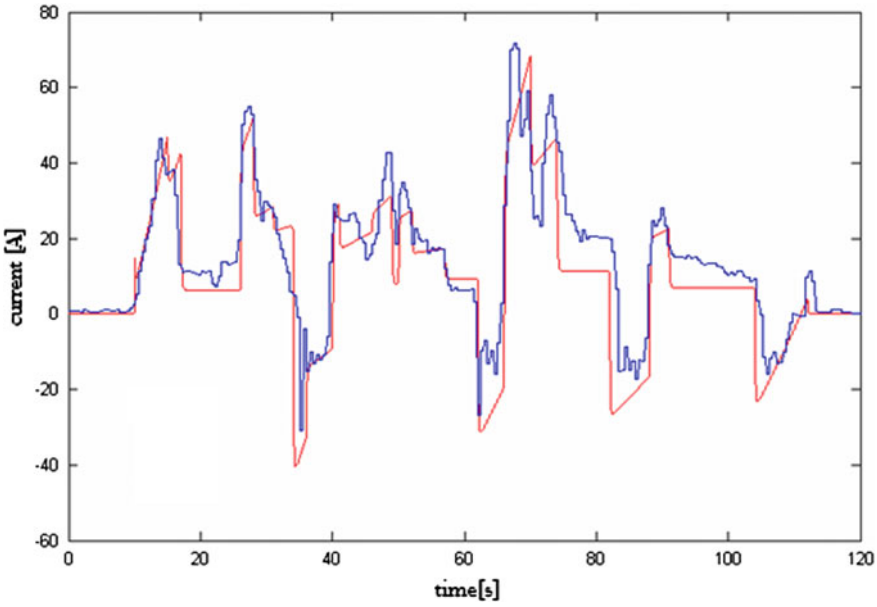

Fig. 11 Battery current (A)

and does not take into account the operating temperature, life of the battery, dispersion of production; it is a phenomenon that affects batteries, particularly in the lead-based technology.

2.3 Some Aspects Regarding the Efficiency

The main characteristics of the EV architectures components are as follow: fuel cell (FC) rated power 30 kW, FC voltage (200–250) V, FC maximum current 200 A; the Ni-Mh battery pack rated voltage 216 V, battery back rated capacity 6.5 Ah, the traction power of the electrical machine 15 kW, rated voltage 80 V, rated speed 2200 rpm, rated torque 65 N m, the weight of the 4 wheels EV 1200 kg. Taking into account the Load Sharing topology, the following efficiency characteristics are obtained (Figs. 12 and 13).

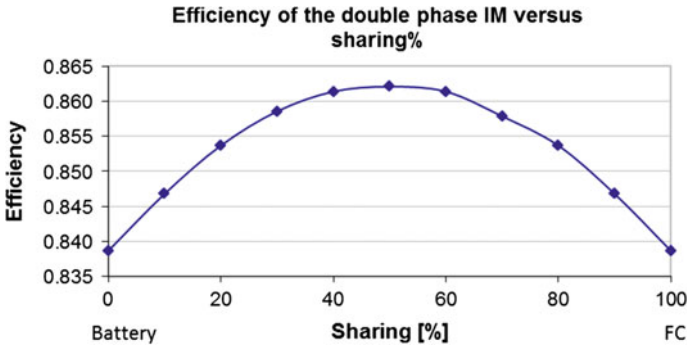

Fig. 12 The efficiency of the electric motor versus degree of sharing

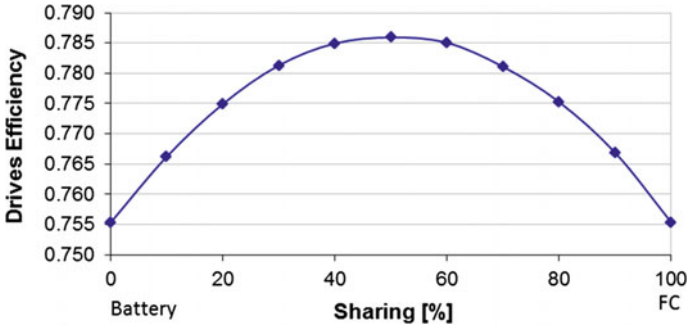

Fig. 13 The efficiency of the drives system according to the degree of sharing energy sources

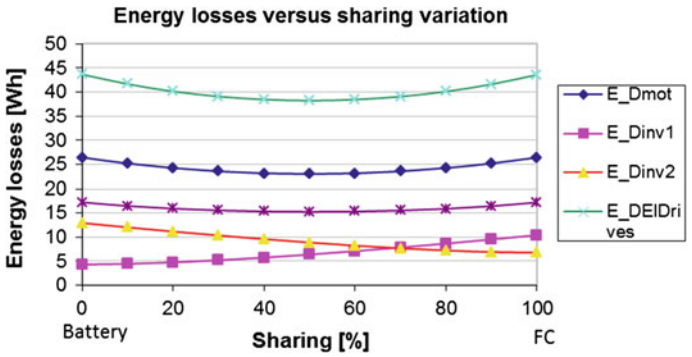

Fig. 14 The energy losses components versus degree of sharing

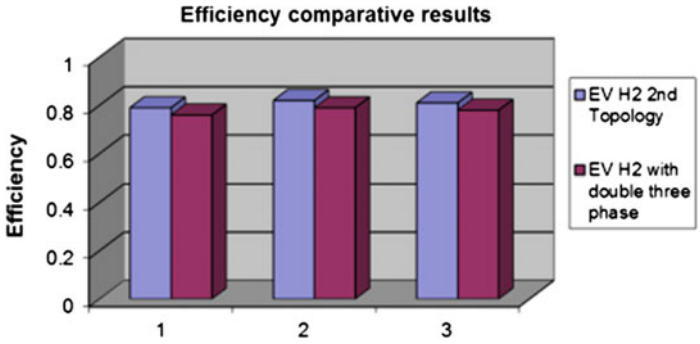

Fig. 15 The efficiency comparative results versus driving cycle: *1* UDC cycle, *2* EUDC cycle, *3* NEDC cycle

In Fig. 14, the energy losses components versus degree of sharing are shown. Taking into account the types of cycles: UDC, EUDC, and NEDC, in Fig. 15 the efficiency comparative results are shown, and in Fig. 16, the energy losses comparative results are depicted. In Fig. 17 the autonomy of the electric vehicle versus driving cycles is obtained.

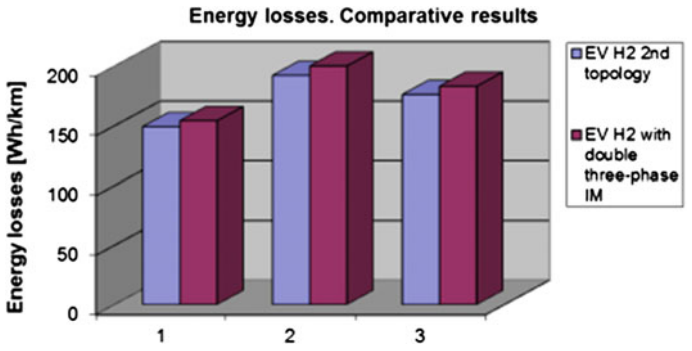

Fig. 16 The energy losses comparative results versus driving cycle: *1* UDC cycle, *2* EUDC cycle, *3* NEDC cycle

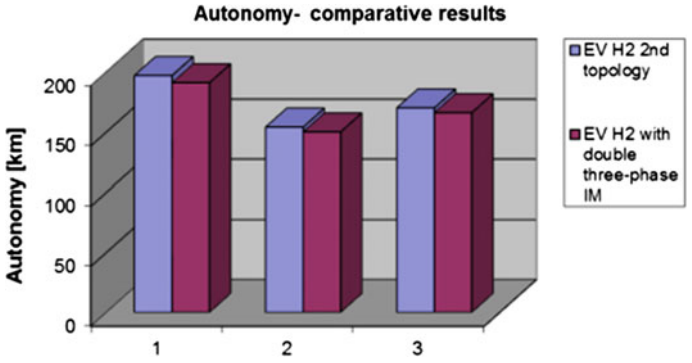

Fig. 17 The autonomy comparative results versus driving cycle: *1* UDC cycle, *2* EUDC cycle, *3* NEDC cycle

3 Conclusions

From Figs. 7, 8, 9, 10 and 11 it could be noticed that only a little mismatch exists between the real battery voltage and the simulated one. The explanations is that temperature has a strong influence on battery parameters. The model is considered to have set values obtained from the experimental measurements at 25 °C and does not take into account the operating temperature, battery life, dispersion of battery production: it is a phenomenon that affects batteries, particularly in the lead-based technology. The first fuel cell topology using INV based on H2 is primarily intended to be used mainly on urban routes; for extra-urban cycle it was noticed the inability of the fuel cells to charge the batteries; The dual-phase configuration with 50 % sharing strategy optimizes the EV but not the sources used; Comparing the second topology with the third it is observed that the first topology has a higher

efficiency, this means lower fuel consumption and greater autonomy. It can be said that among the analyzed architectures, the fuel cell as load follower is an excellent solution for hybrid vehicles with fuel cells.

Acknowledgments This work was supported by a grant of the Romanian National Authority for Scientific Research, CNDI—UEFISCDI, project number PN-II-PT-PCCA-2011-3.2-1680.

References

1. Giménez, R., Luengo, I., Mereu, A., Adamopoulou, E., Demestichas, K.: EVE: fully electric vehicle traffic simulator for technological validation and decision making. Procedia Soc. Behav. Sci. **160**(19), 459–464 (2014). doi:10.1016/j.sbspro.2014.12.158
2. Saxena, S., Le Floch, C., MacDonald, J., Moura, S.: Quantifying EV battery end-of-life through analysis of travel needs with vehicle powertrain models. J. Power Sources **282**(15), 265–276 (2015). doi:10.1016/j.jpowsour.2015.01.072
3. Baptista, P., Ribau, J., Bravo, J., Silva, C., Adcock, P., Kells, A.: Fuel cell hybrid taxi life cycle analysis. Energy Policy **39**(9), 4683–4691 (2011). doi:10.1016/j.enpol.2011.06.064
4. Broughton, K.L.M., Switzer, F., Scott, D.: Car following decisions under three visibility conditions and two speeds tested with a driving simulator. Accid. Anal. Prev. **39**(1), 106–116 (2007). doi:10.1016/j.aap.2006.06.009
5. Raslavičius, L., Azzopardi, B., Keršys, A., Starevičius, M., Bazaras, Ž., Makaras, R.: Electric vehicles challenges and opportunities: Lithuanian review. Renew. Sustain. Energy Rev. **42**, 786–800 (2015). doi:10.1016/j.rser.2014.10.076
6. http://www.iphe.net

Impacts of Network Structure on the Optimum Design of Hybrid Standalone Microgrid

Sobhy M. Abdelkader, Abubakar Abdulkarim and D. John Morrow

Abstract In this paper a new methodology is proposed to investigate the impacts of network structure on the optimum design of microgrids. The proposed microgrid consists of PV, wind, battery storage and diesel generator. By introducing some approximations the relationships between wind turbine and PV module were expressed as linear functions of wind speed and solar radiation respectively. Therefore, the problem is formulated as a linear optimization problem that minimized the annual cost of the system. A computer program is developed in Matlab to formulate the optimization problem. Output of the optimization procedure show the viability of the proposed method by reducing the carbon emission by 70.40 % compared to operating the system on diesel generator alone. The result also shows that DC and AC coupled microgrid could reduce the system annual cost of hybrid microgrid by 5 and 2.8 % respectively. In addition, the effects of diesel prices, battery storage parameter, storage technology on the optimum system configurations have been investigated.

Keywords Renewable energy · Optimization · Diesel prices · Battery

S.M. Abdelkader (✉)
Electrical Engineering Department, Mansoura University,
Mansoura 35516, Egypt
e-mail: sobhy_abdelkader@yahoo.com

A. Abdulkarim
Department of Electrical and Electronics Engineering, University of Ilorin,
Pmb 1515, Ilorin, Nigeria
e-mail: abkzarewa@yahoo.com

D.J. Morrow
EPIC School of Electronics, Electrical Engineering and Computer Science,
The QUB, Belfast, UK
e-mail: dj.morrow@ee.qub.ac.uk

A.Y. Oral and Z.B. Bahsi Oral (eds.), *3rd International Congress on Energy Efficiency and Energy Related Materials (ENEFM2015)*, Springer Proceedings in Energy, DOI 10.1007/978-3-319-45677-5_7

1 Introduction

Some of the problems with the present day sources of energy such as nuclear, fossil fuels along with public awareness of the environmental consequences have created interest in the renewable energy resources. The present decade has witness growing interest in the utilization of the renewable energy for the electricity generation. One of the possibilities of higher penetration of the renewable energy system is by the use microgrid.

Microgrid is a small electrical distribution system that connects multiple customers to multiple distributed sources of generation and storage through power electronic devices that provide the necessary interface [1]. Microgrid are usually designed on a small scale with either solar or wind or a combination of the two sources. These types of systems should be installed where the renewable energy resources are available. In this work, the proposed microgrid is assumed to consist of both wind and solar sources. Different methods of coupling exist for the microgrid consisting of more than one renewable energy source. Moreover, these couplings may affect the optimum design of the proposed system. In addition, being exposed to other environmental conditions, such as weather, fault and component failure. There are also possibilities of been affected by these conditions. Another issue of concern with the renewable energy sources is economy and reliability of the power supply to the isolated load [2]. Other factors that may affect the operation of the proposed system include prices of diesel, load demand, storage technology and other components.

Several efforts have been done in the optimal design of standalone microgrid. Some of the efforts include [3], in which the influences of components on the system structure have been investigated. In [4], the system designed considered uncertainty in the load, wind speed and solar radiation by modifying the particle swarm optimization. Optimum design of microgrid consisting of wind, diesel generator and battery storage system has been proposed in [5], the design determined the reliability of the system considering component failures.

2 Hybrid Microgrid

In this section, specifications, formulation of the proposed hybrid system are presented. The proposed system has six major building blocks as shown in Fig. 1. These include wind energy conversion system (WECS), solar energy conversion system (SECS), storage system, diesel generator, static energy conversion system and the load unit. These components operate in parallel to guarantee continuous power supply to the load. The intermittent nature of the renewable energy sources causes the output to fluctuate. In some cases, the storage system is connected to reduce the fluctuations and store the excess power produced by the renewable energy sources. In his arrangement, the diesel generator operates when renewable

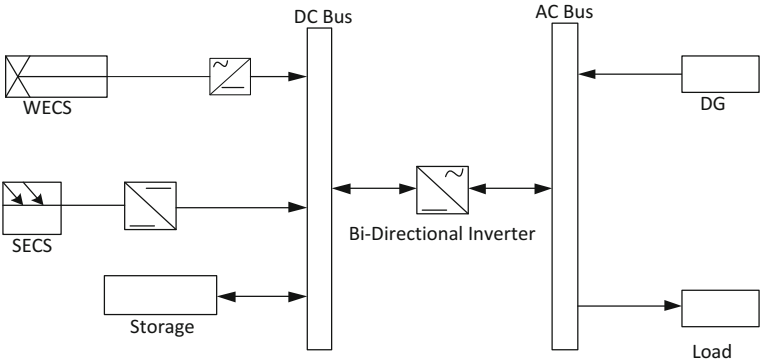

Fig. 1 Proposed hybrid microgrid

energy and storage can satisfy the demand. The objective cost function is obtained by the summation of the components cost that make up the microgrid system. In this case, the cost is subdivided into the cost of WECS, SECS, static energy conversion system, storage system, diesel generating system and the cost of fuel. Therefore, the problem is formulated in Eq. 1.

$$F = CT_{INVO} \times PINV_r + CST_o \times QS + CW \times PWR + CS \times PSR + Cd_1 \times PDR + Cd_2 \cdot \sum_{i=1}^{T} \Delta t_i \cdot PD_i \quad (1)$$

where, CT_{INVO} and $PINV_r$: are cost and rate power of inverter-rectifier unit, CST_o: energy storage cost, in \$/kWh and QS: capacity of the storage, kWh. CW and PWR: total cost, and power rating of WECS, kW, CS and PSR: total cost of SEC, and rating of solar energy conversion system, Cd_1: The total cost of the diesel generator, PDR rated power of the diesel generator, $Cd_1, PDR, Cd_2, \Delta t_i, PD_i$: Operational cost, rated power, fuel cost (\$/L), time interval and output power of the DG at each. All other powers and cost are in kW and \$/kW respectively. The constraints in this optimization problem maintain a balance between the power generation and system demand. Therefore, the constraints are classified under three main sub headings. These include power balance, energy balance and component rating constraints.

3 Effects of Network Configuration

This section investigated how different network configurations influenced the optimal design of microgrid. In order to achieve this goal, two more system configurations have been analysed. Analysis of the result is presented in this section.

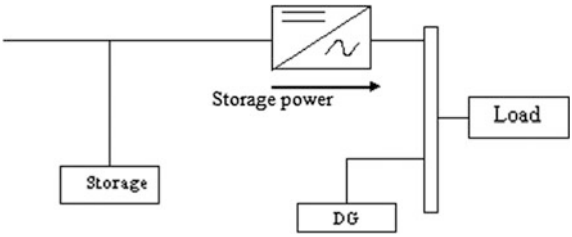

Fig. 2 Inverter mode

Table 1 output of the optimization

Components	Hybrid	AC	DC	Units
WECS	334.75	334.75	334.75	kW
SECS	0.83	0.83	0.83	kW
Diesel generator	162.35	162.35	162.35	kW
Battery storage	89.84	89.84	89.84	kWh
Rectifier/inverter	276.86	121.94	Nill	kW
ATSC	14,987	14,568.61	14,239.29	$

The two additional models analysed include AC and DC couple microgrids. In order to analyse the different microgrid structure, the optimal model developed is modified accordingly. The first model considered is the AC couple microgrid. The section modified is the inverter-rectifier constraints. Figure 2 shows the rectifier-inverter unit acting in inverted mode, the power is the power from the storage unit. Therefore, a new constraint is defined, but this is not shown here.

In this case, the rated power of the rectifier-inverter unit is lower than the hybrid microgrid counterpart by 56 % of the hybrid couple microgrid. Also, the annual cost of the AC couple microgrid is cheaper than hybrid microgrid by 197 $. In the case of DC couple microgrid, the procedure is the same as that of hybrid microgrid with modifications in the objective and constraints. According to the DC microgrid, the new objective function is defined in Eq. 2. The modification is the removal of the component limitation related to the inverter-rectifier unit. In the same way, the optimal solution of the mathematical model is presented in Table 1. It can be observed that the problem solution is not different from the previous two sections. The difference is the on the total annual cost of the plant. Thus when compared with hybrid and AC couple microgrid, it is possible to observe that this configuration is the cheapest of all three coupling methods.

$$\begin{aligned} \boldsymbol{F} = & \boldsymbol{CST_o} \times \boldsymbol{QS} + \boldsymbol{CW} \times \boldsymbol{PWR} + \boldsymbol{CS} \times \boldsymbol{PSR} + \boldsymbol{Cd}_1 \times \boldsymbol{PDR} \\ & + Cd_2 \sum_{i=1}^{T} \Delta t_i \times PD_i \end{aligned} \tag{2}$$

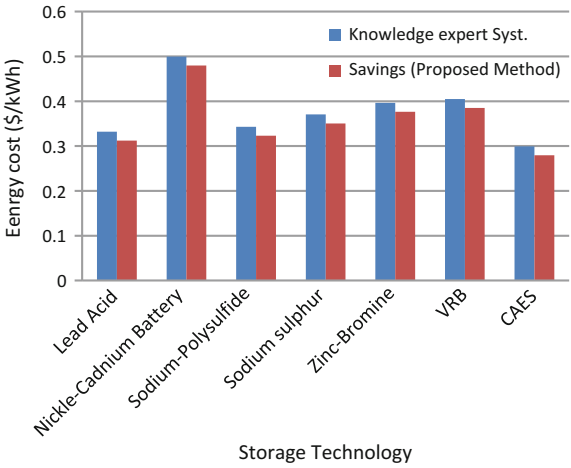

Fig. 3 Effects of battery storage

4 Effects of Battery Storage

This section explored the effects of battery storage on the proposed hybrid microgid. The effects have been categorized into two main sections. Section one is on the relationship between the annual cost of the plant and the minimum storage level. Section two is on the effects of different storage technology on the energy cost. Section one, the effects are analysed from the rated power of the unit. In order to achieved this, the minimum storage level is changed from 0.2 to 0.35. Different optimisations runs shows that, the annual cost of the plant is not very sensitive to the minimum storage level. The factor that varies with system minimum storage level is the rated power of the storage unit. In addition, the result has shown that the rated capacity of the storage unit increased with minimum storage level. The second section of this analysis compared the cost of energy due to the proposed model and the knowledge expert system proposed [6]. The result of the cost saving caused due to the proposed method and the knowledge expert system is shown in the Fig. 3. Therefore, the proposed method shows a realistic cost savings compared to the existing method.

5 Effects of Diesel Prices

In order to establish the relationship between the diesel price and the annual cost of the plant, the diesel price has been varied from 0.5 to 0.9 ($/L). Table 2 shows the relationship between the diesel price and the annual cost of the system. It can be observed that, the total annual cost of the plant depends on the range of the diesel

Table 2 Variation of system cost with diesel price

TACS ($)	Diesel price ($/L)
14,987.01	0.5
16,471.25	0.6
17,955.49	0.7
36,261.95	0.8
63,825.14	0.9

price. Between 0.5 and 0.7 $/L the total annual cost of the plant increased by 10 and 20 % respectively. The trend is different when the diesel prices increased between 0. 7 and 0.9 $/L.

6 Conclusions

A model for the optimum design of standalone hybrid renewable energy microgrid has been developed. The model determined the optimum system configuration such that the ratio of cost to the reliability is minimized. Application of the model has shown a decreased in the cost of energy and carbon dioxide emission by 80 and 70 % compared to operating the system on diesel generator alone. Further analysis shows that DC and AC microgrid could reduce the annual cost of the hybrid system by 5 and 2.8 % respectively. In the same way the annual cost of the plant increased with the minimum storage level. Finally, the relationship between the annual costs of the system increased with the diesel price. However, the variation is not uniform throughout the diesel price.

References

1. Hassan, M., Abido, M.: Optimal design of autonomous microgrid using particle swarm optimization. IEEE Trans. Power Electron. **26**(3), 755–769 (2012). doi:10.1109/ISIE.2010.5636580
2. Chowdhury, S., Chowdhury, S., Crossley, P.: Microgrid and Active Distribution Networks, London. IET, United Kingdom (2009). ISBN 978-1-84919-014-5
3. Abdulkarim, A., Abdelkader, S., Morrow, D.: Reliability importance measures of components for standalone hybrid renewable energy microgrid. In: Proceedings in Energy, 2nd International Congress on Energy Efficiency and Energy Related Materials (ENEFM2014), Switzerland, pp. 9–14. Springer, Berlin (2015). ISBN: 978-3-319-16901-9
4. Wang, L., Singh, C.: PSO-based hybrid generating system design incorporating reliability evaluation and generation/load forecasting. Power tech, 2007 IEEE, Lausanne (2007). doi:10.1109/PCT.2007.4538519
5. Riahy, F., Jahanbani, G.H.: Optimum design of hybrid renewable energy system. Renew. Energy Trend Appl. **11**(1), 231–250 (2013). doi:10.5772/27085
6. Ross, M., Hidalgo, R., Abbey, C., Joos, G.: Analysis of energy storage sizing and technologies. Electric power and energy conference (EPEC), IEEE. Halifax, NS (2010). doi:10.1109/EPEC.2010.5697212

Energy Yield Potential Estimation Using Marine Current Turbine Simulations for the Bosphorus

Hasan Yazicioglu, K.M. Murat Tunc, Muammer Ozbek and Tolga Kara

Abstract In this work, several simulations and analyses are carried out to investigate the feasibility of generating electricity from sea underwater currents at Istanbul Bosphorus Strait. Bosphorus is a natural canal which forms a border between Europe and Asia by connecting Black Sea and Marmara Sea. The differences in elevation and salinity ratios between these two seas cause strong underwater currents. Depending on the morphology of the canal the speed of the flow varies and at some specific locations the energy intensity reaches to sufficient levels where electricity generation by marine current turbines becomes economically feasible. In this study, several simulations are performed for a 10 MW marine turbine farm/cluster whose location is selected by taking into account several factors such as the canal morphology, current speed and passage of vessels. 360 different simulations are performed for 15 different virtual sea states (for 5 significant wave heights and 3 peak periods). Similarly, 8 different configurations are analyzed in order to find the optimum spacing between the turbines. Considering that the complicated morphology of the strait may cause some spatial variations in the current speed within the selected region, the analyses are performed for three different flow speeds corresponding to 10 % increase and decrease in the average value. For each simulation the annual energy yield and cluster efficiency are calculated.

H. Yazicioglu
Department of Wind Energy, Technical University of Denmark, Kongens Lyngby, Denmark
e-mail: hasannyazicioglu@gmail.com

K.M.M. Tunc · M. Ozbek (✉) · T. Kara
Faculty of Engineering and Natural Sciences, Istanbul Bilgi University, Istanbul, Turkey
e-mail: muammer.ozbek@bilgi.edu.tr

K.M.M. Tunc
e-mail: murat.tunc@bilgi.edu.tr

T. Kara
e-mail: tolga.kara@engr.bilgi.edu.tr

A.Y. Oral and Z.B. Bahsi Oral (eds.), *3rd International Congress on Energy Efficiency and Energy Related Materials (ENEFM2015)*, Springer Proceedings in Energy, DOI 10.1007/978-3-319-45677-5_8

Keywords Renewable energy · Marine current turbine · Cluster optimization · Energy yield simulations · Offshore engineering · Dynamic interactions

1 Introduction

Turkey, as a rapidly growing economy with very limited national hydrocarbon resources, is heavily dependent on fossil fuels (e.g. natural gas) imported for electricity production [1]. However, some recent political instabilities in the supplier countries, the heavy economic burden of importing these resources and the most importantly, the increasing awareness of environmental issues have been encouraging policy makers to increase the use of renewable energy sources. Indeed, very detailed investigations and analyses were performed to determine the wind, solar and geothermal energy capacity of the country [1]. However, the potential of harnessing some other renewable sources, particularly sea current energy has not been fully realized yet.

Compared to the other types of renewable energy such as wind and solar, current energy can still be considered in development phase and is not commercially available in large scales. Existing marine turbine systems are mostly in prototype testing stage. Although initial results are quite promising [2, 3] some further verification for long term performance and durability under severe environmental conditions is still required.

The average current speed needed for most commercial turbines is approximately 4–5 knots (2–2.5 m/s). Areas that typically experience high marine current flows are in narrow straits, between islands and around headlands. Entrances to lochs, bays and large harbors often also have high marine current flows. Generally the resource is largest where the water depth is relatively shallow and a good tidal range exists [4].

This paper aims at investigating the feasibility of generating electricity from the streams at Bosphorus by using marine current turbines. Extensive simulations and analyses are performed for a 10 MW marine turbine farm (10—SeaGen 1 MW) where several important design parameters such as the size, orientation, depth and spacing of the turbines are optimized according to the specific morphology and flow patterns seen at Bosphorus.

2 Morphology and Flow Characteristics of Bosphorus

The currents seen in the Bosphorus Strait is an example of a two layer exchange flow that is characterized by brackish waters originating in the Black Sea and moving southward and more saline, denser waters from the Marmara Sea and flowing northward [5].

Black Sea has a positive water balance due to the excess hydrological input from five major and countless minor rivers. The only exit point of this flow is the Bosphorus resulting in a net outflow of 300 km^3 water through the strait in a year. The sea level difference between the two ends of the strait has an average value of 30 cm. The Elevation difference caused by river flows, leads surface currents with speeds reaching 7–8 knots at windy seasons. It is very well known that the surface current has a very high potential for energy production [6]. However, Istanbul Strait is a major sea access route and has one of the heaviest maritime traffics in the world. According to the statistics [7] 38,000 vessels have passed through the strait in 2014. More than 15,000 of these vessels were large size crude oil tankers having lengths of 200 m or more. Considering the intensity of the traffic load it can be realized that electricity generation from surface currents is not feasible due to high risk of accident.

Similarly, the difference in salinity ratios and density between two seas cause a deep layer current flowing from south to north. The salinity ratios of Black Sea and Marmara Sea are 1.8 and 2.5 % respectively. Compared to the surface current, the speed of deep layer current is low (2–3 knots). However, depending on the morphology at certain locations the energy intensity of this flow can reach to sufficient levels making electricity production feasible.

In this work, location of the farm/cluster together with other design parameters such as the size, orientation, depth and spacing of the turbines are determined according to the specific morphology and flow pattern seen at Bosphorus. 1 MW SeaGen marine current turbine [8] with a rotor diameter of 18 ms is considered to be the most appropriate turbine for the project. In order not to obstruct the passage of vessels, the turbines are placed at an average depth of 42 m. This enables a clearance of 24 m to be left for the ships passing over the region. The turbine selected for the project and the corresponding power curve can be seen in Figs. 1 and 2, respectively.

Fig. 1 SeaGen marine current turbine [8]

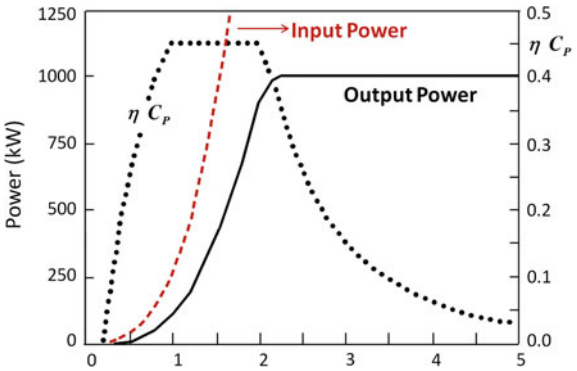

Fig. 2 1 MW tidal-current turbine power curve [10]

3 Modeling

The methodology applied in this work can be summarized as follows;

- The simulations are performed for 15 different virtual sea states (5 significant wave heights and 3 peak periods). For each state, the downstream velocity profile is interpolated and centerline velocities for the turbines are determined by using irregular wave theory.
- The centerline velocity calculated for the hub (31 m below the sea surface) is then superimposed on the average current speed and the resultant flow speed is obtained. Frandsen model [9] is used to represent the dynamic interactions among the turbines and the resulting wake effects and to calculate the current speeds experienced by each turbine. Wake analyses are conducted for 8 different configurations in order to find the optimum spacing between the turbines.
- Considering the spatial variations in the current speed within the selected region, these analyses are performed for three different flow speeds. The simulations are repeated for speeds corresponding to 10 % increase and decrease in the average value. For each simulation the corresponding AEP (Annual Energy Production) is calculated and stored in a database.

In order to find the optimum layout and spacing between the turbines wake analyses are conducted for 8 different configurations, namely for distances corresponding to 5, 6, 7, 8, 9, 10, 12 and 15 times the rotor diameter (18 m). Figure 3 shows how the current speeds experienced by the 10 turbines in the cluster change depending on the spacing ratio.

In Fig. 3, the x axis shows the number of the turbine in the cluster. Similarly, the y axis represents the current speed which is normalized with respect to the current speed experienced by the 1st turbine in the row.

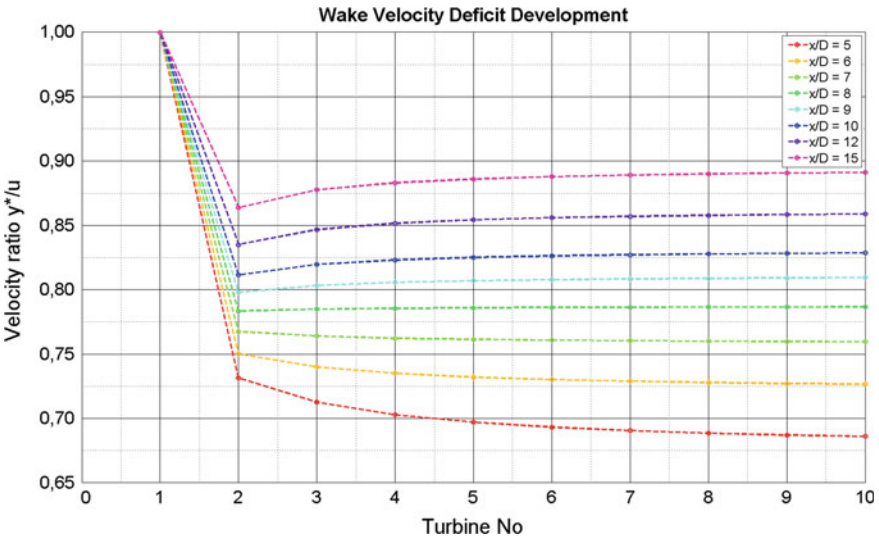

Fig. 3 Current speed experienced in the farm for different spacing ratios

4 Annual Energy Production Calculation

The power generated by each turbine in the cluster is calculated separately by using the equation shown below.

$$P_n = \frac{1}{2} A_r \, \rho \, u_n^3 \, C_p$$

Where A_r, ρ and C_p represent rotor area, density of water and power coefficient, respectively. Similarly u_n is the effective current speed experienced by the nth turbine in the row and is calculated by using Frandsen Wake Model. The speeds experienced by different turbines are then scaled by using the normalized velocity ratios shown in Fig. 3.

Table 1 shows the annual energy production [GWh] results calculated for varying current speeds and turbine spacing. In the table, the 1st row represents spacing ratios changing between 5 and 15. Similarly the 1st column includes the

Table 1 Annual energy production AEP matrix for 10 turbines

Spacing ratio x/D	5	6	7	8	9	10	12	15
Current speed (m/s)	Total energy generated (GWh)							
1.70	20	22	24	26	28	29	32	35
1.85	26	28	31	34	36	38	41	45
2.00	32	36	39	42	45	47	52	57

average currents speeds. The generated power calculated for a specific current speed and spacing can be obtained simply by intersecting the corresponding row and column.

5 Conclusion

This paper aims at investigating the feasibility of generating electricity from sea underwater currents at Istanbul Bosphorus Strait. Several simulations are performed for 8 different configurations to find the optimum spacing between the turbines. Considering that the complicated morphology of the strait may cause some spatial variations in the current speed within the selected region, the analyses are performed for three different flow speeds. The simulations are conducted for speeds corresponding to 10 % increase (2.0 m/s) and decrease (1.70 m/s) in the average value of 1.85 m/s

In order to determine how the distance between the turbines affect the generated power, the calculations are repeated for 8 different spacing ratios changing between 5 and 15. Although the simulations are performed for a cluster of 10 (1 MW of each) marine turbines, the obtained results can also be used to roughly estimate the total power and relative efficiencies of the clusters having more than 10 turbines. The results of the analyses show that two different approaches namely, *power maximizing* and *efficiency maximizing* approaches can be followed in designing the cluster. If the length of the available cluster area is considered as the limiting parameter, selecting a smaller spacing ratio makes it possible to install more turbines within the same region. Such an approach results in an increase in the total energy but it also decreases the cluster efficiency.

References

1. Energy Resources Database: Republic of Turkey, Ministry of Energy and Natural Resources. http://www.enerji.gov.tr (2016). Accessed 13 Feb 2016
2. Liu, P., Veitch, B.: Design and optimization for strength and integrity of tidal turbine rotor blades. Energy **46**, 393–404 (2012). doi:10.1016/j.energy.2012.08.011
3. Barbarelli, S., Florio, G., Amelio, M., Scornaienchi, N.M., Cutrupi, A., Lo Zupone, G.: Design procedure of an innovative turbine with rotors rotating in opposite directions for the exploitation of the tidal currents. Energy **77**, 254–264 (2014). doi:10.1016/j.energy.2014.08.044
4. Development of Marine Energy in New Zealand. EECA Energy Efficiency and Conservation Authority. https://www.ea.govt.nz/dmsdocument/17345 (2008). Accessed 13 Feb 2016
5. Jarosz, E., Teague, W.J., Book, J.W., Beşiktepe, S.: On flow variability in the Bosphorus Strait. J Geophys. Res.: Oceans **116**, (2011). doi:10.1029/2010JC006861
6. Oguz, T., Ozsoy, E., Latif, M.A., Sur, H.I., Unluata, U.: Modelling of hydraulically controlled exchange flow in the Bosphorus Strait. J. Phys. Oceanogr. **20**, 945–965 (1990)

7. Marine Transportation Database: Republic of Turkey, Ministry of, Maritime Affairs and Communications. http://www.ubak.gov.tr (2016). Accessed 13 Feb 2016
8. Marine Current Turbines. http://www.marineturbines.com (2016). Accessed 13 Feb 2016
9. Frandsen, S., Barthelmie, R., Pryor, S., Rathmann, O., Larsen, S., Højstrup, J., Thøgersen, M.: Analytical modelling of wind speed deficit in large offshore wind farms. Wind Energy **9**, 39–53 (2006). doi:10.1002/we.189
10. Matching Renewable Electricity Generation with Demand. Scottish Government Publications. http://www.gov.scot/resource/doc/112589/0027358.pdf (2006). Accessed 13 Feb 2016

Co-pyrolysis of Lignite-Oil Shale Mixtures

Uğur Hayta, Pınar Acar Bozkurt and Muammer Canel

Abstract In this study, conversion of lignite has low calorific value with oil shale have been co-pyrolysed to investigate as an energy source and chemical feedstock. Pyrolysis of Balıkesir Dursunbey lignite (Turkey), Seyitömer oil shale (Turkey), and co-pyrolysis of their mixtures were carried out in a fixed bed reactor at different temperatures and mixture ratios. Pyrolysis experiments were performed in the temperature range of 400–700 °C with mixtures consisting of lignite/oil shale at a weight ratio of 33 % (w/w), 50 % (w/w) and 67 % (w/w). The effect of temperature and different ratios of lignite/oil shale in mixtures on product distribution and fuel properties were investigated. Tars obtained by different experimental conditions were characterized using spectroscopic and chromatographic techniques such as GC-MS and FTIR and the effect of experimental conditions on the formation of this valuable product was determined. The highest tar yield was obtained at 600 °C with a 67 % weight ratio of lignite to oil shale.

Keywords Lignite · Oil shale · Co-pyrolysis · Tar · Energy

1 Introduction

Energy is one of the basic requirements in providing technological development with continuity and fulfillment of people's needs. Increasing world population, continuous improvement in living standards together with technological and economic development have led to drastic increases in the demand for energy. As a consequence, the supply of energy has become a worldwide problem in recent years. Increasing demand for fuels and for chemical feedstock and the awareness of the finite nature of petroleum deposits results in great interest in alternate sources of fossil fuel, such as coal, asphaltite and oil shales [1].

U. Hayta · P.A. Bozkurt (✉) · M. Canel
Department of Chemistry, Science Faculty, Ankara University, 06100 Ankara, Turkey
e-mail: p3acar@hotmail.com

A.Y. Oral and Z.B. Bahsi Oral (eds.), *3rd International Congress on Energy Efficiency and Energy Related Materials (ENEFM2015)*, Springer Proceedings in Energy, DOI 10.1007/978-3-319-45677-5_9

Lignite takes a large proportion of low-rank coals which is a major part of the total global coal reserves in Turkey. However, a large part of present reserves cannot be utilized directly due to its low heating value and high moisture content and negative environmental contributions. Co-utilization of lignite and other renewable fuels can solve this problem to a large extent. Co-pyrolysis, deemed as a promising method, has been extensively investigated by many researchers [2–5]. The thermal co-processing methods could be environmentally friendly ways for the conversion of lignite and oil shale into valuable products such as fuels or chemicals. Oil shale is the second largest fossil fuel source following the lignite reserves in Turkey that can be co-processed with lignite. Oil shale contains significant amounts of kerogen [6]. Industry can use oil shale as a fuel for thermal power-plants, burning (like coal) to actuate steam turbines and to produce liquid and gas fuel. The use of oil shales, which are located in large quantities in Turkey as organic rich sedimentary rock, exists less effort for source of energy and hydrocarbons. Therefore, it is significant to study the energy utilization and development of oil shale.

The aim of this study was to evaluate pyrolysis of lignite (BDL lignite, Balıkesir, Turkey), oil shale (SOL oil shale, Kütahya, Turkey) and their mixtures using a fixed bed reactor under different temperatures and mixture ratios. Liquid products (tar) were characterized by GC-MS and FTIR, the solid products were also analyzed by elemental analysis. The effect of temperature and different ratios of oil shale in mixtures on the thermal degradation of lignite, on yield and properties of pyrolysis products was investigated.

2 Experimental

BDL lignite is from the Dursunbey region of Balıkesir, Turkey and SOL oil shale is from the Seyitömer, Kütahya, Turkey. Firstly, BDL lignite and SOL oil shale are pyrolysized at the temperatures between 400 and 700 °C. Then, lignite and oil shale are mixed together in weight ratio of 33 % (w/w), 50 % (w/w) and 67 % (w/w) of lignite. The schematic diagram of pyrolysis experimental system is displayed in Fig. 1.

The reactor is externally heated by an electrical furnace in which the temperature is measured by a thermocouple inside the reactor. The air of the reactor is purged with nitrogen flow of 30 ml min^{-1} and reactor is heated up to the desired temperature with a heating rate of 10 °C min^{-1}. The outlet of the reactor was connected to a round-bottomed flask with a reflux condenser where condensation of pyrolysate occurred. The reaction mixture was cooled with an ice-salt bath. The yield of tar collected in the round-bottomed flask, and the yield of residual coke as the char remaining inside the reactor after the experiment. The gas products collected by a receiver vessel connected to the end of the reflux condenser.

Gas chromatography mass spectrometry (GC-MS) analysis of the tar is conducted by an AGILENT 6890 GC System 5973 MSD. GC-MS conditions are as follows: capillary column, HP-5MS (50 m × 0.32 mm × 0.52 μm); carrier gas,

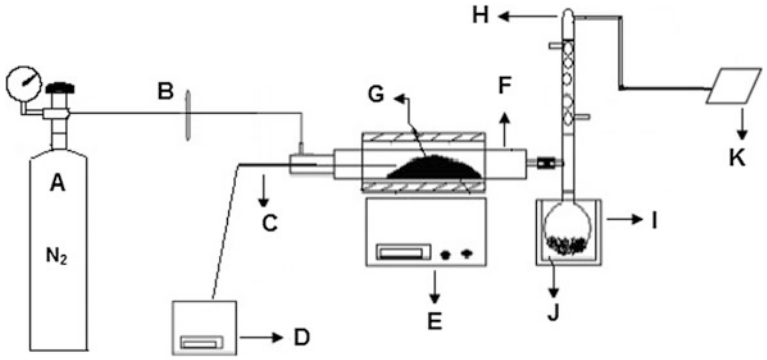

Fig. 1 The schematic diagram of the experimental system. *A* Nitrogen bottle, *B* float flowmeter, *C* thermocouple, *D* the temperature controller, *E* tube furnace, *F* reactor, *G* sample, *H* condenser, *I* cooling unit, *J* liquid collecting vessel, *K* gas collecting vessel

Helium (flow rate 0.7 ml min^{-1}); temperature program of oven: initial hold at to 50 °C during 15 min, heating to 300 °C at 5 °C min^{-1}, and hold 17 min. The Fourier transform infrared spectroscopy (FTIR) spectra's of the tar on a KBr disk are recorded using a Perkin-Elmer Spectrum 100 (ATR-kit) Model FTIR spectrophotometer. Elemental analysis of residual coke is determined by a LECO 932 CHNS elemental analyzer.

3 Results and Discussion

The variations of residual coke, tar and gas products at temperatures between 400 and 700 °C during the co-pyrolysis of lignite with oil shale are given in Fig. 2, respectively. As seen from Fig. 2a, increase in temperature leads to a decrease in the residual coke yields. It means that the conversion degree of the BDL lignite/SOL oil shale mixtures into the mixture of volatile product is increased. According to the results in Fig. 2b, the maximum tar yield is obtained at 600 °C when 67 % of lignite is added to the oil shale. The increase of tar yields by adding lignite to oil shale might be explained by besides the cracking in the structure due to the temperature rise, the catalytic interaction resulting from inorganic structure of the lignite and creating of an extraction medium by oil shale. Yield of tar increases with increasing temperature. The reason for this variation is related to enhance thermal degradation of synergetic effects during co-pyrolysis. As shown in Fig. 2c, increase in temperature leads to an increase in the gas yields for all mixing ratios. The maximum gas yield is obtained at 700 °C due to secondary decomposition reactions of the liquid fractions to the gases.

One of the effects that are being studied in this work is the effect of synergism. The different pyrolytic behaviours of the individual fuel components and the fuel

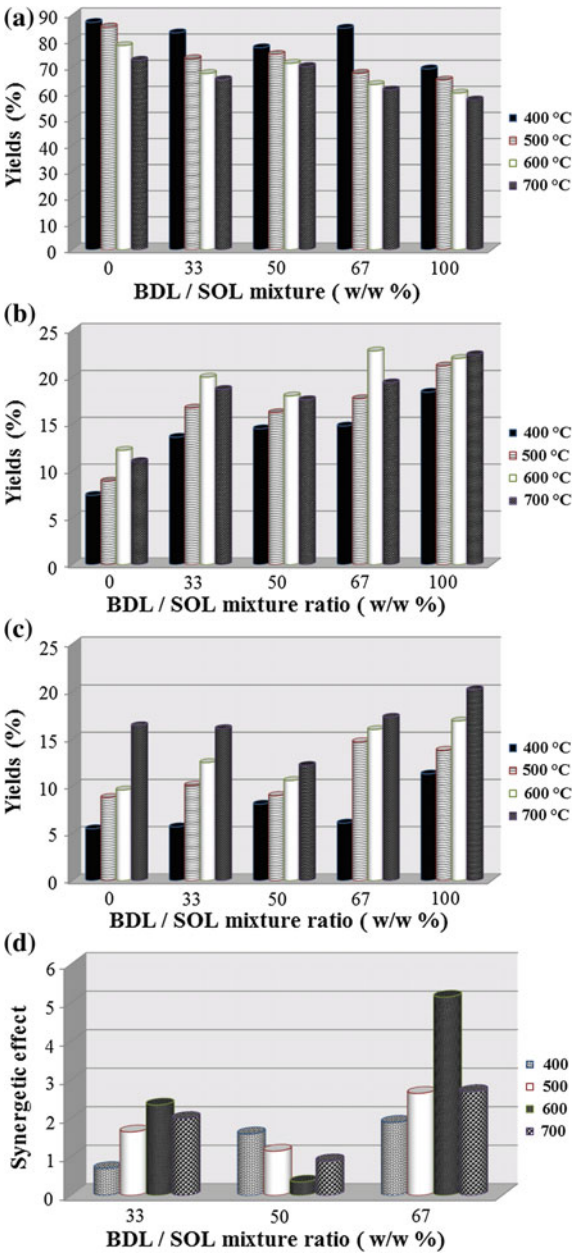

Fig. 2 Effect of the BDL lignite contents in the mixtures on **a** the residual coke, **b** tar and **c** gas products at various temperatures, **d** synergetic effects obtained for the tar during the copyrolysis of lignite-oil shale mixtures

mixture is called synergism. Figure 2d show the synergetic effects obtained for the tar yields in the co-pyrolysis of lignite and oil shale. As shown in figure, an increase in the lignite content of the mixture leads to the increased synergetic effect in the production of tar.

GC-MS analysis results of the tars from pyrolysis of BDL lignite, SOL oil shale and BDL: SOL 67 % (w/w) at 600 °C are presented in Fig. 3a. When the product groups between lignite and lignite-oil shale mixture is compared, it has been seen that adding lignite to the oil shale leads to decrease in the amount of alkane compounds and an increase in the amount of alkene compounds. On the contrary observe no significant change in the amount of aromatic compounds. From the GC-MS composition it has been found that the derivatives of phenol and some

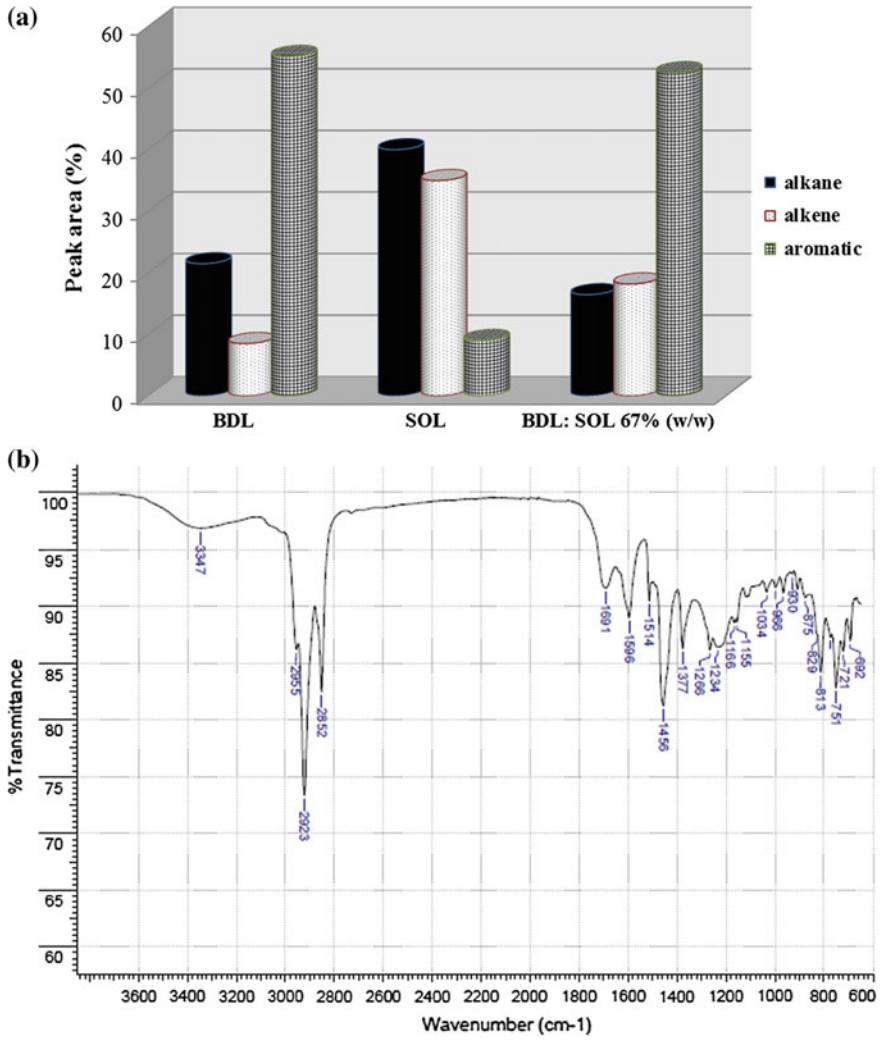

Fig. 3 Result of **a** GC-MS analysis of the tars obtained by pyrolysis at 600 °C, **b** FTIR of the tars obtained from co-pyrolysis BDL:SOL 67 % (w/w) at 600 °C

Table 1 Elemental analysis of the residual coke obtained by pyrolysis at 600 °C

	Elemental analysis, wt%				
	C	H	N	S	O
BDL	66.23	2.96	0.15	–	30.66
SOL	28.09	1.37	0.27	–	70.27
BDL:SOL 67 %	52.29	0.88	–	–	46.83

polycyclic aromatic hydrocarbons such as naphthalene, its derivatives, and phenanthrene structures are increased as a result of adding lignite to the oil shale.

The FTIR spectra of the tar from co-pyrolysis of BDL: SOL 67 % (w/w) mixture at 600 °C is given in Fig. 3b. The analysis of the regions at 2850–2980 cm^{-1} and 1350–1480 cm^{-1} shows that aliphatic hydrogen is mainly as $–CH_2$ structures. The broad peak around at 3000 cm^{-1} represents –OH stretching vibrations indicating the presence of phenols and alcohols. The region between 700 and 900 cm^{-1} contains various bands related to aromatic out of plane C–H banding in the tar. The band in 1260–1280 cm^{-1} indicates C–O–C etheric structure representing the formation of etheric structures.

Elemental analysis results of the residual coke obtained by pyrolysis of BDL lignite, SOL oil shale and BDL: SOL 67 % (w/w) mixture at 600 °C are given in Table 1. It is seen that, the amount of hydrogen in the residual coke obtained by co-pyrolysis of lignite-oil shale mixture appears to be the lowest level due to the leaving of volatile products from the solid structure.

4 Conclusions

The conclusions of this study are given below:

- Adding lignite to the oil shale 67 % (w/w) leads to an increased tar yield at all temperatures.
- Co-pyrolysis of lignite-oil shale mixtures is the main source of production of higher phenols and some polycyclic aromatic hydrocarbons such as naphthalene, its derivatives phenanthrene.
- The synergetic effect of lignite-oil shale mixture for tar yield is positive.

References

1. Lee, S., Speight, J.G., Loyalka, S.K: Handbook of Alternative Fuel Technologies. CRC Press, Boca Raton (2007)
2. Guan, Y., Ma, Y., Zhang, K., Chen, H., Xu, G., Liu, W., Yang, Y.: Co-pyrolysis behaviors of energy grass and lignite. Energy Convers. Manag. **93**, 132–140 (2015). doi:10.1016/j.enconman.2015.01.006

3. Yang, X., Yuan, C., Xu, J., Zhang, W.: Potential method for gas production: high temperature co-pyrolysis of lignite and sewage sludge with vacuum reactor and long contact time. Bioresour. Technol. **179**, 602–605 (2015). doi:10.1016/j.biortech.2014.11.104
4. Fei, J., Zhanga, J., Wang, F., Wang, J.: Synergistic effects on co-pyrolysis of lignite and high-sulfur swelling coal. J. Anal. Appl. Pyrol. **95**, 61–67 (2012). doi:10.1016/j.jaap.2012.01.006
5. Acar, P., Sinağ, A., Misirlioğlu, Z., Canel, M.: The pyrolysis of scrap tire with lignite. Energy Sour. Part A Recovery Util. Environ. Eff. **34**, 287–295 (2012). doi:10.1080/15567030903586063
6. Yahya, H.K., Nabih, A.I., Ihsan, M.S.: Spectroscopic and chromatographic analysis of oil from an oil shale flash pyrolysis unit. Energy Convers. Manag. **44**, 125–134 (2003). doi:10.1016/S0196-8904(02)00047-X

Airborne Wind Energy—A Review

Mahdi Ebrahimi Salari, Joseph Coleman and Daniel Toal

Abstract Airborne Wind Energy (AWE) is a new approach to harvest stronger wind streams at higher altitudes for renewable energy. This paper reviews recent developments in this field. Conventional wind energy and current constrains for its development are discussed and airborne wind energy as an appropriate solution in the literature is reviewed. Different AWE technologies are reviewed and appraised and other related issues such as transmission and curtailment are discussed.

Keywords Airborne wind energy (AWE) · Synchronous generator · Direct interconnection · Power to gas

1 Introduction

At present, with rising concerns about global warming and limited fossil resources, renewable energy is more popular than ever. In recent decades, renewable energy has seen faster growth than other forms of energy production. Among different non-hydro renewable energies, wind energy has seen the biggest absolute increase. It is anticipated that the share of wind energy in total worldwide electricity generation will be 4.5 % in 2030 and that wind power will be the second most significant source of renewable electricity production after hydropower [1].

Despite the rapid development of wind energy in recent decades, it is still expensive and most wind energy projects encounter financing problems [1]. Investors are demanding more profit from wind energy projects and researchers are

M. Ebrahimi Salari (✉) · J. Coleman · D. Toal
Mobile and Marine Research Centre, University of Limerick, Limerick, Ireland
e-mail: Mahdi.Ebrahimisalari@ul.ie

J. Coleman
e-mail: Joseph.Coleman@ul.ie

D. Toal
e-mail: Daniel.Toal@ul.ie

A.Y. Oral and Z.B. Bahsi Oral (eds.), *3rd International Congress on Energy Efficiency and Energy Related Materials (ENEFM2015)*, Springer Proceedings in Energy, DOI 10.1007/978-3-319-45677-5_10

looking for solutions to decrease the total cost of wind energy by reducing cost of construction, repair & maintenance and transmission to grid. According to [2], 91 % of a typical wind turbine cost is allocated to the turbine, grid connection and foundation costs forming 75.6, 8.9 and 6.5 % respectively. Airborne wind energy can provide a significant cost reduction in turbine and foundation costs. Also, by using new technologies such direct interconnection and hydrogen production from curtailed winds, grid connection cost will be reduced considerably.

In this chapter, different airborne wind energy technologies are reviewed and recent developments in utilizing curtailed winds and a new interconnection scheme are presented.

2 Airborne Wind Energy

An AWE system typically consists of a free flying airborne element such as a kite, glider or floating horizontal axis wind turbine, which is connected to ground through a tether. The first study of airborne wind energy was conducted in 1930 in California, USA, though the first attempt to produce electricity from an airborne wind energy device was in Minnesota, USA; a generator was installed on a balloon and it was capable of producing 350 W electrical power [3]. Loyd in 1980 reported the first analysis of kite based wind energy systems. He modeled large-scale power production by means of an aerodynamically efficient kite. According to his work with use of a tethered wing as big as a C-5A aircraft, it is possible to generate 6.7 MW of electrical energy with a 10 m/s wind [4].

The primary motivation for developing airborne wind energy systems is low cost access to stronger winds at higher altitudes. With increasing altitude, the speed of wind increases and winds are more consistent and less turbulent. At altitudes above 200 m, wind energy devices can provide the highest capacity factor at lower cost [5]. According to (1) the wind power density at altitude (WPD_h) increases to the cube of wind speed [6]. This cubic relationship can be seen also in Fig. 1 where increase of wind speed and power density with altitude is illustrated. This is the main motivation driving AWE device development; generating wind energy at higher altitude than possible with civil structures. With even small increases in the height of the wind energy device, the generated power increases significantly.

$$WPD_h = \frac{1}{2}\rho V_{w\_h}^3 \tag{1}$$

In (1), ρ is the air density and V_{w_h} is the wind speed at altitude h.

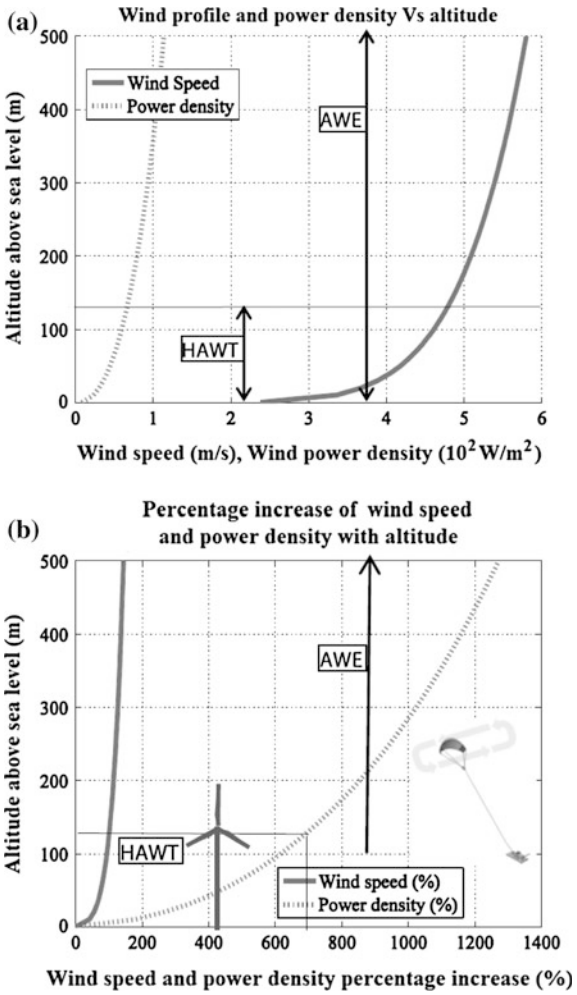

Fig. 1 **a** Wind speed and power density with altitude, **b** wind density and power density percentage increase with altitude [37, 38]

2.1 Ampyx Power

Ampyx Power is a Dutch company that is developing a pumping mode AWE system with a tethered rigid wing glider called PowerPlane. Pumping mode AWE is a reciprocating operation which consists of two phases; the pumping phase and recovery phase. During the pumping phase, a tethered glider pulls on the ground station tether drum through the tether. The drum is connected to generator by a drivetrain. With rotation of the tether drum, the generator will rotate, producing electricity. When the tether reaches the maximum length, the glider will change its flight path toward ground station and tether will be rewound onto the drum. This phase is called the recovery phase. Power is consumed during the recovery phase

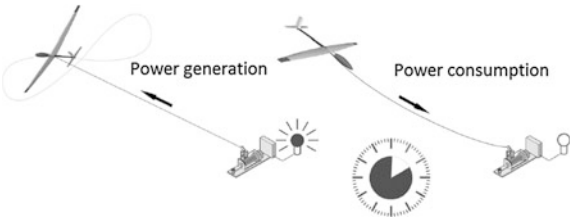

Fig. 2 Ampyx PowerPlane [9]

but it is considerably less than generated power in pumping mode [7]. Ampyx Power AWE concept is demonstrated in Fig. 2. This company developed a prototype in 2013. The proposed system is a 12 kW PowerPlane which is described as a six degree of freedom rigid wing system. The electrical power takeoff for this prototype is a single direct driven electrical machine with grid connection through a power converter [8]. Ampyx Power is planning to develop two 250 kW and 3 MW prototypes by 2018 [9].

2.2 WindLift

WindLift was founded in 2006 and developed a ground actuated kite control system. This American company developed an AWE prototype which utilized a 40 m^2 inflatable kite as the prime mover. The kite is tethered to a ground station by three tethers; one main tether that rotates the electrical generator and two steering tethers that provide ground based steering actuation. This system is capable of producing 12 kW peak electrical power form winds with speeds between 12 and 40 mph. The ground station of WindLift prototype is shown in Fig. 3 [10]. As can be seen, the main tether is wound onto a drum which is connected to a generator. In the power phase, the kite rotates the generator through the tension in tether. In the recovery phase, the generator operates as a motor, winding the tether onto the drum. The WindLift pumping mode prototype uses a 90 cm diameter drum, which is

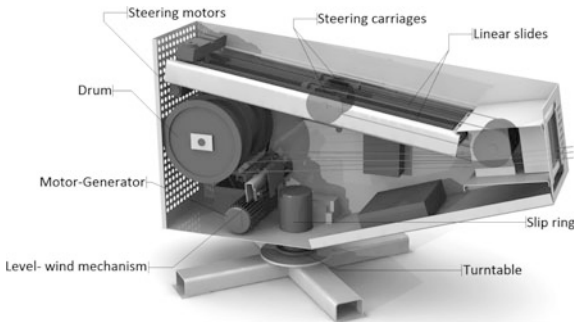

Fig. 3 WindLift ground station [10]

connected to 60 kW motor-generator built originally for a hybrid electric bus. In the future, WindLift plan to improve the wing characteristics to increase power in generation phase and decrease consumption during recovery phase [11].

2.3 *EnerKite*

EnerKite was founded in 2010 in Germany. The core team behind EnerKite has been active in the area of AWE related systems since 2002. In 2008, Aeroix and Festo tested a prototype called 'CyberKite'. This prototype used an innovative hybrid kite designed with a bionic stingray shape and helium supported wings. The development of the control mechanism for this 24 m^2 kite ended in 2010 after several hundred hours of testing [12].

After the establishment of EnerKite this company drew on its experiences from CyberKite to develop a new prototype 'EK30'. This AWE device is a 30 kW prototype which is driven by a three line ground actuated kite power system. This prototype has been developed as a mobile AWE system mounted on a vehicle and works off-grid using battery storage. It can operate at altitudes between 100 and 300 m and uses a 30 m^2 wing [12, 13]. The EK30 is shown in Fig. 4.

EnerKite is planning to develop two new prototypes in 2017 and 2018. EK200 is designed to generate 100 kW electricity as a standalone system or within an isolated grid. The wing area of this system is 30 m^2 and it will be capable of operating in wind speeds between 3 and 20 m/s. EK1M is a large-scale commercial product which is planned to be on the market by 2018. This system can generate 500 kW electrical energy connected to a power grid. The EK1M is projected to use a 125 m^2 area kite and it will operate in wind speeds from 3 to 25 m/s. The maximum operating altitude for this system will be 300 m [12, 13].

Fig. 4 EnerKite [12]

2.4 SkySails

SkySails was established in 2001 to develop airborne wind energy devices for ship propulsion augmentation. Between 2001 and 2006, they tested small scale prototypes on various vessels. In 2013 SkySails developed a ship towing kite which is capable of displacing up to 2 MW propulsion power. This 320 m^2 kite can allow a ship to reduce fuel oil consumption by up to 10 tons per day. This company has extended its interests to electrical power generation. In 2011, SkySails developed a 55 kW prototype for producing electrical energy. The prototype is a pumping mode airborne wind energy system, which uses a single motor/generator for electrical power takeoff and kite recovery in the pumping mode cycle. SkySails are planning to develop a 1 MW offshore airborne wind energy device, which would use a 400 m^2 kite on a 1000 m tether. SkySails are considering the development of the first offshore AWE farm with over 7 MW per device [14, 15]. The Skysails ship propulsion system and AWE off-shore farm have been shown in Fig. 5.

2.5 Makani Power

Makani Power, a Google X company, has developed a unique type of airborne wind energy, which is called an Airborne Wind Turbine (AWT). The AWT is a rigid

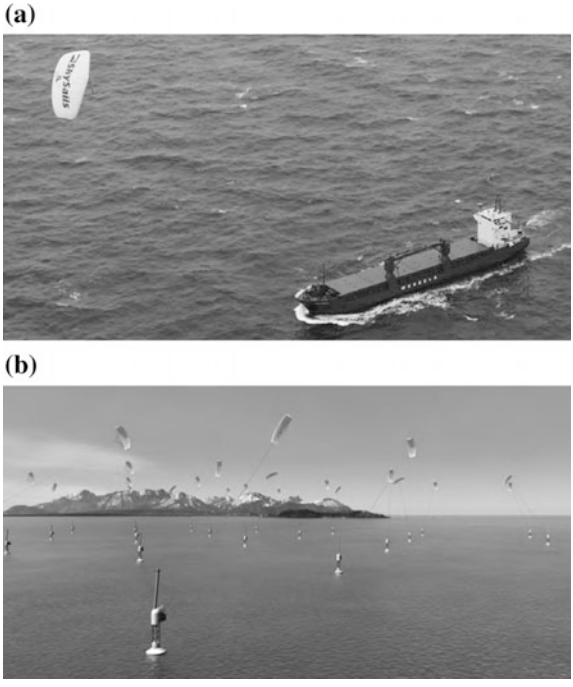

Fig. 5 SkySails productions, **a** ship propulsion system, **b** airborne power generator [14]

wing which carries eight propeller/turbines with each connected to motor/generator. During launch, the electrical machines drive the propellers consuming power to bring the system from the ground station to the desired starting altitude. The propellers are then adjusted to act as turbines driving the electrical machines as generators, producing electricity. The generated power is transferred to the ground station through the tether. The tether is made of conductive aluminum wires and high strength carbon fiber core [16]. In addition to power transmission, the tether provides communications between AWT and ground station. Installing electrical power take off machinery on the wing increases the airborne system mass. For a 100 kW AWT with 8 turbines the overall weight of power electronics converters and generators/motors on the airfoil would be 70 kg and tether weight will be 320 kg. A related paper unaffiliated with Makani claims the optimal tether voltage for minimum mass is 8 kV DC [17]. Makani Power has tested two 10 kW and 30 kW prototypes and currently they are working on an AWT device with 600 kW rated power in an 11.5 m/s wind, which operates at altitudes between 140 and 310 m with a 145 m circling radius [16].

2.6 Sky WindPower

Sky WindPower is developing an innovative type of airborne wind energy device. This system is an autonomous quad-copter, which consumes electrical energy to reach the appropriate altitude for power generation. When the device arrives at the desired altitude, it inflects itself to the wind at a specific pitch angle to allow the rotors to be driven by the wind, consequently generating electrical power and lift simultaneously. Their device, which is called Wind Airborne Tethered Turbine System (WATTS), is nearly ready for customer testing and can generate 240 kW nominal electrical power at altitudes up to 2000 m with high wind speeds from 9 mph to greater than 65 mph [18]. WATTS is designed to operate in off-grid sites such as military outposts, naval vessels, mining operation, oil drilling platforms, agricultural, scientific and research facilities. In addition, WATTS will be capable of performing other roles such as “Eye in the Sky” security systems, remote antenna elevation, atmospheric sampling, weather monitoring, etc. [18, 19].

2.7 Academic Research

In several universities, airborne wind energy is under investigation. TU Delft is one of the leading universities working on AWE systems. In 1999, they undertook their first AWE system analysis [20, 21]. This system consists of a number of wings that are connected to each other by a single tether driving a ground located generator. In 2013, a 20 kW rated ground station and kite control system for a pumping mode

AWE prototype was developed by researchers in TU Delft [22]. Developing novel control methods, ground station and kite design are other issues that are under investigation in TU Delft [23–25].

In Politecnico di Torino, a prototype called KiteGen has been simulated and tested. Two different topologies have been presented by researches in Politecnico di Torino, yo-yo and carousel configuration [26]. The yo-yo configuration is the same as pumping mode AWE, while the proposed carousel configuration consists of several airfoils, each one connected to a kite steering unit (KSU) placed on a vehicle moving along a circular rail path. Each airfoil pulls one vehicle on the carousel while the vehicles maintain constant separation from each other on the rail. Electrical power is generated through motor/generators driven by the wheels of each rail vehicle [27, 28].

Neural network controllers for controlling airborne wind energy systems have been developed at the University of Sussex. The evolution of neural network controllers has been carried out by genetic algorithms. It has been shown that continuous time recurrent networks (CTRNN) are capable of being trained for flying AWE kites in an appropriate repetitive trajectory even when the length of tether is changing [29, 30].

A two-line kite control algorithm has been developed in KU Leuven. This controller is capable of controlling the lateral angle of kite and feedback is used to stabilize the orbit of the kite. For monitoring of the motion of the kite, polar coordinates are used in four degrees of freedom [31]. Optimization of towing kites, developing a non-linear model of predictive control, new approaches for launch and recovery of glider AWE systems and trajectory optimization of AWE devices are other research works which have been carried out at KU Leuven [32–35]. In addition, in [36] the use of two airfoils for airborne wind energy systems on a single main tether has been investigated.

A new power take off method for pumping mode airborne wind energy has been developed at the University of Limerick. This AWE prototype does not reverse the generator to perform the recovery task, but rather this is performed by a fractional scale recovery motor. In this arrangement, the two pumping mode operations are separated and performed by optimally specified electrical machines for each task. Using a non-reversing generator is more suitable for power generation and delivery to grid especially at large scales. Furthermore, direct interconnection of AWE generators and distributed control for the flight of tethered kites have been developed at the University of Limerick [37–39] and remains an active area of research.

Currently, six universities consisting of TU Delft, KU Leuven, TU Munich, ETH Zurich and University of Limerick and four industrial partners are cooperating in the AWESCO ITN, a Marie Skłodowska-Curie action under the Horizon 2020 framework program of the European Union [40]. This network is focused on the development and optimization of AWE technology and methods and will ensure the continued development of AWE within the EU.

3 Dispatch and Curtailment

Dispatching generated power is a challenge in dealing with airborne wind energy systems, especially with offshore devices. Conventional wind energy technology deploys power converters in each unit where the generated power is converted to DC and recovered to gird compliant AC for supply to the distribution network. Using power converters for each unit will increase rate of failure and cost of systems, as according to [41] the converter has the third highest failure rate among wind turbine subassemblies. In offshore airborne wind energy devices, the failure rate and cost would be even more because of high expenses of offshore repair and maintenance and the novelty of the technology. In [42] a new approach, called direct interconnection, has been proposed and tested for offshore wind energy systems. In this method, power converters are removed from the individual power devices and the generators are synchronized directly onto an offshore power bus by means of a synchronization controller. After synchronization, overall generated power is dispatched to on-shore station. In an onshore station, a back-to-back converter provides a grid-code compliant AC output from the interconnected off-shore bus. This approach has been analyzed for pumping-mode airborne wind energy systems in [37, 38] and conventional wind turbines in [42] with promising results.

In a curtailment situation, wind is available but the grid operator does not allow the wind farm to dispatch the generated power to the grid. A wind turbine or AWE system might be curtailed when the transmission system is under loaded due to lack of demand. In this situation, the system is subjected to overvoltage conditions and network operators try to relieve this by decreasing power production on the network. Curtailment may also happen for other system reasons such as frequency control or market based protocols [43].

During curtailment conditions, it may be possible to store energy locally rather than ceasing operation or reducing/curtailing generated power. Different methods for storing curtailed wind energy exist such as pumped hydroelectricity storage (PHES) [44] and compressed air energy storage (CAES) [45]. Power to gas (P2G) is a new approach, where curtailed wind energy is converted to methane gas which can be sold for gas network consumption, transportation, heating, etc. P2G systems convert electrical energy to hydrogen through an electrolysis process. The produced hydrogen is then converted to methane by reaction with CO_2. The required CO_2 could be achieved from different resources such as ambient air, thermal power plant exhaust or biogas. The overall efficiency of power to gas conversion is between 55 and 80 % depending on the efficiency of the electrolysis and methanation processes [46]. Winds in higher altitudes are more consistent and hence AWE systems can operate more often than conventional wind turbines. Since it is not always possible to dispatch generated power to grid, using power to gas technology would be a very helpful technology for utilizing curtailed winds.

4 Conclusion

Different AWE technologies under development have been reviewed. In some technologies, soft wings provide the mechanical prime mover while some others are using rigid wings to harness wind energy. AWE systems with rigid wings are more efficient and easier to control. In the case of soft wings, researchers are developing new kite models and construction methods to improve their efficiency. Using a pumping mode operated ground station is the most popular electrical power take-off method. In some cases such as Makani AWT and Sky WindPower WATTS, generators are mounted on the wing. In these cases, high voltage tethers, increased weight and mechanical strength of cables for transmitting power from wing to ground station are fundamental challenges, especially in large-scale devices.

Dispatching generated power is a very significant factor in the cost of generated power. In the case of offshore AWE systems, dispatch becomes much more important because of the long distance from the shore and the high expenses of offshore repair and maintenance. Direct interconnection is an appropriate solution for reducing the cost of generated power by minimizing the number of power electronic converters offshore. Using curtailed wind energy for producing gas would be a very useful technology to store generated power by AWE devices during the periods when it is not possible to deliver electrical power to the grid.

Various companies and universities are developing AWE systems with many promising commercial products by 2020. Despite the widespread developments of airborne wind energy systems, this technology is still very young and much work remains to move towards commercial devices.

Acknowledgments This publication has emanated from research supported by the Science Foundation Ireland under the MaREI Centre research program [Grant No. SFI/12/RC/2302] and through the support of the European Commission under the H2020 Marie Skłodowska-Curie action: ITN AWESCO [Reference No. 642682].

References

1. International Energy Agency (IEA): World Energy Outlook 2014. http://www.iea.org (2014). Accessed 1 Oct 2015
2. The European Wind Energy Association: The economics of wind energy. http://www.ewea.org/fileadmin/files/library/publications/reports/Economics_of_Wind_Energy.pdf (2009). Accessed 1 Oct 2015
3. Manalis, M.S.: Airborne windmills and communication aerostats. J. Aircraft **13**(7), 543–544 (1976). doi:10.2514/3.58686
4. Loyd, M.L.: Crosswind kite power. Energy **04**(03), 106–111 (1980). doi:10.2514/3.48021
5. Archer, C.L., Calderia, K.: Global assessment of high-altitude wind power. Energies **2**, 307–319 (2009). doi:10.3390/en20200307
6. Archer, C.L.: An introduction to meteorology for airborne wind energy. In: Ahrens, U., et al. (eds.) Airborne Wind Energy, pp. 81–94. Springer, Heidelberg (2013). doi:10.1007/978-3-642-39965-7_5

7. Sieberling, S.: Flight guidance and control of a tethered glider in an airborne wind energy application. In: Qiping, C., et al. (eds.) Advances in Aerospace Guidance Navigation and Control (Selected Papers of the Second CEAS Specialist Conference on Guidance, Navigation and Control), Delft, pp. 337–351. Springer, Heidelberg (2013). doi:10.1007/978-3-642-38253-6_21
8. Ruiterkamp, R., Sieberling, S.: Description and preliminary test results of six degrees of freedom rigid wing pumping system. In: Ahrens, U., et al. (eds.) Airborne Wind Energy, pp. 443–458, Springer, Heidelberg (2013). doi:10.1007/978-3-642-39965-7_26
9. Ampyx Power: Airborne wind energy. http://www.ampyxpower.com (2015). Accessed 1 Oct 2015
10. Creighton, R.: Go fly a kite. IEEE Spect. **49**(12), 46–51 (2012). doi:10.1109/MSPEC.2012.6361763
11. WindLift: Airborne wind energy. http://windlift.com/technology.html (2015). Accessed 1 Oct 2015
12. Bormann, A., et al.: Development of a three-line ground-actuated airborne wind energy converter. In: Ahrens, U., et al (eds.) Airborne Wind Energy, pp. 427–436. Springer, Heidelberg (2013). doi:10.1007/978-3-642-39965-7_24
13. EnerKite: Airborne wind energy. http://www.enerkite.de/en/ (2015). Accessed 1 Oct 2015
14. Fritz, F.: Application of an automated kite system for ship propulsion and power generation. In: Ahrens, U., et al. (eds.) Airborne Wind Energy, pp. 359–372, Springer, Heidelberg (2013). doi:10.1007/978-3-642-39965-7_20
15. SkySails: Airborne wind energy. http://www.skysails.info/english/power/development/3-product-35-mw-and-first-test-wind-farm/ (2015). Accessed 1 Oct 2015
16. MakaniPower: Airborne wind energy. http://www.google.com/makani/technology/ (2015). Accessed 1 Oct 2015
17. Kolar, J.W., et al.: Conceptualization and multi-objective optimization of the electric system of an airborne wind turbine. In: IEEE International Symposium on Industrial Electronics (ISIE 2011), Gdansk, pp. 26–31, 27–30 June 2011. IEEE, Gdansk (2011). doi:10.1109/ISIE.2011.5984131
18. Sky Wind Power: Airborne wind energy. http://www.skywindpower.com/ (2015). Accessed 1 Oct 2015
19. Roberts, B.W., et al.: Harnessing high altitude winds power. IEEE Trans. Energy Convers. **22** (1), 136–144 (2007). doi:10.1109/TEC.2006.889603
20. Ockels, W.J.: Laddermill, a novel concept to exploit the energy in the airspace. Aircr. Des. **4**, 81–97 (2001). doi:10.1016/S1369-8869(01)00002-7
21. Ockels, W.J., et al.: The Laddermill: work in progress. In: European Wind Energy Conference, London, 22–25 Nov 2004
22. Jehle, C., Schmehl, R.: Applied tracking control for kite power systems. J. Guid. Control Dyn. **37**(4), 1211–1222 (2014). doi:10.2514/1.62380
23. Fechner, U., Vlugt, R.V., Schreuder, E., Schmehl, R.: Dynamic model of a pumping kite power system. Renew. Energy **83**, 705–716 (2015). doi:10.1016/j.renene.2015.04.028
24. Lansdorp, B., Ockels, W.J.: Design and construction of a 4 kW ground station for the Laddermill. In: 7th IASTED International Conference on Power and Energy systems (EuroPES 2007), Palma de Mallorca, pp. 1–8, 29–31 Aug 2007, IASTED (2007)
25. Williams, P., et al.: Modeling, simulation, and testing of surf kites for power generation. In: AIAA Modeling and Simulation Technologies Conference and Exhibit, Hawaii, 18–21 Aug 2008
26. Canale, M., et al.: High altitude wind energy generation using controlled power kites. IEEE Trans. Control Syst. Technol. **18**(2), 279–292 (2010). doi:10.1109/TCST.2009.2017933
27. Canale, M., Fagiano, L., Milanese, M., Ippolito, M.: Control of tethered airfoils for a new class of wind energy generator. In: Parisini T., et al. (eds.) Proceedings of the 45th Conference on Decision and Control, San Diego, pp. 4020–4026, 13–15 Dec 2006. IEEE (2006). doi:10.1109/CDC.2006.376775

28. Canale, M., Fagiano, L., Milanese, M.: Power kites for wind energy generation. IEEE Control Syst. Mag. **27**(6), 25–38 (2007). doi:10.1109/MCS.2007.909465
29. Furey, A.D.: Evolutionary robotics in high altitude wind energy application. Dissertation, University of Sussex (2011)
30. Furey, A., Harvey, I.: Evolution of neural networks for active control of tethered airfoils. In: Almeida e Costa, F. (eds.) Proceedings of 9th European Conference, ECAL 2007, Lisbon, vol. 4648, pp. 746-755, 10–14 Sep 2007. Springer, Heidelberg (2007). doi:10.1007/978-3-540-74913-4_75
31. Diehl, M., et al.: Real-time optimization for large scale nonlinear processes. Dissertation, Heidelberg: Ruprecht Karls University (2001)
32. Geebelen, K., et al.: An experimental test set-up for launch/ recovery of an Airborne Wind Energy (AWE) system. In: Proceedings of the American Control Conference (ACC), Montreal, pp. 4405–4410, 27–29 June 2012. IEEE, Montreal (2012). doi:10.1109/ACC.2012.6315033
33. Houska, B., Diehl, M.: Optimal control of towing kites. In: Proceedings of 45th IEEE Conference on Decision and Control, San Diego, pp. 2693–2697, 13–15 Dec 2006. IEEE, San Diego (2006). doi:10.1109/CDC.2006.377210
34. Houska, B., et al.: Robustness and stability optimization of power generating kite systems in a periodic pumping mode. In: IEEE International Conference on Control Applications (CCA), Yokohama, pp. 2172–2177, 8–10 Sept 2010. IEEE, Yokohama (2010). doi:10.1109/CCA.2010.5611288
35. Ilzhoefer, A., et al.: Nonlinear MPC of kites under varying wing conditions for a new class of large scale wind power generators. Int. J. Robust Nonlinear Control **17**(17), 1590–1599 (2007). doi:10.1002/rnc.1210
36. Zanon, M., et al.: Airborne wind energy based on dual airfoils. IEEE Trans. Control Syst. Technol. **21**(4), 1215–1222 (2013). doi:10.1109/TCST.2013.2257781
37. Coleman, J., Ahmad, H., Pican, E., Toal, D.: Modeling of a synchronous offshore pumping mode airborne wind energy farm. Energy **71**, 569–578 (2014). doi:10.1016/j.energy.2014.04.110
38. Coleman, J.: Distributed control system and novel power take off method for pumping-mode airborne wind energy. Dissertation, University of Limerick (2014)
39. Coleman, J., Ahmad, H., Pican, E., Toal, D.: None-reversing generators in a novel design for pumping mode airborne wind energy farm. In: Ahrens, U., et al. (eds.) Airborne Wind Energy, pp. 587–597. Springer, Heidelberg (2013). doi:10.1007/978-3-642-39965-7
40. AWESCO: Airborne wind energy. http://www.awesco.eu/ (2015). Accessed 1 Oct 2015
41. Spinato, F., et al.: Reliability of wind turbine subassemblies. IET Renew. Power Gener. **3**(4), 1–15 (2009). doi:10.1049/iet-rpg:20080060
42. Pican, E., Omerdic, E., Toal, D., Leahy, M.: Analysis of parallel connected synchronous generators in a novel offshore wind farm model. Energy **36**(11), 6387–6397 (2011). doi:10.1016/j.energy.2011.09.035
43. Bird, L., et al.: Wind and solar energy curtailment: experience and practices in the United States. National Renewable Energy Laboratory (NREL). http://www.nrel.gov/publications (2014). Accessed 1 Oct 2015
44. Deane, J.P., Gallachoir, B.P.O., McKeogh, E.J.: Techno-economic review of existing and new pumped hydro energy storage plant. Renew. Sustain. Energy Rev. **14**(4), 1293–1302 (2010). doi:10.1016/j.rser.2009.11.015
45. Beaudin, M., Zareipour, H., Schellenberglabe, A., Rosehart, W.: Energy storage for mitigating the variability of renewable electricity sources: an updated review. Energy. Sustain. Dev. **14**(4), 302–314 (2010). doi:10.1016/j.esd.2010.09.007
46. Ahern, E.P., Deane, P., Persson, T., Gallachoir, B.O., Murphy, J.D.: A perspective on the potential role of renewable gas in a smart energy island system. Renew. Energy **78**, 648–656 (2015). doi:10.1016/j.renene.2015.01.048

Full Utilization Control of Stored Energy in Lithium-Ion Batteries Based on Forecasted PV Output for HEMS

Ahmad Syahiman Mohd Shah, Yuki Ishikawa, Hiroki Takahashi, Suguru Odakura and Naoto Kakimoto

Abstract Renewable energy resources such as photovoltaic (PV) are crucial to counter an incoming energy crisis in the future. Nevertheless, when PV generators are integrated with storage batteries, a constructive mechanism needs to be structured in order to securely control the energy flow in the batteries during the charging/discharging process so that the risk of over-charge/over-discharge of the batteries can be prevented. Furthermore, it is extremely essential to implement a control method that is capable to fully utilize a stored energy in the scope of small-scale BESS to the load regularly in the first place before it is further scaled up to a mega-structure. In this study, an energy control scheme that considers and executes a next-day forecast of generation based on Grid Point Value as an input data has been proposed. Experimental equipment was structured and the system's operation was completely administered by an RX621 microcontroller. Good experimental results were obtained corresponding to the trend of simulation results.

1 Introduction

Day by day, the availability of primary energy resources like oil and gas is approaching an alarming level since the global demand has exceeded its production. This huge demand has accelerated the worldwide research focusing on the alternative energies such as PV. Although the use of PV system does not contribute risky emissions to the environment, it is fluctuating due to the meteorological conditions [1]. Thus, a conventional solution that can be considered in order to suppress this unsteady output power is to integrate PV panels with rechargeable batteries [2]. On the other hand, in order to stabilize the daily supplied energy from the PV generator to the load continuously, it is extremely necessary to predict the amount of energy generation for the next day in advance [2]. For example, J. Han et al. [3] has included an estimation of energy generation based on the weather

A.S.M. Shah · Y. Ishikawa · H. Takahashi · S. Odakura · N. Kakimoto (✉)
Department of Electrical and Electronic Engineering, Ibaraki University, Hitachi, Japan
e-mail: naoto.kakimoto.ee@vc.ibaraki.ac.jp

A.Y. Oral and Z.B. Bahsi Oral (eds.), *3rd International Congress on Energy Efficiency and Energy Related Materials (ENEFM2015)*, Springer Proceedings in Energy, DOI 10.1007/978-3-319-45677-5_11

forecast in their HEMS application but, since their systems are not equipped with batteries for energy storage, the focus is mainly on saving the electricity cost by monitoring the home energy use in real-time only. In this study, main approach is to test how sensitive the proposed scheme works with the entire system, experimentally and how effective it deals with errors that caused by the forecast data.

2 Forecasting Model Based on Grid Point Value (GPV)

Numerical weather predictions of solar radiation are performed based on Meso-Scale Model (MSM) developed by Japan Meteorology Agency (JMA). From our previous study [4], the hourly horizontal solar radiation is defined as;

$$S_i = S_0 \cos z \cdot f(C) \tag{1}$$

where S_0 and z are the clear-sky solar radiation and solar zenith angle, respectively.

By including five parameters, i.e. relative humidity (RH), precipitation (P), low-level cloud cover (C_L), middle-level cloud cover (C_M) and high-level cloud cover (C_H) in this formulation, the function $f(C)$, in (1) can be interpreted as;

$$f(C) = \exp\left[-\left(\frac{aRH + bP + cC_L + dC_M + eC_H}{C_0}\right)\right] \tag{2}$$

where a, b, c, d and e are variables. Hence, the detail explanation of this model is further elaborated in [4].

Furthermore, it is well known that this seasonal variation of solar radiation is considerably leveled by tilting the PV panel toward the south depending on the geographical latitude of the place [5]. Thus, the tilted solar radiation, S_T can be modified from one-day horizontal solar radiation, S as follows;

$$S_T = \frac{\cos\theta \sin\beta}{\cos\phi \cos\theta \sin\beta + \beta \sin\phi \sin\theta} S(\beta \geq 90^\circ,\ \sin\beta = 1) \tag{3}$$

$$\beta = \cos^{-1}(-\tan\theta \tan\phi) \tag{4}$$

where θ and ϕ are the solar declination angle and latitude (Hitachi: 36.6°), respectively.

Then, the absorbed solar radiation is converted to electric energy, denoted by G, by the PV panel. From our different work [5], a good correlation is observed between daily generation, G and solar radiation, S_T as described by

$$G[\mathrm{Ah}] = 1.25 \times S_T\left[\mathrm{MJm}^{-2}\right] \tag{5}$$

3 Control Procedures

3.1 Source of Data

The data of forecast meteorological elements (i.e. *RH, P, CL*, etc.), measured S_i and measured *G* are originally extracted from the JMA's GPV Datasets [6], Hitachi City Hall Database [7] and our proposed measurement system, respectively.

3.2 Determination of Weather

Sunny and cloudy/rainy days are differentiated based on the estimation of dew-point depression, *Tdd,* considered on each geopotential level of 300, 400, 500, 600, 700, 800, 900 and 1000 mb, which is extracted from the GPV-MSM datasets.

3.3 Determination of Battery's State-of-Charge (SOC)

Two methods are applied. First, an ampere-hour counting is mainly used to determine the instantaneous state-of-charge of the batteries during the charging/discharging process. Second, a method of open-circuit voltage (OCV) is implemented in order to determine the empty and full level conditions of the stored energy in the batteries, precisely. Originally, the actual unit is indicated in percentage (%) but here, for better understanding, SOC is expressed in Ah and redefined as Storage Level, *E* [2]. Thus, several derivatives of *E* can be expressed as;

$$\begin{aligned} E_{G_{i-1}} &= E_0 \\ E_{C_i} &= E_{G_{i-1}} - C_i \\ E_{G_i} &= E_{C_i} + G_{i+1} \end{aligned} \tag{6}$$

where E_0, G_i, C_i, E_{Gi} and E_{Ci} are initial storage level, generation on the i-th day, consumption on the i-th day, storage level after generation for the i-th day and storage level after consumption for the i-th day, respectively.

3.4 Determination of Consumption

The essential step is to decide the most optimized amount of consumption, *C* based on the forecasted *G* so that the remaining energy in the batteries can be fully utilized. The aim is to ensure that the batteries are always fully charged at the end of

the day in whatever conditions. Firstly, the necessary energy to fully charge the batteries, E_N, from initial storage level, E_0, is defined as;

$$E_N = E_{FULL} - E_0 \tag{7}$$

Next, target C_i is determined by the deduction of this E_N from the forecasted G_i as;

$$C_i = G_i - E_N \tag{8}$$

where if $C_i < 10$ ($C_i > 30$), this C_i will be approximated to 10 (30) Ah. Here, full battery level, E_{FULL} is 38 Ah and precautionary level is underlined at 8 Ah.

4 Simulation Results

Before the experiment is conducted, the proposed control is first compared numerically using the C++ with a method from our previous study [5]. As a result, Table 1 represents the number of insufficient days (NID) that occurred over a period of 4 years from 2011 to 2014. The NID is the day when the minimum target of C (10 Ah) cannot be attained [2, 5]. Apparently, the proposed control with measured input data produced NID exactly the same as that of method [5] for all 4 years. The use of measured input data means the forecasted G is ideal with zero errors since it was basically derived from the measured solar radiation data in [7]. Nevertheless, when the GPV-based forecast data was applied into the control scheme, the NID increased to 4 days for all years except 2013. On the other hand, a yearly-average C in Table 1 suggests that 30 Ah of battery capacity was sufficient to capture most energy through the year in the case of Hitachi as the amount of yearly-average G was in the range of 21.4–22.1 Ah. Furthermore, all measured values succeeded to supply enough energy to the load which whose amount equaled to at least 97 % and utmost 98.1 % of the average G in 2013 and 2012, respectively. Impressively, when the GPV-forecast data was executed into the scheme, the decline trend was not really significant as it dropped to an acceptable level with a marginal decrease of 1.1 Ah in all years except 2013 from the measured values.

Table 1 The simulation results for number of insufficient days, NID and average energy consumption for the year 2011–2014

Year	NID (days)			Average C (Ah)			Average G (Ah)
	10 Ah [5]	Meas.	Forecast	10 Ah [5]	Meas.	Forecast	
2011	1	1	4	10.0	21.0	19.9	21.4
2012	0	0	4	10.0	21.2	20.1	21.6
2013	0	0	3	10.0	21.5	20.7	22.1
2014	2	2	4	10.0	21.3	20.2	21.9

5 Experimental Structure and Results

The experimental equipment of PV system structured in this study is represented as Fig. 1. This structure is basically consisted of PV panels (5 pcs), 30 pieces of series-connected WB-LYP40AHA batteries to form 100 V DC sources, LCD display for energy visualization, Xbee modules for forecast and system's data transmission, RX621 microcontroller, FET switches, PCU, AC load and monitoring PC. Here, the charging and discharging processes were operated separately during the day from 6:00 to 20:00 and night from 23:00 to 5:00, respectively. The experiment was strictly monitored during the period of 1st–31st Jan. 2015.

Figure 2 presents an experimental result of energy control implemented on all days in Jan. 2015. By referring to a movement of the line of E in Fig. 2, a one-day routine is defined as it starts with a decreasing trend that describes a discharging process of the batteries, followed by an increasing trend that represents a process of generating energy. It is obvious that the RX621 microcontroller worked very well with the system as the precautionary and full levels of batteries were successfully controlled to exact values of 8 and 38 Ah, respectively. Plus, the system managed to control the batteries to supply 10 Ah of energy to the load on days where the forecasted G values were below 10 Ah (Jan. 15, 22 and 30). On the contrary, even though the forecasted G on Jan. 8 and 12 was beyond 30 Ah, operation of the batteries that was mandatorily controlled by the RX621 never allowed energy more than 3 kWh (30 Ah) to be supplied to the loading rheostat, precisely. On the other hand, a measurement result of voltage and current for the case of sunny days that happened continuously from Jan. 10 to 13 is shown as Fig. 3. It is apparent that the input switch stopped instantaneously as the curve of open circuit voltage, V_{OC} reached its maximum value of 102 V which is represented as section (b) in this figure and the output switch was turned off when the target C was fulfilled as represented in section (a). Also, since the flowing output current was marginally

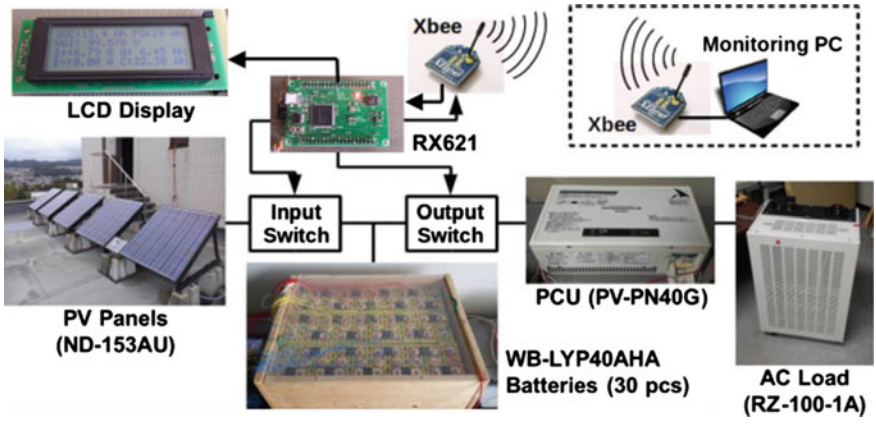

Fig. 1 Experimental structure based on PV system constructed in this study

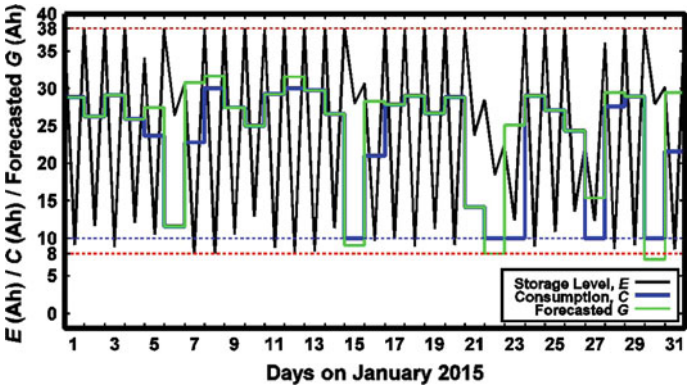

Fig. 2 Result of energy control on January 2015. *Black*, *blue solid* and *green lines* are the storage level, *E*, consumption, *C* and forecasted *G*, respectively. The precautionary and full levels of batteries were successfully controlled to exact values of 8 and 38 Ah, respectively

fluctuating between 4.9–5.4 A during the (a) process, 30 Ah of capacity was successfully discharged by the time it got to several minutes before 5 a.m. on Jan. 12. No sign of over-charged or over-discharged phenomenon was observed during this period since the batteries worked normally after those days. Impressively, an average *C* for January 2015 is considerably high with approximately 23.3 Ah per day which suggests that the proposed control succeeded in utilizing 78 % of the effective storage of 30 Ah. Moreover, this *C* was above the range of average *G* for 2011–2014 in Table 1 which proves that the target of utilizing the energy as much as the average *G* has been achieved.

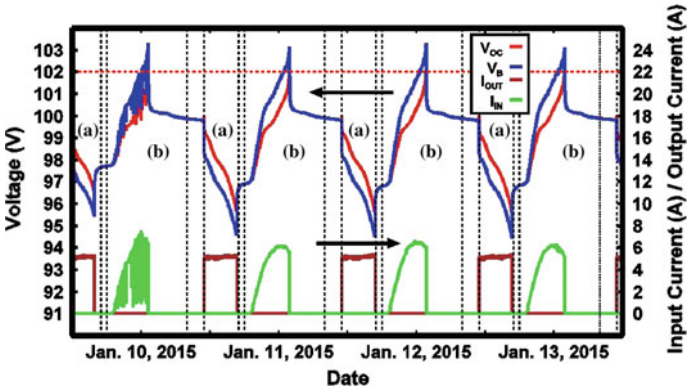

Fig. 3 Voltage and current's measurement results for the case of continuous sunny days that happened on Jan. 10–13. V_{OC}, V_B, I_{OUT} and I_{IN} are the open circuit voltage, battery voltage, output (discharging) current and input (charging) current of 30-piece's WB-LPY40AHA lithium-ion batteries, respectively

6 Conclusion

In this paper, an energy control that considers the next-day forecast of generation for the purpose of fully utilizing the stored energy in the batteries has been proposed. This study is located in Hitachi, Japan. As a result, any forecasting error that arose on the day where generation was less than 10 Ah (more than 30 Ah), was negligible since 10 Ah (30 Ah) of energy were supplied from the batteries to the load consistently during rainy (sunny) days. Impressively, average energy consumption for January 2015 is considerably high with approximately 23.3 Ah, which suggests that the proposed control succeeded in fully utilizing energy in the batteries corresponded to above the range of the average G for 2011–2014.

References

1. Jou, H.-L., Chang, Y.-H., Wu, J.-C., Wu, K.-D.: Operation strategy for a lab-scale grid-connected photovoltaic generation system integrated with battery energy storage. Sci. Direct Energy Convers. Manage. **89**, 197–204 (2015). doi:10.1016/j.enconman.2014.09.069
2. Shah, A.S.M., Ishikawa, I., Odakura, S., Kakimoto, N.: Numerical model of energy control for lithium-ion batteries based on PV system. Int. J. SIM. Syst. Sci. Technol. **15**(6), 67–74 (2014). doi:10.5013/IJSSST.a.15.06.07
3. Han, J., Choi, C.-S., Lee, I., Kim, S.-H.: Smart home energy management system including renewable energy based on ZigBee and PLC. IEEE Trans. Consum. Electron. **60**(2), 198–202 (2014). doi:10.1109/TCE.2014.6851994
4. Shah, A.S.B.M., Yokohama, H., Kakimoto, N.: High-precision forecasting model of solar irradiance based on grid point value data analysis for an efficient photovoltaic system. IEEE Trans. Sustain. Energy **6**(2), 474–481 (2015). doi:10.1109/TSTE.2014.2383398
5. Kakimoto, N., Matsumura, S., Kobayashi, K., Shoji, M.: Two-state Markov model of solar radiation and consideration on storage size. IEEE Trans. Sustain. Energy **5**(1), 171–181 (2014). doi:10.1109/TSTE.2013.2278547
6. Japan Meteorological Agency. Index of weather data based on grid point value numerical prediction. http://database.rish.kyoto-u.ac.jp/arch/jmadata/data/gpv/original/ (2015). Accessed 2 Feb 2015
7. Hitachi City Hall (Weather division). Index of observed weather database for Hitachi (Japanese). http://www.jsdi.or.jp/～hctenso/ (2015). Accessed 3 Mar 2015

Optimization of Hydropower Plants' Tailwater Energy: A Case Study for 317 MW Adana Sanibey Dam, Turkey

K.M. Murat Tunc, Sedat Sisbot and Muammer Ozbek

Abstract This work is concerned with the optimization of use of tailwater energy at hydropower plants. As a case study, extensive analyses are performed to determine the main features of the array of low-head turbines that are planned to be installed at the tailwater of the two main generators of Sanibey Dam. Sanibey Hydropower Plant is constructed on Seyhan River at Aladag region, Adana, Turkey. The plant has currently two Francis turbines (158.5 MW of each) with a total capacity of 317 MW. Tailwater can be briefly defined as the water leaving the main generators of the hydropower plant. Although most of its energy is converted to mechanical energy by rotating the blades of the turbine, it has still some energy which can be exploited by using low head run-of-river type turbines. Design and optimization of these secondary systems are nowadays among the popular research topics. This work investigates the feasibility of developing such a hydro-matrix structure consisting of an array of low-head small size turbines. Several analyses are performed to determine the optimum number and technical specifications of the generators. In this work, two different approaches aiming at maximizing the power output or minimizing the investment return period are utilized in the optimizations. Two year outflow statistics and hourly data of several operational parameters of the existing Francis turbines (provided by the operators of the dam) are analyzed to maximize the power output. Similarly, energy markets hourly price data is used for calculating the corresponding payback period and to minimize the return time of the

K.M. Murat Tunc (✉) · M. Ozbek
Faculty of Engineering and Natural Sciences, Istanbul Bilgi University, Istanbul, Turkey
e-mail: murat.tunc@bilgi.edu.tr

M. Ozbek
e-mail: muammer.ozbek@bilgi.edu.tr

S. Sisbot
Engineering Faculty Electrical Engineering Department, Izmir University, İzmir, Turkey
e-mail: sedat.sisbot@izmir.edu.tr

A.Y. Oral and Z.B. Bahsi Oral (eds.), *3rd International Congress on Energy Efficiency and Energy Related Materials (ENEFM2015)*, Springer Proceedings in Energy, DOI 10.1007/978-3-319-45677-5_12

investment. The results of the analyses obtained by using different design objectives are quite similar. The approach aiming at minimizing the payback period yields the optimal number of turbines as 27. The return time and the cost of the investment are 8.13 years and 4,940,310 USD, respectively. In power maximizing approach, the optimum number of turbines is calculated as 30. The return time and the cost of the investment are 8.15 years and 5,490,978 USD, respectively. The re-use of expensive raw material (water in this case) also results in approximately 6 % increase in the overall efficiency of the hydropower plant.

Keywords Hydropower plant · Tailwater energy · Low-head turbines · Hydro-matrix array structure · Energy optimization

1 Introduction

The increasing awareness on environmental issues has been encouraging the use of renewable energy more and more. Hydropower is by far the most important form of renewable energy. It is simply based on conversion of the potential energy of water into mechanical energy to be exploited for electricity production.

Flowing water resources are stored at a dam which is constructed to accumulate the water at relatively high locations. Water released from the reservoir flows through the inlet valves that lead to the turbines. The high flow rated water reaches to the turbine; forces the blades with its kinetic energy and activates a generator to produce electricity.

Tailwater can be briefly defined as the water leaving the main generators of the hydropower plant. Although most of its energy is converted to mechanical energy, it has still some energy which can be exploited by using low head run-of-river type turbines. Heads between 2 and 20 m are considered as low heads. Cost estimation of low head small hydropower schemes has been investigated in literature [1]. The head range of 3–20 m and unit size of 1–5 kW have been carried out recently [2].

This work aims at investigating the feasibility of using tailwater energy by constructing a low head turbine array on an existing hydropower plant. As a case study, the flow characteristics and corresponding power generation data of Adana Sanibey Hydropower plant is analyzed to determine type, size and optimum number of tail water turbines. Hydro-matrix turbines are thought to be the best for the present work and optimum number of turbines and their geometrical specifications are determined. Depending on the results of the analyses, several financial parameters such as investment payback periods and profitability indices are calculated.

Fig. 1 Sanibey hydropower plant top view

2 Sanibey Hydropower Plant

Yedigöze Sanibey Hydropower Plant (shown in Fig. 1) is constructed on Seyhan River at Aladag region, Adana, Turkey. Sanibey Dam has a total capacity of 317 MW. The highest and lowest water levels in the reservoir are 235 and 210 m, respectively. The active volume flow rate is 300.48 m^3/h. Two vertical shaft Francis turbines each of which has an installed power 158,500 kW are used. The maximum gross head is 100 m and the minimum head of 68 m in the project.

3 Modeling and Optimization

Kaplan turbines [3], which form the hydro-matrix array structure described in this work, are reaction type turbines. Their basic advantage at low head conditions is the high rotational speed at the energy production point. Kaplan turbines, which show a large overload capacity, have a radial flow intake. The inlet flow makes a right angle turn and enters the runner in an axial direction.

Application of the Kaplan turbines to tail water as in the form of the hydro-matrix structure can be used for the heads from 2 to 40 m. At Sanibey hydropower plant the tail water width is 40 m and the available tail water head for energy production is approximately 3 m. Hydro-matrix solution [4] is based on the serial application of low-head small hydropower turbines. Hydro-matrix turbine is a

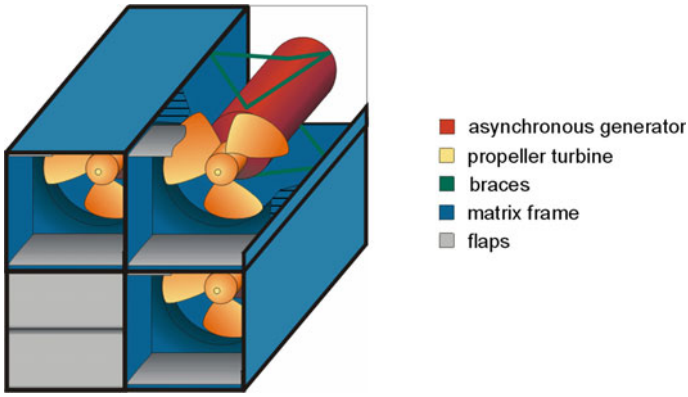

Fig. 2 Hydro-matrix scheme

multi combination of the identical small turbines. The name "*matrix*" comes from the fact that the distribution of the turbines seems like an entry of a matrix as seen in Fig. 2.

Power calculations are based on the equation shown below:

$$P = Q\,H\,\eta_h\,\rho\,g$$

where Q and H represent discharge (m^3/s) and gross head (m) respectively. In the equation above η_h represents the hydraulic efficiency and equals to 0.9. Similarly, ρ and g stand for the water density (998 kg/m^3) and gravitational acceleration (9.81 m/s^2).

4 Optimization of the Number of Hydro-Matrix Turbines

The main purpose of this work is to determine the optimum number of hydro-matrix turbines to be mounted. In order to accomplish this objective two different approaches namely, minimizing initial investment costs or maximizing the power output, can be followed. Since Sanibey Hydropower plant has already been in operation, it is not possible to rebuild or reconstruct the project according to theories and forecasts. The existing tailwater canal has a width of 40 m. So this is a constraint used for determining the optimum number of hydro-matrix turbines. The amount of water taken from the Sanibey dam is directly emitted to tailwater canal after being processed. It can be 0, 180 or 360 m^3/sec which correspond to no working, one Francis process and two Francis process, respectively.

Since one of the objectives of the optimization is to maximize the profit or to minimize the costs, the financial constraints of the problem are also included in the mathematical model used. As a regular application, the government determines the

power demand for a specific date, asks the companies to make their offers and finally selects the best price. Therefore, the electricity prices starting from the date the plant became operational are known very precisely. Similarly, the amount of water stored in the dam is known and used as an input for the calculations. The availability of these data makes it possible to determine the optimum number of the hydro-matrix turbines for maximizing the profit as objective function.

The main Francis turbines have two exiting penstocks, if both turbines are operational, the outflow is 360 m^3, and if one turbine is operational only, it is half of it. As the Sanibey hydropower plant has been working for four years the outflow statistics and hourly data of the Francis turbines are known and taken from the operators of the plant.

The energy markets' hourly price data and flow characteristics are used as the input parameters to calculate the profit and other financial indicators such as the return period of the investment. Table 1 shows an example of energy prices and the corresponding income changing hourly depending on the demand.

Table 1 Energy prices and the income changing depending on the demand

Time	Price (USD/MWh)	Energy (MWh)	Income (USD)
00:00	75.73	3.42	259.11
01:00	82.61	3.43	283.10
02:00	55.76	3.44	191.57
03:00	08.05	3.43	027.66
04:00	07.59	3.43	026.04
05:00	07.56	3.39	025.61
06:00	08.05	3.41	027.46
07:00	08.19	3.40	027.83
08:00	52.32	3.42	178.84
09:00	53.01	3.41	180.85
10:00	65.06	3.40	222.51
11:00	75.73	3.40	257.30
12:00	55.76	3.39	189.69
13:00	65.06	3.42	220.64
14:00	75.73	3.40	259.10
15:00	86.05	3.39	292.83
16:00	89.49	3.40	303.55
17:00	97.07	3.41	329.59
18:00	96.38	3.42	328.72
19:00	86.05	3.42	294.71
20:00	72.28	3.41	247.38
21:00	62.62	3.41	210.38

5 Conclusion

Depending on the results of the analyses and simulations, the optimal number of hydro-matrix turbines to be installed is determined. The optimal number is found by maximizing the profit with respect to the past year's hourly data of energy prices. In addition to this, the minimization of the return of investment is optimized. Both of the analyses produce very similar results. The return of investment minimization solution approach results the optimal number of turbines as 27 and return of an investment is 8.13 years with an investment cost of 4,940,310 USD. In the power maximization solution, the optimal number of turbines is 30 and the return of the investment is 8.144 years while the corresponding cost is 5,490,978 USD. In addition, since the expensive raw material (water in this case) is reused or used for two times, the overall energy efficiency of the plant is increased by 6 %.

Acknowledgments Hereby we thank Zafer Karakuzu, acting manager and Kandemir Haktan, technical manager of the Sanibey Hydropower Plant for their valuable comments and suggestions.

References

1. Singal, S.K., Saini, R.P., Raghuvanshi, C.S.: Analysis for cost estimation of low head run of river small hydropower schemes. Energy. Sustain. Dev. **14**(2), 117–126 (2010). doi:10.1016/j.esd.2010.04.001
2. Singal, S.K., Saini, R.P.: Cost analysis of low-head dam-toe small hydropower plants based on number of generating units. Energy. Sustain. Dev. **12**(3), 55–60 (2008). doi:10.1016/S0973-0826(08)60439-1
3. Schweiger, F., Gregory, J.: Developments in the design of Kaplan turbines. Water Power Dam Constr. **39**(11), 16–20 (1987)
4. Schneeberger, M., Schmid, H.: StrafloMatrix™—further refinement to the HYDRO-MATRIX technology. In: Proceedings of Hydro 2004 Conference, Porto, Portugal (2004)

Part II
Environmental Issues

Adsorption Study of Reactive Blue 2 Dye on CTAB-Bentonite in Aqueous Solution

Kheira Chinoune, Zohra Bouberka, Nesrine Touaa and Ulrich Maschke

Abstract Cetyltrimethylammoniumbromide-bentonite (CTAB-bentonite) was synthesized by placing alkylammonium onto B-Na^+, and investigated for adsorption of reactive Blue 2 dye from aqueous solution. The adsorption capacity of reactive blue 2 onto organo-bentonite was found to increase with the dye concentration. The evaluated activation energy was found as 8.02 kJ/mol. Equilibrium adsorption isotherms were satisfactorily described by Langmuir model.

Keywords Adsorption · Environment · Dye pollutant

1 Introduction

Dyes are extensively used by industries including textile leather, paper printers, plastics, cosmetics, food and pharmaceuticals [1, 2]. They can be classified according to a criterion which reflects their chemical structures [3] as anionic (acid, direct, and reactive dyes), cationic (basic dyes) and non ionic (disperse dyes and vat dyes), and also according to their compatibility with the type of substrate to be coloured. Discharge of untreated dye wastewater is not without consequence for the environment [4]. Most of dyes are toxic, mutagenic and carcinogenic. It is estimated that 1–20 % of these dyes are wasted in industrial effluents during textile dyeing and finishing processes [5]. Therefore, the removal of dyes from waste effluents is of significant environment importance. Moreover, the complex aromatic molecular

K. Chinoune · Z. Bouberka · N. Touaa
Laboratoire Physico-Chimie des Matériaux-Catalyse et Environnement,
Université des Sciences et de la Technologie d'Oran «USTO»,
BP 1505 El M'naouer, 31000 Oran, Algeria

Z. Bouberka · U. Maschke (✉)
Unité Matériaux et Transformations—UMET (UMR CNRS N°8207),
Bâtiment C6, Université Lille 1—Sciences et Technologies,
59655 Villeneuve d'Ascq Cedex, France
e-mail: ulrich.maschke@univ-lille1.fr

A.Y. Oral and Z.B. Bahsi Oral (eds.), *3rd International Congress on Energy Efficiency and Energy Related Materials (ENEFM2015)*, Springer Proceedings in Energy, DOI 10.1007/978-3-319-45677-5_13

structures of dyes make them more stable and difficult to biodegrade [6, 7]. Many investigations in this regard must be done in search of efficient means for treatment of effluents prior to discharging them to the surrounding environment. In water reuse technology, various physical, chemical and biological pre-treatments and post-treatments can be used to treat textile effluent. The adsorption methods for the colour removal are based on the high affinity of many dyes for the adsorbent materials, and were found effective for the removal of a wide range of dyes [8]. Currently, the most common procedure involves the use of activated carbons as adsorbents because of their high adsorption capacities [9, 10].

Clay minerals have received increasing potential for application as environmental remediation agents because they are cheap and abundant materials. Among these clay minerals, bentonite represents one of the most extensively used adsorbents [11]. However, its adsorption capacity towards anionic dyes was found to be very low due to the negatively charged hydrophilic particle surfaces [12]. Intercalation of organic surfactant between layers of clays cannot only change the surface properties from hydrophilic to hydrophobic, but also greatly increase the basal spacing of the layers. All the results obtained up to now, concerning the various interactions of organophilic clays towards the organic pollutants, showed the great efficiency of adsorption of these materials [13–15].

2 Experimental Part

The bentonite used was obtained from the Algerian company ENOF [16]. The bentonite loaded with CTAB, used for the adsorption experiments with reactive blue 2, was prepared according to the method described in a previous report [14]. The dye used, reactive blue 2 (C.I. 61211) commercialized by the Acros company, is a coloring reagent containing a dichlorotriazine group (Fig. 1).

Concentrations of reactive blue 2 in the solution were determined spectrophotometrically using a UV/Vis spectrophotometer Safas mc^2. XRD patterns of the prepared samples were acquired with an X ray diffractometer (Philips PW 1800). FTIR spectra were obtained using the KBr-disk technique on a Perkin-Elmer spectrophotometer.

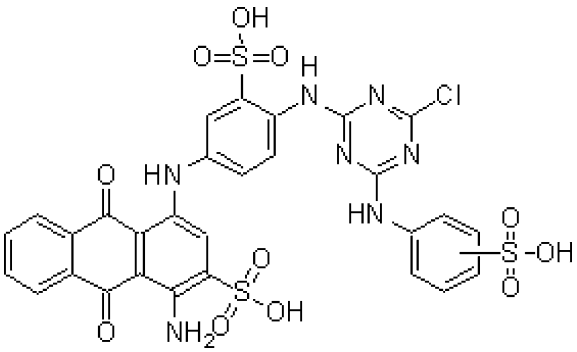

Fig. 1 The molecular structure of reactive blue 2

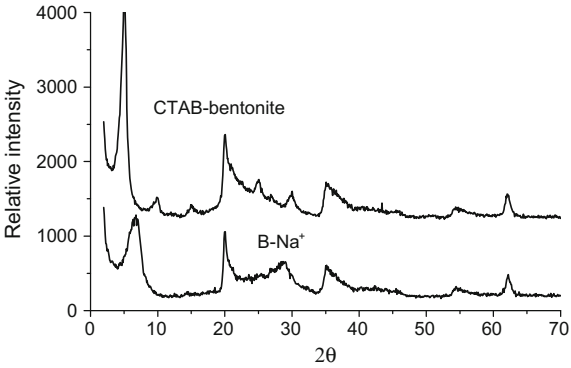

Fig. 2 XRD patterns for B-Na^+ and CTAB-bentonite

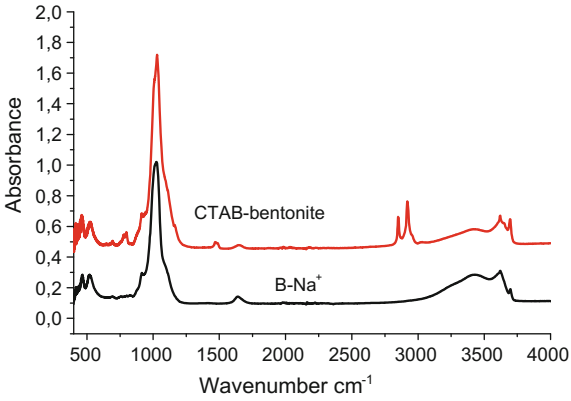

Fig. 3 FTIR spectra of B-Na^+ and CTAB-bentonite

After treating the sodium exchanged bentonite with CTAB, the basal spacing increases from 1.26 to 1.84 nm. The significant increase in d_{001} of organoclays shows the effective quaternary ammonium cation intercalation in the layers (Fig. 2). The FTIR spectrum of CTAB-bentonite (Fig. 3) reveals the presence of intense bands between 2850 and 2920 cm^{-1} corresponding to symmetric and asymmetric stretching vibrations of methylene and methyl groups of the aliphatic chain of the surfactant [17]. The C–H bending bands of methylene and methyl groups were found at 1468 cm^{-1} and the aromatic C=C skeleton stretching band at 1600 cm^{-1}.

3 Results and Discussion

As seen in Fig. 4, the equilibrium adsorption capacity decreased from 2.745×10^{-4} to 0.291×10^{-4} mol/g when the pH increased from 2 to 12. The high adsorption capacity may be attributed to both the strong electrostatic interaction between $-N^+ (CH_3)_3$ of CTAB-bentonite and anionic dye molecules

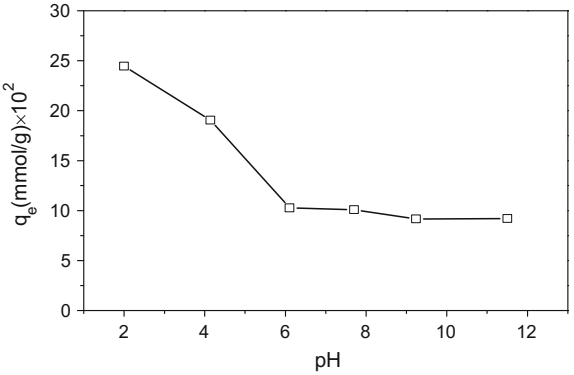

Fig. 4 Effect of pH on adsorption of reactive blue 2 onto CTAB-bentonite ($C_0 = 6 \times 10^{-2}$ mmol/L, adsorbent dose = 0.2 g/L, reaction time 1 h, T = 20 °C)

(as $-SO_3^-$ anion), and the replacement of the surfactant entities by anionic dye species. The adsorption capacity at equilibrium q_e increased from 5.95×10^{-2} to 10.20×10^{-2} mmol/g with an increase of the initial dye concentrations from 2×10^{-2} to 6×10^{-2} mmol/L. The three-dimensional plot (Fig. 5) represents the generalized model for reactive blue 2 adsorbed at any contact time and initial reactive blue 2 concentration within the specified concentration range. It indicates that the amount of reactive blue 2 adsorbed at any contact time increased with increasing initial reactive blue 2 concentration. This is obvious for higher values, as a more efficient use of the adsorptive capacities of the adsorbent would be expected due to the greater adsorption driving force. The plot of Fig. 5 can then be used to derive the amount of reactive blue 2 dye adsorbed at any given dye concentration and reaction time.

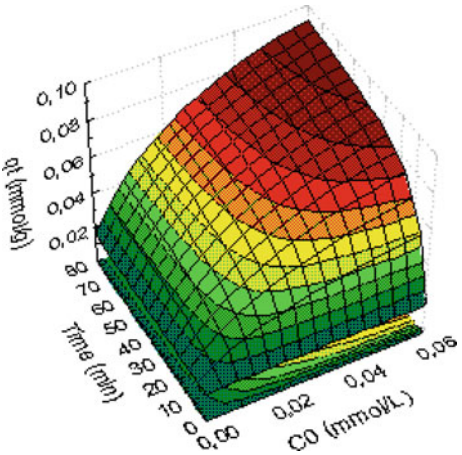

Fig. 5 Relationship between time, C_0 and q_t on the adsorption of reactive blue 2 onto CTAB-bentonite

Table 1 Temperature effect on adsorption of reactive blue 2 onto CTAB-bentonite: ($C_0 = 6 \times 10^{-2}$ mM, adsorbent dose = 0.2 g/L and pH = 6)

C_0 (mmol/L)	T (°C)	(mmol/g)
0.06	20	10.11
	40	8.68
	60	7.58

The effect of temperature on adsorption was also examined using a constant initial amount of reactive blue 2 dye, and a CTAB-bentonite concentration of 0.2 g/L at various temperatures. The activation energy of adsorption E_a was found as 8.02 kJ/mol for the adsorption of reactive blue 2 on CTAB-bentonite. Since adsorption is an exothermic process, it would be expected that an increased solution temperature would result in a decreasing adsorption capacity (Table 1). Figure 6 shows the amount of reactive blue 2, adsorbed per unit mass of CTAB-bentonite, as function of the concentration of reactive blue 2 remaining in solution, C_e (equilibrium concentration), for initial dye concentrations from 6×10^{-3} to 10^{-2} mmol/L. The isotherm shows L-type behavior according to the Giles classification [18]. The amount of reactive blue 2 adsorbed increased largely at low concentration, decreased around the equilibrium concentration, followed by a tendency of formation of a plateau when the concentration becomes higher. The isotherms which show steep initial slopes, that level out with a subsequent increase in the equilibrium concentration of the dye, giving rise to a plateau or a linear section with positive slope, are classified as L-type isotherms [19]. Such isotherms reflect a relatively high affinity between the dye and CTAB-bentonite surface.

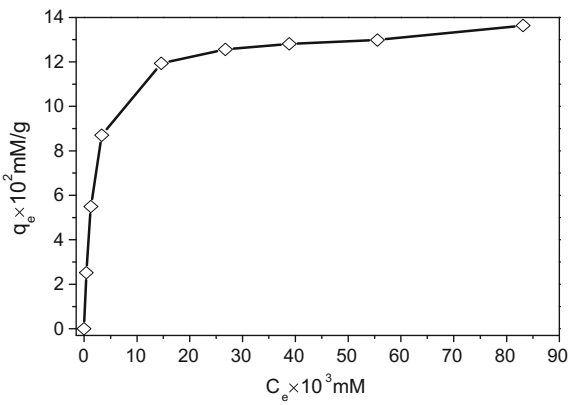

Fig. 6 Relation between time, C_0 and q_t on the adsorption of reactive blue 2 onto CTAB-bentonite

4 Conclusion

The bentonite clay was modified with CTAB in order to obtain organo-bentonite, which was used for retaining reactive blue dye from water solution. The interlayer spacings of the analyzed bentonite increased from 12.6 to 18.4 Å after CTAB treatment. Obviously there are CH_2 stretching bands at 2920 and 2850 cm^{-1}, and a scissoring mode at 1468 cm^{-1} of intercalated surfactant of organo-bentonite. The adsorption capacity of reactive blue 2 onto organo-bentonite increased with the increasing initial dye concentration, and decreased with increasing temperature. The Langmuir model isotherm represents the experimental data well. The coefficient of determination was greater than 0.999.

References

1. Saad, S.A., Daud, S., Kasim, F., Saleh, M.: Methylene blue removal from simulated wastewater by adsorption using treated oil palm empty fruit bunch. In: ICoSM, pp. 293–296 (2007)
2. Setamanit, S., Fongsatikul, P., Sivadechathep, J.: ASEAN achievement and future directions in pollution control, p. 33. Ministry of Science, Technology and Environmental, Thailand (2002)
3. Prasad, A.S.A., Rao, K.V.B.: Physico chemical characterization of textile effluent and screening for dye decolorizing bacteria. Global J. Biotech. Biochem. **5**, 80–86 (2010)
4. Ahmad, M., Bajahlan, A.S., Hammad, W.S.: Industrial effluent quality, pollution monitoring and environmental management. Environ. Monit. Assess. **147**, 297–306 (2008). doi:10.1007/s10661-007-0121-5
5. Ogugbue, C.J., Sawidis, T.: Bioremediation and detoxification of synthetic wastewater containing triarylmethane dyes by aeromonas hydrophila isolated from industrial effluent. Biotechnol Res. Article ID 967925, International Hindawi Publishing Corporation (2011). doi:10.4061/2011/967925
6. Forgacs, E., Cserháti, T., Oros, G.: Removal of synthetic dyes from wastewaters: a review. Environ. Inter. **30**, 953–971 (2004). doi:10.1016/j.envint.2004.02.001
7. Przystaś, W., Zabłocka-Godlewska, E., Grabińska-Sota, E.: Biological removal of azo and triphenylmethane dyes and toxicity of process by-products. Water Air Soil Pollut. **223**, 1581–1592 (2012). doi:10.1007/s11270-011-0966-7
8. Zhu, M.X., Li, Y.P., Xie, M.: Sorption of an anionic dye by uncalcined and calcined layered double hydroxides: a case study. J. Hazard. Mater. **B120**, 163–171 (2005). doi:10.1016/j.jhazmat.2004.12.029
9. Demirbas, O., Alkan, M., Dogan, M.: The removal of Victoria blue from aqueous solution by adsorption on a low-cost material. Adsorption **8**, 341–349 (2002). doi:10.1023/A:1021589514766
10. Singla, P., Mehta, R., Upadhyay, S.N.: Clay modification by the use of organic cations. Green Sustain. Chem. **2**, 21–25 (2012). doi:10.4236/gsc.2012.21004
11. Al-Qunaibit, M.H., Mekhemer, W.K., Zaghloul, A.A.: The adsorption of Cu(II) ions on bentonite—a kinetic study. J. Colloid. Interf. Sci. **283**, 316–321 (2005). doi:10.1016/j.jcis.2004.09.022
12. Redding, A.Z., Burns, S.E., Upson, R.T., Anderson, E.F.: Organoclay sorption of benzene as a function of total organic carbon content. J. Colloid Interf. Sci. **250**, 261–264 (2002). doi:10.1006/jcis.2001.8205

13. Jaynes, W.F., Boyd, S.A.: Trimethylphenylammonium-smectite as an effective adsorbent of water soluble aromatic hydrocarbons. J. Air Waste Manag. Assoc. **40**, 1649–1653 (1990). doi:10.1080/10473289.1990.10466811
14. Bouberka, Z., Khenifi, A., Sekrane, F., Bettahar, N., Derriche, Z.: Adsorption of direct red 2 on bentonite modified by cetyltrimethylammonium bromide. Chem. Eng. J. **136**, 295–305 (2008). doi:10.1016/j.cej.2007.03.086
15. Jaynes, W.F., Boyd, S.A.: Clay mineral type and organic compound by hexadecyltrimethylammonium-exchanged clays. J. Soil Sci. Soc. Am. **55**, 43–48 (1991). doi:10.2136/sssaj1991.03615995005500010007x
16. Bouberka, Z., Kacha, S., Kameche, M., Elmaleh, S., Derriche, Z.: Sorption study of acid dye from an aqueous solutions using modified clays. J. Hazard. Mat. **B119**, 117–124 (2005). doi:10.1016/j.jhazmat.2004.11.026
17. Özcan, A.S., Özcan, A.: Adsorption of acid dyes from aqueous solutions onto acid activated bentonite. J. Colloid Interf. Sci. **276**, 39–46 (2004). doi:10.1016/j.jcis.2004.03.043
18. Giles, C.H., Mc Ewan, T.H., Nakhwa, S.N., Smith, D.: Studies in adsorption. Part XI. A system of classification of solution adsorption isotherms. J. Chem. Soc. 3973–3993 (1960). doi:10.1039/JR9600003973
19. Veeresh, H., Tripathy, S., Chaudhuri, D., Hart, B.R., Powell, M.A.: Sorption and distribution of adsorbed metals in three soils of India. Appl. Geochem. **18**, 1723–1731 (2003). doi:10.1016/S0883-2927(03)00080-5

Deactivation of Polybrominated Flame Retardants by Ultraviolet Radiation

Kahina Bentaleb, Zohra Bouberka, Abdelouahab Nadim, Ulrich Maschke, Yassine Agguine and Said Eddarir

Abstract The European directive RoHS (Restriction of the use of certain Hazardous Substances) limits the use of specific toxic substances for example a number of flame retardants. In the light of this context, this work handles with the implementation of a methodology of deactivation by radiative exposure of Tetrabromobisphenol A bis-(2,3-dibromopropylether) (TBBPA-DBPE), concerned by the RoHS directive. It has been shown that the photodegradation by UV-visible irradiation of TBBPA-DBPE in Tetrahydrofuran as organic environment generates less brominated thus less toxic congeners. Physico-chemical analyses were realized by means of a spectroscopic technique that allows to characterize products before and after irradiation under UV-visible light.

Keywords Photodegradation · Environment · Flame retardant

1 Introduction

A number of substances contained in the Waste of Electrical and Electronic Equipment (WEEE), in particular brominated flame retardants, were identified as molecules with considerable risks for the environment, and forbidden in use. Several brominated flame retardants have proved to be highly bioaccumulative and

K. Bentaleb · Z. Bouberka · A. Nadim · U. Maschke (✉)
Unité Matériaux et Transformations – UMET (UMR CNRS N°8207) Bâtiment C6, Université Lille 1 - Sciences et Technologies, 59655 Villeneuve d'Ascq Cedex, France
e-mail: ulrich.maschke@univ-lille1.fr

K. Bentaleb · Z. Bouberka
Laboratoire Physico-Chimie des Matériaux-Catalyse et Environnement, Université des Sciences et de la Technologie d'Oran – Mohamed Boudiaf « USTO », BP 1505 El M'naouer, 31000 Oran, Algeria

A. Nadim · Y. Agguine · S. Eddarir
Laboratoire de Chimie Bioorganique et Macromoléculaire (LCBM) Faculté des Sciences et Techniques, Université Cadi Ayyad, Guéliz, Marrakech, Morocco

A.Y. Oral and Z.B. Bahsi Oral (eds.), *3rd International Congress on Energy Efficiency and Energy Related Materials (ENEFM2015)*, Springer Proceedings in Energy, DOI 10.1007/978-3-319-45677-5_14

bioavailable, and can be detected in animal and human tissues, explaining the toxicity of these products. These additives would always be present in current and future deposits, collected from the waste of former or imported products. The concentration of brominated flame retardants in various materials can reach 5–30 % by weight. As a consequence, the method of waste recycling of electric and electronic equipments, which contain these pollutants, remains a real challenge. Indeed, in date, only the incineration is practiced in an industrial way with fatal consequences for the environment.

Certain flame retardants, added to diverse materials, are very effective to reduce the flammability of the finished product and specially the halogenic flame retardants because they contain bromine. The bromine intervenes in chemical reactions which slow down the combustion necessary for the inflammation. Among these flame retardants, one of the most used is the Tetrabromobisphenol A bis-(2,3-dibromopropylether) (TBBPA-DBPE) [1–3]. This product can be found incorporated into various materials, in which it is either chemically bound, or simply added, to confer fireproofing properties to these compounds [4, 5].

These flame retardants became common contaminants of the environment that we could find in human and animal bodies and may cause grave and irreversible effects on the body, like spermatogenesis and mental deficiency [6]. However, it seems that not only the targeted molecules as troublemakers could have an impact on the environment, but also their products of degradation stemming from processes of treatment aiming at their elimination. The process of elimination can be realized by the combination of several steps of treatments such as chemical and biological oxidation [7], and adsorption.

From a chemical viewpoint, the degradation of these pollutants until the final stage (completely debrominated molecules as well as low brominated species) can be obtained by a radical pathway [8–11]. The ultraviolet (UV)-visible irradiation technique seems to be a powerful method to generate with significant efficiency highly reactive radicals in a liquid environment which can react with organic compounds. In particular a Xenon lamp was of use to us as source of irradiation of the UV-visible light.

The photodegradation by UV-visible irradiation in organic solutions may generate less brominated congeners. Indeed, TBBPA-DBPE is sensitive to solar and artificial UV light because of the relatively weak dissociation energy (284 kJ/mol) of the carbon-bromine bond (C-Br).

The objective of this work concerns the implementation of a methodology of deactivation by irradiation of a pure brominated flame retardant (TBBPA-DBPE). The degradation by irradiation in the UV-visible range of TBBPA-DBPE will be followed by analytical methods, allowing the characterization of the products of degradation. In particular, the UV-visible spectroscopic method will be applied.

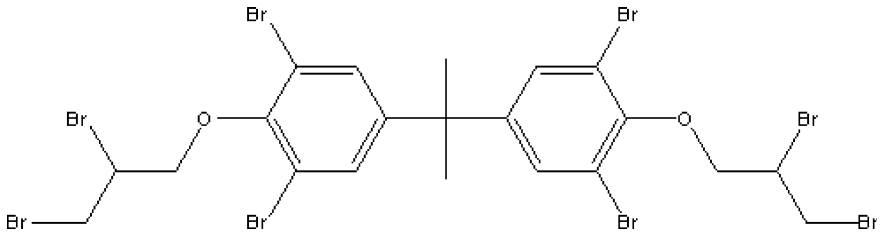

Fig. 1 Molecular structure of Tetrabromobisphenol A bis-(2,3-dibromopropylether) (TBBPA-DBPE)

2 Experimental Part

Tetrabromobisphenol A bis-(2,3-dibromopropylether) (TBBPA-DBPE) (purity 98 %), was obtained from Albemarle corporation. Tetrahydrofuran (THF) was purchased from Merck in HPLC quality. The TBBPA-DBPE molecule as brominated flame retardant is constituted of two phenolic cycles interconnected by an isopropyl group, each one substituted by two bromine atoms situated in ortho-position of the dibromopropylether groups [12]. The corresponding chemical structure of TBBPA-DBPE is shown in Fig. 1.

The irradiation process was carried out using standard 10 mm thick Hellma quartz cells, and the light source was fixed through the central axis of the cell. The distance between UV source and quartz cell was kept at 3 cm. A 150 W Xenon light source from Hamamatsu (model LC8) was used for the irradiation experiments.

During photodegradation experiments, aliquots of solutions containing TBBPA-DBPE were placed in the Hellma cells and submitted to UV irradiation. The initial concentration of TBBPA-DBPE was varied between 0.13 and 0.30 mg/mL in THF. At appropriate sampling times, the photodegradation was finished by removing the vials from the light exposure and immediately initiating analysis.

Absorption spectra were recorded using a Varian Cary 100 UV-visible double-beam spectrophotometer, equipped with a Peltier accessory for precise temperature control (±0.1 °C). All UV absorption spectra were recorded with THF for the determination of quantum yields and computed from the calibration curves in the range 200–400 nm, using the above mentioned Hellma cells at the wavelengths of maximum absorption of TBBPA-DBPE and its photoproducts.

3 Results and Discussion

The radiative effect of the pollutant/solvent system was followed according to the time of exposure to artificial radiation by means of a UV-visible source. This allowed to optimize a number of corresponding parameters (dose of irradiation, distance UV-sample source, temperature, intensity and power of the UV-visible

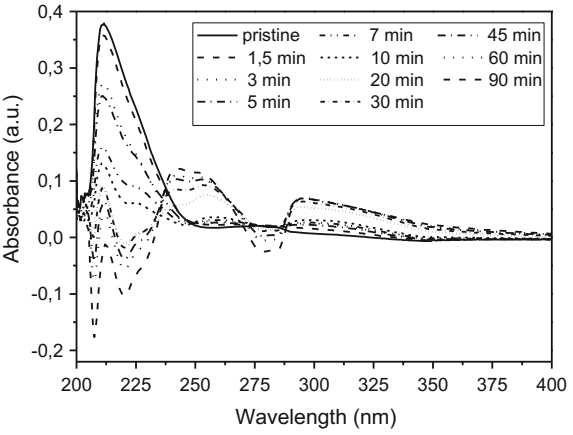

Fig. 2 Photolysis of TBBPA-DBPE in THF by artificial UV-visible light (initial concentration of TBBPA-DBPE: 0.05 mg/mL)

lamp), to increase the efficiency of the photodegradation. The UV-visible spectroscopy was applied to characterize products before and after irradiation under UV-visible light.

The study was realized on dissolved solutions in various organic solvents such as Tetrahydrofuran (THF). The UV-visible light exposure of these solutions as function of time varying from 1 to 90 min allowed to remove the characteristic band of the product at 211 nm [13] and to obtain by-products at 245 and 290 nm, less dangerous than the initial molecule (Fig. 2) [14–18]. It can be concluded that the degradation of TBBPA-DBPE reveals to be very important in THF. An exposure time of 90 min under UV-visible light allowed to degrade 98 % of TBBPA-DBPE for a concentration of 0.05 mg/mL.

Since the pollutant concentration could be an important parameter controlling the degradation process, the effect of the initial concentration of TBBPA-DBPE on the photodegradation rate was investigated over the concentration range from 0.05 to 0.3 mg/mL. Absorption versus irradiation time curves for the 212 nm-band decrease rapidly and exponentially until total disappearance of TBBPA-DBPE after 90 min. The disappearance of TBBPA-DBPE during the first 15 min of debromination can be described by first-order reaction kinetics with regards to the initial concentrations. Figure 3 represents plots of $-\mathrm{Ln}\ C(t)/C_0$ versus exposure time showing linear dependencies, where C_0 represents the concentration of TBBPA-DBPE at time zero and C(t) stands for its concentration at time t.

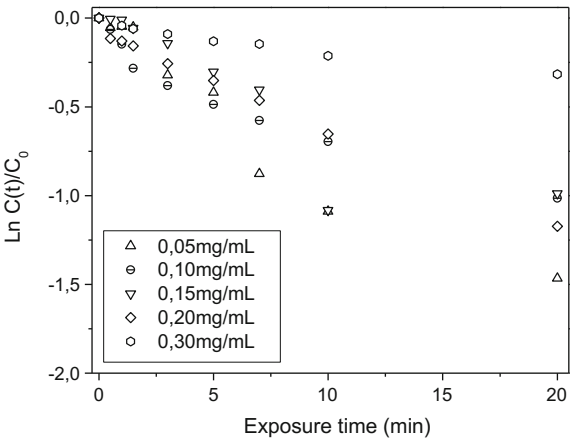

Fig. 3 Results from photodegradation experiments obtained from UV-visible measurements: effect of the initial concentration of TBBPA-DBPE

4 Conclusion

The degradation of TBBPA-DBPE in an organic solvent (THF) has been conducted by exposure to radiation in the UV-visible wavelength range, in order to obtain less harmful molecules for the environment. The UV-visible spectroscopy technique was applied to monitor the photolysis as function of irradiation time. The use of a Xenon light source allowed to reveal sequential degradation up to a total deactivation of the TBBPA-DBPE molecule. Especially remarkable was the rapid degradation efficiency shown by the irradiation device, which yields a successful degradation of TBBPA-DBPE, forming lower brominated products. The kinetics of formation and disappearance of intermediate species were determined to follow first order kinetics.

References

1. Covaci, A., Harrad, S., Abdallah, M.A.E., Ali, N., Law, R.J., Herzke, D., de Wit, C.A.: Novel brominated flame retardants: a review of their analysis, environmental fate and behaviour. Environ. Int. **37**, 532–556 (2011). doi:10.1016/j.envint.2010.11.007
2. Law, R.J.: Tetrabromobisphenol A: Investigating the worst-case scenario. Mar. Pollut. Bull. **58**, 459–460 (2009). doi:10.1016/j.marpolbul.2009.02.023
3. Covaci, A., Voorspoels, S., Abdallah, M.A.E., Geens, T., Harrad, S., Law, R.J.: Analytical and environmental aspects of the flame retardant tetrabromobisphenol-A and its derivatives. J. Chromatogr. A **1216**, 346–363 (2009). doi:10.1016/j.chroma.2008.08.035
4. Haneke, K.E.: Tetrabromobisphenol A bis(2,3-dibromopropylether) review of the toxicological literature. Integrated Laboratory Systems, North Carolina (2002)
5. European Brominated Flame Retardant Industry Panel (EBFRIP), Statement June 4 (2007)
6. Lyubimov, A.V., Babin, V.V., Kartashov, A.I.: Developmental neurotoxicity and immunotoxicity of 2,4,6-tribromophenol in Wistar rats. Neurotoxicology **19**, 303–312 (1998)

7. Ronen, Z., Abeliovich, A.: Anaerobic–aerobic process for microbial degradation of tetrabromobisphenol A. Appl. Environ. Microbiol. **66**, 2372–2377 (2000). doi:10.1128/AEM.66.6.2372-2377.2000
8. Eriksson, J., Rahm, S., Green, N., Bergman, Å., Jakobsson, E.: Photochemical transformations of tetrabromobisphenol A and related phenols in water. Chemosphere **54**, 117–126 (2004). doi:10.1016/S0045-6535(03)00704-5
9. Summary risk assessment report prepared by the United Kingdom on behalf of the European Union in http://www.bsef.com/uploads/library/
10. Lin, K., Liu, W., Gan, J.: Reaction of tetrabromobisphenol A (TBBPA) with manganese dioxide: kinetics, products, and pathways. Environ. Sci. Technol. **43**, 4480–4486 (2009). doi:10.1021/es803622t
11. Guo, Y., Chen, L., Ma, F., Zhang, S., Yang, Y., Yuan, X., Guo, Y.: Efficient degradation of tetrabromobisphenol A by heterostructured $Ag/Bi_5Nb_3O_{15}$ material under the simulated sunlight irradiation. J. Hazard. Mater. **189**, 614–618 (2011). doi:10.1016/j.jhazmat.2011.02.054
12. Hamers, T., Kamstra, J.H., Sonneveld, E., Murk, A.J., Zegers, B.N., Boon, J.P., Brouwer, A.: In vitroscreening of the endocrine disrupting potency of brominated flame retardants and their metabolites. Organohalogen Compd. **66**, 3016–3020 (2004)
13. Zhu, L., Hites, R.A.: Brominated flame retardants in tree bark from North America. Environ. Sci. Technol. **40**, 3711–3716 (2006). doi:10.1021/es060225v
14. Faust, B.: Modern chemical techniques. The Royal Society of Chemistry, London (1997)
15. Stuart, H., Ibarra, C., Abdallah, MA-E., Boon, R., Neels, H., Covaci, A.: Concentrations of brominated flame retardants in dust from United Kingdom cars, homes, and offices: causes of variability and implications for human exposure. Environ. Int. **34**, 1170–1175 (2008). doi:10.1016/j.envint.2008.05.001
16. Guo, Y., Zhou, J., Lou, X., Liu, R., Xiao, D., Fang, C., Wang, Z., Liu, J.: Enhanced degradation of tetrabromobisphenol A in water by a UV/base/persulfate system: kinetics and intermediates. Chem. Eng. J. **254**, 538–544 (2014). doi:10.1016/j.cej.2014.05.143
17. An, J., Zhu, L., Wang, N., Song, Z., Yang, Z., Du, D., Tang, H.: Photo-fenton like degradation of tetrabromobisphenol A with grapheme-$BiFeO_3$ composite as a catalyst. Chem. Eng. J. **219**, 225–237 (2013). doi:10.1016/j.cej.2013.01.013
18. Zhong, Y., Liang, X., Zhong, Y., Zhu, J., Zhu, S., Yuan, P., He, H., Zhang, J.: Heterogeneous UV/Fenton degradation of TBBPA catalyzed by titanomagnetite: catalyst characterization, performance and degradation products. Water Res. **46**, 4633–4644 (2012). doi:10.1016/j.watres.2012.06.025

Bandwidth Improvement of Patch Antenna Printed on Anisotropic Substrate with Modified Ground Plane

Amel Boufrioua

Abstract Today, the state of the art antenna technology allows the use of different types and models of antennas, depending on the area of application considered. The antenna must be small enough for miniaturizing the wireless communication system, which have been extensively and rapidly used in the modern word, also the future communication terminal antennas must meet the requirements of multiband or wideband, the difficulty of antenna design increases when the number of operating frequency bands increases. Microstrip patch antennas are now extensively used in various communication systems due to their compactness, economical efficiency, light weight, low profile and conformability to any structure. This paper is focused on the multiband application of the microstrip patch antenna, the effects of different physical parameters on the characteristics of the structure are investigated, the results in terms of return loss, bandwidth and radiation pattern are given, the proposed structure can be scaled to meet different frequencies of wireless communication systems just by changing the dimension of the main antenna. An inset L-shaped feed rectangular patch antenna with dual rectangular slots etched on the ground plane is proposed and analyzed for increasing bandwidth of microstrip patch antenna. The results in terms of return loss, bandwidth and radiation pattern are given. The results show that dual wide bands are achieved and a better impedance matching for the upper and lower resonances are obtained. Simulation results for the effect of uniaxial anisotropic substrate on the return loss and bandwidth of the rectangular patch antenna using inset L-shaped feed with dual rectangular slots on the ground plane are also presented. This novel wideband proposed antenna provides a significant size reduction and can improve the bandwidth. Furthermore, comparative studies between our results and those available in the literature is done and showed to be in good agreement.

Keywords Wideband antenna · Rectangular patch · Slot · Anisotropic substrate · Modified ground plane

A. Boufrioua (✉)
Electronics Department, Technological Sciences Faculty, University of Mentouri brothers Constantine, Ain El Bey Road, 25000 Constantine, Algeria
e-mail: boufrioua_amel@yahoo.fr

A.Y. Oral and Z.B. Bahsi Oral (eds.), *3rd International Congress on Energy Efficiency and Energy Related Materials (ENEFM2015)*, Springer Proceedings in Energy, DOI 10.1007/978-3-319-45677-5_15

1 Introduction

Today, the state of the art antenna technology allows the use of different types and models of antennas, depending on the area of application considered. Microstrip antennas are now extensively used in various communication systems due to their compactness, economical efficiency, light weight, low profile and conformability to any structure.

The rectangular and circular patches are extensively used radiators which have very limited bandwidth, these limits the applications in several practical cases, and the narrow bandwidth of the microstrip antenna can be widened. Recently, most of the research on microstrip antennas focused on methods to increase their bandwidth [1–14]. Several patch designs with single feed, dual frequency operation have been proposed recently [1–14]. When a microstrip patch antenna is loaded with reactive elements such as slots, stubs or shorting pin, it gives tunable or dual frequency antenna characteristics [7]. Since the slots are cut at an appropriate position inside the patch, they neither increase the patch size nor largely affect the radiation pattern of the patch [9]. These slots can take different shapes like, rectangular or square slot, step slot, tooth-brush shaped slot, V-slot, U-slot, etc. [9]. The slot adds another resonant mode near the fundamental mode of the patch and realizes a dual frequency response [9].

The development of modern wireless communication leads to the need for broadband antennas (Wideband antennas) found a widespread application in the wireless communication industry because of their attractive features such as easy fabrication, cost, linear and circular polarized radiation characteristics. Because of these attractive features of the broadband antennas are used in many wireless applications such as Wi-Fi, Bluetooth, GSM and GPRS.

The study of anisotropic substrate is interesting since it has been found that the use of such materials may have a beneficial effect on a circuit or antenna [8]. However, the designers should carefully check for the anisotropic effects in the substrate materials with which they will work. In this paper, a novel wideband rectangular patch antenna printed on isotropic or uniaxial anisotropic substrate is designed by using inset L-shaped feed with dual rectangular slots on the ground plane. The proposed antenna provides a significant size reduction and can improve the bandwidth. In this paper the performance analyses of the proposed antenna is presented using Ansoft HFSS software, which is based on Finite Element Method, different parametric studies will be allowed and the effect of the various antenna parameters on the return loss and the radiation of the proposed antenna will be presented, also we will present the effect of the uniaxial substrate on the bandwidth and the return loss with lower and upper resonant frequencies.

2 Antenna Design

In this study, the proposed structure of inset L-shaped feed with dual rectangular slots on the ground plane is given to increase the bandwidth; this proposed structure is based on the simple rectangular microstrip patch which is designed first. The geometry for the simple rectangular microstrip patch of dimension W × L printed on the grounded substrate, which has a uniform thickness of h and having a relative permittivity ε_r and the dielectric material is assumed to be non-magnetic with permeability μ_0 (see Fig. 1).

Table 1 shows the different parameters of the simple rectangular patch antenna and Fig. 2 shows the frequency response of this simple structure, which is designed first in order to compare it with the proposed rectangular patch antenna using inset L-shaped feed with dual rectangular slots on the ground plane. When slots are incorporated on the ground plane, it modifies the resonance behaviour of the simple rectangular patch antenna. Thus, the current of different lengths, directions and strength flow along the slots are responsible for wide bandwidth.

The geometry of the proposed antenna based on the previous simple rectangular patch is shown in Fig. 3 with the different parameters given in Table 2, in this case, two rectangular slots with the same size etched on the ground plane are fixed to the center of the length (L) of the rectangular patch antenna with a distance (S_h) and the feeding is accomplished with inset L-shaped feed.

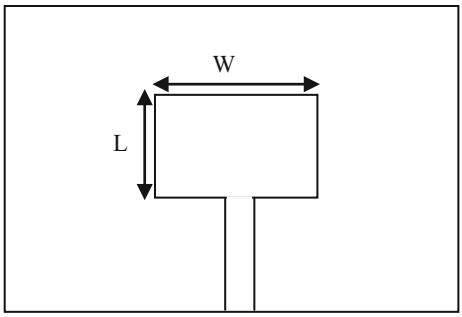

Fig. 1 Geometry of a simple rectangular patch antenna

Table 1 Design parameters of the simple rectangular patch antenna

Parameters	Value
W	15.8 mm
L	8 mm
h	1.6 mm
Relative permittivity	4.5
Ground plane	34 * 20 mm^2

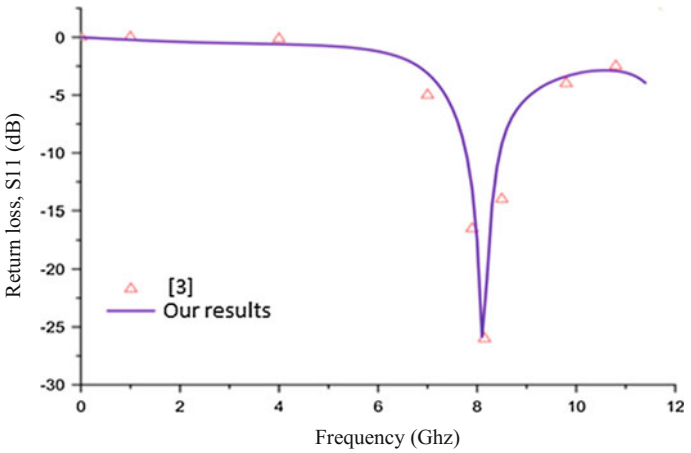

Fig. 2 Simulation of return loss S11 of a simple rectangular patch antenna

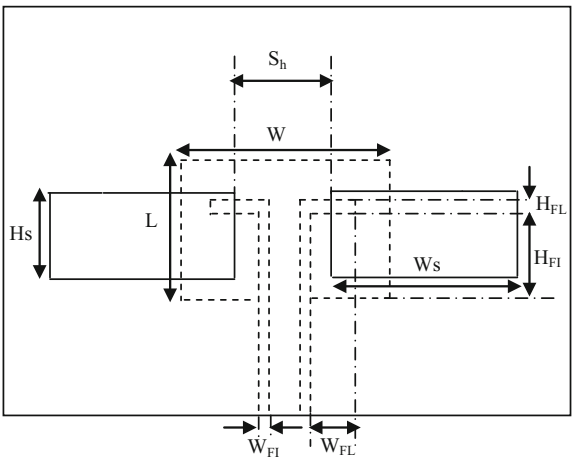

Fig. 3 Geometry of inset L-shaped feed with rectangular slots in the ground plane

Table 2 Design parameters of the rectangular patch antenna using inset L-shaped feed with dual rectangular slots on the ground plane

Parameters	Value
W	15.8 mm
L	8 mm
h	1.6 mm
Microstrip feed line	2.8 mm
Hs = H_{FI}	6 mm
W_{FI} = H_{FL}	0.5 mm
W_{FL}	2 mm
Ws	12 mm
Relative permittivity	4.5
Ground plane	34 * 20 mm^2

3 Different Parametric Study

The parameters given in Table 2 are fixed; we varied W_{FL}. Variation of return loss as a function of frequency for different value of W_{FL} is shown in Fig. 4.

In the case of Fig. 5 we fixed the length of the slot (Ws) to 12 mm and we varied the width of the slot (Hs) from 2, 4, 6 and 8 mm, respectively. Also, it is worth noting that in this case we take $W_{FL} = 0$ and $H_{FI} = 6$ mm.

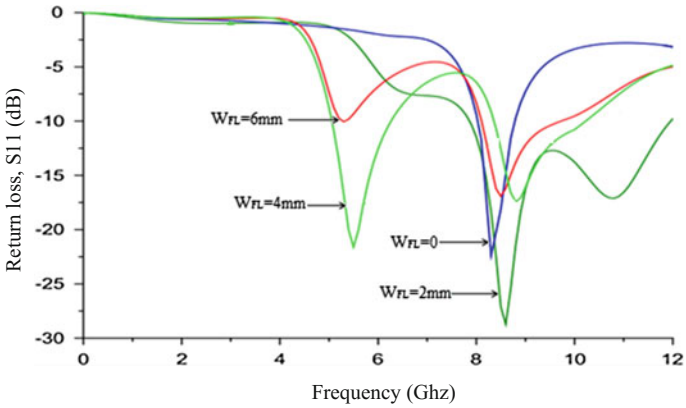

Fig. 4 Variation of return loss as a function of frequency for different value of the length notch of the inset L-shaped feed W_{FL}

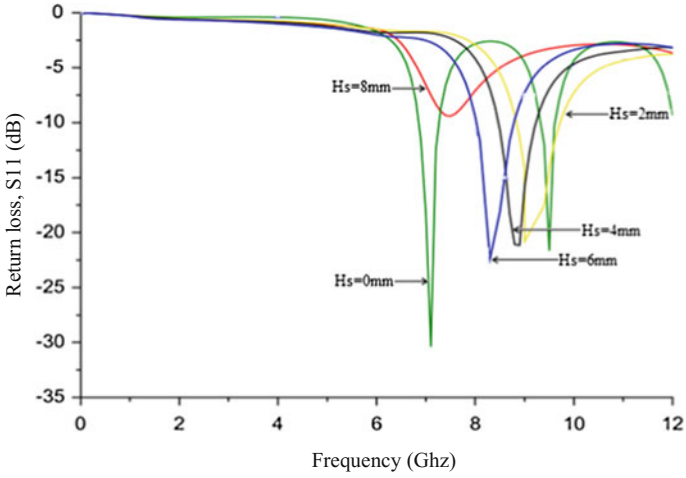

Fig. 5 Variation of return loss as a function of frequency for different value of the rectangular slot length etched on the ground plane Hs

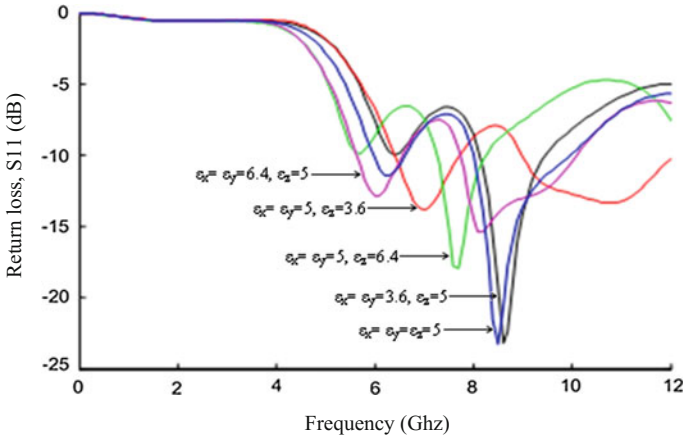

Fig. 6 Effect of the uniaxial anisotropic substrate on the bandwidth and the return loss of the rectangular patch using an inset L feed with dual rectangular slots on the ground plane

The results of Figs. 4 and 5 agree very well with those obtained by Satthamsakul et al. [3].

In the case of Fig. 6, the rectangular patch using an inset L feed with dual rectangular slots on the ground plane is also studied; the patch is embedded in a substrate containing anisotropic materials with the optical axis normal to the patch and has a uniform thickness *h*. The relative permittivity in this case can be presented by a tensor with the relative permittivity in the direction perpendicular to the optical axis denoted ε_x (with $\varepsilon_x = \varepsilon_y$) and the relative permittivity in the direction of the optical axis denoted ε_z as given by [8, 11].

The proposed antenna characteristics are observed for different substrate materials with a different anisotropic ratio as shown in Fig. 6. It is found that the antenna is very sensitive to the dielectric properties of the materials. The resonant frequencies and bandwidths are completely changed by changing the substrate material, moreover, the obtained results show that a significant improvement in the bandwidth is achieved for an anisotropic ratio greater than one (AR > 1).

With

$$\mathrm{AR} = \varepsilon_x/\varepsilon_z$$

From the radiation pattern given in Fig. 8 we can see clearly a change of directivity and the appearance of two secondary lobes, especially for (Hs = 8 mm), compared to the simple rectangular patch given in Fig. 7.

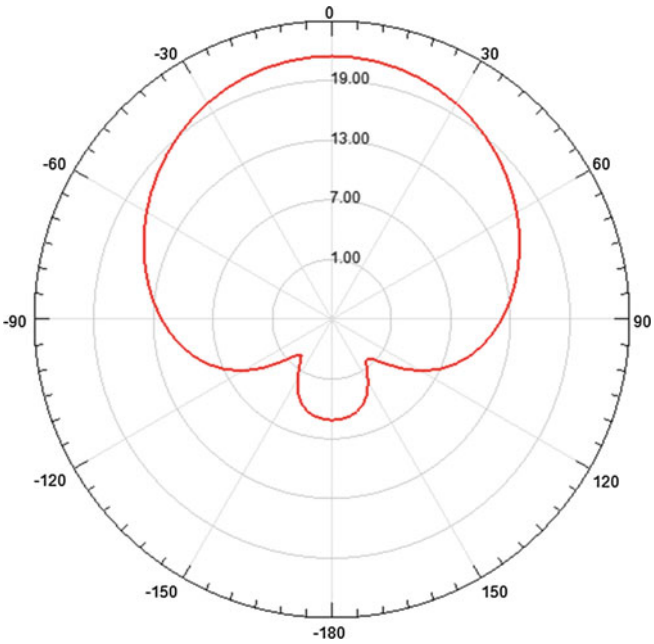

Fig. 7 Radiation pattern of a simple rectangular patch with the different parameters given in the first table

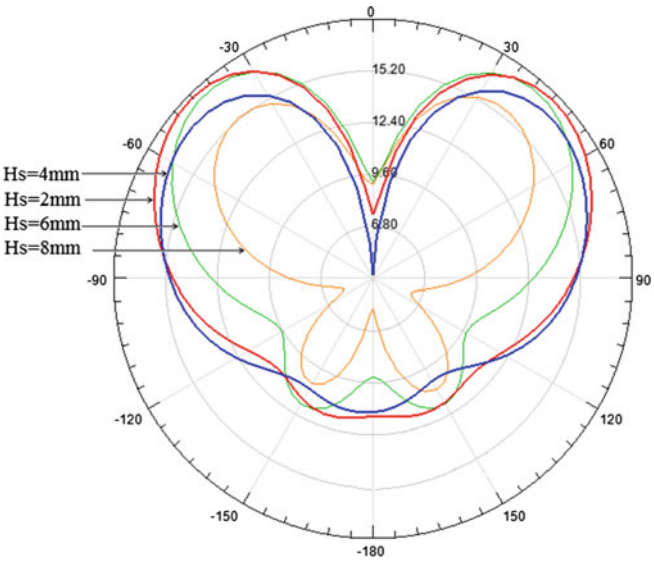

Fig. 8 Radiation pattern of the rectangular patch antenna using inset L-shaped feed with dual rectangular slots on the ground plane for different value of Hs (mm)

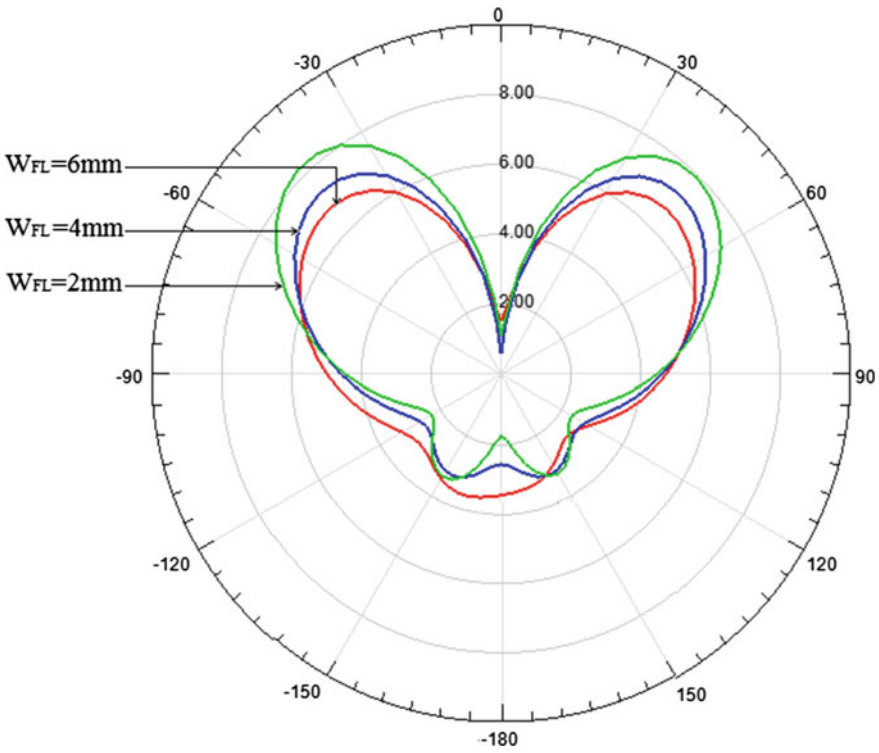

Fig. 9 Radiation pattern of the rectangular patch antenna using inset L-shaped feed with dual rectangular slots on the ground plane for different value of W_{FL} (mm)

In Fig. 9, results show that when the parameter (W_{FL}) is smaller, the intensity of the two main lobes increases and is a maximum when (W_{FL} = 2 mm).

The dimensions and locations of the slots on the ground plane and the anisotropic substrate play an important role for both bandwidth enhancement and radiation efficiency, this proposed antenna is very useful for many modern applications.

4 Conclusion

In this paper, analysis of inset L-shaped feed rectangular patch antenna with dual rectangular slots etched on the ground plane has been studied, it is found that this novel structure can increase the bandwidth of the simple patch antenna and consequently this antenna is very suitable for many applications, especially for applications in the access points of wireless communications. Moreover, simulation results for the effect of uniaxial substrate on the return loss and bandwidth of the rectangular patch antenna using inset L-shaped feed with dual rectangular slots on

the ground plane are presented. Also the effects of different physical parameters on the characteristics of this structure are investigated.

References

1. Mak, C.L., Luk, K.M., Lee, K.F.: Microstrip line-fed L-strip patch antenna. IEE P-Microw. Anten. P **146**, 282–284 (1999). doi:10.1049/ip-map.19990569
2. Su, C.M., Chen, H.T., Chang, F.S., Wong, K.L.: Dualband slot antenna for 2.4/5.2 GHz WLAN operation. Microw. Opt. Technol. Lett. **35**, 306–308 (2002). doi:10.1002/mop.10591
3. Satthamsakul, S., Anantrasirichai, N., Benjangkaprasert, C., Wakabayashi, T.: Rectangular patch antenna with inset feed and modified ground-plane for wideband antenna. In: SICE Annual Conference 2008, 20–22 Aug 2008, Japan. doi:10.1109/SICE.2008.4655253
4. Pues, H.F., Van De Capelle, A.R.: An impedance matching technique for increasing the bandwidth of microstrip antennas. IEEE Trans. Antennas Propaga. **37**, 1345–1354 (1989). doi:10.1109/8.43553
5. Boufrioua, A.: Bilayer microstrip patch antenna loaded with U and half U-shaped slots. In: ICMCS'14, 4th IEEE International Conference on Multimedia Computing and Systems, 14–16 Apr 2014, pp. 1338–1342, Marrakech. doi:10.1109/ICMCS.2014.6911325
6. Meshram, M.K., Vishvakarma, B.R.: Gap-coupled microstrip array antenna for wide-band operation. Int. J. Electron. **88**, 1161–1175 (2001). doi:10.1080/00207210110071288
7. Ansari, J.A., Mishra, A., Vishvakarma, B.R.: Half U-slot loaded semicircular disk patch antenna for GSM mobile phone and optical communications. Prog. Electromagnet. Res. C **18**, 31–45 (2011). doi:10.2528/PIERC10100704
8. Boufrioua, A.: Analysis of a rectangular microstrip antenna on a uniaxial substrate, Chapter 2. In: Nasimuddin (ed.) Microstip Antennas, pp. 27–42, 2011. InTech Publishers, Croatia. doi:10.5772/609. ISBN 978-953-307-247-0
9. Deshmukh, A.A., Ray, K.P.: Resonant length formulations for dual band slot cut equilateral triangular microstrip antennas. Wirel. Eng. Technol. **1**, 55–63 (2010). doi:10.4236/wet.2010.12009
10. Deshmukh, A., Kumar, G.: Formulation of resonant frequency for compact rectangular microstrip antennas. Microw. Opt. Technol. Lett. **49**, 498–501 (2007). doi:10.1002/mop.22161
11. Boufrioua, A., Benghalia, A.: Effects of the resistive patch and the uniaxial anisotropic substrate on the resonant frequency and the scattering radar cross section of a rectangular microstrip antenna. Aerosp. Sci. Technol. **10**, 217–221 (2006). doi:10.1016/j.ast.2005.11.010
12. Ansari, J.A., Singh, P., Dubey, S.K., Khan, R.U., Vishvakarma, B.R.: H-shaped stacked patch antenna for dual band operation. Prog. Electromagnet. Res. B **5**, 291–302 (2008). doi:10.2528/PIERB08031203
13. Wang, E., Zheng, J.: A novel dual-band patch antenna for WLAN communication. Prog. Electromagnet. Res. C **6**, 93–102 (2009). doi:10.2528/PIERC09010704
14. Boufrioua, A.: L-shaped slot loaded semicircular patch antenna for wideband operation. IJWMN Int. J. Wirel. Mob. Netw. **6**, 101–112 (2014). doi:10.5121/ijwmn.2014.6608

Part III
Economical Issues

An Expert Committee Evaluation for Load Forecasting in a Smart Grid Environment

Th. Boutsika, G. Sideratos and A. Ikonomopoulos

Abstract Electricity markets as well as integration of renewables and electric vehicles impose new requirements for efficient energy management, turning load forecasts into an essential tool for safe system operation at the lowest cost. However, the diverse load dynamics identified in a distribution system necessitate the development of novel forecasting models capable of accurate load forecast provision in a smart grid environment. The load forecasting system under evaluation is an expert committee which comprises four prediction models (PMs) and one combination model (CM) and provides forecasts in a 24-h ahead forecasting horizon. The load forecasting system performance is validated using data from four actual load time series characterized by large diversity. The expert committee exhibits satisfactory performance on all load profile tested, effectively capturing the load dynamics.

Keywords Load forecasting · Expert committee · Random forests

1 Introduction

Meeting the goals of energy policies requires large-scale integration of renewable energy sources and electric vehicles in distribution systems, while at the same time electricity markets call for higher flexibility and more efficient energy management. Many of these novel load monitoring and control functionalities can only be implemented within a smart grid infrastructure [1, 2] where load forecasting is essential for safe system operation and high quality energy supply at the lowest cost [3, 4].

Th. Boutsika (✉) · G. Sideratos · A. Ikonomopoulos
National Center for Scientific Research DEMOKRITOS,
Institute of Nuclear and Radiological Sciences and Technology, Energy and Safety,
15310 Aghia Paraskevi, Attiki, Greece
e-mail: thbouts@ipta.demokritos.gr; thbouts@gmail.com

A.Y. Oral and Z.B. Bahsi Oral (eds.), *3rd International Congress on Energy Efficiency and Energy Related Materials (ENEFM2015)*, Springer Proceedings in Energy, DOI 10.1007/978-3-319-45677-5_16

To this end various load forecasting approaches applicable in a smart grid environment have been proposed, among which artificial neural networks and support vector machines gain the highest acclaim [5]. However, the diverse load dynamics identified in a distribution system mandate the studying of new forecasting approaches, endowed with qualities such as being parameter-free, employing fast estimation computing schemes, and being able to capture the load time series dynamics.

In that respect, the performance of an expert committee which provides load forecasts in a 24-h ahead forecasting horizon is evaluated. The forecasting system architecture is described in Sect. 2, its performance using data from four actual load time series with diverse profiles is presented in Sect. 3, and Sect. 4 summarizes the conclusions drawn from the work presented.

2 Load Forecasting System Architecture

The load forecasting system under evaluation is an expert committee comprising four independent prediction models (PM) identified as PM_1, PM_2, PM_3, and PM_4, and one combination model (CM) which assembles the individual predictions of the PMs to provide forecasts in a 24-h ahead forecasting horizon. Along the line of the expert committee presented in [6], the PMs handle incoming data according to the hour of the day or the month of the year and are designed to perform better either in short- or in long-term horizons capturing the entire load time series dynamics. The architecture of the load forecasting system is illustrated in Fig. 1.

The PMs utilize historical load data, calendar data, maximum and minimum forecasted temperature values and special indices corresponding to the prediction day and the seven days prior to it. Moreover, the PMs receive either the most recent

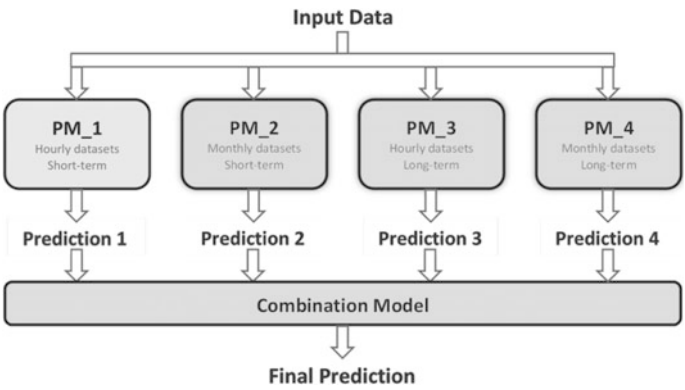

Fig. 1 Architecture of the load forecasting system under evaluation

load data along with predictions made by the forecasting system in previous time steps or only load data with at least a 24-h lag from the forecast time to provide accurate predictions both in short- and long-term horizons. More details regarding the selection of the PMs' input data can be found in [6].

The load predictors of the PMs are trained with the random forest (RF) algorithm proposed by Breiman using as parameters 500 trees to form each forest and one third the number of input variables to build each tree [7]. The hourly or monthly datasets used for the training of each RF are defined with respect to the load time series resolution so as to ensure the presence of at least 500 entries in each training set. In the current implementation of the expert committee each PM contains ten RFs for load prediction; eight applied during normal days and two applied during special days.

Going into detail, during normal days a different RF is activated in PM_1 and PM_3 at each of the eight three-hour intervals of a day (e.g., from 0:00 to 2:59, from 3:00 to 5:59, etc.). In PM_2 and PM_4 two different RFs are activated at each season of a year (e.g., winter containing the months of December, January, and February, spring containing the months of March, April and May, etc.); one predictor is applied during high demand hours of a day (from 09:00 to 15:59 and from 18:00 to 22:59) and the other during low demand hours (from 16:00 to 17:59 and from 23:00 to 08:59). Moreover, for load prediction during special days two RFs are activated in each PM. In PM_1 and PM_3 one is applied during high and the other during low demand hours of a day, while in PM_2 and PM_4 one is applied for special days occurring from April to September (higher temperatures) and the other for special days occurring from October to March (lower temperatures).

Finally, the CM employs 24 multi-layer perceptrons (MPLs)—one for each hour of the 24-h ahead forecasting horizon—to combine the PM predictions into a final load forecast. The applied MLPs have 24 linear hidden layer neurons in a typical three layer architecture (i.e., an input, a hidden and an output layers) and are trained with the PM predictions obtained during the training period.

3 Expert Committee Evaluation

The performance of the load forecasting expert committee is evaluated using four actual load time series (identified as TS-1, TS-2, TS-3, TS-4) obtained from customer meters connected at the medium voltage level of a distribution system. The meters record consumed energy over hourly intervals and the available records span a period of 34 months, from January 2011 to October 2013. For each load time

series the training sets for the RFs of the PMs contain all available load data. The training set of the 24 MLPs of the CM contains all PM predictions except the ones made for the last 200 days of recorded data which are used as the evaluation period, during which the expert committee provides load forecasts at an hourly resolution in a 24-h ahead forecasting horizon.

The obtained load time series exhibit large diversity in terms of magnitude and dispersion. As shown in Table 1 the maximum load values range between 350 kW for TS-3 and 750 kW for TS-4, while the coefficient of variation (ratio of the standard deviation to the mean) is close to 0.45 for TS-3 and TS-4 and almost double for TS-1 and TS-2, significantly affected by large intra-day periods of very low consumption evidenced in TS-1 and TS-2.

Moreover TS-1 and TS-2 demonstrate a flat high consumption load profile during business hours, whereas TS-3 and TS-4 showcase morning and afternoon peak hours of smaller duration. In addition, TS-1 and TS-2 display large differentiations between normal and special days, whereas in TS-3 and TS-4 differentiations appear only in terms of magnitude while the shape of the load curve is preserved. Finally, with respect to seasonality TS-4 and TS-3 present a higher weather dependency, identified by higher correlation coefficients between maximum and minimum temperatures and daily energy consumption.

Figure 2 presents observations along with 3-h ahead predictions made for three consecutive days in January 2013, one special (New Year's day) and two normal days, for all load time series. Observations and predictions are given in p.u. values for easier comparison between the load time series. The forecasting system's ability to capture the diverse load dynamics is indicated by small forecasting errors during high and low demand hours, as well as during hours with high and low load variability. Moreover, similar magnitude forecasting errors for 12-h ahead predictions for the same three days presented in Fig. 3 reveal the forecasting system's satisfactory performance both in short- and long-term forecasting horizons.

Table 1 Load time series statistics

	TS-1	TS-2	TS-3	TS-4
Minimum (kW)	27.78	0.78	17.46	0.72
Maximum (kW)	736.44	609.78	374.34	552.72
Mean (kW)	198.54	150.91	111.97	120.32
Standard deviation (kW)	170.67	115.31	48.99	53.72
Coefficient of variation (–)	0.86	0.76	0.44	0.45

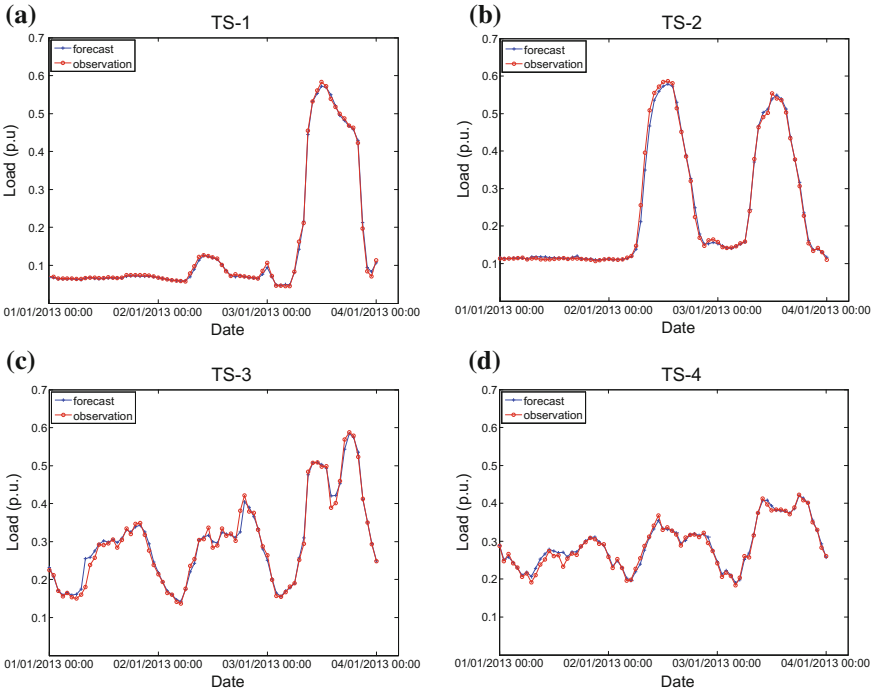

Fig. 2 3-h ahead predictions along with observations during a three-day period for load time series: **a** TS-1, **b** TS-2, **c** TS-3 and **d** TS-4

The mean absolute percentage error (MAPE) of the load predictions over the entire evaluation period (last 200 days of recorded data), depicted in Fig. 4, is used to evaluate and compare the performance of the forecasting system on the four actual load time series. It appears that MAPE increases with increasing look-ahead hours and remains almost constant for forecasting horizons longer than six hours ahead. The performance of the load forecasting system is regarded satisfactory and acceptable within a smart grid environment, with MAPE values ranging between 2.2 and 7.5 % for one-hour ahead predictions, and between 2.8 and 11.4 % for 24-h ahead predictions.

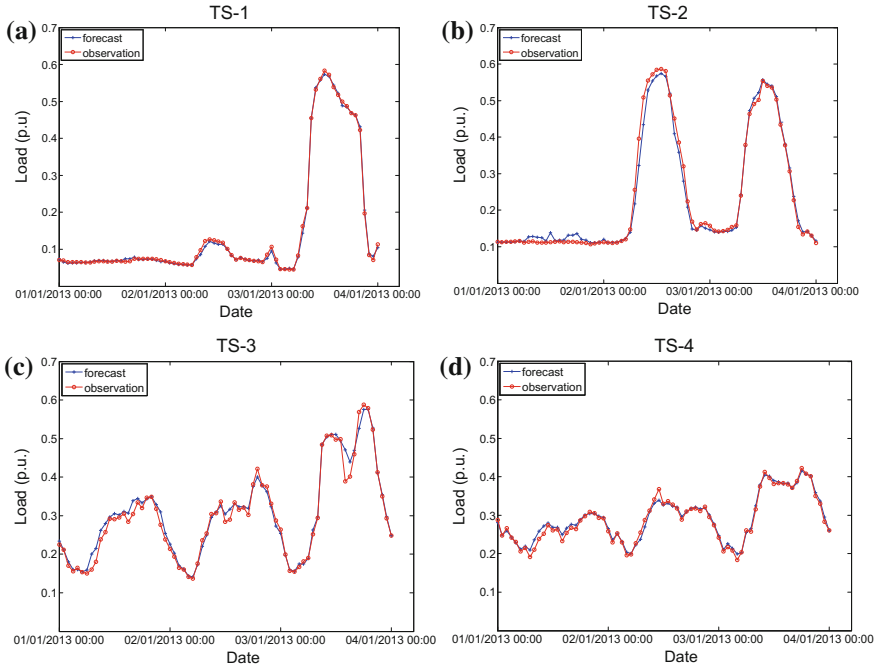

Fig. 3 12-h ahead predictions along with observations during a three-day period for load time series: **a** TS-1, **b** TS-2, **c** TS-3 and **d** TS-4

Fig. 4 Mean absolute percentage error during the entire evaluation period

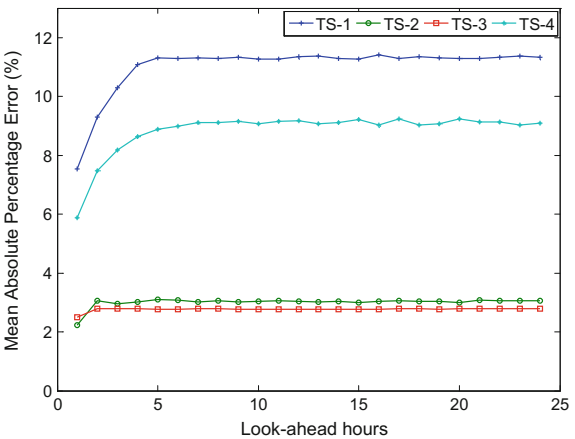

4 Conclusions

This paper evaluates the performance of a load forecasting system using data from actual load time series. The forecasting system consists of an expert committee with four independent prediction models, using hourly or monthly data sets and tuned for better performance either in short- or in long-term horizons, and one combination model, which provides the final predictions at an hourly resolution in a 24-h ahead forecasting horizon.

Data from four actual load time series which exhibit large diversity in terms of magnitude, fluctuations, peak hours, periodicity, and seasonality are used to validate the performance of the forecasting system. The satisfactory performance on all load profile tested, with mean absolute percentage errors for the entire evaluation period ranging from 2 to 12 %, reveals the forecasting system's ability to effectively capture diverse load time series dynamics identified in a distribution system.

Acknowledgments The authors acknowledge funding from the Greek General Secretariat for Research and Technology and the European Regional Development Fund under the Action 'Development Grants for Research Institutions-KRIPIS' of OPCE II.

References

1. EU Commission Task Force for Smart Grids Expert Group 1: Functionalities of smart grids and smart meters. https://ec.europa.eu/energy/en/topics/markets-and-consumers/smart-grids-and-meters/smart-grids-task-force (2010). Accessed 1 Jun 2015
2. Fang, X., Misra, S., Xue, G., et al.: Smart grid–the new and improved power grid: a survey. Commun. Surv. Tuts. **14**(4), 944–980 (2012). doi:10.1109/SURV.2011.101911.00087
3. SAS Institute. How does forecasting enhance smart grid benefits (White paper). http://www.sas.com/en_us/whitepapers/how-does-forecasting-enhance-smart-grid-benefits-106395.html (2010). Accessed 15 Jun 2015
4. Aung, Z., Toukhy, M., Williams, J., et al.: Towards accurate electricity load forecasting in smart grids. In: 4th International Conference on Advances in Databases, Knowledge, and Data Applications (DBKDA), Saint Gilles (2012)
5. Hernandez, L., Baladron, C., Aguiar, J., et al.: A survey on electric power demand forecasting: Future trends in smart grids, microgrids and smart buildings. Commun. Surv. Tuts. **16**(3), 1460–1495 (2014). doi:10.1109/SURV.2014.032014.00094
6. Sideratos, G., Ikonomopoulos, A., Hatziargyriou, N.: A committee of machine learning techniques for load forecasting in a smart grid environment. Int. J. Energy Power **4**, 98–108 (2015). doi:10.14355/ijep.2015.04.016
7. Breiman, L.: Random forests. Mach. Learn. **45**(1), 5–32 (2001). doi:10.1023/A:1010933404324

Linking Smart Energy and Smart Irrigation: Integration, System Architecture, Prototype Implementation and Experimentation

Elias Houstis, Antonia Nasiakou, Manolis Vavalis and Dimitris Zimeris

Abstract Irrigation is, for certain geographical regions, a vital activity which often happens to be an expensive one. For those regions, irrigation commonly accounts to significant energy consumption. In this paper, we propose to investigate the possibility of reducing the cost of irrigation by utilizing techniques, methods and practices that are common in the next generation energy systems, known also as smart energy systems. Specifically, we design, implement and evaluate a software platform that couples the smartness of the irrigation systems with the smartness of the energy systems. The resulting simulation engine allows large scale and very detailed experimentation which allow irrigation experts to specify energy effective configurations that lead to the reduction of the irrigation cost through smart utilization of Renewable Energy Sources.

Keywords Renewable energy resources · Irrigation · Energy · Agriculture

1 Introduction

Irrigation has been around for as long as humans have been cultivating plants. Irrigation procedures mainly depend on the water availability, while water requirement is the main parameter for calculating equivalent energy demand.

Direct coupling of agricultural processes to Renewable Energy Sources (RES) has been considered for centuries. In principle, it reduces energy cost, by consuming the

E. Houstis (✉) · A. Nasiakou · M. Vavalis · D. Zimeris
IRETETH/CERTH and University of Thessaly, 37 Gklavani Str, 38221, Volos, Greece
e-mail: enh@uth.gr

A. Nasiakou
e-mail: adnasiak@uth.gr

M. Vavalis
e-mail: mav@uth.gr

D. Zimeris
e-mail: zimeris@uth.gr

A.Y. Oral and Z.B. Bahsi Oral (eds.), *3rd International Congress on Energy Efficiency and Energy Related Materials (ENEFM2015)*, Springer Proceedings in Energy, DOI 10.1007/978-3-319-45677-5_17

free energy offered by RES and often going off the grid, in a micro-grid form or as energy autarky islands [1].

The main objective of this paper is to provide a practical tool that allows us to elucidate several issues concerning the various characteristics of the coupling of smart grid with smart irrigation. More specifically, we propose a simulation approach based on RES (solar panels, wind turbines) installations for serving agricultural and perhaps residential loads. This approach utilizes a software platform capable of simulating technical and financial aspects of the proposed installation. We design and develop a prototype implementation of such a platform. An initial experimentation indicates that the irrigation and to a great extent the agricultural sector, can potentially be a very challenging area of RES research and development, especially when liberalized auction-based energy market is involved.

The rest of this paper is organized as follows. In Sect. 2 we present related efforts that motivate our study and develop the appropriate background. Section 3 contains the main characteristics of our prototype implementation and the proposed integrated system. Associated elementary simulation results are given in Sect. 4 and our concluding remarks in Sect. 5.

2 State of the Art

We have identified several agricultural projects around the globe that emphasize on the need for further research and development towards the improvement of irrigation applications and beyond, in terms of better energy management and reduced cost.

A sizing procedure for calculating the variables involved in a solar panel installation for agricultural processes is presented in [2]. Vick and Almas [3] proposes methods for the irrigation management via a central coordinator. Based on several parameters, it suggests various alternative implementations involving solar and/or wind energy, while simultaneously comparing with each other, also taking advantage of storage ability of excess energy and water storage in surface reservoirs for future irrigation and other on-farm uses. Similar to the above, [4] presents a modernized irrigation system, already in operation, coordinated by a central management operator. The central system involves elementary and remote control that manages the automated frequency controlled pumping stations, while an on-demand program schedules different farmers' irrigation processes.

Among other papers, [5, 6] and [7] present sizing and optimization algorithms focusing on evaluating technical (dependent on soil, climate, geography, agriculture, and hydrogeology) as well as economical (dependent on the electricity price, life cycle cost of investment) feasibility of solar and/or wind energy installations for irrigation purposes.

Our simulation system has been developed on top of the GridLAB-D system [8] for simulating the distribution energy network. It is based on four major components, namely, the power flow, the building, the market and finally the generators,

that describe the most representative distribution systems operation, technically as well as financially. It is important to point out that although GridLAB-D includes a residential module and a market module, it lacks an agriculture module.

3 Prototype Implementation

The basic concept of our research study is the ability of RES to handle primarily agricultural and secondly residential loads, the former, demanding mainly pumping load for a period of four months while the second lasts for the rest eight months serving residential loads.

From GridLAB-D's **generators** module, solar panels, wind turbines and batteries are selected for serving both the agricultural and residential load. RES always respond first in case of a demand load, regardless its nature. However, they also have the ability of storing excess energy in batteries for use in case of insufficient operation. EV charger stations will additionally demand load in order to cover the vehicle's needs. RES will operate normally with the DC-AC inverters assistance.

Residential devices modeled through the house, object of the **residential** module, are controlled by active controllers, while loads described by ZIPload properties for non-thermostatically appliances, are controlled by passive controllers. The object house is also used to describe, through similarity, new properties and definitions of terms engaged in agricultural engineering. In that sense, *humidity_setpoint* acting as a user-defined command and the *crop_type* property defining the necessary crop characteristics are additionally incorporated at object ZIPload in order to be available for the associated controller. Another new agricultural object, namely ***soil_sensor*** for implementing metrics of soil humidity required by the controller, is modeled and designed via GridLAB-D source code. The soil humidity function is in our study naive and its values follow the normal distribution function. Additional parameters describing surface geometry like ***floor_area*** are also incorporated.

Furthermore, for our implementation purposes, we extend the functionality of **market** module in order to develop a controller, named ***irrigation_controller***, suitable for price responsive control of agricultural loads. Based on the metrics of soil sensor (soil humidity) and on the willingness of the customer to pay in order for the system to operate, the *irrigation_controller* should adjust the system's set-points. The willingness of a customer to pay can be translated into a comfort zone where the customer can tolerate a delay of irrigation so as to achieve a more profitable price. In addition to the bid price, controller is also responsible for submitting the demanded load as well.

As far as the distribution system topology concerns, we choose the R4-25.00-1 feeder from GridLAB-D libraries which can support a maximum load of 948 kW, therefore it is a good candidate for supplying the residential network while the IEEE-4 node test feeder is selected for supporting the agricultural network. Both feeders are connected through a meter (object of **powerflow** module) which gives

the opportunity to simultaneously, control the amount of energy needed and the amount of energy provided. The distributed resources and the batteries are placed in the agricultural network and the energy is transferred, through the grid, to serve both residential and agricultural loads.

4 Simulation Results

As described in Sect. 3, we use R4-25.00.1 prototypical feeder to simulate the distribution-residential network. Approximately 170 houses are supported. For the needs of our experimentation we have designed two scenarios that are as realistic as possible. However, due to lack of space, only the simpler one is presented in this paper.

In this scenario, there exist a surface water reservoir and the irrigation system demand load is satisfied directly from the RES or the batteries, acting both separately or in combinations, as the producing units. Batteries are charged during the daylight when the RES have energy that is not consumed and they discharge during the night. Each battery is associated with either a solar panel or a wind turbine. More details about the characteristics of the producing units, used for our experiments, are depicted in Table 1.

Regarding the consuming units, except the agricultural load and the appliances, an EV-charger station with three electric vehicle chargers is also included. Each of these chargers are associated with the same configuration regarding the vehicle travel information but with different characteristics for the capacity of the EV-charger battery.

Both consuming and producing units participate in the market by submitting their bids every 15 min. In this scenario, the required power concerns only the load demanded by the pumping system which is responsible for the irrigation process, unlike the full drilling system whose task is serving both water elevation power and surface irrigation requirements. The load required to irrigate an area of 150,000 m^2 is approximately 20 kW. A ZIPload object of 20 kW base power simulates the load needed for such an irrigation system.

Due to lack of space, we consider only two days of a yearly simulation, one for the irrigation season and one for the residential one. The days are illustrated sequentially in Fig. 1 where we observe the clearing quantity and the demand for the "two days" period. As seen, for the first half, associated with the irrigation load,

Table 1 Energy Resources configuration

	Solar panel (500 m^2)	Wind turbine	Battery1	Battery2
Max capacity (kW–kWh)	85	150	250	100
Type	Single crystal silicon	Medium size	Li-ion	Lead-acid

Fig. 1 The clearing quantity (*blue line*) matching the total demand (*green line*). x axis corresponds to the simulation time while y axis to the power in kW. The first half indicates the irrigation season and the second half the season of the eight months serving residential loads

the maximum satisfied demand, corresponding to the irrigation plus the EV-charger load, is approximately 25 kW, fully served by the producing units. The maximum power for both solar panels and wind turbines is approximately 160 kW and the minimum is 40 kW. In the second day, it is observed that there are time intervals that the demand (green line) does not coincide with the available power supply (blue one). That happens because the bid price of some of the appliances is lower than the cheapest producer and the demand satisfied from the main grid.

In Fig. 2, we observe the state of one of the batteries during the two-day simulation period. The battery discharges when the energy from RES is not enough to serve the demanded load. It is worth mentioning that as the battery bids into the market, the amount of energy, added or subtracted, is associated with the energy of the battery that is sold, and the amount of energy that is not sold in the market from RES. So, if the amount of energy offered from solar panels and wind turbines is not higher than the amount of energy offered from the batteries, in the market, the battery is discharging in slower pace and it could provide energy for longer time. Moreover, the battery due to its high price could participate in the market but the demand is satisfied primarily from RES and its energy is used during the night.

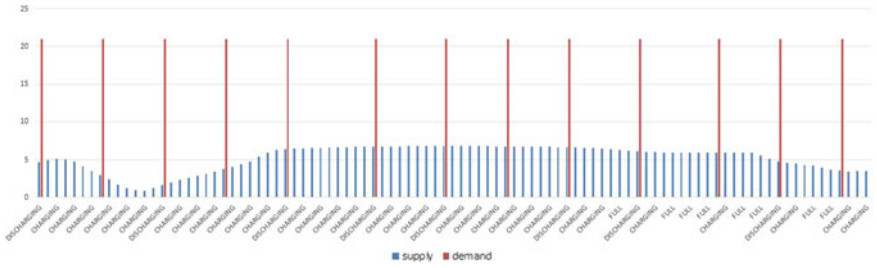

Fig. 2 Battery state when the energy from RES is limited (the red line corresponds to the demand for the irrigation process while the blue one to the supplied by the RES energy)

5 Summary and Recommendation

Smart energy focuses largely on residential and industrial issues and less on transportation and commercial, for several and diverse reasons. The agricultural aspect of the smart energy has been relatively untouched. It is our belief, that the agricultural sector is very crucial for many countries, in order to succeed further growth and development. In that sense, and due to the drawback of relatively high electric costs, it is a rather promising field for research and development of microgrid structures and smart grid applications. A reduction of grid-connected costs, by utilization of alternative physical resources operating off-grid, can potentially be a strong motivation for the participants (professional agriculturists that live in rural villages). The viability of such an effort could be gained, if several physical as well as, policy parameters are considered. Seeing it, by an investment viewpoint, the feasibility depends on the number of agriculturists they wish to participate. It is our belief, that the greater the number of end-users, the greater the investments prospects, and the equivalent cost savings for both the investor and the user. Based on that fact, a possible deal of a future investor with agricultural cooperative associations is a first step towards a medium to a large scale implementation. An alternative, even more profitable, for the agriculturists themselves, could be the investment prospect by their own, that is, a number of them agree to such an investment and they become generators and consumers at the same time.

Acknowledgments This work was performed in the framework of the EPEA-TH project within the KRIPIS action of the GSRT. Work also supported in part by the GSRT Aristeia Research Grant with title "Towards Next Generation Intelligent Energy Systems" and with acronym Hephaestus. The authors wish to thank Margaritis Gotinakos, Apostolos Papadoulis and Christos Kokalis for their valuable help on practical irrigation issues.

References

1. Melton, F.S., Johnson, L., Lund, C., Michaelis, A., Pierce, L., Guzman, A., Hiatt, S., Purdy, A. J., Lee, C., Rosevelt, C., Fletcher, N., Votava, P., Milesi, C., Hashimoto, H., Wang, W., Sheffner, E. J., Nemani, R.: Web services for satellite irrigation monitoring and management support. AGU Fall Meeting Abstracts (2011). doi:http://adsabs.harvard.edu/abs/2011AGUFMIN11B1297H
2. Morales, D.T., Busch, J.: Designs of small photovoltaic solar-powered water pump systems. Technical Report 28. U.S. Department of Agriculture (2010)
3. Vick, B.D., Almas, L.K.: Developing wind and/or solar powered crop irrigation systems for the great plains. Appl. Eng. Agric. **27**(2), 235–245 (2011). doi:10.13031/2013.36494
4. Stambouli, T., Faci, J.M., Zapata, N.: Water and energy management in an automated irrigation district. Agric. Water Manag. **142**, 66–76 (2014). doi:10.1016/j.agwat.2014.05.001
5. Glasnovic, Z., Margeta, J.: Maximum area that can be economically irrigated by solar photovoltaic pumping system. J. Irrig. Drain. Eng. **135**(1), 44–49 (2009). doi:http://dx.doi.org/10.1061/(ASCE)0733-9437(2009)135:1(44)

6. Kelley, C.L., Gilbertson, E., Sheikh, A., Eppinger, D.S., Dubowsky, S.: On the feasibility of solar-powered irrigation. Renew. Sustain. Energy Rev. **14**(9), 2669–2682 (2010). doi:10.1016/j.rser.2010.07.061
7. Shivrath, Y., Narayana, B., Thirumalasetty, S., Narsaiah, L.: Design and integration of wind-solar hybrid energy system for drip irrigation pumping application. Int. J. Modern Eng. Res. **2**(4), 2947–2950 (2012). doi:10.1016/j.agwat.2014.05.001
8. Chassin, P.D., Fuller, C.J., Djilali, N.: GridLAB-D: An agent-based simulation framework for smart grids. J. Appl. Math. **2014**(2014), 1–12 (2014). doi:10.1155/2014/492320

Part IV
Materials for Sustainable Energy

Some Issues of Industrial Scale Silicon Isotopes Separation by the Laser Assisted Retarded Condensation Method (SILARC)

K.A. Lyakhov and H.J. Lee

Abstract Advancing miniaturization of microelectronic devices makes the heat removal problem extremely important. It makes to search for cheaper ways for silicon isotopes production. We discuss a number of important constraints to be considered for optimal design of industrial scale silicon isotopes separation facility relying on the laser assisted retarded condensation method. Our calculations are based on the transport model for overcooled, rarefied, and supersonic gas flow in the laser field with frequency tuned for excitation of specific isotopomer.

Keywords Method of isotope separation by laser assisted retarded condensation · Resonator · Rarified supersonic overcooled gas flow dynamics · Quantum control

1 Introduction

Currently well-developed non-laser based methods, which are attractive for industrial scale Si isotopes separation, are gas centrifuging, and chemical exchange reaction due to their relatively high production rate and low energy consumption. However, the disadvantage of gas centrifuging is high cost of its equipment, and of chemical exchange is rather low separation efficiency and instability of operation [1]. Limiting factors for extended employment of other traditional methods like electromagnetic separation and gas diffusion are high initial and operational cost and the difficulties of converting traditional isotope production plant from one product to another (the latter also concerns to gas centrifuging). In a semiconductor industry this property is the most important, because it is desirable to obtain different isotopes of such elements as Si, Ge, Pb, B, C as a part of the whole industrial cycle. Laser assisted methods lend themselves naturally for this purpose because of

K.A. Lyakhov (✉) · H.J. Lee
Plasma Physics Lab, Department of Nuclear and Energy Engineering,
Institute for Nuclear Science and Technology, Jeju National University,
Ara-Dong 1, Jeju 690-756, South Korea
e-mail: lyakhov2000@yahoo.com

A.Y. Oral and Z.B. Bahsi Oral (eds.), *3rd International Congress on Energy Efficiency and Energy Related Materials (ENEFM2015)*, Springer Proceedings in Energy, DOI 10.1007/978-3-319-45677-5_18

possibility to vary setup parameters required for separation of isotopes of different elements. Production of different isotopically pure elements can be automatized by control over laser frequency and intensity as well as pumping out speed and irradiation chamber length by implementing skimmer blade as a movable part.

Laser based methods include Atomic Vapour Laser Isotope Separation (AVLIS) and Molecular Laser Isotope Separation. AVLIS provides very high selectivity but has very expensive implementation and operational cost (electricity consumption and maintenance cost) and small production rate [2]. MOLIS methods based on multiphoton dissociation are more(less) competitive in terms of electricity consumption comparing to AVLIS (gas centrifuge), while methods based on single photon absorption to prevent dimerization as in SILARC or wall sticking as in SILARC-II can compete with gas centrifuging in this aspect. However, isotope production rate provided by SILARC-II is unacceptably small for industrial deployment unless for medicine purposes.

In this paper we briefly sketch some of our results for variety of constraints on irradiation cell (IC) length imposed by gas flow temperature, amplification and absorption of laser radiation in resonant multipass cavity, and gas flow condensation. Operational principles of prospective experimental setup and its upscaling to industrial facility can be found in Ref. [3].

2 The Model of Laser Assisted Isotope Separation in Supersonic Gas Flow

Gas flow is a mixture of target and carrier gases. As a target gas for Si isotopes separation SiF_4 was chosen due to its relatively high vapor pressure at room temperature (no need in additional energy supply to vaporize it), and argon is chosen as a carrier gas. At room temperatures polyatomic molecules feature broad electronic absorption bands and, therefore, demonstrate low spectral selectivity to laser excitation. However, spectral lines are significantly simplified and their broadening can be significantly diminished by letting diluted gas to supersonically expand. Laser frequency ν_L should be tuned to specific vibrational mode of excited isotopomer. The ν_3 vibrational frequencies for ^{29}Si and ^{30}Si are 1022.9 and 1014.4 cm^{-1} respectively, Ref. [4]. To assure a coincidence of the incident laser radiation with the $^{28}SiF_4$, the CO2 laser was operated on the 9P(36) transition band which possesses a frequency of 1031.5 cm^{-1}. Photons absorption and reabsorption in gas flow takes place repeatedly. For effective enrichment the rate of this process should exceed the rate of excitation loss caused by collisions in the gas flow. Selectively excited monomers escape overcooled gas flow with higher rates than heavier dimers [5]. Migration of selectively excited molecules to gas flow periphery is similar to diffusion process.

Dimerization is described by Eerkens's 2-body collisions approach. The model is formulated within material and kinetic balance equations approach for four (three-for dimers excitation) fractional population groups: nonexcited dimer f_{id},

epithermal particles $f_{i!}$, and excited monomers f_{i*} population in the external laser field derived in Ref. [5] (Eqs. 56–64):

$$\begin{aligned}\frac{df_{i*}}{dt} =&(1-f_{i*}-f_{i!}-f_{id})n_i k_A \\ &-f_{i*}n_i\{(1-e_*)(k_{df}+k_{VV}+k_{VT}+k_{se})+e_* k_W\},\end{aligned} \tag{1}$$

where $n_i = n_i(\vec{r},t)$ is the density distribution of selected isotopomer ${}^{i}SiF_4$ (in further consideration we assume uniform distribution). To-the-wall (gas flow surface) survival probability e_* is also vanishing unless gas flow is very thin. In our case of stationary gas flow, stationary pumping of medium by laser radiation, partial overlap between laser beam and gas flow, and assuming that irradiation cell is implemented as a resonant cavity, this equation is transformed to

$$\begin{aligned}\frac{df_{i*}}{dt} =&(1-f_{i*}-f_{i!}-f_{id})n_i \frac{t_{tr}^{(g)}}{t_{tr}} \sum_{j=0}^{N_{tr}-1} k_A^{(j)} - \\ &-f_{i*}n_i\{k_{df}+k_{VV}+k_{VT}+k_{se}\}=0,\end{aligned} \tag{2}$$

where transition time of gas molecules across laser beam is given by $t_{tr}^{(g)} = \frac{l}{\langle U\rangle}$, where intercept length is related with laser beam radius as $l = 2R_L/cos\alpha$. Laser excitation rate of monomers by selective photoabsorption on each intersection of gas flow with laser beam is given by $k_A^{(j)}(\vec{r},t) = \varphi_I^{(j)}\sigma_A,\ s^{-1}per\ molecule$, where photon flux density is given by $\phi_I^{(j)} = \frac{\phi_\varepsilon^{(j)}}{\varepsilon_L}$, where $\varepsilon_L = hv_f$ is the laser photon energy corresponding to selectively excited vibrational mode, σ_A is multi-photon absorption cross. Laser energy density in the case of pencil-like laser field is given by $\phi_\varepsilon^{(j)} = I^{(j)}(x)/(\pi R_L^2)$, where $I^{(j)} = I_{CW}f^{(j)}(x)$ is distribution of laser intensity across resonant cavity on j-th intersection,I_{CW} is laser intensity in contnous mode, R_L is the laser beam radius.

3 Constraints on IC Length and Width Imposed by Amplification and Absorption of Laser Radiation

In our case of IC is implemented as a resonant multipass cavity the following additional constraints on its width and length should be applied

$$l_{int}n' = q\frac{\lambda_f}{2},\ L_{IC} = N_{tr}q\frac{\lambda_f}{2}\sin\ \alpha + l/2\ q \in \mathbb{Z}, \tag{3}$$

where interaction length is given by $l_{int} = W_{IC}/\cos\ \alpha$. By applying the principle superposition for electric fields and resonator conditions (3), laser field amplification/damping factor on j-th intersection can be written as

$$f^{(j)}(x) = \frac{T}{n'} \frac{\tilde{\rho}^{2j} + \tilde{\rho}^{2(2N_{tr}-1-j)} + 2\tilde{\rho}^{2N_{tr}-1}\cos\{\phi'(x)\}}{(1-\tilde{\rho}^{2N_{tr}})^2} \exp\{-2\phi''(x)\},$$
$$\tilde{\rho} = \rho \exp\{-\phi''(W_{IC})\}. \tag{4}$$

In our calculations we took into account that ZnSe window transmittance on power of impinging laser beam $T = t^2$ is slowly varying functions over quite broad interval of wavelength in infrared region $T \approx 0.7$, while from inside IC semi-transparent mirror is fully reflective $t^2 = 0$ In calculations we assume that R = 0.98. Spatial variations of standing waves (resulting laser intensity) in the plane perpendicular to the gas flow at different values of resonant photoabsorption cross section are shown in Fig. 1b. Moreover, as seen from Fig. 1a, instead of expected amplification at resonant frequency we have its strong damping due to absorption by mirrors and target gas (see Fig. 1a). Photons emitted due to subsequent fluorescence cannot be used due to their larger wavelength. Therefore, in order to have laser intensity in the end of resonator still higher than the minimal level I_{min} required to promote selective gas flow separation, initial laser intensity should be quite large. In Table 1 it is shown I_{CW} at different photoabsorption cross sections, which increase over IC length, due to laser intensity decrease caused by absorption. I_{CW} should not exceed maximal allowed level in order to prevent multiphoton dissociation (I_{max} = 2019 W).

The minimal continuous mode laser intensity required for multi-photon dissociation can be estimated from the condition that number of photons absorbed by molecule before excitation loss $k_{ph} = \frac{I_{max}}{\varepsilon_L} \frac{\sigma_A(k_{ph})}{\pi R_L^2} \tau_{ex}$ is not smaller than required to dissociate it $k_t = D/\varepsilon_L$. Therefore, the maximal laser intensity constrained by

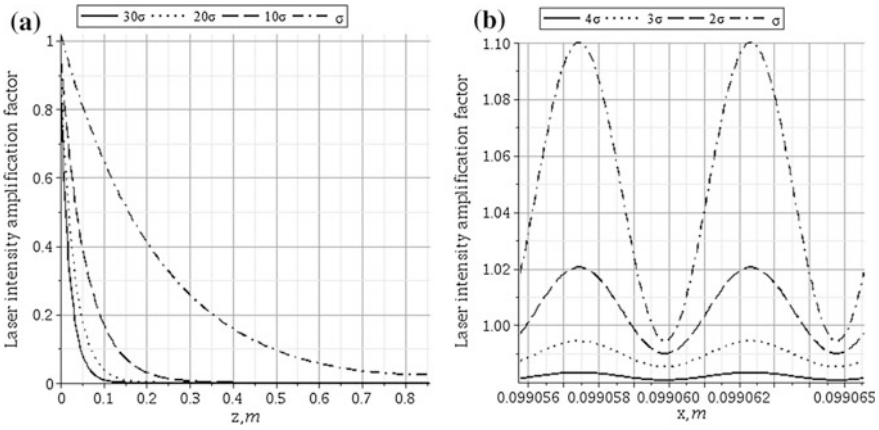

Fig. 1 Laser intensity damping factor evolution along gas flow centerline (**a**) and across gas flow (**b**) at different resonant photoabsorption cross sections (s corresponds to dissociation limit). Mirror reflectivity R = 0.98

Table 1 Minimal initial laser intensities required to promote selective gas flow separation until the end of irradiation cell (L_{IC} = 43 cm)

σ_A	$\sigma_A(k_{ph})$	$3\sigma_A(k_{ph})$	$5\sigma_A(k_{ph})$	$7\sigma_A(k_{ph})$
I_{min},W	35.33	11.78	7.06	5.05
I_{CW},W	254.56	271.1	536.3	1290.44

dissociation threshold is given by $I_{max} = \frac{\pi R_L^2 D}{\sigma_A(k_{ph})\tau_{ex}}$. Therefore, in order to avoid multiphoton absorption, series of CO2 laser should be used. Mirrors in the end of chamber are inclined in such a way that each laser beam sweeps all irradiation cell many times until its full absorption.

By analogy, the minimal laser intensity required to initiate gas flow separation due to selective excitation is $I_{min} = \frac{\pi R_L^2 \varepsilon_L}{\sigma_A(k_{ph} \sim 1)\tau_{ex}}$.

4 Constraints on IC Length Imposed by Gas Flow Condensation

As shown in Ref. [5], only dimer population is significant at gas flow temperature, which provides the highest enrichment factor. However, the largest enrichment factor does not necessarily correspond to optimal conditions, other factors such as product cut and gas flow rate should be also considered. The model for estimation of equilibrium [6] and non-equilibrium concentrations of clusters in overcooled supersonic gas flow was given in Ref. [7] by consideration of chain-like monomer clusterization on example of (SF_6) clusters. Normally, $y_Q^N \ll y_G$, where y_Q, and y_G are equilibrium concentrations of monomers and carrier gas molecules respectively. Therefore, chain-like clusterization of homo-N-mers is much less probable than chain-like clusterization of hetero-mers such as SiF_4:Ar_{N-1}.

According to Ref. [7], only oligomers which have critical monomer loading are susceptible for non-equilibrium production and growth, which begin after vapor supersonic cooling takes place, while production of subcritical clusters is equilibrated by their dissociation. Population of subcritical clusters SiF_4:Ar_{N-1} can be deduced inductively for chain-like cluster growth

$$y_{QG\ldots G_j} \equiv y_{j+1} = y_G y_j g_{GG} K_j, \quad j = 2, \ldots, N_{cr} - 2, \tag{5}$$

$$K_j = \left(\frac{r_Q + j r_G}{r_Q + (j+1) r_G}\right)^2 \sqrt{M_Q + (j-1) M_G}\, \frac{M_Q + j M_G}{(M_Q + (j+1) M_G)^{3/2}}, \tag{6}$$

where M_Q and r_Q correspond to target gas molecule mass and Lennard-Jones potential range parameter respectively, Lennard-Jones potential well depth $D\alpha$ and bond vibration energy ϵ_α correspond to Ar:Ar bond.

The maximal cluster loading depends on gas flow temperature, pressure, and transition time across IC. As seen from Fig. 2, the longer transition time the larger cluster loading can be produced

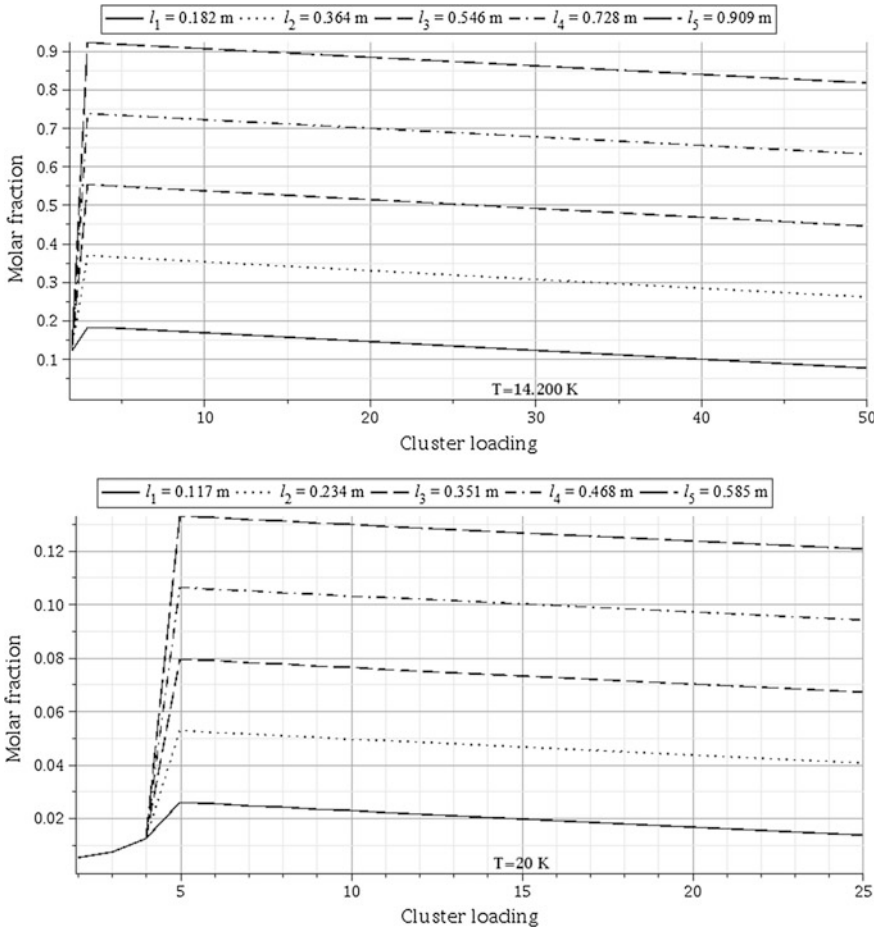

Fig. 2 Molar fraction of clusters as a function of its loading, corresponding to different distances from the nozzle outlet and different gas flow temperatures (mixture of SiF_4 and argon is considered)

5 Constraints on IC Width and Length Imposed by Gas Flow Temperature

In this section we consider one more important constraint on IC geometry, which is the gas flow region with optimal temperature inside (gas flow and ambient gas pressures should coincide in order to provide perfectly expanded gas flow, and fixed to some optimal level p_{tot} = 10 mtorr). This region is constrained cross-wise to gas flow direction by the distance between individual gas flows (in the case of industrial facility), by the distance between gas flow and chamber wall, and along gas flow direction by its maximal length, corresponding to the highest tolerable temperature level, which is controlled by parameter s (see equation below). The distance between gas flows and walls should not be smaller than mixing layer width. Otherwise, additional gas flow deceleration by IC walls and neighbor gas flows in industrial facility should be taken into account. Gas flow length is defined, as shown later, by boundary layer thickness a well.

In our case of low temperature rarified gas flow, Knudsen number is very small, and Reynolds number is small as well. Hence, gas flow can be treated as continuous and laminar. In a turbulent gas flow boundary layer grows faster than in laminar gas flow. Dimensions of the optimal temperature field inside turbulent flow are smaller than for laminar flow, and, therefore, can be considered as a lower limit for temperature field conditioned constraints on irradiation chamber length and as an upper limit for irradiation chamber height and width.

Upper limit for the length of gas flow region with optimal variation of temperature, can be found from relation between temperature and velocity in the free turbulent jet

$$\frac{T(z,0)-T_0}{T_{nozz}-T_0}=\kappa_T\frac{U(z)}{U(z_{nozz})}, \tag{7}$$

and assuming that

$$\begin{cases} \Delta T = sT_{opt}; \\ T_{opt}=\frac{T_{nozz}+T_{max}}{2} \\ T_{max}-T_{nozz}=\Delta T. \end{cases} \tag{8}$$

Velocity field distribution along jet axis is governed by Eq. from Ref. [8]

$$\left(\frac{U_{max}}{U_{nozz}}\right)^2 n\bar{F}=\left(\frac{T_{max}-T_0}{\kappa_T(T_{nozz}-T_0)}\right)^2 n\bar{F}=\frac{n_2 u}{A_{20}}, \tag{9}$$

6 Conclusions

In this paper implications of such constraints on IC geometry as gas flow deceleration and condensation rate, absorption of laser radiation by interior gas and mirrors, interaction of gas flows between each other and with IC walls were analyzed. We conclude that further progress in application of SILARC method for industrial scale isotope separation is possible by development of powerful and efficient continuous wave CO2 lasers, development of technology for highly reflective thin film coating of large surface area to provide maximal reflectivity of resonator mirrors, and development of highly efficient, high speed oil-free vacuum pumps.

Acknowledgments This work was supported by Priority Research Centers Program through the National Research Foundation of Korea (NRF) funded by Ministry of Education, Science and Technology (2010-0020077)

References

1. Wang, C., Bai, P., Guo, X.: Advances in Separation Methods for large scale production of silicon isotopes. Radioanal. Nucl. Chem. J. **304**, 989–999 (2015). doi:10.1007/s10967-015-3950-7
2. Bokhan, P.A., et al., Laser Isotope Separation in Atomic Vapor. WILEY-VCH Verlag GmbH & Co. KGaA, Weinheim (2006). doi:10.1002/352760894X
3. Lyakhov, K.A., Lee H.J.: Perspectives of industrial separation of zirconium isotopes by laser assisted retarded condensation method. In: Oral, A.Y., Oral, Bahsi, Z.B., Ozer, M. (eds.) Second International Congress on Energy Efficiency and Energy Related Materials (ENEFM2014), p. 99–104. Springer, Heidelberg (2015)
4. Lyman, J.L., Rockwood, S.D.: Enrichment of boron, carbon, and silicon isotopes by multiphoton absorption of 10.6 μm radiation. J. Appl. Phys. **47**, 595–601 (1976). doi:10.1063/1.322619
5. Eerkens, J.W.: Laser-induced migration and isotope separation of epi-thermal monomers and dimers in supercooled free jets. Laser and Part. Beams **23**, 225–253 (2005). doi:10.1017/S026303460522325X
6. Eerkens, J.W.: Equilibrium dimer concentration in gases and gas mixtures. Chem. Phys. **269**, 189–241 (2001). doi:10.1016/S0301-0104(01)00346-9
7. Eerkens, J.W.: Nucleation and particle growth in super-cooled flows of SF6/N2 and UF6/N2 mixtures. Chem. Phys. **293**, 112–153 (2003). doi:10.1016/S0301-0104(03)00300-8
8. Abramovich, G.N.: Applied Gas Dynamics. Foreign Technology Division, Ohio (1973)

Inkjet Printing and Inkjet Infiltration of Functional Coatings for SOFCs Fabrication

R.I. Tomov, M. Krauz, Chenlong Gao, S. Hopkins, R.V. Kumar and B.A. Glowacki

Abstract The feasibility of the inkjet printing technique in the fabrication and modification of electrodes and electrolytes for Solid Oxide Fuel Cells (SOFCs) was studied. A variety of suspension (NiO, YSZ, Gd-doped ceria, LSM) and solution inks (Co nitrate) were optimised for inkjet printing of functional coatings and infiltration of electrodes' backbone structures. The printing parameters were studied in order to optimize the inks jetting and the uniformity of the inks delivery which allowed for precise thickness and infiltration depths control. Maximum power density of $\sim$0.220 W cm^{-2} was measured in H_2 at 800 °C on Ni-8YSZ/YSZ/LSM single cell 50 $\times$ 50 mm in size. Inkjet printed symmetrical LSM cathodes cells were inkjet infiltrated with Co nitrate inks and characterized by impedance spectroscopy in order to study the relation between the nano-decoration of the cathode scaffold and its electrochemical performance.

Keywords SOFC · Inkjet printing · Infiltration

1 Introduction

Solid Oxide Fuel Cells (SOFCs) facilitate direct electrochemical conversion of fuel into electricity and heat without efficiency limitations inherent to heat engines governed by the Carnot cycle. Depending on the design SOFCs can operate at

R.I. Tomov (✉) · C. Gao · S. Hopkins · R.V. Kumar · B.A. Glowacki
Department of Materials Science and Metallurgy, University of Cambridge, 27 Charles Babbage Road, Cambridge CB3 0FS UK
e-mail: rit21@cam.ac.uk

M. Krauz
Ceramic Department CEREL, Institute of Power Engineering, Warsaw, Poland

B.A. Glowacki
Department of Physics and Energy, University of Limerick, Plassey, Ireland

B.A. Glowacki
Institute of Power Engineering, Warsaw, Poland

A.Y. Oral and Z.B. Bahsi Oral (eds.), *3rd International Congress on Energy Efficiency and Energy Related Materials (ENEFM2015)*, Springer Proceedings in Energy, DOI 10.1007/978-3-319-45677-5_19

temperatures within the region of 550–1000 °C. The state-of-the-art commercial SOFCs are based on a combination of cermet anodes (e.g. Ni-YSZ) and ion-conducting ceramic electrolyte materials (e.g. yttria-stabilized zirconia (8YSZ) or Gd-doped ceria (GDC). Both materials offer the required chemical and thermal stability in oxidizing and reducing atmospheres and good oxygen ionic conductivity over a wide range of conditions [1, 2]. Ni-YSZ anodes are preferred due to the exemplary catalytical properties of Ni for hydrogen oxidation as well as their sufficient electrical conductivity, mechanical strength and good compatibility with common electrolytes [3]. Currently a shift towards intermediate temperatures (<700 °C) is considered essential for the commercialisation of SOFCs technology. The strategies for compensating the incurred drop in ionic conductivity include lowering the electrolyte resistance by implementing thinner electrolyte and reduction of the potential interfacial polarization losses through nano-engineering of the electrodes microstructure [4]. This study reports on the application of Direct Ceramic Inkjet Printing (DCIJP) for fabrication and manipulation of SOFC components—thin electrolytes and engineered porous electrodes. The DCIJP technique is simple and cost-effective non-contact "wet" technique applicable onto variety of surfaces which allows utilization of very thin fragile and/or non-even porous supports (ceramic or metal). It can reproducibly dispense droplets in the range of nL to pL volumes at high rates (kHz). Drop-on-demand DCIJP allows excellent thickness and uniformity control and introduces the possibility of printing 2D and 3D patterns as well as continuous coatings. Inkjet systems offers wide scale of application—from experimentation platforms working with customized inks, up to mass manufacturing systems that can print rapidly and competitively on industrial scale. The technology is cost effective and environmentally friendly through waste minimization of the expensive precursors. The production of anodes and electrolyte coatings with a modified Domino print head was reported previously by Tomov et al. [5, 6] using suspension inks. Wang et al. [7] deposited GDC electrolytes on NiO-8YSZ cermet anodes using sol–gel-based precursor solutions.

2 Experimental

The electrolyte depositions and the catalytic precursor infiltrations were performed by an electromagnetically (EM) driven print head (100 µm ruby nozzle orifice) using stable suspension (8YSZ, GDC, LSM) and sol-gel ($Co(NO_3)_2x6H_2O$) inks respectively. For the suspension inks commercial powders were mixed with alpha-Terpineol and binders, and ball milled with 3YSZ beads in 3YSZ bowls in a planetary mill. The sol-gel ink (1.0 M total metal concentration) was prepared by dissolving $Co(NO_3)_2x6H_2O$ and gelling agents in Ethanol. Jetting of both types of inks was optimized by drop visualization procedure in order to avoid satellite drops formation at practical Weber and Reynolds numbers. Anode supported cells were fabricated by printing electrolyte suspension ink onto pre-fired tape casted NiO-3YSZ anodes. After sintering at 1400 °C LSM cathodes were prepared by screen printing. Uniform electrolyte printing procedures involved repeated printing

of hexagonal lattices with different lattice constants at optimized jetting parameters. Cathode symmetrical cells were fabricated by inkjet infiltration of Co nitrate into GDC/LSM composite cathodes inkjet printed on each side of circular dense 8YSZ substrates. The infiltrations were performed at variable substrate temperature (25–50 °C) in order to investigate the influence of the ink viscosity variation on Co distribution. Each drop (40 nL, determined by drop visualisation) contained 0.69 μg of $Co(NO_3)_2x6H_2O$ and each layer of infiltration (resulting from the infiltration of 64 drops) contained 24 μg of Co_3O_4 nanoparticles.

3 Results and Discussions

3.1 Fabrication of Thin Electrolytes by Inkjet Printing

After choosing the optimum printing parameters, complete electrolyte coatings were printed on square NiO-YSZ ceramic supports using a hexagonal array of droplets printed in reciprocating raster pattern. The I-V tests of as-prepared cells were performed at 700, 750 and 800 °C using humidified hydrogen as a fuel (with different H_2: N_2 mixture ratios at constant flow rate of 200 ml/min) and static ambient air as the oxidant. The YSZ membranes (~5.7–5.9 μm thick as measured by SEM) were highly dense having good interfacial cohesion with the anode. The OCV value of 1.077 V measured at 800 °C confirmed the gas-tightness of the electrolyte and was consistent with the cross-section appearance (no open porosity (see Fig. 1)). The tests showed maximum power densities of ~220 mW/cm^2 achieved with pure humidified

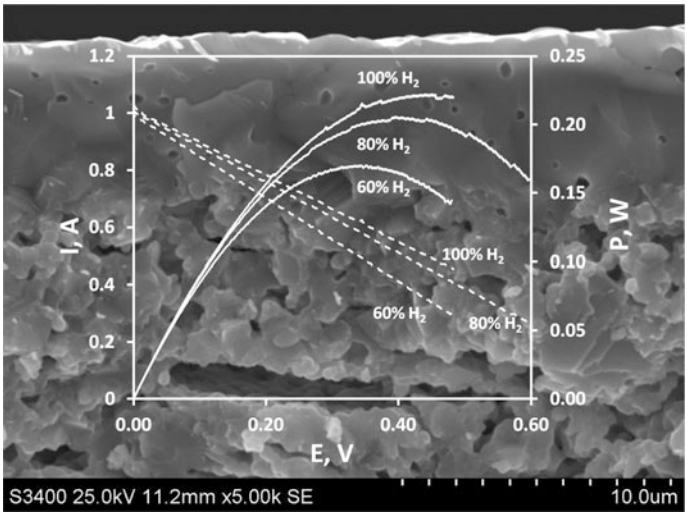

Fig. 1 SEM micrograph of the half cell cross-section sintered at 1400 °C and I–V results of the cell measured at 800 °C at different levels of fuel dilution with N_2

hydrogen stream. Diluting the fuel with N_2 led to gradual reduction of the maximum output power. The latter suggested the existence of a sharp interface between the free-standing electrolyte membrane and the anode without suspension ink infiltrating and blocking the porous gas channelling structure.

3.2 *Co_3O_4 Nano Decorated Cathode Symmetrical Cells*

The area-specific resistances (ASRs) of the infiltrated and non-infiltrated cathode symmetric cells were measured at 600 and 800 °C in static air (shown in Fig. 2a). A significant reduction of the activation polarization losses was observed as a direct result of Co nitrate ink infiltration. The differences in the measured ASR values suggest that at 600 °C the sample infiltrated at elevated temperature (50 °C) has lower losses. One can speculate that this is a result of a better coverage of the composite cathode scaffold with Co_3O_4 nanoparticles due to the lowered viscosity and the improved wetting of the ethanol-based Co nitrate ink. EDS line scans of Co as seen in Fig. 2b, c confirm the superior more uniform distribution of Co in the case

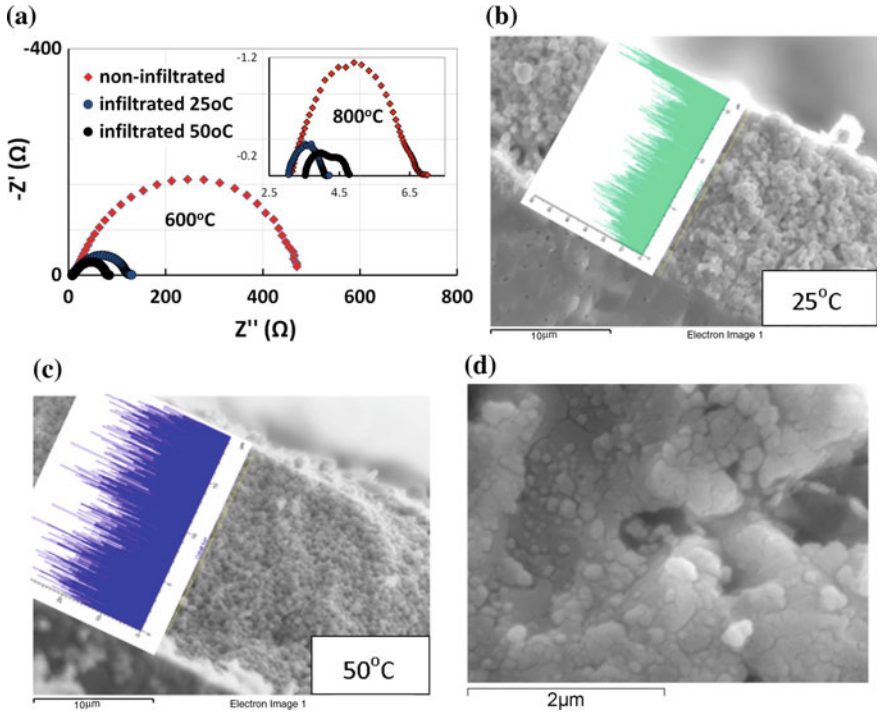

Fig. 2 (**a**) EIS spectra of LSM/GDC symmetrical cathode cells (non-infiltrated and infiltrated) at 25 and 50 °C sample temperatures. SEM cross-section micrographs and EDS scans of Co depth distribution for the samples infiltrated at 25 °C (**b**) and 50 °C (**c**); high resolution SEM of Co_3O_4 particles decorated LSM/GDC composite cathode scaffold (**d**)

of the infiltration done at 50 °C. A residue of non-infiltrated portion of the ink can be detected on the surface of the sample infiltrated at lower temperature (25 °C).

EIS data taken at 800 °C reveals the evidence of concentration losses appearing in the sample infiltrated at 50 °C most likely as a consequence of the effectively reduced porosity of the cathode (see inset in Fig. 2a). The Co_3O_4 particles sizes ranging between 50 and 100 nm were estimated by high resolution SEM (see Fig. 2d).

4 Conclusions

The results of this study proved the feasibility of DCIJP technology for fabrication of SOFC functional coatings. Gas-tight free standing electrolyte membranes as thin as ~6 μm were routinely produced by the inkjet printing having coherent interface with the anode porous structure. The employment of inkjet infiltration of Co-nitrate ink produced Co_3O_4 nano-decoration of the composite LSM/GDC cathode scaffolds which led to a substantial performance improvement achieved via precise control of the catalytic element depth distribution and minimum wastage of expensive precursors.

Acknowledgments The authors wish to acknowledge the EU 7th Framework Programme grants agreements 205854 (EFECTS) and 286100 (SENERES), as well as EPSRC grant "Tailoring of microstructural evolution in impregnated SOFC electrodes" for the financial support.

References

1. Weber, A., Ivers-Tiffee, E.: Materials and concepts for solid oxide fuel cells (SOFCs) in stationary and mobile applications. J. Power Sources **127**, 273–283 (2004). doi:10.1016/j.jpowsour.2003.09.024
2. Gibson, I.R., Dransfield, G.P., Irvine, J.T.S.: Influence of yttria concentration upon electrical properties and susceptibility to ageing of yttria-stabilised zirconias. J. Eur. Ceram. Soc. **18**, 661–667 (1998). doi:10.1016/S0955-2219(97)00173-8
3. Jiang, S.P., Chan, S.H.: A review of anode materials development in SOFC. J. Mater. Sci. **39**, 4405–4439 (2004). doi:10.1023/B:JMSC.0000034135.52164.6b
4. Ding, D., Li, X., Lai, S.Y., Gerdes, K., Liu, M.: Enhancing SOFC cathode performance by surface modification through infiltration. Energy Environ. Sci. **7**, 552–575 (2014). doi:10.1039/c3ee42926a
5. Tomov, R.I., Krauz, M., Jewulski, J., Hopkins, S.C., Kluczowski, J.R., Glowacka, D.M., Glowacki, B.A.: Direct ceramic inkjet printing of yttria-stabilized zirconia electrolyte layers for anode-supported solid oxide fuel cells. J. Power Sources **195**, 7160–7167 (2010). doi:10.1016/j.jpowsour.2010.05.044
6. Wang, C., Hopkins, S.C., Tomov, R.I., Kumar, R.V., Glowacki, B.A.: Optimisation of CGO suspensions for inkjet-printed SOFC electrolytes. J. Eur. Ceram. Soc. **32**, 2317–2324 (2012). doi:10.1016/j.jeurceramsoc.2012.03.001
7. Wang, C., Tomov, R.I., Kumar, R.V., Glowacki, B.A.: Inkjet printing of gadolinium-doped ceria electrolyte on NiO-YSZ substrates for solid oxide fuel cell applications. J. Mater. Sci. **46**, 6889–6896 (2011). doi:10.1007/s10853-011-5653-y

Modelling of the Bending Behaviour of a Double-Reinforced Beam from Recycled Materials for Application in NZEBs

Anguel Baltov, Ana Yanakieva and Gergana Nikolova

Abstract A number of design approaches of nearly zero energy buildings (NZEBs) are known in literature. The aim of the present paper is to study the bending behavior of a structural bi-material element of a recycled concrete beam reinforced along its lower and upper side by highly-tough thin layers. On one hand, the design of such a structural element would produce a light weight element, since no conventional reinforcement would be involved, and on the other hand, the recycled aggregate of the concrete matrix would make the element applicable to NZEBs. Thus, natural energy resources may be saved. Moreover, thin reinforcing layers guarantee good bearing capacity due to their high toughness, excellent crack resistance under dynamic impacts, as well as fire resistance when fabricated from special polymer materials. The approach of employing such lightweight structural bi-material elements in constructions is energy saving and innovative. The study provides a method of specifying the thickness of the reinforcing layer assuming the existence of a transition area between the two materials and smooth transition between the reinforcing layer and the concrete bulk. It is also assumed that the element operates within the materials linear-elastic zone, without generation of macrocracks within concrete and debonding along the interface. The analytical results found are verified by subsequent experimental evidence available in literature.

Keywords Thin reinforcing layers · Beam bending · Recycled concrete

A. Baltov · A. Yanakieva (✉) · G. Nikolova
Institute of Mechanics, Bulgarian Academy of Sciences, Sofia, Bulgaria
e-mail: aniyanakieva@imbm.bas.bg

A. Baltov
e-mail: anguelbaltov@gmail.com

G. Nikolova
e-mail: gery@imbm.bas.bg

A.Y. Oral and Z.B. Bahsi Oral (eds.), *3rd International Congress on Energy Efficiency and Energy Related Materials (ENEFM2015)*, Springer Proceedings in Energy, DOI 10.1007/978-3-319-45677-5_20

1 Introduction

Thin reinforcing layer are more and more frequently deposited on beams undergoing bending and fabricated form concrete, steel reinforced concrete, undergoing bending and fabricated form concrete, steel reinforced concrete, polymers, metals, wood etc. Respectively, the reinforcing layers are fabricated form special polymers, nanomaterials or other materials of high strength. The technology of layer deposition can be different. Such a treatment not only increases beam load bearing capacity but also provides various insulations and protections. Being an important aspect of building design, energy efficiency is an actual issue, while structures of combined elements of the above type (with reinforcing layers) meet its requirements. Layer deposition may strengthen beams from recycled concrete and lighten them, resulting in less material and energy consumption for their fabrication. Consequently, the application of deposition technologies of lower energy consumption could also be an energy saving option.

Consider a concrete beam with rectangular cross section (CS) with a reinforcement of thin highly strong layers deposited on the upper and lower beam surface. Assume that the maximal deflection of a test sample (a reinforced beam-RB) subjected to one of the loads (a), (b), (c), Fig. 1, can be experimentally measured. Let $w = w(x)$ be the current deflection, and the maximal deflection corresponding to those loads, while the span is l.

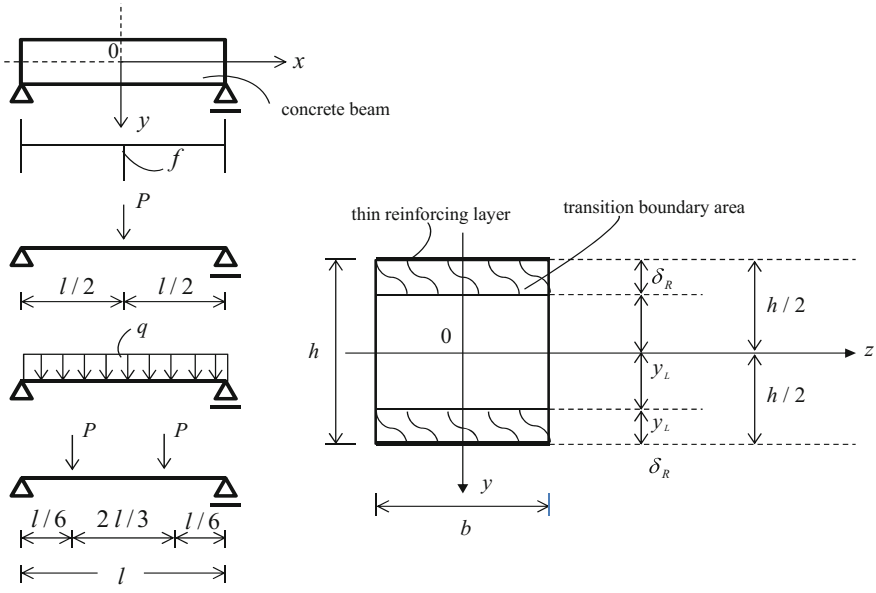

Fig. 1 Loading schemes. Cross section with reinforcing layers and transition areas

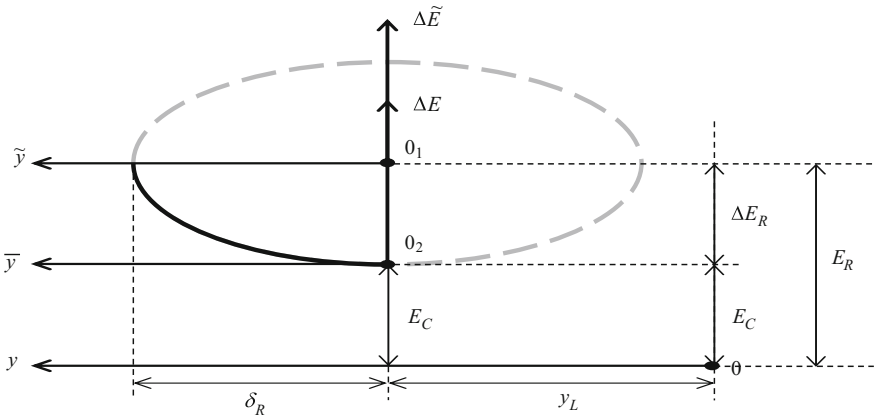

Fig. 2 Distribution of the elasticity modulus in the transition area

In recent papers [1, 2] we motivated the development of transition boundary layers in a beam when it deforms linearly-elastic and no macrocracks and debonding of the reinforcing layers emerge. An analogy with the boundary layer in hydrodynamics was made [3]. The beam was assumed to consist of two areas: main concrete core for $y \in [0, y_L]$ and a transition boundary layer $y \in [y_L, h/2]$ with thickness $\delta_R = (h/2) - y_L$. We designed a model where the concrete core undergoes bending and the cross sections are kept planar under deformation, while the boundary layer is characterized with smooth transition of stresses, strains (with deplanation) and variation of the E modulus. We assumed that the E modulus varies smoothly, from the concrete modulus E_C to that of the thin boundary layer E_R. That form of transition is technologically motivated (accounting for the partial penetration of the reinforcing compound into concrete). Thus, an appropriate analytical model was designed. We assume here that the approximating smooth transition is not parabolic, as a first approximation, but follows a section of an ellipse (Fig. 2). Thus, transition becomes smoother.

2 Smooth Transition of the Elastic Modulus in the Transition Boundary Layer

The smooth transition is based on the assumption that the beam deformation is purely elastic, without development of macrocracks and debonding. The larger E modulus in the transition area can be explained by change of the deformation at the beam boundary where a highly tough coating has been deposited. We assume approximation of the smooth transition using a quarter of an ellipse (Fig. 2). The ellipse equation in the coordinate system $(O_2, \Delta E, \bar{y})$ is

$$(\bar{y}/\delta_R)^2 + ((\Delta E - \Delta E_R)/\Delta E_R)^2 = 1,\ \Delta E = E - E_C,\ \Delta E_R = E_R - E_C$$
$$E = E_R - \Delta E_R\sqrt{1-\eta^2},\ \eta = \frac{\bar{y}}{\delta_R},\ \eta \in [0,\ 1],\ \bar{y} = y - y_L \tag{1}$$

3 Determination of the Stiffness of the Combined Beam

By definition, the beam stiffness reads:

$$K_f = 2b\int_0^{h/2} E(y)\,.\,y^2 dy \tag{2}$$

$E(y)$ is the modulus distribution in the CS, conforming to Sect. 2, for $y \in [0,\ y_L]$, $E(y) \equiv E_C = const$; for $y \in [y_L,\ h/2]$, $E = E_R - \Delta E_R\sqrt{1-\eta^2}$.

Present the stiffness as a sum of two integrals:

$$1/2K_f = K_L + K_R,\ K_L = bE_C/\left(h/2 - \delta_R\right)^3 .0.333$$
$$K_R = b\int_0^1 \left[E_R - \Delta E_R\sqrt{1-\eta^2}\right](y_L + \delta_R\eta)^2\delta_R d\eta \tag{3}$$

Performing the subsequent transformations, we obtain:

$$\sum_{i=0}^{3}\Lambda_i\delta_R^i = 0,\quad \begin{array}{l}\Lambda_0 = (h^3/24) - \left(K_f/2bE_C\right),\ \Lambda_1 = 0.059h^2\left(E_R/E_C - 1\right)\\ \Lambda_2 = -0.048h(E_R/E_C - 1),\ \Lambda_3 = 0.018(E_R/E_C - 1)\end{array} \tag{4}$$

while K_f of the statically determined simple beam is found using scheme (b), $K_f = ql^4/48f$. Where f is experimental value for specific q. K_f is calculated according to Eq. (3) is constant, and it characterizes the respective beam undergoing bending, having assumed a specific distribution of the elasticity modulus in the transition boundary layer and having calculated its δ_R.

4 Deplanation of the CS in the Transition Boundary Layer

We assume a parabolic approximation of the deplanation of the CS, [1, 2]. According to the assumed model of planar sections of the concrete core we find: For $y \in [0,\ y_L]$: $\varepsilon(x,\ y) = \chi(x)\,y$, where $\chi = w''(x)$ is the curvature of the elastic axis and $w = w(x)$ is beam deflection. For $y \in [y_L,\ h/2]$:

$\varepsilon(x,y) = a_0(x) + a_1(x)y - a_2(x)y^2$, where $a_i(x)(i = 0,1,2) \geq 0$ are constants found from the condition: For $y = y_L, \varepsilon(y_L) = \chi \,.\, y_L = \varepsilon_L, \frac{\partial \varepsilon}{\partial y} = \chi$. For $y = h/2$, $\varepsilon(h/2) = \varepsilon_R$ while $\varepsilon_R < \varepsilon_H = \chi h/2$, $\Delta\varepsilon_R = \varepsilon_R - \varepsilon_L$. Thus, we find a_0, a_1, a_2: For $y \in [y_L, h/2]$ can be written using also the non-dimensional variable $\eta \in [0,1]$: $\varepsilon(x,\eta) = \sum_{i=0}^{2} \bar{a}_i \,.\, \eta^i - \Delta\varepsilon_R \,.\, \eta^2$, $\bar{a}_0 = \varepsilon_L$, $\bar{a}_1 = \chi\delta_R$, $\bar{a}_2 = \Delta\varepsilon_R - \chi\delta_R$.

Knowing δ_R from the previous solution of Eq. (4), the unknown quantity remains ε_R. To find it, we use the equilibrium condition for equalization of the external and internal moments due to stresses normal to the cross section.

5 Determination of the Normal Stresses in the CS of the RB

Consider beam operation in real conditions and deformation of the reinforced complex beam as a linearly elastic body consisting of a concrete core and a transition boundary layer. According to Hooke's law:

$$\begin{gathered} \sigma(x,y) = E(y)\varepsilon(x,y), y \in [0,y_L], \sigma(x,y) = E_C\chi(x)y \\ y \in [y_L, h/2], \eta \in [0,1], \sigma = \Delta E_R \Psi(\eta) \sum_{i=0}^{2} \bar{a}_i(x)\eta^i \end{gathered} \tag{5}$$

$$\begin{gathered} \sigma = \sigma_1 + \Delta\varepsilon_R\sigma_2, \ \sigma_1 = (E_C + \Delta E_R\Psi(\eta))\left(\sum_{i=0}^{2} \bar{a}_i'\eta^i\right), \\ \sigma_2 = (E_C + \Delta E_R\Psi(\eta))\,\eta^2, \ \bar{a}_0' = \varepsilon_L, \bar{a}_1' = \chi\delta_R, \ \bar{a}_2' = \Delta\varepsilon_R - \chi\delta_R \end{gathered} \tag{6}$$

6 Determination of the Edge Deformation by Equalization of the Internal and External Moments

By definition, $M(x)$ is counterbalanced by the internal moment generated by the normal stresses. We equalize the internal and external moments

$$M(x) = M_1(x) + M_2(x), \ x \in [0, l/2] \tag{7}$$

$$M_1(x) = 2b\int_0^{y_L} \sigma(x,y)ydy = \frac{2}{3}bE_C\chi(x)y_L^3$$

$$M_2(x) = 2b\int_{y_L}^{h/2} \sigma(x,y)ydy = 2b\int_0^1 \sigma(x,\eta)(y_L + \delta_R\eta)\delta_R d\eta$$

In view of the further determination of $\varepsilon_R(x)$, we present M_2 in the form:

$$M_2 = M_2' + \Delta\varepsilon_R M_2'' \tag{8}$$

$$M_2' = 2bE_C y_L(\varepsilon_L + 1/6\chi\delta_R) + 2bE_C\delta_R(0.167\varepsilon_L + 0.004\chi\delta_R)$$
$$M_2'' = 2/3bE_C + 1/2bE_C\delta_R + 0.274b\Delta E_R y_L + 0.266b\Delta E_R\delta_R$$

We find ε_R from the following expressions:

$$\Delta\varepsilon_R(x) = L(x)/M_2''(x),\ L(x) = M(x) - M_1(x) - M_2'(x) \tag{9}$$

Thus, we find the edge deformation in a double reinforced beam undergoing bending. If we find ε_R experimentally, the above expression provides a verification of the proposed numerical model.

7 Numerical Example. Parametric Analysis

We use the theoretical results to analyze an example presented in [4]. The example treats a simple CB with span $l = 5.63$ m loaded by a distributed load q. Its CS is rectangular ($b = 0.305$ m, $h = 0.768$ m) with E_C. The beam is reinforced by a polymer composite with $E_R = 13.1 \times 10^{10}$ N/m^2. The δ_R of the transition layer is found according to the proposed model. The calculations are performed, assuming different variants (I, II, III) of the E_C and q/f: $E_C = (1.7;\ 1.4;\ 2.2) \times 10^{10}$ N/m^2, and $q/f = (0.2;\ 0.15;\ 0.1) \times 10^8$ N/m. The results are shown in Fig. 3. We find the thickness of the area of deplanation of the beam CS for combination I-1. Input data: $x = l/4 = 1.41$ m, $q/f = 0.2 \times 10^8$ N/m^2, $q = 0.2 \times 10^6$ N/m, $\delta_R = 0.08$ m, $y_L = 0.304$ m, $\chi(l/4) \approx 0.034 \times 10^{-3}[\text{m}^{-1}]$.

$\varepsilon_H(l/4) = 1.165 \times 10^{-3}$, $\varepsilon_L(l/4) = 0.922 \times 10^{-3}$, $\Delta\varepsilon_R = -0.364 \times 10^{-3}$, $\varepsilon_R = 0.558 \times 10^{-3}$. The results are shown in Fig. 4. The numerical results found show the possibility to adopt model with transition areas and cross section deplanation.

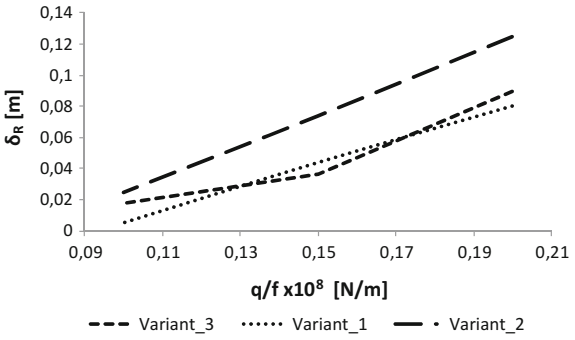

Fig. 3 Variation of the thickness of the transition area for different combinations

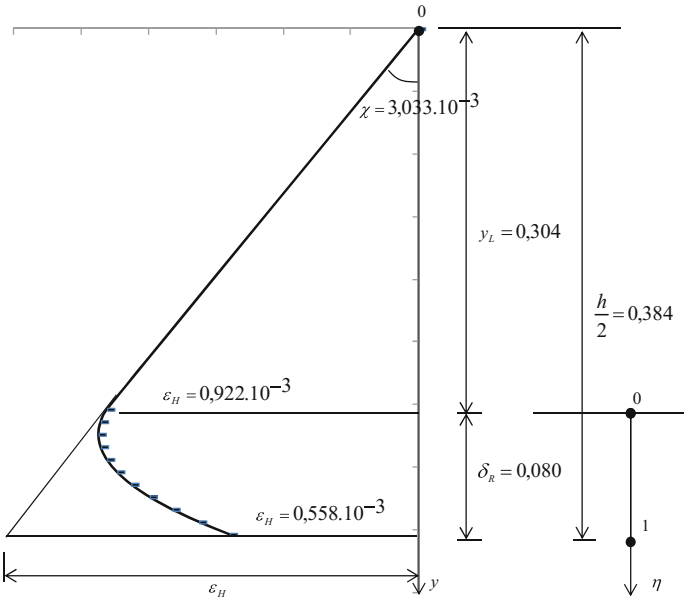

Fig. 4 CS deplanation for numerical example, combination I-1

8 Conclusion

The designed model, although approximate, provides a good description of the operation of double reinforced concrete beams assuming the formation of transition areas. The numerical example illustrates the model plausibility. A theory of bending of complex reinforced beam systems may be developed on such basis, and the problems can be solved using the FEM. Thus, reinforcement of recycled concrete may be performed which may have an essential impact on the energy saving as an important issue of building design.

References

1. Baltov, A., Yanakieva, A.: Bending of CBs reinforced via thin layers. In: Proceedings of the XV International Science Conference, VSU, Sofia, 4–5 June 2015
2. Baltov, A., Yanakieva, A.: Local deplanation of the CS of a double reinforced beam under bending. J. Theor. Appl. Mech. **45**(4) (2015). doi:10.1515/jtam-2015-0022
3. Emmanuil, G.S., Moritz, B. (eds.): Hydromechanics: theory and fundamentals. Wiley-VCH, Hoboken (2011)
4. Dinev, D.: Investigation of constructions under bending. Reinforced composite materials, Bulgarian. Ph.D. thesis, University of Architecture, Civil Engineering and Geodesy, Sofia (2006)

Tuning of Dielectric Parameters of $(CNT_S)_X$/Cutl-1223 Nanotubes-Superconductor Composites

M. Mumtaz and Zahir Usman

Abstract Carbon nanotubes (CNTs) and $(CuTl)_{0.5}Ba_2Ca_2Cu_3O_{10-\delta}$ (CuTl-1223) superconducting phase were mixed in appropriate ratios to obtain $(CNTs)_x$/CuTl-1223 ($0 \leq x \leq 2.00$ wt%) nanotubes-superconductor composites. Crystal structure and chemistry of CuTl-1223 phase were not affected significantly but superconducting properties were suppressed after inclusion of CNTs. The decrease in dielectric parameters can be attributed to reduction of polarization due to semiconducting nature of CNTs in these composites. Positive space charges around the electrodes may be the possible cause of negative capacitance (NC) in these composites. The dielectric parameters of these composites can be tuned by the frequency, operating temperature and CNTs content in these composites.

Keywords $(CNTs)_x$/CuTl-1223 nanotubes-superconductor composites · Structural properties · Superconducting properties · Dielectric properties

1 Introduction

CuTl-1223 is one of the most promising phase of $(CuTl)_{0.5}Ba_2Ca_{n-1}Cu_nO_{2n+4-\delta}$ (n = 2, 3, 4,…) homologous superconducting series due to its highest values of superconducting parameters [1, 2]. Different strategies have been made to minimize the inter-grain voids, micro-cracks and pores to further improve the performance of bulk CuTl-1223 high temperature superconductor (HTSCs) [3–5]. One of the easiest, effective and suitable techniques is the inclusion of nanostructures in bulk HTSCs to address this issue [6, 7]. We added CNTs in bulk CuTl-1223 superconductor by adopting this technique. The charge reservoir layer, inter-grain boundaries and micro-cracks may act as dielectric media, which can be polarized by the displacement of charge carriers with the assistance of an external electric

M. Mumtaz (✉) · Z. Usman
Materials Research Laboratory, Department of Physics FBAS,
International Islamic University (IIU), Islamabad 44000, Pakistan
e-mail: mmumtaz75@yahoo.com

A.Y. Oral and Z.B. Bahsi Oral (eds.), *3rd International Congress on Energy Efficiency and Energy Related Materials (ENEFM2015)*, Springer Proceedings in Energy, DOI 10.1007/978-3-319-45677-5_21

ac-field from their equilibrium position. The materials may undergo four primary polarizations (i.e. lattice polarization, electronic polarization, dipolar polarization, and polarization at interfaces) [8, 9]. The dielectric properties of layered $Tl_2Ba_2Ca_1Cu_2O_x$ and $Tl_2Ba_2Ca_2Cu_3O_x$ superconductors were investigated in frequency range of 10 kHz to 10 MHz at different operating temperatures from 92 to 287 K [10]. They observed NC, which was referred to the fact that current lags behind the agitation voltage. It was observed that dielectric parameters strongly depend upon the test frequencies and operating temperatures. We have explored temperature and frequency dependent dielectric properties of $(CNTs)_x$/CuTl-1223 ($0 \leq x \leq 2.00$ wt%) nanotubes-superconductor composites. Dielectric parameters {i.e. real part (ε_r') and imaginary part (ε_r'') of dielectric constant, and ac-conductivity (σ_{ac})} have been calculated with in 10 kHz to 10 MHz frequency at different operating temperatures from 92 to 287 K. Conduction process of electronic equipments and devices intensely depend on impurity concentration, frequency, operating temperature, fabrication conditions, and surface charges. Therefore, it is very important to study the dielectric properties of HTSCs over the wide range of operating temperature and frequency. The materials having giant dielectric constants are useful for capacitors and memory storage appliances [11]. The conductance, capacitance, dielectric constant and ac-conductivity are the major constraints for the choice of dielectrics for electronic appliances [12].

2 Samples Synthesis and Characterization Techniques

$(CNTs)_x/Cu_{0.5}Tl_{0.5}Ba_2Ca_2Cu_3O_{10-\delta}$ ($0 \leq x \leq 2.00$ wt%) nanotubes-superconductor composites were prepared by solid-state reaction method [13]. The samples were characterized by different experimental techniques, but in this article we have reported dc-resistivity measurements and dielectric measurements.

3 Results and Discussion

The crystal structure and phase purity of $(CNTs)_x$/CuTl-1223 ($0 \leq x \leq 2.00$ wt%) were determined by X-ray diffraction (XRD) [14]. No major change in cell parameters was noticed after addition of CNTs in CuTl-1223 matrix. The stresses and strains within the material can slightly vary the unit cell parameters and shift the diffraction peaks towards greater angles after addition of CNTs in CuTl-1223 phase. The morphology of $(CNTs)_x$/CuTl-1223 ($x = 0$ and 2.00 wt%) nanotubes-superconductor composites was examined by scanning electron microscopy (SEM) [14]. The improvement in inter-grains connections after the inclusion of CNTs was observed. The activation energy of reaction may help small sized grains to fuse together and grow in larger sizes after CNTs addition in the host CuTl-1223 matrix [13].

Temperature dependent dc-resistivity of $(CNTs)_x$/CuTl-1223 ($0 \leq x \leq 2.00$ wt%) nanotubes-superconductor composites is given in the Fig. 1. Metallic behavior has been seen in dc-resistivity of all the samples till the T_c^{onset} (K) temperature. Normal state room temperature dc-resistivity of pure CuTl-1223 phase is 3.7×10^{-4} Ω-m and for $(CNTs)_x$/CuTl-1223 with x = 2.0 wt% is 5.3×10^{-4} Ω-m.

So the normal state resistivity has been increased after addition of CNTs in CuTl-1223 matrix. This increase is attributed to the enhanced scattering cross-section of carriers and suppression of carrier's density due to reduced superconducting volume fraction after addition of CNTs. The values of T_c (0) for $(CNTs)_x$/CuTl-1223 composites are around 90 and 77 K for x = 0 and 2.00 wt%, respectively.

The energy stored inside the sample is determined from the real part (ε_r') of dielectric constant when external electric field is applied, which can be calculated by the following relation,

$$\varepsilon_r' = \frac{CD}{A\varepsilon_o} \tag{1}$$

Here 'C' is capacitance, 'D' is thickness and 'ε_o' is permittivity of free space [15]. The variation of ε_r' for various concentrations of CNTs (i.e. x = 0, 0.25, 0.50, and 2.00 wt%) in $(CNTs)_x$/CuTl-1223 composites is given in Fig. 2a–d.

The maximum value of ε_r' varies from −494 to −427, −558.9 to −378.4, −293.6 to −29.66, and −331.9 to −29.66 for $(CNTs)_x$/CuTl-1223 composites with x = 0, 0.25, 0.50 and 2.00 wt% at different operating temperatures from 92 K to 287 K, respectively. The decrease in polarization with increasing CNTs content gradually decreases ε_r', which is not influenced at greater values of frequencies due to less polarization effects [15]. Negative value of ε_r' is due to reduction in

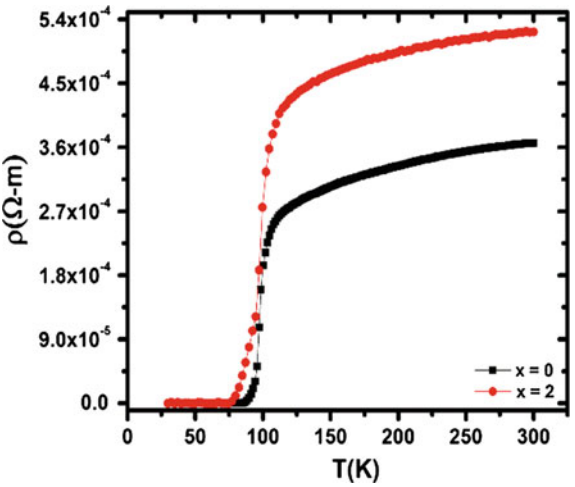

Fig. 1 Resistivity versus temperature measurements of $(CNTs)_x$/CuTl-1223 nanotubes-superconductor composites with x = 0 and x = 2.00 wt%

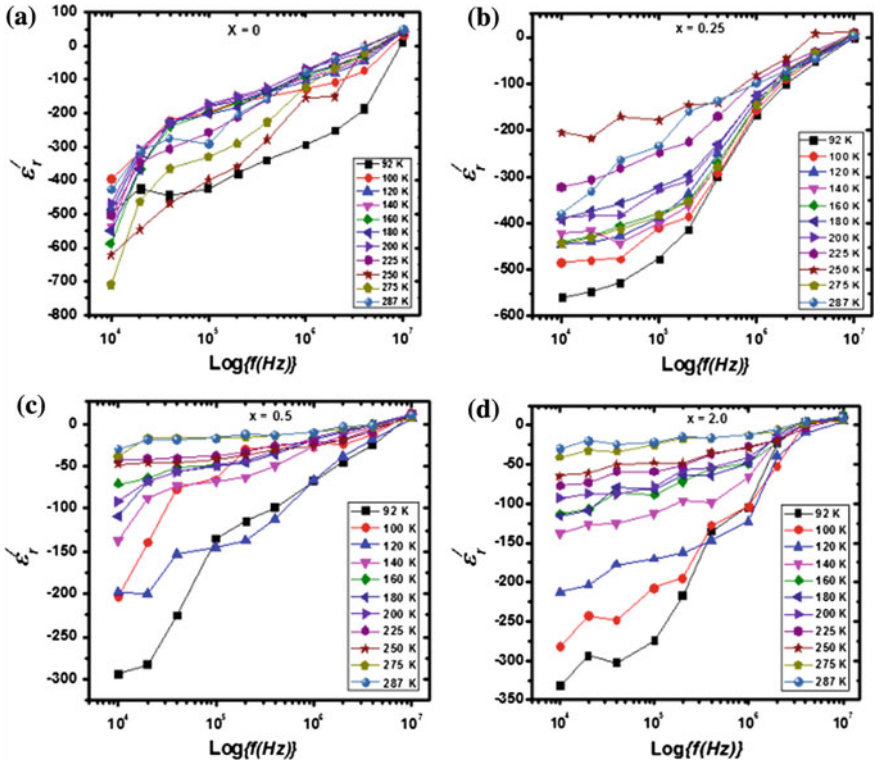

Fig. 2 **a–d** Real part of dielectric constant (ε_r') versus Log{f(Hz)} of $(CNTs)_x$/CuTl-1223 nanotubes-superconductor composites with **a** x = 0, **b** x = 0.25 wt%, **c** x = 0.50 wt%, **d** x = 2.00 wt%

capacitance of the sample as compared to its geometric capacitance without sample, which may be due to positive space charge effects around the electrodes [16, 17].

The imaginary part (ε_r'' of dielectric constant gives information about the energy dissipation inside the material with external applied electric ac-field [18], which can be determined by relation;

$$\varepsilon_r'' = \frac{GD}{\omega A \varepsilon_o} \tag{2}$$

where 'G' is the conductance. Dielectric response of $(CNTs)_x$/CuTl-1223 composites can be understood with the help of Maxwell-Wagner model and Koop's theory [19]. The variation of ε_r'' as a function of frequency at various operating temperatures from 92 to 287 K is given in Fig. 3a–d.

The values of ε_r'' are maximum at lower frequencies and lower operating temperatures [20, 21]. The maximum value of ε_r'' varies from 1.34×10^9 to 7.18×10^8, 9.06×10^8 to 7.61×10^8, 2.8×10^8 to 1.28×10^8 and 1.78×10^6 to 7.2×10^5

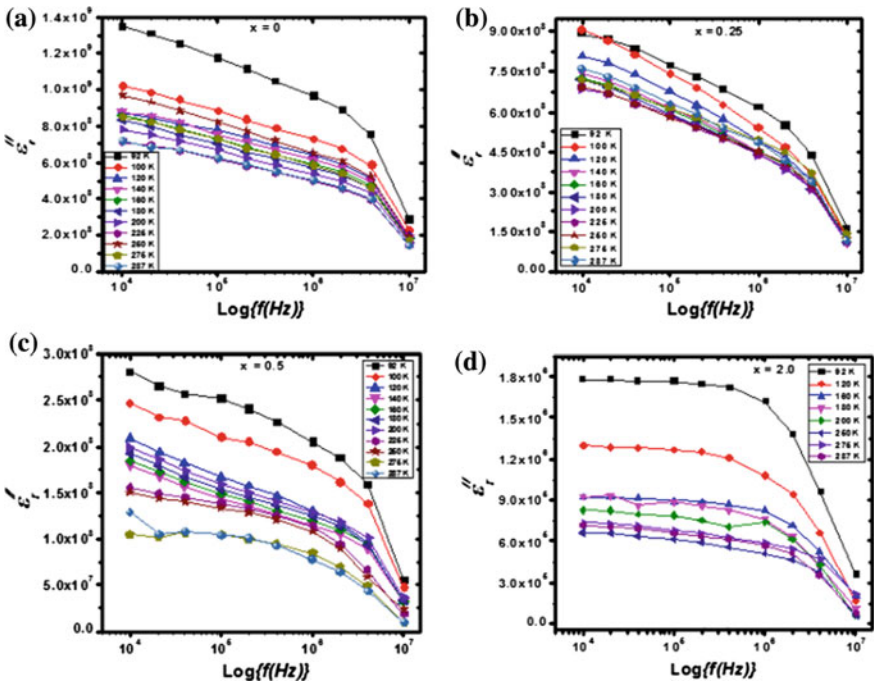

Fig. 3 **a–d** Imaginary part of dielectric constant (ε_r'') versus Log{f(Hz)} of $(CNTs)_x$/CuTl-1223 nanotubes-superconductor composites with r **a** x = 0, **b** x = 0.25 wt%, **c** x = 0.5 wt%, **d** x = 2.0 wt%

for $(CNTs)_x$/CuTl-1223 composites with x = 0, 0.25, 0.50 and 2.00 wt% at 10 kHz. The overall energy loss is reduced with the increase in wt% of CNTs in $(CNTs)_x$/CuTl-1223 composites, which can be attributed to semiconducting nature of CNTs. The presence of CNTs at crystallite-boundaries decreases the polarization and assists the charge carrier's movement in bulk CuTl-1223 superconducting matrix. The reduction in accumulation of charge carriers at crystallite-boundaries reduces interfacial polarization, which ultimately affect the dielectric parameters.

Ac-conductivity (σ_{ac}) for $(CNTs)_x$/CuTl-1223 nanotubes-superconductor composites as a function of frequency at different values of operating temperatures is shown in Fig. 4a–d. The maximum values of σ_{ac} at 10 kHz vary from 0.328 to 0.173, 0.221 to 0.209, 0.062 to 0.035, 0.022 to 0.012 for $(CNTs)_x$/CuTl-1223 composites with x = 0, 0.25, 0.50 and 2.00 wt% at various operating temperatures from 92 to 287 K, respectively. The maximum values of σ_{ac} have been reduced with greater wt% addition of CNTs in $(CNTs)_x$/CuTl-1223 composites. At higher frequencies, σ_{ac} becomes approximately independent for all samples but at lower frequencies, it highly depends on operating temperature values.

The regular increase in σ_{ac} with reducing operating temperatures illustrates lower scattering cross-section of moving charge carriers around T_c (0) [8]. The

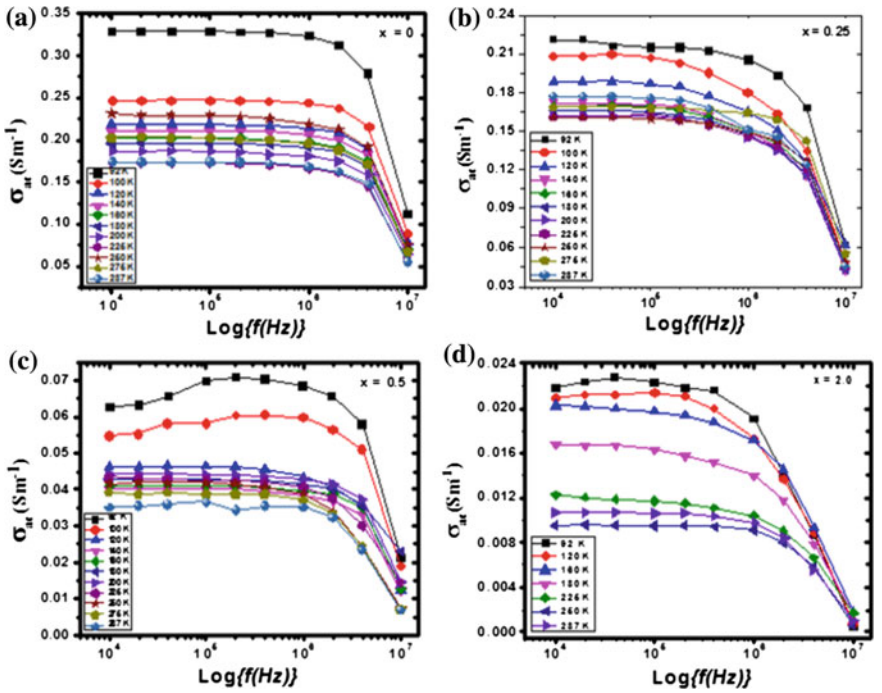

Fig. 4 **a–d** The ac-conductivity (σ_{ac}) versus Log{f(Hz)} of (CNTs)x/CuTl-1223 nanotubes-superconductor composites with **a** x = 0, **b** x = 0.25 wt%, **c** x = 0.5 wt%, **d** x = 2.0 wt%

semiconducting nature of CNTs plays an important role in reducing σ_{ac} because of reduced carrier's density at lower operating temperature values.

4 Conclusion

$(CNTs)_x$/CuTl-1223 ($0 \leq x \leq 2.00$ wt%) nanotubes-superconductor composites were synthesized by solid-state reaction technique. The dispersion of CNTs has not altered the crystal structure of host CuTl-1223 phase. The morphology of $(CNTs)_x$/CuTl-1223 composites revealed improvement in inter-grains weak-links after CNTs addition. The fusion of small sized grains with each other by the activation energy of reaction improves the grains size as well as inter-grains connectivity. CNTs addition in CuTl-1223 matrix reduced the superconducting properties due to reduction of superconducting volume fraction and trapping of charge carriers. Dielectric properties were reduced with increasing wt% of CNTs, which can be due to reduced polarization and carriers density associated with semiconducting nature of CNTs. Therefore, dielectric response of CuTl-1223 matrix can be tuned by varying the frequency, operating temperatures and CNTs content.

References

1. Yamamoto, H., Tokiwa, K., Hirabayash, H. i, Tokumoto, M., Khan, N.A., Ihara, H.: Synthesis of $Cu_{1-x}Tl_xBa_2Ca_2Cu_3O_{11-y}$ (x ∼ 0.7) superconductor by hot press. Physica C 302, 137 (1998). doi:10.1016/S0921-4534(98)00192-0
2. Tanaka, K., Iyo, A., Terada, N., Tokiw, K. a, Miyashita, S., Tanaka, Y., Tsukamoto, T., Agarwal, K. S., Watanabe, T., Ihara H.: Tl valence change and T_c enhancement (>130 K) in (Cu,Tl)$Ba_2Ca_2Cu_3O$ due to nitrogen annealing. Phys. Rev. B 63, 064508 (2001). doi:http://dx.doi.org/10.1103/PhysRevB.63.064508
3. Ihara, H.: How to achieve the best performance superconductor based on Cu-1234. Physica C **364**, 289 (2009). doi:10.1016/S0921-4534(01)00774-2
4. Khan, N.A., Mumtaz, M.: Absence of a pair-breaking mechanism in $Cu_{0.5}Tl_{0.5}Ba_2Ca_3Cu_{4-y}Zn_yO_{12-\delta}$. Phys. Rev. B **77**, 054507 (2008). doi:10.1103/PhysRevB.77.054507
5. Mumtaz, M., Khurram, A.A.: Inter-grain connectivity in $(Cu_{0.5}Tl_{0.5-x}Hg_x)Ba_2Ca_3Cu_4O_{12-\delta}$ superconductor. J. Alloys Compd. **463**, 591 (2008). doi:10.1016/j.jallcom.2008.03.126
6. Jabbar, A., Qasim, I., Mumtaz, M., Zubair, M., Nadeem, K., Khurram, A.A.: Suppression of activation energy and superconductivity by the addition of Al_2O_3 nanoparticles in CuTl-1223 matrix. J. Appl. Phys. **115**, 203904 (2014). doi:10.1063/1.4879197
7. Jabbar, A., Qasim, I., Khan, M.K., Ali, Z., Nadeem, K., Mumtaz, M.: Synthesis and superconducting properties of $(Au)_x$/CuTl-1223 composites. J. Alloys Compd. **618**, 110 (2015). doi:10.1016/j.jallcom.2014.08.162
8. Mumtaz, M., Kamran, M., Nadeem, K., Jabbar, A., Khan, N.A., Saleem, A., Tajammul Hussain, S., Kamran, M.: Dielectric properties of $(CuO,CaO_2$, and $BaO)_y$ /CuTl-1223 composites. J. Low Temp. Phys. 39, 806 (2013). http://dx.doi.org/10.1063/1.4813737
9. Mumtaz, M., Khan, N.A.: Dielectric response of $Cu_{0.5}Tl_{0.5}Ba_2(Ca_{2-y}Mg_y)(Cu_{0.5}Zn_{2.5})O_{10-\delta}$ bulk superconductor to frequency and temperature. Physica C **469**, 182 (2009). doi:10.1016/j.physc.2009.01.010
10. Cavadar, S., Koralay, H., Tugluglu, N., Gunen, A.: Frequency-dependent dielectric characteristics of Tl–Ba–Ca–Cu–O bulk superconductor. Supercond. Sci. Technol. **18**, 1204 (2005). doi:10.1088/0953-2048/18/9/010
11. Li, L., Richter, C., Paetel, S., Kopp, T., Mannhart, J., Ashoori, C.R.: Very large capacitance enhancement in a two-dimensional electron system. Science **332**, 825 (2011). doi:10.1126/science.1204168
12. Afandiyeva, M.I., Dökme, I., Alt1ndal Bülbül, M.M., Tatarolu, A.: Frequency and voltage effects on the dielectric properties and electrical conductivity of Al–TiW–Pd_2Si/n-Si structures. Microelectron. Eng. **85**, 247 (2008). doi:10.1016/j.mee.2007.05.044
13. Khan, N.A., Aziz, S.: Single and multi-walled carbon nanotubes doped $(Cu_{0.5}Tl_{0.5})Ba_2Ca_2Cu_3O_{10-\delta}$ superconductors. J. Alloys Compound. **538**, 183 (2012). doi:10.1016/j.jallcom.2012.05.074
14. Mumtaz, M., Hussain, G., Rabbani, W.M., Waqee-ur-Rehman, M., Qasim, I., Jabbar, A., Khan, N.A.: Infield superconductivity of carbon nanotubes-$Cu_{0.5}Tl_{0.5}Ba_2Ca_2Cu_3O_{10-\delta}$ superconductor composites. AIP Adv. **5**, 107148 (2015). doi:10.1063/1.4935191
15. Vijaya, S.M., Rangarajan, G.: Materials Science, 1st edn. Tata McGraw-Hill Publ. Comp. Ltd., New Delhi, India (2004)
16. Mumtaz, M., Khan, N.A., Khan, S.: Study of delectric properties of oxygen-postannealed $Cu_{0.5}Tl_{0.5}Ba_2Ca_2(Cu_{3-y}M_y)O_{10-\delta}$ Superconductor. IEEE Tran. Appl. Supercond. **23**, 2 (2013). doi:10.1109/TASC.2013.2245505
17. Younis, A., Khan, N.A.: Dielectric properties of $Cu_{0.5}Tl_{0.5}Ba_2Ca_3Cu_{4-y}Zn_yO_{12-\delta}$ (y = 0, 3) superconductors. J. Korean Phys. Soc. **57,** 1437 (2010). DOI:10.3938/jkps.57.1437
18. Nadeem, K., Ali, L., Gul, I., Rizwan, S., Mumtaz, M.: Effect of silica coating on the structural, dielectric, and magnetic properties of maghemite nanoparticles. J. Non Cryst. Solid. **404**, 72 (2014). doi:10.1016/j.jnoncrysol.2014.07.036

19. Cohen, E.R.: Theory of ferroelectrics: a vision for the next decade and beyond. J. Phys. Chem. Solids **61**, 139 (2000). doi:10.1016/S0022-3697(99)00272-3
20. Kleemann, W., Dec, J., Wang, G.Y., Lehnen, P., Prosandeev, A.S.: Phase transitions and relaxor properties of doped quantum paraelectrics. J. Phys. Chem. Solid. **61**, 167 (2000). doi:10.1016/S0022-3697(99)00278-4
21. Ershov, M., Liu, C.H., Li, L., Buchanan, M., Wasileweki, R.Z., Ryzhii, V.: Unusual capacitance behavior of quantum well infrared photodetectors Appl. Phys. Lett. **70**, 1828 (1997). http://dx.doi.org/10.1063/1.118704

Modeling of a Heat Pipe for Using in Thermoelectric Energy Harvesting Systems

Marco Nesarajah and Georg Frey

Abstract Thermoelectric energy harvesting systems (EHS) consist of thermoelectric generators (TEG), which generate electrical power due to a temperature difference. Consequently, a main challenge to build up such an EHS is a good heat transfer to and from the TEG. On the one hand heat has to be send to the hot TEG side and on the other hand the waste heat from the cold TEG side has to be dissipated. For this heat transfer heat pipes are very reasonable. They have a 1000-fold better thermal conductivity than copper and so the existing heat quantity can be used more effectively. To model a heat pipe in a most general way, the modeling language Modelica® is used. Thereby, the model can be build based on its physics as well as its material properties. The dimensions of the pipe as well as the used working fluid or the used heat pipe material are parameters adjustable for specific cases. In this contribution, the theoretical aspects of a heat pipe will be described and the modeling with Modelica® for different modeling approaches in the simulation environment Dymola® will be shown. Finally, the model of the heat pipe will be validated with laboratory measurements.

Keywords Energy harvesting · Heat pipe · Modelica® · Modeling

1 Introduction

Energy harvesting systems (EHS) convert ambient energy, for instance solar, wind, thermal, magnetic, or kinetic energy into electrical energy. In the case of thermoelectric EHS, thermoelectric generators (TEG) are used to produce electrical energy from heat sources [1, 2]. TEGs are small devices, consisting of a multiplicity of

M. Nesarajah (✉) · G. Frey
Chair of Automation and Energy Systems, Saarland University,
66123 Saarbrücken, Germany
e-mail: marco.nesarajah@aut.uni-saarland.de

G. Frey
e-mail: georg.frey@aut.uni-saarland.de

A.Y. Oral and Z.B. Bahsi Oral (eds.), *3rd International Congress on Energy Efficiency and Energy Related Materials (ENEFM2015)*, Springer Proceedings in Energy, DOI 10.1007/978-3-319-45677-5_22

thermoelectric legs, which are connected electrically in series and thermally in parallel. A part of the heat flowing through the TEG is converted into electrical energy, based on the Seebeck effect. A main challenge to increase the energy yield is the maintenance of a high temperature difference between the two TEG surfaces. It is therefore important to transfer as much heat as possible to the hot TEG side and to dissipate the heat on the cold TEG side. For this purpose, heat pipes are very suitable. They have a 1000-fold better thermal conductivity than copper [3] and so the existing heat quantity can be used more effectively. Moreover, they are closed systems, so they do not need maintenance. The first heat pipe was presented by Gaugler in 1942 [4]. Nowadays, they are used in spacecraft applications and computer systems for the thermal management of the components. The basic operating mode of a heat pipe is comparable with a thermodynamic cycle. At the heat absorbing side, the working fluid in the heat pipe evaporates and flows to the other end of the pipe, where the fluid condenses under dissipation of the latent heat. A capillary force moves the liquid medium back to the heat absorbing side.

A more detailed description of the heat pipe theory is presented in Sect. 2. The modeling of a heat pipe with Modelica® is shown in Sect. 3. In Sect. 4, the models are validated with laboratory measurements. In Sect. 5 conclusions are given.

2 Heat Pipe Theory

Heat pipes belong to the category of heat exchangers. They are heat transfer devices containing a working fluid. The main physical effects responsible for the heat transfer are thermal conduction and phase transition. Figure 1a shows the basic structure of a heat pipe. Normally, a heat pipe is an evacuated pipe with a wick structure inside, soaked with the working fluid. The wick structure is arranged such that a vapor space is in the middle.

Also presented in Fig. 1a is the working principle. At the hot surface of the heat pipe, the working fluid absorbs the heat and evaporates. Then, the vapor streams to the cold surface of the heat pipe and releases the latent heat, whereby it condenses. Due to the capillary action the condensed working fluid flows back to the hot surface, where the cycle starts anew [3]. There is no pump necessary meaning a heat pipe is a passive heat transfer device and the return takes place through the capillary structure. The process corresponds to a thermodynamic cycle. Theoretically, the heat pipe can be separated into three zones, the evaporation, the adiabatic and the condensation zone, cf. Fig. 1. In general, different combinations of wall material, wick material and working fluid are possible.

Figure 1b shows the thermal equivalent network of a heat pipe. The equations to calculate the thermal resistances are primarily the ones for radial and axial resistances. Only the equivalent resistance R_{va} for the axial heat transfer in the core is different.

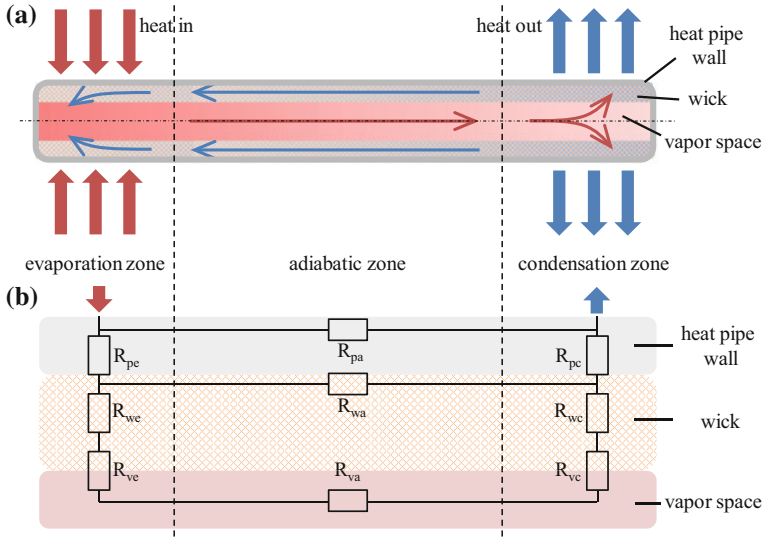

Fig. 1 **a** Basic structure and working principle of a heat pipe; **b** thermal equivalent network of a heat pipe

The radial thermal resistances are given by Eq. 1, the axial resistances by Eq. 2:

$$R_{jk} = \frac{\ln(r_o/r_i)}{2\pi L_k k_j}, \tag{1}$$

$$R_{jk} = \frac{L_k}{\pi k_j \left(r_o^2 - r_i^2\right)}. \tag{2}$$

With R_{jk} is the thermal resistance, r_o and r_i the outer and inner radii for the appropriate section, L_k the length and k_j the thermal conductivity, whereby $j \in \{p =$ 'pipe', $v =$ 'vapor', $w =$ 'wick'$\}$ and $k \in \{a =$ 'adiabatic', $c =$ 'condensation', $e =$ 'evaporation'$\}$. . R_{ve} and R_{vc} are the thermal resistances of the vapor-liquid surfaces at the evaporation and the condensation zone. R_{va} is the thermal resistance for the axial heat transfer of the vapor in the vapor space. It is calculated from Eq. 3, according to [5].

$$R_{va} = \frac{8\mu_v L_{\text{eff}} T_v}{\pi \rho_v^2 r_v^4 h_{fg}^2}, \tag{3}$$

with μ_v is the dynamic viscosity of the vapor, L_{eff} is the effective length of the heat pipe, see Eq. 4, T_v the temperature of the vapor, ρ_v the density of the vapor, r_v the radius of the vapor space and h_{fg} the latent heat of vaporization.

$$L_{\text{eff}} = l_a + 0.5 \cdot (l_e + l_c), \tag{4}$$

with l_k is the length of the adiabatic (a), evaporation (e) or condensation (c) zone.

A more detailed physical view on the processes in a heat pipe is described in Sect. 3.3.

3 Modeling Approaches

For modeling a heat pipe for thermoelectric EHS in Modelica®/Dymola®, three different modeling approaches are studied, namely the single resistance approach, the resistance network approach and the physical approach, as described below.

3.1 Single Resistance Approach

This is a very simple modeling approach. A single thermal resistance represents the heat pipe behavior. The value of the thermal resistance is normally given by the datasheet of the heat pipe. In this contribution, the heat pipe QY-SHP-D8-400SA from Quick-cool [6] is used, with thermal resistance given as $0.1\,\frac{K}{W}$.

3.2 Resistance Network Approach

A more detailed modeling approach is the use of the thermal equivalent network of a heat pipe as shown in Fig. 1b. Here, "ThermalResistor" components of the "Thermal library" of the Modelica® Standard Libraries [7] can be used to build up the network. In this approach, material, medium and geometrical properties are included. The single components are modified according to Eqs. (1–4).

3.3 Physical Approach

The last approach is the physical approach for a steady state. Here, the physical equations for heat transfer and fluid flow theory are summarized to model the heat pipe behavior. The following equations are from [8], [9] and [10] and are valid for the assumption of a laminar flow in the vapor space under steady state conditions. A more detailed description of the physics, also considering turbulent flows and different limitations to heat transport in a heat pipe can be found in [9] and [10].

As the working fluid flows in a closed system, for correct operation, the following condition has to be met:

$$0 = \Delta p_c + \Delta p_v + \Delta p_l, \tag{5}$$

with Δp_c is the capillary pressure difference, Δp_v the vapor pressure difference and Δp_l the liquid pressure difference. The capillary pressure difference is calculated by Eq. (6):

$$\Delta p_c = \frac{2\sigma}{R_{\text{eff,min}}} \cos \vartheta, \tag{6}$$

with σ is the surface tension of the working fluid, ϑ the wetting angle and $R_{\text{eff,min}}$ is calculated by Eq. (7), with the groove width w and the diameter of the wire d,

$$R_{\text{eff,min}} = \frac{w + d}{2}. \tag{7}$$

The liquid pressure difference Δp_l is calculated by two summands, one reflects the hydrostatic pressure $\Delta p_{l,h}$ and the other the flow pressure loss $\Delta p_{l,s}$, which is identified with the help of Darcy's Law.

$$\Delta p_l = \Delta p_{l,h} + \Delta p_{l,s}, \tag{8}$$

$$\Delta p_{l,h} = -\rho_l g h = -\rho_l g \cdot (\pm l \sin \varphi), \tag{9}$$

$$\Delta p_{l,s} = -\frac{v_l}{K A_l \Delta h_v} \cdot \dot{Q} l_{\text{eff}}. \tag{10}$$

Here, ρ_l is the density of the liquid, g the gravity constant, h the height, l the length of the heat pipe and φ the angle between heat pipe and horizontal. v_l is the kinematic viscosity of the working fluid, K the permeability of the wick structure, see Eq. (11), and Δh_v the evaporation enthalpy. The negative sign in Eq. (9) is valid if the evaporator side is below the condenser side; otherwise the positive sign has to be used.

$$K = \frac{d^2 \epsilon^3}{122(1 - \epsilon)^2}, \tag{11}$$

with ϵ is the porosity of the wick structure. The last summand of Eq. (5), Δp_v, is calculated by Eq. (12):

$$\Delta p_v = \sum_k \Delta p_{v,k}. \tag{12}$$

$$\Delta p_{v,k} = -\frac{32\eta_v}{A_{v,a}\Delta h_v d_v^2} \cdot \dot{Q} \cdot l_k, \tag{13}$$

with η_v is the dynamic viscosity of the vapor, $A_{v,a}$ the vapor cross-sectional area and d_v the hydraulic diameter of $A_{v,a}$.

Equation (5)–(13) are the main physical equations for the steady-state behavior of a heat pipe and contain the physical, material and geometrical properties as well as the properties of the medium and are implemented in a Modelica® model. However, it is not always possible or easy to gain access to all needed parameters.

4 Validation

To validate the different developed heat pipe models, a test bed is build up, see Fig. 2, and measurements are recorded. To guarantee an almost adiabatic heat transfer in the heat pipe, glass wool is used to coat the pipe, see Fig. 2b. The result of the comparison of measured data with the simulation data for steady-state scenarios are given in Table 1. All modeling approaches of the heat pipe, described in Sect. 3, conform very well to the measurement data. The error fluctuates in the range of ±4.2 %. Surprisingly, the simplest approach is the most accurately one for the steady-state scenario.

The result of a dynamic scenario is presented in Fig. 3. However, only the single resistance and the resistance network approach are considered, as the physical approach is only valid for steady state conditions. Moreover, the simulation result for a solid copper rod is also shown in the diagram. Visible is that the heat transfer performance of a heat pipe is significantly better than the performance of a comparable pure copper rod. In the inset diagram, it is apparent that both approaches

Fig. 2 **a** Test bed showing the heat source (heating plate), the heat coupling elements on both sides with the heat pipe between them, the cooling element as well as the two temperature sensors (PT1000), **b** test bed as in **a**, though completely coated with glass wool

Table 1 Comparison of real measurement data with the simulation results for a steady-state scenario

Hot side temp. (°C)	Real cold side temp. (°C)	Approach 1		Approach 2		Approach 3	
		Sim. (°C)	**Error** (%)	Sim. (°C)	**Error**	Sim. (°C)	**Error** (%)
140	132.9	135.5	**2**	138.5	**4.2**	130.6	**−1.7**
130	125.6	125.9	**0.2**	128.6	**2.4**	127.7	**1.7**
120	115.8	116.3	**0.4**	118.9	**2.7**	113.3	**−2.2**

Bold values are the errors between simulation and measurement data
The measured hot side temperature is given as input to the simulation model. Approach 1 corresponds to the single resistance approach (Chap. 3.1), Approach 2 to the resistance network approach (Chap. 3.2) and the physical approach (Chap. 3.3) is represented by Approach 3

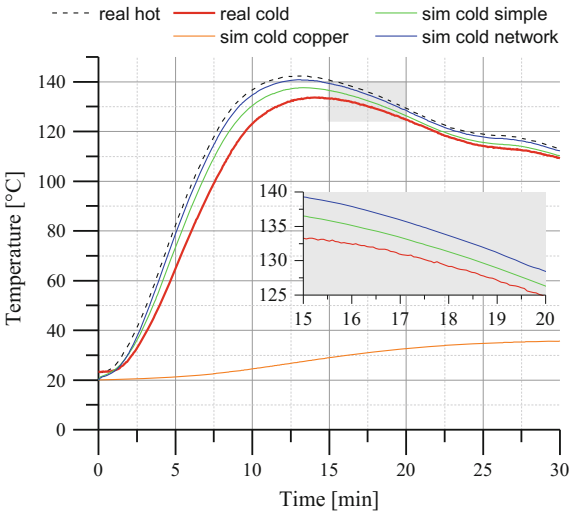

Fig. 3 Comparison of real measurement with the simulation result of approach 1 (simple resistance) and approach 2 (resistance network) as well as a solid copper rod

only slightly differ from measurement. Notable is the fact, that again the simple resistance model shows the best conformity with measurements.

5 Conclusions

In this contribution, three approaches to model heat pipe behavior were presented and validated with measurement data. All three models have shown a very good accuracy and consider partially physical, material and geometrical properties as well as the properties of the medium. Interestingly, the simplest approach is the most accurately one and thus is appropriate for energy harvesting applications, where only the temperature difference and heat transfer are of interest. As soon as more information about the heat pipe itself is required, the more complex models have to be used.

References

1. Priya, S., Inman, D.J.: Energy Harvesting Technologies. pp. 325–336. Springer, New York, London (2008)
2. Nesarajah, M., et al.: Energy Harvesting from Open Fireplaces. In: Oral A., Bahsi Oral Z., Ozer M. (eds.), 2nd International Congress on Energy Efficiency and Energy Related Materials (ENEFM2014), Oludeniz, Turkey, October 2014. Springer Proceedings in Energy, pp. 525–531. Springer International Publishing (2015). doi:10.1007/978-3-319-16901-9_64
3. Ong, K.S.: Heat pipes. Jurutera, 17–18 (2008)
4. Gaugler, R.S.: Heat transfer device. US Patent US 2350348 A, 06 June 1944
5. Shabany, Y.: Heat Transfer: Thermal Management of Electronics, pp. 421–435. CRC Press, Boca Raton (2010)
6. Conrad Electronic, HeatPipe QY-SHP-D8–400SA. http://www.conrad.de/ce/de/product/182587/Heatpipe-02-KW-x-L-8-mm-x-400-mm-QuickCool-QY-SHP-D8-400SA (2015). Accessed 06 Oct 2015
7. Modelica Association: Modelica Homepage. https://www.modelica.org/ (2015). Accessed 06 Oct 2015
8. Klotsche, M.: Entwicklung. Lehrstuhl für thermische Kraftanlagen mit Heizkraftwerk, Technische Universität München, München, Fertigung und experimentelle Untersuchung von kostengünstigen Hochtemperatur-Heatpipes. Diplomarbeit (2004)
9. Reay, D.A., McGlen, R., Kew, P.A., Heat pipes, pp. 15–64. Butterworth-Heinemann, Oxford (2013)
10. Stephan, P.: Wärmerohre. In: VDI, VDI-GVC (eds.) VDI-Wärmeatlas: CD-ROM 3.0, Chap. Ml. Springer, Berlin (2006)

Electron Thermostating Elements for Controlling Consumption of Heat Transfer Agent in the Heating Systems

Yury I. Shtern, Ya S. Kozhevnikov, I.S. Karavaev, V.M. Rykov and M. Yu Shtern

Abstract Electron thermostating elements (ETE) mounted on the regulating radiator valves are developed. ETE are designed for the automatic controlling of the consumption of heat transfer agent in the heating systems by a special program. So, ETE are intended for the controlling of the temperature in the heated placements. ETE have autonomous power supply. Optimization of the working algorithm of ETE in conjunction with the high efficiency of the servomotor, and low level of power consumption of the electronic circuit allowed authors to increase the time of autonomous work of ETE. Proposed design solutions of ETE can be used also in different fields of science and technology for the automatic controlling of the consumption of liquid and gaseous agents.

Keywords Thermostating elements · Automatic control · Thermal energy · Power supply · Intellectual system for controlling

1 Introduction

Development of the automated energy-saving system for controlling and monitoring of the energy consumption is actual direction in science and technology. The most acute problem is regulation and controlling of individual heat consumption in the heating systems [1–3]. Original hardware-software and design solutions for electron thermostating elements (ETE) are proposed, which are installed on the regulating radiator valve of the heating systems for the automatic controlling of the heat consumption by a program. So, temperature regulation in heated rooms is carried out with using of this device by a special program.

Analysis of the state of development of ETE indicates that their number is very limited. The main drawback of the known analogs is connected with the resource of

Y.I. Shtern · Y.S. Kozhevnikov · I.S. Karavaev · V.M. Rykov · M.Y. Shtern (✉)
National Research University of Electronic Technology,
Bld. 5, Pas., 4806 Zelenograd, Moscow, Russia
e-mail: m.y.shtern@gmail.com

A.Y. Oral and Z.B. Bahsi Oral (eds.), *3rd International Congress on Energy Efficiency and Energy Related Materials (ENEFM2015)*, Springer Proceedings in Energy, DOI 10.1007/978-3-319-45677-5_23

their work. ETE have stand-alone power supply, and one of the main problems is connected with the duration of their work, which is determined by the resource of chemical power sources (CPS). Special attention in this work is paid to the increase of the ETE operating time by decreasing power consumption, which is supported by the effective hardware and software solutions.

2 Electron Thermostating Elements

Two versions of ETE constructions determining their functionality were developed. ETE-T construction for the controlling ETE working regimes with using room thermostat (RT) is proposed. Structural scheme of ETE-T is presented in Fig. 1. Structural scheme include: servo with reducer, motor and controlling circuit; microcontroller with built-in analog-digital converter (ADC); transceiver of radio signals; built-in antenna and CPS—2 elements of AA type (1.5 V).

RT is programmed on the temperature regime during definite time interval (day, week, etc.). Changing temperature in the room RT transmits controlling signal on ETE-T by radio channel. Regulation of temperature regime in the room is carried out by proportional-integral-differential law. Motor is started on a definite time controlling reducer with rod, which regulate opening of radiator valve, and so heat carrier flow.

Microcontroller fabricated with using of MSP430F2132 microcircuit determine ETE operation regime by given program. Transceiver of radio signals is fabricated with using of TI CC1101 microcircuit. Electric drive 25BYJ is chosen as motor and

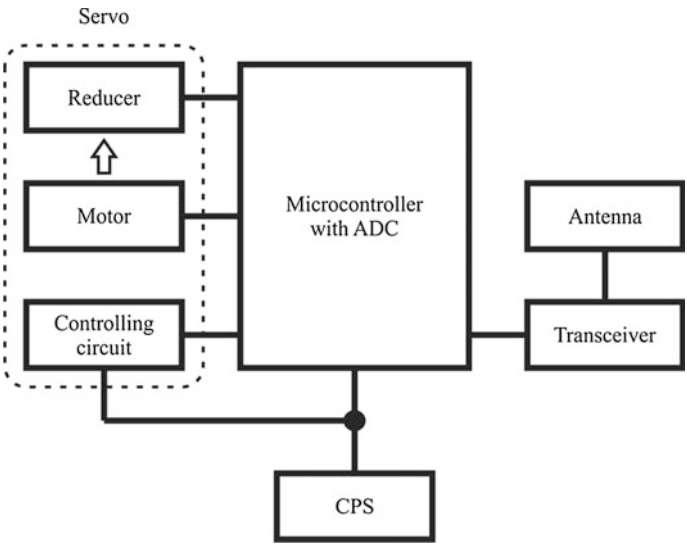

Fig. 1 Structural scheme of ETE-T

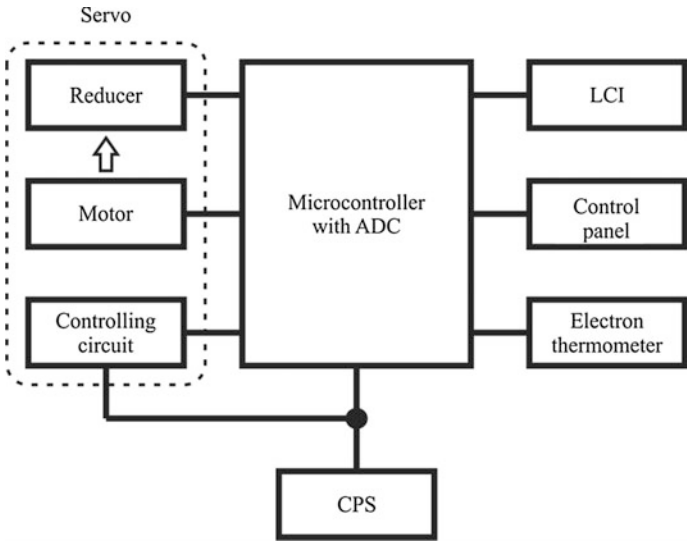

Fig. 2 Structural scheme of ETE-P

reducer. Driver has supply voltage of 3 V, current at nominal load of 400 mA, output force of 70 N, rate of rod motion of 0.5 mm/s, rod moving length of 2.5 mm. Proposed ETE-T construction is advisable to use in the rooms with several heaters.

Another way of controlling temperature in the room is realized without RT with the help of programmable ETE-P. In this case temperature regime is programmed by control panel. Structural scheme of ETE-P is presented in Fig. 2. ETE-P consists of servo; microcontroller with ADC; electron thermometer; alphanumeric liquid crystal indicator (LCI); control panel and CPS.

Time, operational regime and temperature are displayed by LCI of ETE-P. Temperature measurement with the error 0.5 °C in ETE-P is carried out by sensor on the basis of DS18B20 microcircuit. The algorithm of the servo controlling circuit in ETE-P is similar to that of RT.

3 Methodic and Investigation of ETE Operation Life

Low operation life is one of the main problems of ETE with CPS. CPS work was analyzed in order to estimate CPS resource in real conditions of exploitation taking into account following. Room temperature must be maintained with the accuracy of ±1.5 °C. The daily working regime of ETE maintaining given room temperature is mainly determined by the street temperature fluctuations, room thermoisolation and heaters power, which influence on the time necessary to rich temperature regime.

Authors proposed modelling of the temperature variation in the room taking into account daily external temperature fluctuations in some districts in Russia for every month of the heating season. Modelling was carried out for residential buildings with different thermoisolation. It was established that at worst with the sharp external temperature fluctuations it is necessary up to 20 times correct temperature in the room during the day with using ETE, i.e. nearly every hour. Results of modelling are confirmed by the experimental investigations in Moscow and Moscow district during heating season in 2014 year.

Depending on the construction ETE have several operating regimes.

1. Regime of moving the rod of radiator valve (for ETE-T and ETE-P) every hour during the period not more than 1 s, consuming current does not exceed 400 mA. As a result of single rod moving, heat carrier flow changes on 20 %.
2. Regime of radio communication (for ETE-T) with duration of 0.1 s is carried out every hour, consuming current does not exceed 30 mA.
3. Regime of measuring ambient air temperature (for ETE-P) with duration of 10 ms, interval between measurements is 10 min, consuming current is 1 mA.
4. Regime of data indication (for ETE-P) is continuous; consuming current does not exceed 5 mcA.
5. Sleeping regime (for ETE-T and ETE-P) is necessary for the work of internal timer and microcontroller, works continuously, consuming current is 1 mcA.

Taking into account main parameters of existing CPS (electric circuit, self-discharge and cost) preference is given to alkaline sources: electric capacity is 2700–3000 mA·h; self-discharge is 20 % after 3 years.

Operation life of CPS in ETE can be calculated as:

$$\tau = \frac{C_{AH}}{I_C},$$

where τ is CPS operation life; C_{AH} is capacity of power supply in A·h; I_C is consuming current by ETE.

Taking into account operating regimes for ETE-T was obtained value of daily consumption of electric capacity equal to 2.71 mA·h, while for ETE-P—2.81 mA·h. It means that operation life of ETE-T is 797 days, and ETE-P is 768 days. So, both types of ETE can work continuously more than 2 years. However, as usual, in most countries heating season at worst continue not more than 8 months. In this case operation life of ETE will be more than 3 years.

Methodic and hardware-software measuring complex (Fig. 3) were developed for estimation of the reliability of calculations of ETE operation life and investigation of CPS parameters.

Investigations of CPS operation life were carried off with using of the complex. Measurements were fulfilled in automated regime with different values of output current (load current) and exploitation temperature. Complex includes: microprocessor control unit (MCU); power supply (PS) Motech 305 for MCU; thermostat (TT) Memmert UE 300 for controlling CPS exploitation temperatures

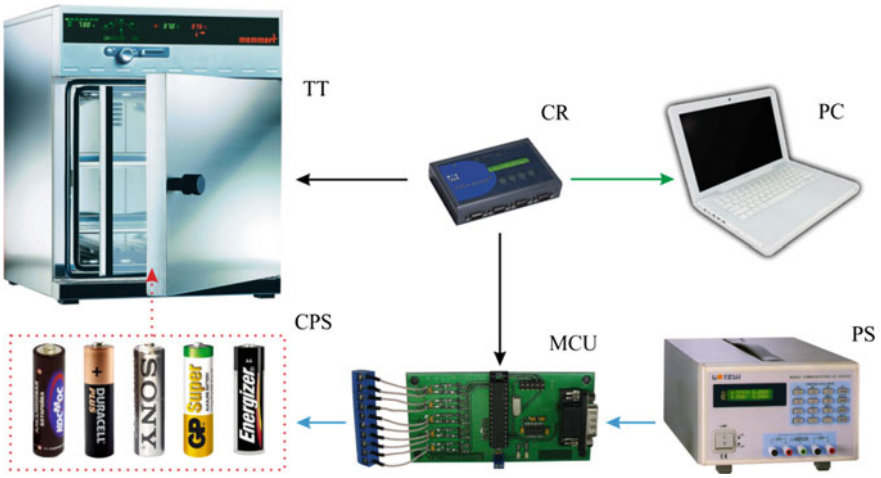

Fig. 3 Structural scheme of hardware-software measuring complex for the investigation of CPS operation life

(from 20 to 100 °C); converter (CR) N-port for adjusting signals with TT and MCU, and personal computer (PC).

Methodic of accelerated tests was developed to decrease the time of resource research, in which CPS working time was shortened 100 times. So, 1 day of the work in normal conditions is imitated by 864 s in accelerated tests. Wherein, energy consumption corresponding to the real process exploitation of CPS is provided. Regime of indication by LCI and sleeping regime in accelerated tests are also working continuously, however current is increased 100 times. In regimes of rod moving and radio session switching period is changed and is equal to 36 s. Self-discharge of CPS is also considered, the value of self-discharge current is equal to 2 mA.

Following CPS samples were chosen for the resource tests: GP Super Alkaline (1); Cosmos Maxlife (2); Energizer Maximum (3); Duracell Turbo (4); Panasonic Xtreme Power (5). Investigations were carried out at maximum possible exploitation temperature of ETE (50 °C) till the decrease of CPS voltage to 2.5 V. This level is determined by the operation abilities of an electronic circuit of ETE. Table 1 presents results of accelerated resource tests of CPS ETE-P.

Table 1 Resources of CPS used in ETE-P

Number of CPS sample	1	2	3	4	5
Resource at accelerated tests, hour	169	177	178	180	184
Operation resource, days	705	738	741	748	766

Given that heating period does not exceed 8 months, then operation resource of CPS N 2–5 used in ETE-P is more than 3 years. ETE-T with these CPS can be exploited even more time. Obtained experimental results correlate with calculated data presented in this work. This parameter of ETE is better than for known analogs.

4 Conclusions

Versions of original hardware-software and design solutions for ETE are proposed. Optimization of the working algorithm of ETE in conjunction with low level of power consumption of the electronic circuit allowed to increase the time of autonomous work of these devices. This parameter of ETE is better than for known analogs. Developed measuring complex and methodic allows accelerated tests of the resources of batteries used in different electronic instruments and devices. Proposed solutions of ETE can be used for the automatic control by certain program of the liquid and gaseous media consumption, for example in conditions systems, boilers for heating and hot water using liquid and gas fuel.

This work was supported by Ministry of Education and Science of RF (project N 14.575.21.0032, project ID: RFMEFI57514X0032).

References

1. Shnayder, D.A.: A WSN-based system for heat allocating in multiflat buildings. In: Herencsar N., Molnar K. (eds.) 2013 36th International Conference on Telecommunications and Signal Processing (TSP) Proceedings, pp. 181–185. Rome, Italy (2013). doi:10.1109/TSP.2013.6613915
2. Fu, M., Zhang, Y.J., Ye, J.D., Jiang, J.Y., Zhang, F.: Optimal design for the room temperature control and household heat metering system. Appl. Mech. Mater. **724–725**, 969–975 (2013). doi:10.4028/www.scientific.net/AMR.724-725.969
3. Shtern Yu.I., Kozhevnikov Ya.S., Medvedev V.A., Mironov R.E., Karavaev I.S.: Methods of determining individual heat energy consumption using an intelligent system for monitoring power supplies. Measur. Tech. **56**(2), 178–184 (2013). doi:10.1007/s11018-013-0177-2

Investigation and Calibration Methods of Precise Temperature Sensors for Controlling Heat Consumption

Yury I. Shtern, Ya. S. Kozhevnikov, I.S. Karavaev, M. Yu. Shtern, A.A. Sherchenkov and Maxim S. Rogachev

Abstract Authors developed precise temperature sensor with wireless interface (WTS). Methods of thermocompensation and individual calibration of WTS were developed in order to provide high requirements of the temperature measurement accuracy (0.02 °C). Measuring hardware-software complexes for the realization of this methods and carrying investigations were also developed.

Keywords Intellectual temperature sensor · Calibration method · Mathematical model · Software

1 Introduction

Precise temperature sensor with wireless interface (WTS), having measurement error up to ±0.02 °C were developed. Measured data are transferred by radio channel on the frequencies of 434 and 868 MHz. WTS is designed for the contact temperature measurements in not aggressive environment. WTS is used by authors in automated controlling systems for the determination of individual heat consumption in the heating systems of the apartment buildings [1]. High requirements for the temperature measurement accuracy cannot be satisfied without taking into account influence of the temperature on the parameters of the electronic circuit components, and without individual calibration of WTS. However, these sufficiently increase the final price of the product. To reduce cost we developed appropriate methods and hardware–software measuring complexes, which allows to carry on thermocompensation and individual calibration of WTS automatically and for a large part of product simultaneously.

Y.I. Shtern · Ya.S. Kozhevnikov · I.S. Karavaev · M.Yu. Shtern (✉) · A.A. Sherchenkov · M.S. Rogachev
National Research University of Electronic Technology, Bld. 1, Shokin Square, Zelenograd, Moscow, Russia 124498
e-mail: m.y.shtern@gmail.com

A.Y. Oral and Z.B. Bahsi Oral (eds.), *3rd International Congress on Energy Efficiency and Energy Related Materials (ENEFM2015)*, Springer Proceedings in Energy, DOI 10.1007/978-3-319-45677-5_24

2 Thermocompensation Method for Electron Circuit of WTS

During exploitation of WTS in the heating systems temperatures of the environment and heat transfer agent can be varied in the ranges from 5 to 50 °C, and from 5 to 95 °C, respectively. In this case temperature of the electronic circuit components of WTS changes, which provide measurement error. To investigate and eliminate this negative phenomenon method for thermocompensation of the WTS electronic circuit, and measuring complexes for its realization were developed.

Temperatures of the electronic circuit components of WTS in the mentioned exploiting conditions were determined with using of measuring complex, which includes following elements. Thermally isolated camera with liquid-air heat exchanger imitating ambient temperature. Thermostat *Lauda PR* 3530 for controlling temperature of the heat transfer agent in the closed loop imitating pipeline of the heating system with WTS. Precise thermometer TEN-4 for the temperature measurements. It was established that at mentioned ambient and heat transfer agent temperatures maximum temperature of the WTS circuit components does not exceed 60 °C.

Measuring complex is developed for the investigation of the influence of temperature variation of the circuit components on the error of WTS. Main elements of this complex are following: thermoelectric thermostat UT-10/60, precise resistance box M-602A-V 1000, wireless repeater (WR) for reception and transmission of data by radio channel, and personal computer (PC). Resistance box is connected to the input of electron circuit instead of platinum thermoresistance for the determination of error introduced by WTS electron circuit components during temperature measurements. The value of resistance corresponding to the platinum resistance at 25 °C is set by resistance box. Then WTS is put in the thermostat, which temperature is successively changed as 5, 30 and 60 °C. At each temperature, which corresponds to the temperatures of electron circuit components, the value of resistance measured by WTS is determined. Temperature of the electron circuit components is also controlled by the internal microcontroller detector of WTS. To exclude errors introduced by the mathematical conversion of analog-digital converter (ADC) code first into the resistance, and then into the temperature, measured by WTS data are fixed as ADC code (N_R).

Results of investigations for seven WTS are presented in Fig. 1. As can be seen, resistivity N_R linearly depends on temperature. Error during the measurement of the components temperature in the range from 5 to 60 °C with conversion of ADC code in temperature does not exceed 0.15 °C.

The true value of N_R can be determined as:

$$N_R = N'_R - \Delta N_R, \tag{1}$$

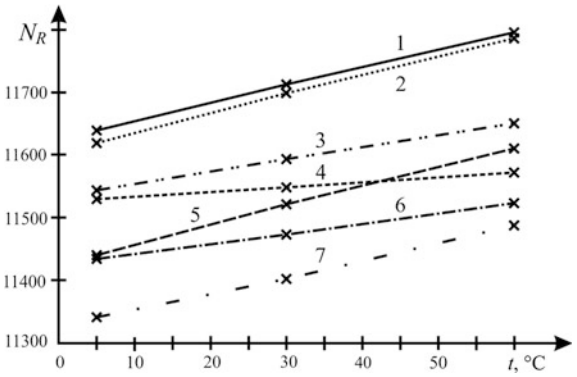

Fig. 1 Temperature dependence of NR

where N'_R is resistance determined by WTS during the influence of heating on the circuit components; ΔN_R is deviation of N_R from the initial value (error) caused by the change of temperature.

Because the change of N_R linearly depends on the temperature, ΔN_R can be determined as:

$$\Delta N_R = a * N_{mc} + b, \tag{2}$$

then taking into account (2) true value of N_R is determined as:

$$N_R = N'_R - (a * N_{mc} + b), \tag{3}$$

where N_{mc} is temperature of the microcontroller as ADC code.

Thermocompencating method includes experimental determination and automatic programmable adjustment of coefficients in Eq. (3) carried out during the individual calibration of WTS, which allows to eliminate ΔN_R. For the realization of thermocompencating method and WTS calibration hardware–software measuring complex was developed [2]. Complex includes following elements. Precise liquid thermostat *Lauda PROLINE RP* 3530 with installed measuring cell for the calibration and thermocompensation of WTS. Measuring cell includes massive copper plate (with thickness of 25 mm) with screw-thread holes for the location of 56 WTS. Plate is covered by thermoinsulating screen forming working volume in which temperature is controlled. Electron thermometers: *DTI*-1000 for the calibration of WTS, and 4-channel TEN-4 for the determination of the copper plate temperature profile, which have errors 0.005 and 0.05 °C, respectively. WR for receiving information by radiochannel from the WTS radio transceivers, and data transmission by *RS*-232 channel to the computer.

Process of WTS thermocompensation is following. Temperature of 25 °C is stabilized in the measuring cell of thermostat. Next, temperature is measured with using of three measuring channels (Fig. 2). Channel 1 is used for measuring of the resistance of the WTS platinum thermoresistor (line 1); channel 2 is used for the

measuring of microcontroller temperature (line 2); channel 3 is used for measuring of the temperature of copper plate (line 3). For data of the channels 1 and 2 ADC codes are used: $N_{R(25)}$ and $N_{mc(25)}$. Next temperature, for example 50 °C, is set up in the working volume of cell without changing temperature of the heat transfer agent, and resistance of thermoresistor and microcontroller temperature are measured.

When WTS circuit components has temperature of 50 °C the value of $N_{mc(50)}$ is obtained by the channel 2. At the same time WTS thermoresistor has temperature of 25 °C. However its reading includes error due to the shift of the circuit components temperature $N'_{R(25)}$. To exclude error in the WTS thermoresistor measurements, thermocompensating coefficients are determined with using of Eqs. (4) and (5):

$$a = \frac{N_{R(25)} - N'_{R(25)}}{N_{mc(25)} - N_{mc(50)}}, \tag{4}$$

$$b = \frac{N_{mc(25)}\left(N_{R(25)} - N'_{R(25)}\right)}{N_{mc(25)} - N_{mc(50)}}. \tag{5}$$

Using of the corrected coefficients in Eq. (3) allows to obtain true value of $N_{R(25)}$ (line 3) for 50 °C.

Diagram of the thermocompensating process as displayed by PC is presented in Fig. 3.

Results of thermocompensation for 5 WTS are presented. Measuring of the heat transfer agent temperature is carried out by channel 1 with using of WTS thermoresistor. Variation of the temperature of electron circuit components is determined by channel 2. Range A corresponds to the stabilization of thermostat temperature at 25 °C. Next, temperature of WTS circuit components is increased to 50 °C (channel 2, range B), and measurements of the temperature of the heat transfer agent are carried out by each WTS (channel 1, range B). After the stabilization of the temperature of WTS circuit components (range C) measuring and

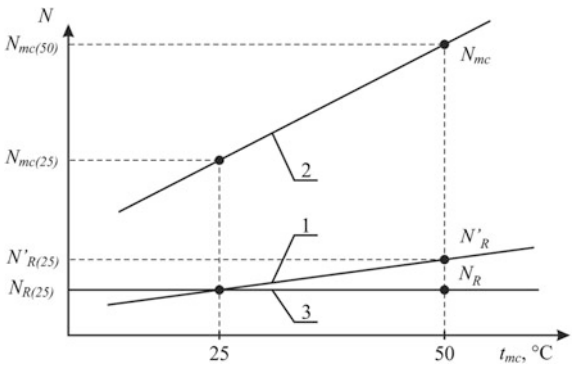

Fig. 2 Dependence of ADC code on the temperature of WTS circuit components

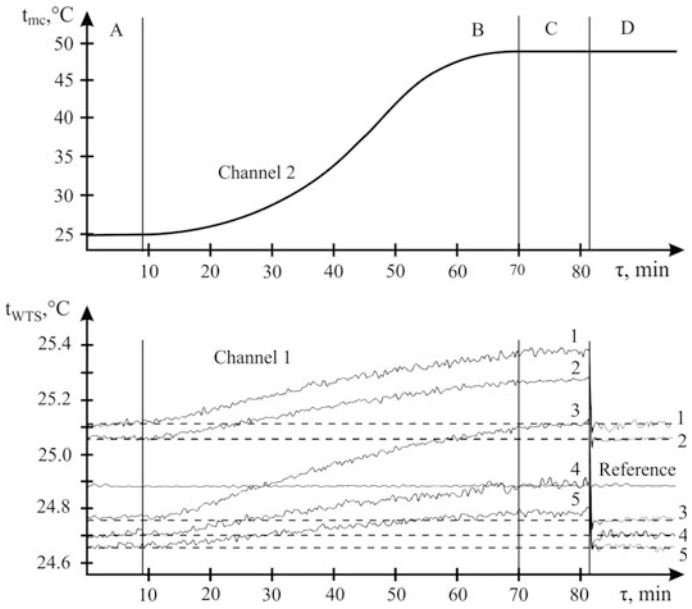

Fig. 3 Diagram of thermocompensating process

calculation of thermocompensating coefficients for each WTS is carried out. Results of the measuring of WTS temperature after thermocompensation are presented in range D.

3 Methodic for Individual Calibration of WTS

Deviations of the WTS readings from those of the reference resistance thermometer after thermocompensation (Fig. 3) are determined by the individual characteristics of platinum thermoresistor including R_0 and scatter of electrical parameters of circuit components. These deviations are eliminated by the individual WTS calibration, which is carried out in parallel with thermocompensation.

WTS calibration is carried out automatically at two temperatures of 25 and 85 °C with using of developed software. Discrepancy of the temperatures of each WTS and reference thermometer mounted on the copper plate of the measuring cell is determined. Then calculation and automatic correction of coefficients in the mathematical models of each WTS are carried out at the temperature of 85 °C (Fig. 4).

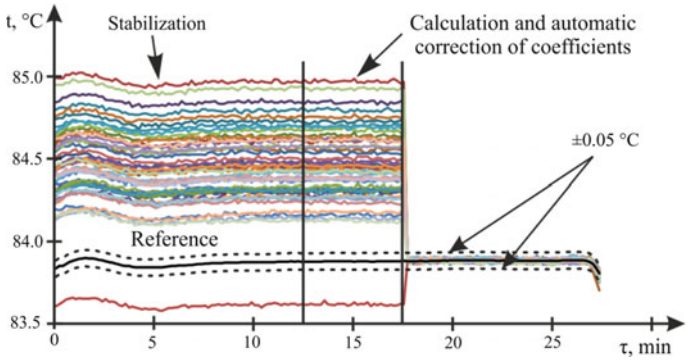

Fig. 4 Diagram of WTS calibration at 85 °C

4 Conclusion

Results of investigations allow sufficient decrease of measuring error and can be used for the development and production of the temperature sensor with wireless interface. Automatic calibration of the large part of product sufficiently decreases time and cost price.

Acknowledgments This work has been carried out under a sponsorship of the Ministry of Education and Science of the Russian Federation project number 14.575.21.0013 (UN RFMEFI57514X0013).

References

1. Shtern, Y.I., Kozhevnikov, Y.S., Medvedev, V.A., Mironov, R.E., Karavaev, I.S.: Methods of determining individual heat energy consumption using an intelligent system for monitoring power supplies. Measur. Tech. **56**, 178–184 (2013). doi:10.1007/s11018-013-0177-2
2. Shtern, Y.I., Kozhevnikov, Y.S., Mironov, R.E., Shtern, M.Y., Karavaev, I.S.: A procedure and a hardware–software system for the automated calibration of temperature measuring instruments. Measur. Tech. **56**, 497–502 (2013). doi:10.1007/s11018-013-0234-x

Thermoelectric Generators: A Review of Present and Future Applications

Daniel Champier

Abstract In the last centuries, men have mainly looked into increasing their production of energy in order to develop their industry, their means of transport and their quality of life. Since the recent energy crisis, researchers and industrials have mainly been looking into managing energy in a better way, especially by increasing the efficiency of energy systems. This context explains the growing interest for thermoelectric generators (TEG). Today, TEGs allow us to collect lost thermal energies, to produce energy in extreme environment, to produce electric power generation in remote areas and to produce micro production for sensors. Direct solar thermal energy can also be used to produce electricity. This review begins with the basic principles of thermoelectricity and with a presentation of existing and future materials. The design and optimisation of generators are tackled. Many recent applications are presented as well as the future applications which are being studied in laboratories or in industry.

Keywords Thermoelectric generators · Review · Thermoelectricity

1 Introduction and Basics

Electricity production is an important issue for our societies. Waste heat is also an important topic. It is in this context that the thermoelectric generators (TEG) are taking off. TEG directly convert a part of thermal energy that passes through them into electricity. The main actor of this transformation is the thermoelectric (TE) module which usually contains tens to hundreds of thermocouples connected together electrically in series and thermally in parallel.

D. Champier (✉)
Université Pau & Pays Adour, SIAME, Pau, France
e-mail: daniel.champier@univ-pau.fr

A.Y. Oral and Z.B. Bahsi Oral (eds.), *3rd International Congress on Energy Efficiency and Energy Related Materials (ENEFM2015)*, Springer Proceedings in Energy, DOI 10.1007/978-3-319-45677-5_25

The efficiency (defined as the ratio of the electrical energy produced Welec on thermal energy entering the hot face Qh) of a thermoelectric module used as a generator can be approximated by the following relationship [1–3] for an optimal electric load:

$$\eta_{TEmax} = \frac{W_{elec}}{Q_H} = \frac{\Delta T}{T_H} \cdot \frac{\sqrt{1+ZT}-1}{\sqrt{1+ZT}+\frac{T_C}{T_H}} \quad (1)$$

$$with\ Z = \frac{(\alpha_p - \alpha_n)^2}{\left((\lambda_p.\rho_p)^{1/2} + (\lambda_n.\rho_n)^{1/2}\right)^2} \quad (2)$$

with T_H the temperature of the hot side of the TE modules, T_C the temperature of the cold side of the modules, $\Delta T = T_H - T_C$ the temperature difference and T the average temperature. Z is the factor of merit of the thermoelectric materials and can be expressed as a function of the electrical resistivities ρ_p and ρ_n, the thermal conductivities λ_p and λ_n and the Seebeck coefficients α_p and α_n of each of the two materials of the thermocouple.

ZT is a very convenient way to compare materials properties.

2 Materials

For a long time, the only modules available for industrial applications (with the exception of the Space) were Bismuth Telluride modules (Bi_2 Te_3). ZT is approximately 1 around 50 °C and then decreases at higher temperature. The maximum operating temperature is between 200 and 300 °C depending on the manufacturers. The low abundance of Bismuth and Tellurium in the earth's crust and in the oceans is also a problem for manufacturers. These two points have limited the development of TEG.

Since ten years, laboratories are searching for inexpensive replacement materials, more environmentally friendly and that can be produced commercially in large quantities. These researches have been fruitful. Since a few months, new modules are commercially available or close to commercialization: half heusler, skuterrudites, oxides, magnesium silicides and tetrahedrites.

Half Heusler are coming soon at Evident Thermolectric. 2 types of modules TEG-HH-8 [4] and TEG-HH-15 [5] which can produce respectively up to 7.2 and 15 W when a temperature gradient of 500 °C is applied. The hot side continuous temperature must be maintained below 600 °C with intermittent operation below 700 °C.

The Shanghai Institute of Ceramics has presented at ICT2015, TEG25 a $CoSb_3$-based skuterrudites which can produce up to 25 W when a temperature gradient of 510 °C is applied. The peak ZT for the N-type ($Yb_{0.3}Co_4Sb_{12}$) is around 1.2, the peak ZT for the P-type ($CeFe_3CoSb_{12}$) is around 0.75 at T = 800 K.

Tegma [6] develops Skutterudite Thermoelectric elements.

TECTEG MFR markets modules made of Calcium/Manganese oxide reference CMO-32-62S and CMO-25-42S [7]. The upper Limit of the hot side is 850 °C, but regular temperature is about 800 °C. These modules can produce respectively 12.3 and 7.5 W when a temperature gradient of 750 °C is applied. TECTEG also produces cascade modules: high temperature Calcium/Manganese oxides bonded with Bi2Te3 on the cold side. These are the first cascade thermoelectric modules ever to be available commercially with a hot side up to 600 °C.

Hotblock Onboard [8] produces module (NEMO) made of silicon based alloy. They deliver 3.6 W for a hot side temperature of 580 °C and a cold side temperature of 80 °C.

Romny Scientific [9] develops thermoelectric modules made of magnesium silicide materials. This materials are low cost and earth abundant raw materials.

Alphabet Energy [10, 11] plans to produce thermoelectric modules made of non_toxic compound: p-type tetrahedrites and n-type magnesium silicide (Mg_2Si) pellets. One of the most appealing properties of Mg_2Si is its very low density (i.e. <2 g/cm^3) which for transport applications will be decisive.

As it can be seen many mineral TEGs are available or coming soon. Organic TEGs [12] are still under research but will probably appear in the market in a few years.

3 Design and Optimisation

Industrial use of thermoelectric modules needs to add other elements to form a powerful generator:

- heat exchangers which amplifies the heat transfer between the module and the heat sources,
- an electrical converter which transform the electric power to a voltage level corresponding to the storage device (batteries, capacitors) or to the level corresponding to the need of the end user.

The efficiency of the overall system can be defined as the ratio of the electrical energy stored or provided to the end user on the energy consumed. The energy consumed is mainly collected at the hot source but can also include the mechanical energy required to operate the system such as the cooling of the cold heat sink, or the pressure losses in the heat exchangers.

This efficiency include the efficiency of the heat exchangers, the efficiency of the TE modules, the efficiency of the electrical convertor and its ability to optimize the electrical load.

The performance of thermoelectric modules is small, so the design of generators requires a system approach to optimize the whole system:

- Researches on thermoelectric materials for a zT the largest possible throughout the generator temperature range.
- Works on heat exchangers and coupling with thermoelectric modules.
- Works on electrical converters and on electrical connection (series, parallel or mixed) of modules. These DC DC converters need to be optimized for an electric efficiency close to 1. They must incorporate an algorithm of "maximum power point tracking" or "maximum efficiency point tracking" in order to optimize the point of electrical operation of TEG and to transfer maximum power to the end user [13–15].
- Numerical studies to optimize generators. The numerical models must take in account the variations of materials properties with the temperature, the adequate quantity of modules, the geometry of the modules [16–18].

These aspects are unfortunately not independent and the overall optimization requires many interactions and powerful computing tools.

The economic aspect is also extremely important and must be study [19].

4 Applications

4.1 Electricity Generation in Extreme Environments

Electricity production in extreme environments must meet a set of very strict specifications. This is usually critical applications that require a highly reliable source of energy over very long periods. Weather conditions can be extreme, either very hot or very cold or very wet or very dry. Maintenance must be as low as possible (often access to these place is only done by helicopter or requires several hours of travel) or non-existent in the case of space expeditions. The generators must be able to operate in a vacuum and withstand high vibrations. The economics is not the most important point, far behind the reliability.

The space industry has used thermoelectric generators since the beginning of the conquest of space in combination with thermal generators based on nuclear technology: radioisotope thermoelectric generators (RTG). The first use of thermoelectric generator (Pb–Te) dating back to the Transit satellite navigation (1961) of the US Navy. The satellite was equipped with a space nuclear auxiliary generator SNAP-3 (Space Nuclear Auxiliary Power) which generated electric power of about 2.7 W only, but that worked for over fifteen years [20]. The Voyager I and II spacecraft, launched in 1997, also use generators radioisotope thermoelectric due to their extreme reliability to power the onboard instruments and transmission systems to the ends of the solar system. The probes are now (October 2015) at 19.5 and 16 billion km from Earth. Each spacecraft was equipped with 3 RTG which overall supplied 423 W power from about 7000 W heat. This power decreases gradually from about 7 W by year due to the decay of plutonium and because of the degradation of silicon germanium thermocouples. This power is now about 255 W.

They have sufficient electrical power to operate until 2020 [21]. The main RTG used in space by American missions can be found on the NASA website [22]. The materials used for thermocouples are PbSnTe, TAGS-PbTe, SiGe. Current research focuses on improving the performance of proven materials (decrease of lattice conductivity and improved electrical properties) and the study of other materials and assembly of couples (Zintl, skutterudites and segmented couples).

Historically, about a thousand radio-isotope thermoelectric generators were installed in Russia to power lighthouses and navigation beacons. Very little information is available on those devices that are mostly abandoned [23]. Today the company Gentherm [24] (previously Global Thermoelectric) is the world leader for the production of electricity generators for remote areas. The company exists for 30 years and produced about 22,000 installations. These thermoelectric generators use heat produced by the combustion of natural gas, butane or propane. The burner directly heats a section of the thermoelectric modules are cooled by natural convection fins disposed on their cold sides. Generators have powers between 15 and 550 W and can be combined for installations of up to 5000 W. For example the 8550 Global Thermoelectric model, produce 500 W with an efficiency of around 2.3 %. This low yield is offset by the benefits of the generators which are used in desert, well sites, offshore platforms and telecommunications sites in mountains.

In conclusions these applications have a very high added value but they are niche applications for which the market is very limited.

4.2 Recovery of Thermal Energy Lost

The transportation industry is probably the most attractive sector to use TEG to recover heat lost. Up to now, there is only few solutions to recovery wasted heat from the exhaust gas of engines. The most active area for energy recovery is the automotive sector where competition towards ever cleaner cars is very dynamic and very encouraged by governments. Aeronautics is also looking into the use of hot gases from the engines of airplanes or helicopters. Maritime transport offers interesting perspectives due to the presence of a free cold sink (fresh water, sea water).

Typically the energy used in a gasoline combustion engines splits into 25 % for mobility, 30 % in coolant, 5 % in other parasitic losses and 40 % in exhaust gas. For diesel light duty truck this represents 30 kW of heat loss in the exhaust gas. Converting this energy lost into electricity even with a 3 % efficiency could represent 900 W of electricity. According to Fiat research centre 800–1000 Wel means 12–14 g/km CO_2 reduction.

The installation of a TEG on a vehicle must meet the following conditions. The TEG should not change the operating point of the engine; the acceptable pressure losses are very limited (around a few tens of millibars). The maximum temperature of TE materials must be respected and at the same time, to have a significant temperature difference, it is desirable to operate the TEG near its limits. It is therefore necessary to add control command (sensors and actuators) to bypass

part or all the hot gas. The materials must be recycled and environment friendly. The economic cost must be competitive. Many constructors work on this subject. The company Gentherm (formerly Amerigon) conducts studies and specific geometries modules for BMW and Ford [25]. General Motors installed a TEG on a Chevrolet Suburban. The first results with BiTe modules were disappointing but the contact resistance problems have been identified [26]. More recently FIAT and Chrysler presented the first light commercial vehicle equipped with a TEG [27]. The performance achieved by the TEG are encouraging. 4 % fuel economy improvement over the worldwide harmonized light vehicles test procedure (abbreviated WLTP) cycle has been achieved. This TEG used BiTe modules with limited operating temperature. High temperature material should be used in next applications to fully take advantage of the TEG power generation. The company Valeo (Renoter2 project) plans to produce magnesium silicide TEGs for 10000 vehicle in 2018.

A significant amount of heat is released from the reactors aircraft and turbine engines for helicopters. The integration of thermoelectric generators (0.5 kW/kg-module as state of the art) fulfils the power density requirement (0.15 kW/kg). Several patents have been filed. However a study [28] on turbine nozzle with Bi_2Te_3 modules, shows that the electric power produced in real operating conditions is significant but currently insufficient if the weight of the cold exchanger is included. But with new materials this weight to power ratio should decrease.

Up to now relatively few studies have been done on ships because of the absence of very strict international regulations. Shipping is a large and growing source of the greenhouse gas emissions that are causing climate change. The European Union wants to reduce emissions from international shipping. The European Commission has proposed that owners of large ships using EU ports should report their verified emissions from 2018. This sector is an opportunity for TEGs because weight is not a problem, cold source (water) is free and maintenance must be as low as possible. This sector should grow rapidly due to the arrival of new, more stringent rules [29].

In conclusion, the new materials should allow the imminent arrival of TEG on vehicles, offer very interesting perspectival for the maritime sector and should boost research in the aerospace industry.

4.3 Decentralized Power and Combined Heat and Power Generation Systems

Electricity is mainly produce by centralized power station and distributed by networks. However in developing countries 1.4 billion people are not connected to the electricity grid and despite this situation they have electrical needs. Meanwhile in developed countries, combined heat and power type devices are used to guarantee the autonomy of some devices either for security or for economic reasons.

In developing countries biomass is the main energy source. In these rural areas, wood stoves have very low thermal efficiency (sometimes less than 10 %) and contributes to local deforestation, increasing labor for women and children and insecurity to collect firewood more and more distant. The fumes are also toxic. Installation of efficient wood stoves is critical to their health and safety. These efficient stoves require the use of fume extractor to improve combustion. Thermoelectric generators are a solution to power these fans and to provide a few watts for lighting or for charging mobile phone. Different systems are currently being studied [30–33] and a device is marketed [34]. These systems use Bi_2Te_3 modules and are undersized to withstand wide variations in temperature during wood combustion. The arrival of new materials at higher temperatures should confirm the development of these devices. The thermoelectric performance is not an obstacle compared to improvement brought to combustion efficiency that can go from 10 to 80 % for multifunctional stoves.

In developed countries, the quantity of performing wood stoves is increasing very quickly for economical and environment friendly reasons. These sophisticated stoves need intelligence to control the combustion in order to meet minimum emission requirements. Electric components (sensors, fans, valves, actuators, and microcontrollers) are necessary for these operations. Availability of electricity is essential. In the case of isolated houses used at certain times of the year, second homes, the grid connection can be very expensive for occasional occupants. A system guaranteeing the autonomy of the stove is a great value. By using combined heat and power system [35], the heat going through the TEG is used to heat water. Efficiency of the TEG is no more a problem, the problem is only to get enough electricity.

In conclusion, well-designed systems allow to overcome the low efficiency and can make a significant economic or environmental added value.

4.4 Micro-generation for Sensors and Microelectronics

Competitive industry relies on sensors in its products and in its factories. By incorporating new sensors in factory, manufacturers can improve product quality and reduce downtime. Current intelligent sensors require only a few hundred microwatts or some milliwatts to operate. Power these devices from the electrical network often requires very long cables to provide very little energy and need to plan ahead the passage of these cables. In factories, heat sources are numerous: hot fluid pipes, ovens, steam lines, motors, air conditioning, heating. Very small TEG (a few square millimeters) is a solution to permanently power these sensors. Micropelt [36] and Laird [37] companies are developing such devices. For example, a module $3.3 \times 4.2 \times 1.1$ mm^3 can produce more than 1 mW for a temperature difference of 10 °C and more than 10 mW for a difference of 30 °C. The introduction of phase change materials as a heat storage unit allows the exploitation of temporal temperature changes and can improve these small generators [38].

4.5 Solar Thermoelectric Generator

Massachusetts Institute of Technology [39] has demonstrate a flat-panel solar thermal to electric power conversion technology. The developed solar thermoelectric generators (STEGs) achieved a peak efficiency of 4.6 % under 1 kW m^{-2} solar conditions. The difficulty for this kind of generator is to concentrate the heat on the thermoelectric elements and to find materials that can withstand very high temperature (>1000 °C).

5 Conclusion

For years the development of TEG has been limited to niche markets with high added value like space and extreme environments where liability is critical. The recent availability of new materials and the assembly of TE modules by manufacturers will permit the development of mass market in the transport sector and in combined heat and power systems. The increasing needs of self-powered micro sensors in industry will motivate the development of microTEG. Actual researches for organics TEG are promising and new applications in clothes or human objects can easily be imagined.

References

1. David, M.R.: Chapter 1. Introduction. In: Rowe, D.M. (ed.) CRC Handbook of Thermoelectrics (1995)
2. Snyder, G.J.: Thermoelectrics handbook macro to nano. In: D.M. Rowe, D.S. (eds.) Thermoelectric Power Generation: Efficiency and Compatibility. CRC Press, New York (2006)
3. Goldsmid, H.J.: Theory of thermoelectric refrigeration and generation. In: Introduction to Thermoelectricity, pp. 7–21. Springer, Berlin (2010)
4. TEG-HH-8_module_spec_sheet, http://www.evidentthermo.com/
5. TEG-HH-15_module_spec_sheet, http://www.evidentthermo.com
6. Tegma.: http://tegma.no/
7. tectegcmo-oxide-cmo-cascade-thermoelectric-power-modules, http://tecteg.com/cmo-oxide-cmo-cascade-800c-hot-side-thermoelectric-power-modules/
8. hotblock onboard
9. romny-scientific magnesium silicide modules, http://romny-scientific.com
10. Alphabet Energy's Thermoelectric Advances - Alphabet Energy, http://www.alphabetenergy.com/thermoelectric-advances/
11. Green Car Congress.: Alphabet Energy introduces PowerModules for modular thermoelectric waste heat recovery; partnership with Borla for heavy-duty trucks. http://www.greencarcongress.com/2015/06/20150624-alphabet.html
12. Zhang, Q., Sun, Y., Xu, W., Zhu, D.: Organic thermoelectric materials: emerging green energy materials converting heat to electricity directly and efficiently. Adv. Mater. **26**, 6829–6851 (2014)

13. Montecucco, A., Siviter, J., Knox, A.: Simple, fast and accurate maximum power point tracking converter for thermoelectric generators. In: 2012 IEEE Energy Conversion Congress and Exposition (ECCE), pp. 2777–2783 (2012)
14. Maganga, O., Phillip, N., Burnham, K., Montecucco, A., Siviter, J., Knox, A., Simpson, K.: Hardware implementation of maximum power point tracking for thermoelectric generators. J. Electron. Mater. **43**, 2293–2300 (2014)
15. Yu, C., Chau, K.T.: Thermoelectric automotive waste heat energy recovery using maximum power point tracking. Energy Convers. Manag. **50**, 1506–1512 (2009)
16. Favarel, C., Bédécarrats, J.-P., Kousksou, T., Champier, D.: Numerical optimization of the occupancy rate of thermoelectric generators to produce the highest electrical power. Energy **68**, 104–116 (2014)
17. Montecucco, A., Knox, A.R.: Accurate simulation of thermoelectric power generating systems. Appl. Energy **118**, 166–172 (2014)
18. Montecucco, A., Siviter, J., Knox, A.R.: Constant heat characterisation and geometrical optimisation of thermoelectric generators. Appl. Energy **149**, 248–258 (2015)
19. Yee, S.K., LeBlanc, S., Goodson, K.E., Dames, C.: $ per W metrics for thermoelectric power generation: beyond ZT. Energy Env. Sci. **6**, 2561–2571 (2013)
20. Schwartz, L.I.H.J.: Shure: survey of electric power plants for space applications. In: Fifty-Eight National Meeting of the American Institute of Chemical Engineers Philadelphia, Pennsylvania, 5–9 Dec 1965
21. Voyager, the interstellar mission, http://voyager.jpl.nasa.gov/spacecraft/index.html
22. Radioisotope Thermoelectric Generator, http://solarsystem.nasa.gov/rps/rtg.cfm
23. Alimov: Radioisotope Thermoelectric Generators—Bellona. http://bellona.ru/bellona.org/english_import_area/international/russia/navy/northern_fleet/incidents/31772
24. Welcome to Gentherm Global Power Technologies | Gentherm Global Power Technologies. http://www.genthermglobalpower.com/
25. Crane, D.: Thermoelectric generator performance for passenger vehicles. In: 3rd Thermoelectrics Applications Workshop. Amerigon, Irwnidale, CA (2012)
26. Meisner, G.P.: Skutterudite thermoelectric generator for automotive waste heat recovery. In: 3rd Thermoelectrics Applications Workshop 2012 (2012)
27. Magnetto, D.: HeatReCar : first light commercial vehicle equipped with a TEG. Presented at the 3rd International Conference Thermal Management for EV/HEV, Darmstadt, 24 June 2013
28. Kousksou, T., Bedecarrats, J.-P., Champier, D., Pignolet, P., Brillet, C.: Numerical study of thermoelectric power generation for an helicopter conical nozzle. J. Power Sources **196**, 4026–4032 (2011)
29. Wallace, T.T.: Development of marine thermoelectric heat recovery systems. In: 3rd Thermoelectrics Applications Workshop (2012)
30. O'Shaughnessy, S.M., Deasy, M.J., Doyle, J.V., Robinson, A.J.: Field trial testing of an electricity-producing portable biomass cooking stove in rural Malawi. Energy. Sustain. Dev. **20**, 1–10 (2014)
31. Favarel, C., Champier, D., Kousksou, T., Rozis, J.F., Bédécarrats, J.-P.: thermoelectricity a promising complementary with efficient stoves in off grid areas (2015)
32. Champier, D., Favarel, C., Bedecarrats, J.P., Kousksou, T., Rozis, J.F.: Prototype combined heater/thermoelectric power generator for remote applications. J. Electron. Mater. 1–12 (2013)
33. Rinalde, G.F., Juanico, L.E., Taglialavore, E., Gortari, S., Molina, M.G.: Development of thermoelectric generators for electrification of isolated rural homes. Int. J. Hydrog. Energy. **35**, 5818–5822 (2010)
34. biolite. http://biolitestove.com/

35. Montecucco, A., Siviter, J., Knox, A.R.: A combined heat and power system for solid-fuel stoves using thermoelectric generators. Energy Procedia. **75**, 597–602 (2015)
36. Micropelt: Micropelt thermoelectric generators MPG-D751
37. nextreme Laird: Microscale Thermal and Power Management, http://www.lairdtech.com/products/thermobility-wpg-1
38. Samson, D., Otterpohl, T., Kluge, M., Schmid, U., Becker, T.: Aircraft-specific thermoelectric generator module. J. Electron. Mater. **39**, 2092–2095 (2010)
39. Kraemer, D., Poudel, B., Feng, H.-P., Caylor, J.C., Yu, B., Yan, X., Ma, Y., Wang, X., Wang, D., Muto, A., McEnaney, K., Chiesa, M., Ren, Z., Chen, G.: High-performance flat-panel solar thermoelectric generators with high thermal concentration. Nat. Mater. **10**, 532–538 (2011)

Electron-Spin Resonance of Type II Si-Clathrate Thin Film for New Solar Cell Material

Mitsuo Yamaga, Takumi Kishita, Tetsuji Kume, Koki Uehara, Masaki Nomura, Fumitaka Ohashi, Takayuki Ban and Shuichi Nonomura

Abstract Silicon clathrate thin films, Na_xSi_{136} ($x > 5$), were prepared on Si (111) substrates. The X-ray diffraction (XRD) pattern shows a mixture of the type II Si-clathrate crystalline and amorphous phases. The electron-spin resonance (ESR) spectrum for the Si-clathrate thin film consists of two lines with a set of g value and width, (g, γ(mT)) = (2.005, 1) and (2.002, 0.1). In comparison, the ESR spectra for Na_xSi_{136} (x = 5.5, 11) polycrystalline powders have a fairly broad line with (g, γ(mT)) = ($\sim$2.05, 15) other than the above two lines. Such broad line may be assigned to a Na-Na pair and/or a Na-cluster in the Si-clathrate polycrystalline powders. These ESR results suggest that the dominant line with (g, γ(mT)) = (2.005, 1) observed for the Si-clathrate thin film is assigned to electron trapped at a Si-deficit with a dangling bond created in the amorphous phase.

Keywords Si-clathrate · Thin film · Semiconductor · Electron-spin resonance

1 Introduction

Crystalline silicon (c-Si) solar cells are the most widely used as photovoltaics with high efficiency (25.6 %) [1]. Although amorphous silicon (a-Si) solar cells are sensitive to the visible light, the efficiency (10.2 %) is lower than that of c-Si [1].

M. Yamaga (✉) · T. Kishita · T. Kume
Department of Electrical, Electronic and Computer Engineering,
Gifu University, 501-1193 Gifu, Japan
e-mail: yamaga@gifu-u.ac.jp

K. Uehara · M. Nomura · F. Ohashi · S. Nonomura
Environmental and Renewable Energy Systems Division,
Graduate School of Engineering, Gifu University, 501-1193 Gifu, Japan

T. Ban
Department of Chemistry and Biomolecular Science,
Gifu University, 501-1193 Gifu, Japan

A.Y. Oral and Z.B. Bahsi Oral (eds.), *3rd International Congress on Energy Efficiency and Energy Related Materials (ENEFM2015)*, Springer Proceedings in Energy, DOI 10.1007/978-3-319-45677-5_26

Silicon clathrates (Si-clathrate) were first found as an allotrope of silicon in 1965 [2], and characterized [3, 4]. The Si-clathrates are cage-structured compounds, where cages are formed by covalently bonded Si atoms [2, 4]. Alkali metals intercalated into the cages play an important role for the chemical reaction of the Si-clathrates [5]. The Si-clathrates are classified into type I and type II [2–6]. A unit cell of the type I crystal structure consists of 46 silicon atoms with two Si_{20} and six Si_{24} polyhedra; the chemical composition with eight available Na sites is Na_xSi_{46} ($0 \leq x \leq 8$). A unit cell of the type II crystal structure consists of 136 silicon atoms with sixteen Si_{20} and eight Si_{28} polyhedra; the chemical composition is Na_xSi_{136} ($0 \leq x \leq 24$). The band-gap energy of the type II Si-clathrate was calculated, and observed experimentally to be $\sim$1.8 eV [7, 8], close to that of the a-Si. The direct band-to-band transition leads to strong absorption coefficients. Thus, the type II Si-clathrate thin film is a candidate for new photovoltaics materials.

In this paper, we reports preparation of the type II Si-clathrate thin film and its properties obtained using X-ray diffraction (XRD) and electron-spin resonance (ESR) methods.

2 Experimental Procedure

Thin films of the type II Si-clathrate were grown on Si (111) substrates followed by three different thermal annealing processes [9]. Firstly, Si (111) substrate and Na lump in a Ta crucible were sealed in a stainless container in an Ar atmosphere and annealed at 580 °C for 48 h. This first process was preparation of a NaSi film as a precursor. Secondly, the film, which was moved into a quartz tube, was annealed in a vacuum at 400 °C for 3 h to synthesize Na-contained type II Si clathrate thin film. Finally, in order to remove Na in the Si-clathrate thin film, the thin film was annealed at 460 °C for 20 h in an Ar atmosphere containing iodine. In order to compare the crystalline thin film with Na_xSi_{136} polycrystalline powders, the powders were also prepared using the method described in previous papers [10–12].

The crystal structure of the thin films and the powders was determined by XRD patterns measured using the Cu K α line from a Rigaku RINT Ultima. Na concentrations (x) in the type II Si-clathrate polycrystalline powders were estimated to be 5.5 and 11 by the refinement of the structure using the Rietveld method, but that of the thin film could not be estimated. According to our experience of the powder preparation, x is expected to be above 5.

ESR measurements were done using a Bruker Biospin EMXmicro X-band spectrometer with 9.45–9.54 GHz in a range of 110–500 K in Gifu University and a Brucker E500 with $\sim$9.64 GHz in the range of 3.6–300 K in the Institute of Molecular Science, Japan. These spectrometers employed 100 kHz field modulation and microwave powers were 0.1–1.0 mW.

3 Experiments

3.1 XRD Pattern

Figure 1 shows the XRD pattern of the Na_xSi_{136} ($x > 5$) thin film. The pattern consists of several sharp lines around 20°, 31°, 35°, and 53°, and fairly broad band around 18°. The intense line at 28.4° is due to the (111) plane of a Si-substrate. The positions of the former sharp lines are in agreement with those of the type II Si-clathrate obtained from number 89-5535 in the JCPDS-card of the XRD database. The broad band is due to an amorphous silicon phase in the thin film.

3.2 ESR Spectra

Figure 2 shows the ESR spectrum observed at 110 K and 9.541 GHz for the Na_xSi_{136} thin film on a Si (111) substrate, compared with that for a Si (111) substrate. These spectra indicate that the dominant ESR signal originates from the film.

When the temperature decreased from 110 K down to 3.6 K, the intensity of the dominant line was enhanced in one order of a magnitude, and its g value and width were the same as those at 110 K. Figure 3 shows microwave-power dependence of the ESR spectra for the Na_xSi_{136} thin film at 3.6 K. Although the ESR intensity decreases with a decrease of microwave power, the sharp and weak line appears clearly at 342.0 mT below 1 mW. The g value (2.003) is coincident with that (2.0023) of free electron. Such sharp line is assigned to conduction electrons, being

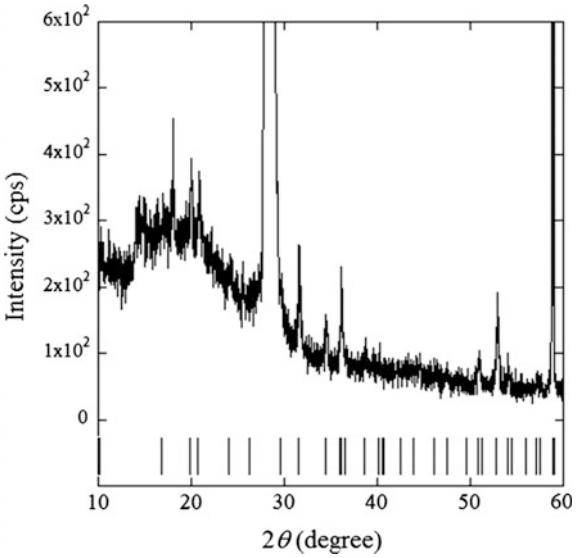

Fig. 1 XDR pattern of Si-clathrate thin film, Na_xSi_{136} ($x > 5$)

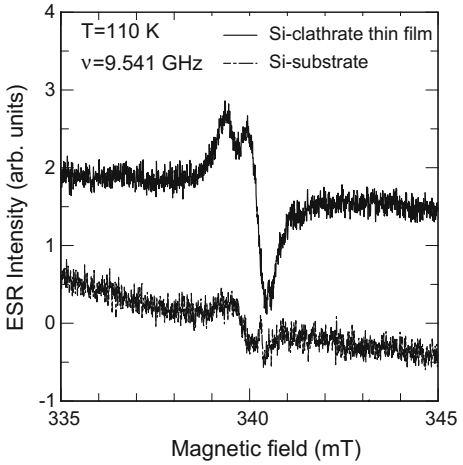

Fig. 2 ESR spectra of Na_xSi_{136} thin film and Si(111) substrate

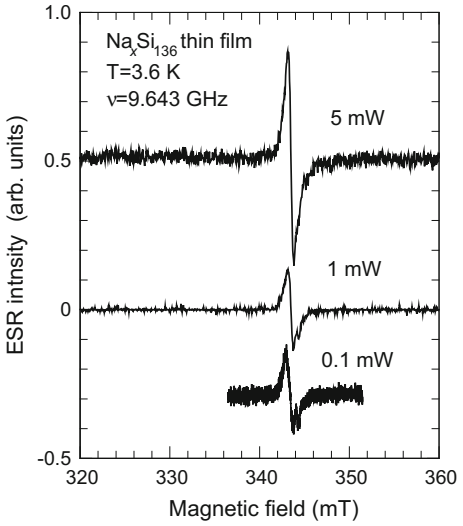

Fig. 3 Microwave-power dependence of ESR spectra for Na_xSi_{136} thin film at 3.6 K

ascribed to free electrons releasing from Na atoms contained in cages of the Si-clathrate. The g value (2.005) and width (1 mT) of the dominant line at 341.6 mT is larger than those (2.002, 0.2 mT) of conduction electron.

Figure 4a shows the ESR spectra for the $Na_{5.5}Si_{136}$ polycrystalline powder at 3.6 and 110 K. The ESR spectrum at 3.6 K consists of several lines. The quartet hyperfine-structure (*hfs*) lines with a g value of 2.036, magnetic field separation of 13.3 mT, and a width (γ) of 0.6 mT, denoted by A1-A4, are due to nuclear spin (I = 3/2) of an isolated Na atom [13, 14]. A single broad line with γ = 15 mT, denoted by C, has the same g value as the quartet *hfs* lines. The C line has been assigned to a Na-Na pair and/or a Na-cluster [13, 14]. A relatively narrow single

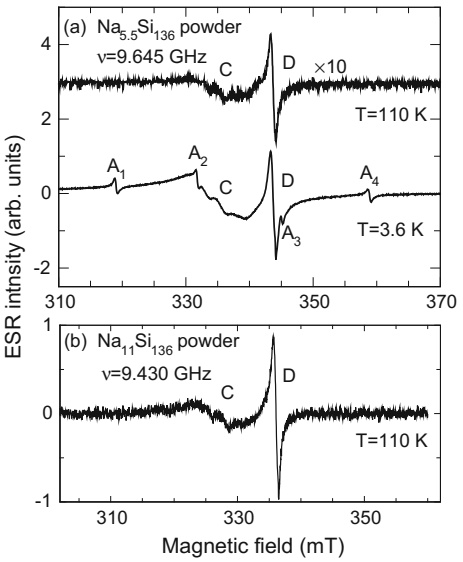

Fig. 4 **a** ESR spectra for $Na_{5.5}Si_{136}$ powder at 3.6 and 110 K. **b** ESR spectrum for $Na_{11}Si_{136}$ powder at 110 K

line with $g = 2.005$ and $\gamma = 1$ mT, denoted by D, is coincident with the dominant line for the Na_xSi_{136} thin film as shown in Fig. 3. When the temperature increases up to 110 K, the ESR spectrum decreases with one order of a magnitude in intensity, the A1-A4 lines disappear at 110 K and the C and D lines remain.

The ESR spectrum for the $Na_{11}Si_{136}$ polycrystalline powder sample at 110 K, as shown in Fig. 4b, is coincident with that for the $Na_{5.5}Si_{136}$ polycrystalline powder sample at 110 K.

The g values and widths of the dominant line for the thin film and the D line for the powders are in agreement with those of Si-deficits associated with the dangling bonds in amorphous Si [15]. As a consequence, these lines are assigned to electrons trapped at Si-deficits with dangling bonds, created in the Si-clathrate thin film and the polycrystalline powders.

4 Discussion and Conclusions

In the previous paper [9], the thin films of the Si-clathrates were grown on (100) and (111) oriented Si-substrates. The first process to deposit a zintl-phase NaSi thin film on the substrate is very important for the selective growth of the type I or II Si-clathrate thin film. The type I or II Si-clathrate thin film is preferentially synthesized on the (100) or (111) Si-substrate, respectively. Another important point is the reacting temperature, which determines the NaSi synthesizing rate. We prepared the type II Si-clathrate thin films with the following conditions of the first process; (i) the (111) Si-substrate and (ii) the reacting temperature of 580 °C.

The 580 °C reacting temperature is below 650 °C obtained for the type II Si-clathrate polycrystalline powders because slow growth is required to form the thin films. However, the XRD pattern of the thin film shows a mixture of the type II phase and the amorphous phase as shown in Fig. 1.

We consider the ESR results for the Na_xSi_{136} ($x > 5$) thin film and the Na_xSi_{136} ($x = 5.5$, 11) polycrystalline powder samples when measured at 3.6 and 110 K, taking account of the XRD patterns of these samples. The Si-clathrate powders consist dominantly of the type II phase. The ESR spectrum of the $Na_{5.5}Si_{136}$ powder consists of several lines assigned to isolated Na atoms, Na-Na pairs, Na-clusters, Si-deficits with dangling bonds [13, 14]. The dangling bond may be produced under the third process to remove Na atoms from the cages. The ESR signal from isolated Na atoms disappears for $Na_{11}Si_{136}$ powder. On the contrary, the ESR spectrum for the Na_xSi_{136} ($x > 5$) thin film consists dominantly of the single line due to Si-deficits with dangling bonds. The ESR spectrum completely lacks the signals related to Na atoms, Na-Na pairs and Na-clusters because of the mixture of the crystalline and amorphous phases.

In conclusions, the XRD and ESR results of the Na_xSi_{136} ($x > 5$) thin film, compared with the Na_xSi_{136} ($x = 5.5$, 11) powders, demonstrate that the thin film is composed of the type II crystalline and amorphous phases. The ESR signal is due to electrons trapped at the Si-deficits with dangling bonds in the amorphous phase. It is important to reduce the amorphous phase in the thin film for solar cell materials. Therefore, we have to examine the formation process of the crystalline and amorphous phases in the Si-clathrate thin film.

Acknowledgments This work was supported by the Advanced Low Carbon Technology Research and Development Program (ALCA, Project Stage) from Japan Science and Technology Agency (JST). ESR measurements at low temperatures were carried out under Nanotechnology Platform Japan Program (S-14-MS-1072) of the Institute of Molecular Science, Japan.

References

1. Green, M.A., Emery, K., Hishikawa, Y., Warta, W., Dunlop, D.: Solar cell efficiency tables (version 46). Prog. Photovolt.: Res. Appl. **23**, 805–812 (2015). doi:10.1002/pip.2637
2. Kasper, J.S., Hagenmuller, P., Pouchard, M., Cros, C.: Clathrate structure of sicon Na_8Si_{46} and Na_xSi_{136} ($x < 11$). Science **150**, 1713–1714 (1965). doi:10.1126/science.150.3704.1713
3. Cros, C., Pouchard, M., Hagenmuller, P.: Cur une nouvelle famille de clathrates mineraux isotypes des hydrates de gaz et de liquids. Interpretation de resultats obtenus. J. Solid State Chem. **2**, 570–581 (1970). doi:10.1016/0022-4596(70)90053-8
4. Roy, S.B., Sim, K.E., Caplin, A.D.: The insulator-to-metal transition in Si–Na 'clathrate' compounds: a search for superconductivity. Philos. Mag. B **65**, 1445–1450 (1992). doi:10.1080/13642819208215112
5. Bobev, S., Sevov, S.: Clathrates of group 14 with alkali metals: an exploration. J. Solid State Chem. **153**, 92–105 (2000). doi:10.1006/jssc.2000.8755
6. Kovnir, K.A., Shevelkov, A.V.: Semiconducting clathrates: synthesis, structure and properties. Russian Chem. Rev. **73**(9), 923–938 (2004). doi:10.1070/RC2004v073n09ABEH000916

7. Demkov, A.A., Sankey, O.F., Schmidt, K.E., Adams, G.B., O'Keeffe, M.: Theoretical investigation of alkali-metal doping in Si clathrates. Phys. Rev. B **50**, 17001–17008 (1994). doi:10.1103/PhysRevB.50.17001
8. Himeno, R., Kume, T., Ohashi, F., Ban, T., Nonomura, S.: Optical absorption properties of Na_xSi_{136} clathrate studied by diffuse reflection spectroscopy. J. Alloys Compd. **574**, 398–401 (2013). doi:10.1016/j.allcom.2013.05.176
9. Ohashi, F., Iwai, Y., Noguchi, A., Sugiyama, T., Hattori, M., Ogawa, T., Himeno, R., Kume, T., Ban, T., Nonomura, S.: Thin-film formation of Si clathrates on Si wafers. J. Phys. Chem. Solids **75**, 518–522 (2014). doi:10.10161/j.jpcs.2013.12.009
10. Ohashi, F., Hattori, M., Ogura, T., Koketsu, Y., Himeno, R., Kume, T., Ban, T., Iida, T., Habuchi, H., Natsuhara, H., Nonomura, S.: High-yield synthesis of semiconductive type-II Si clathrates with Na content. J. Non-Cryst. Solids **358**, 2134–2137 (2012). doi:10.1016/j.jnoncrysol.2011.12.058
11. Himeno, R., Ohashi, F., Kume, T., Asai, E., Ban, T., Suzuki, T., Iida, T., Habuchi, H., Tsutsumi, Y., Natsuhara, H., Nonomura, S.: Optical band gap of semiconductive type II Si clathrate purified by centrifugation. J. Non-Cryst. Solids **358**, 2138–2140 (2012). doi:10.1016/j.jnoncrysol.2011.12.064
12. Ban, T., Ogura, T., Ohashi, Y., Himeno, R., Ohashi, F., Kume, T., Ohya, Y., Natsuhara, H., Iida, T., Habuchi, H., Nonomura, S.: Complex changes in the framework of endohedrally Na-doped type II Si clathrates with respect to Na content. J. Mater. Sci. **48**, 989–996 (2013). doi:10.1007/s10853-012-6886-0
13. Yahiro, H., Yamaji, K., Shiotani, M., Yamanaka, S., Ishikawa, M.: An ESR study on the thermal electon excitation of a sodium atom incorporated in a silicon clathrate compound. Chem. Phys. Lett. **246**, 167–170 (1995). doi:10.1016/0009-2614(95)01110-U
14. Ammar, A., Cros, C., Pouchard, M., Jaussaud, N., Bassat, J.-M., Villeneuve, G., Duttine, M., Menetrier, M., Reny, E.: On the clathrate form of elemental silicon, Si_{136}: preparation and characterisation of Na_xSi_{136} ($x \rightarrow 0$). Solid State Sci. **6**, 393–400 (2004). doi:10.1016/j.solidstatesciences.2004.02.006
15. Morigaki, K.: Physics of Amorphous Semiconductors, pp. 67–97 and pp. 173–216. Imperial College Press and World Scientific Pub., Singapore (1999)

The Power Supply of the Hydrogen Generator

Krzysztof Górecki, Janusz Zarębski, Paweł Górecki and Sławomir Halbryt

Abstract In the paper the circuit supplying the hydrogen generator is considered. The idea of operation of this circuit, its simulation schema and the results of computations are presented. These computations were performed for a wide range of frequency of the supplying current. The correctness of the idea of operation of the supplying circuit is shown and the dependence of efficiency of the hydrogen generator on frequency of the supplying current is presented.

Keywords Hydrogen generator · Switch-mode power supply · SPICE

1 Introduction

Nowadays, greater and greater balance is paid to the environmental protection and the development of technology which makes it possible to generate electrical or thermal energy at possibly low emission of CO_2. The assignment is possibly cashable with leaning technologies using reaction of oxygenation of hydrogen. A product of such reaction is aqueous vapour and electrical or thermal energy [1].

In the literature [2–5] three basic methods of production of hydrogen are presented: reforming of earth gas [2], transformation of biomass [5] and electrolysis [3–5]. The electrolysis deserves special attention as it makes possible generation of hydrogen locally, where it has to be used, and during this process no waste material is produced. According to the data published by the American Department of Energy [5] up to the year 2020 a double decrease of costs of the electrolysis is expected in comparison to the year 2011.

K. Górecki (✉) · J. Zarębski · P. Górecki
Department of Marine Electronics, Gdynia Maritime University,
Morska 83, 81-225 Gdynia, Poland
e-mail: k.gorecki@we.am.gdynia.pl

S. Halbryt
SESCOM S.A., Gdańsk, Poland

A.Y. Oral and Z.B. Bahsi Oral (eds.), *3rd International Congress on Energy Efficiency and Energy Related Materials (ENEFM2015)*, Springer Proceedings in Energy, DOI 10.1007/978-3-319-45677-5_27

Therefore, it is essential to reduce costs involved to gain essential improvement of construction of electrolysers and systems supplying them. Typically, the electrolysis is realised for the aqueous solution of KOH [3, 4] supplied from the dc source. From the point of view of power supply the electrolyser can be treated as a non-linear RLC circuit [1, 4]. Thereby, at least one value of frequency at which the module of electrolyser impedance attains the minimum must exist and the current of its power supply attains the maximum. From the paper [1] it results that the power supply of the electrolyser with the suitable variable signal assures improvement of watt-hour efficiency and efficiency of the electrolysis.

In the paper the practical solution of the system supplying the generator of hydrogen with the variable signal of the shape of the rectangular pulses train with regulated frequency is presented and analysed.

2 Structure of the Power Supply

In Fig. 1 the schema of the supplying circuit is presented. The considered circuit is supplied from the line across the impulse-feeder PS1, which assures the constants output voltage equal to 7.5 V at the output current not exceeding 80 A.

The output voltage of this feeder is switched by an electronic switch consisting of 2 power MOS transistors of the type IRL3803 of low on-resistance of the chan-nel R_{ON} (7 mΩ) operating in the Totem-Pole circuit. The analysis of this circuit loaded with the considered hydrogen generator is presented in the paper [6].

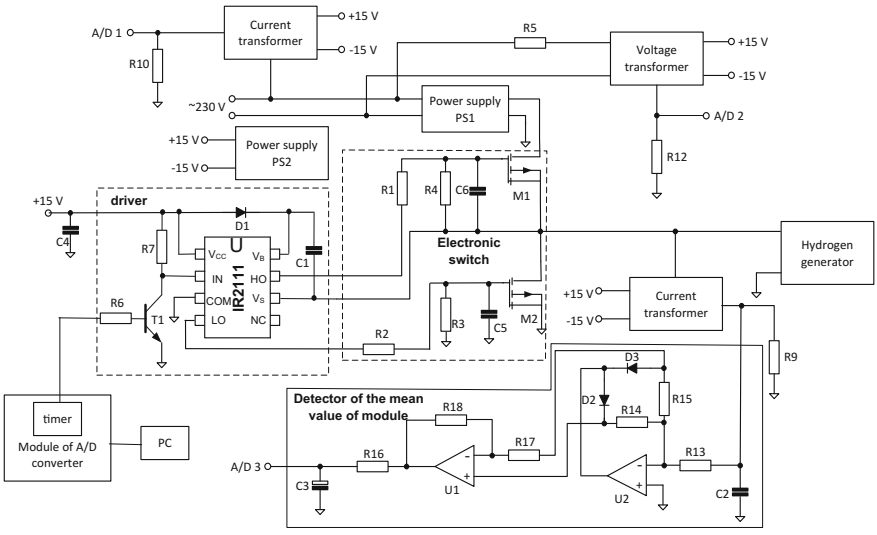

Fig. 1 Schema of the supplying circuit

The value of the current feeding the generator is monitored by the current transformer. The output signal of this transformer is given on the input of the detector of the mean value of the module to which the value of the mass of generated hydrogen [1, 4] is proportional. This detector was built with the use of operating-amplifiers of the type AD712JNZ and diodes UF4007.

The module of the A/D converter of the type USB-1608GX-2AO, containing among others the timer and 16 analog inputs, measures the output voltage of the detector of the mean value of the module and the voltage proportional to the line voltage and the current received from the line (nodes A/D 1—A/D 3). Values of these voltages are used to delimit efficiency of the process of hydrogen generation. The computer PC registers values of voltages measured by the module of the A/D converter and controls the timer producing the rectangular pulses train of regulated frequency.

For the low current efficiency of the timer and the low value of its output voltage the inverter consisting of the transistor T_1, resistors R6, R7 and the driver IR2111 is included between the output of this timer and gates of transistors.

To convert currents and the supply voltage to voltages of values measurable by means of the applied module of the A/D converter the current and voltage transformers LEM of the type LA 100-P and LV 25-P, characterised by the band from 0 to 200 kHz and the range of the measured currents to 150 A and voltages to 500 V, are used. The feeder PS2 produces the constant voltages ±15 V.

3 Simulation Schema of the Considered Supplying Circuit

In order to evaluate the correctness of operation of the worked out circuit computer analyses of principle power and measuring parts of the considered circuit were conducted. In the analyses the simulation model shown in Fig. 2 was used.

In the presented circuit the voltage source V_{zas} together with the resistor R_{zas} represent the impulse-feeder of the constant voltage PS1. Transistors M_1 and M_2

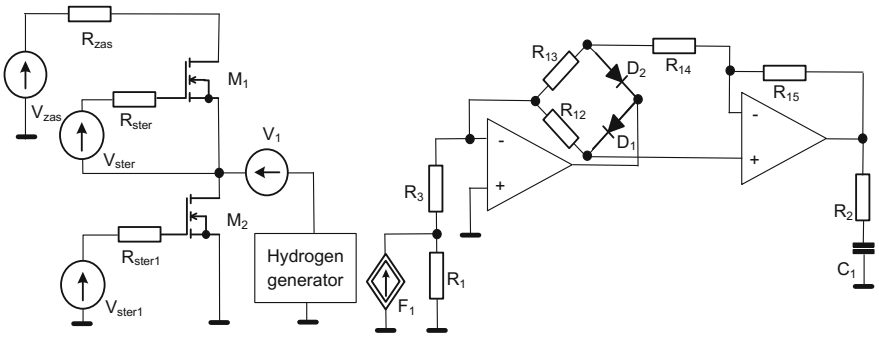

Fig. 2 Simulation schema of the worked out circuit

model the electronic switch with the use of the model for SPICE offered by the producer. The supplementary schema of the hydrogen generator in the form of the non-linear DRLC circuit is described in the papers [1, 6]. Voltage sources V_{ster} and V_{ster1} with resistors R_{ster} and R_{ster1} model the driver IR2111 with the timer. The voltage from sources V_{ster} and V_{ster1} has the rectangular waveform of levels equal to zero and 10 V, the duty factor equal to 0.5 and regulated frequency.

The controlled current source F_1 together with the voltage source V_1 of zero-efficiency represent the current transformer. The detector of the mean value of the module contains two operating-amplifiers, diodes D_1 and D_2, resistors R_3, R_{12}, R_{13}, R_{14}, R_{15}, R_2 and the capacitor C_1. The voltage on this capacitor is proportional to the mean value of the module of the current feeding the hydrogen generator.

4 Computation Results

Using the simulation schema of the considered supplying circuit many computer analyses were conducted and their results illustrate the influence of different factors on the operation of the considered circuit. The selected results, corresponding to the operation of this circuit at the steady-state are presented below.

In Fig. 3 the waveforms of the voltage (Fig. 3a) and the current (Fig. 3b) feeding the hydrogen generator at frequency of the signal from the source V_{ster} equal to 100 kHz are presented. The analogous waveforms of the voltage and the current obtained at frequency equal to 100 Hz are shown in Fig. 4.

As it is visible, the waveforms of the voltage in Figs. 3 and 4 do not have the expected shape of the square wave, and the waveforms of the current—the shape of the triangular wave. The observed character of the dependence $U_{zas}(t)$ and $I_{zas}(t)$ results among others from the non-zero value resistance R_{ON} of the applied MOS transistors and resistance of leads of these devices. Values of the mentioned resistances are on the level from several to a dozen or so mΩ, but at values of the

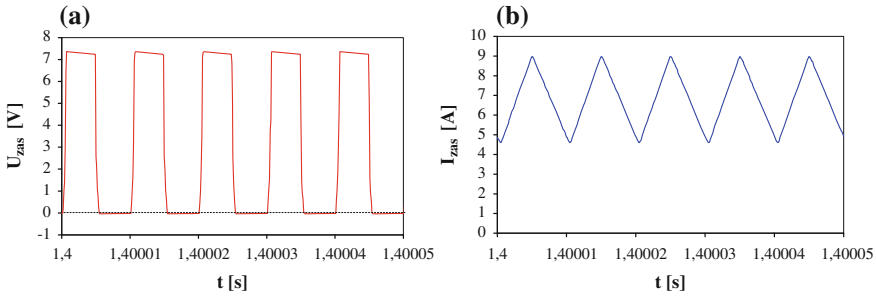

Fig. 3 Calculated waveforms of the voltage (**a**) and the current (**b**) of the power supply of the hydrogen generator at frequency equal to 100 kHz

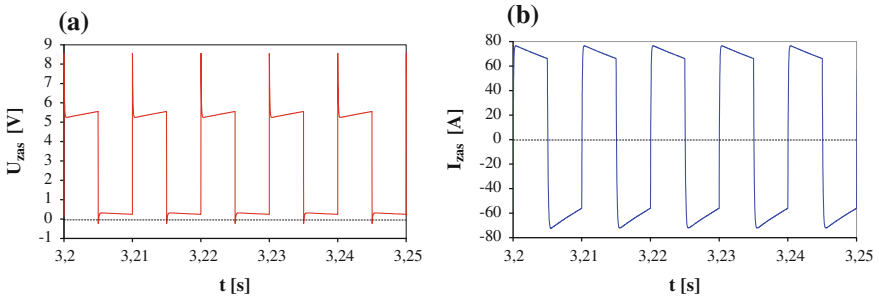

Fig. 4 Calculated waveforms of the voltage (**a**) and the current (**b**) of the power supply of the hydrogen generator at frequency equal to 100 Hz

feeding current exceeding tens amperes these cause visible falls of the output voltage.

In Fig. 3a it is visible that at high frequency of switching, the voltage feeding accepts at some time intervals the negative values, testifying to the reverse mode of the operation of the transistor M_2. In turn, in Fig. 3b it is visible that within the range of high frequency there appears a large dc component of the feeding current. The presented triangular shape of $I_{zas}(t)$ waveforms results from the inductive character of impedance of the hydrogen generator in the range of high frequency [1].

In Fig. 4a it is visible that the feeding voltage accepts only positives values, whereas in Fig. 4b one can notice that the supply current accepts values both positive and negative. In comparison to the results presented in Fig. 3, it can be noticed that at the lower value of frequency greater (even ninefold) maximum values of the current are observed, which is an effect of the fall of the module of impedance of the hydrogen generator at the fall of frequency.

Figure 5 illustrates the results of operation of the detector of the mean value of the module of the current feeding the hydrogen generator at frequency equal to 100 kHz (Fig. 5a) and 100 Hz (Fig. 5b). In this figure, the blue line marks the waveform of the voltage U_C on the output of this detector, the red line—the waveform of the current of the power supply I_{zas} of this generator, and the black line—appoints analytically the mean value of the module of this current.

As it is visible, the detector of the mean value of the module of the current feeding the hydrogen generator operates correctly, which is confirmed by convergence of the detector output voltage and the mean value of the module of the current of the power supply. It is worth noticing that the output voltage of the considered circuit decreases when frequency increases.

In Fig. 6 the dependence of hydrogen masses generated within 1 min on frequency at two concentrations of the water solution of KOH in the electrolyser are shown. In this figure the red curve corresponds to high concentration of the solution, and the blue curve—to low.

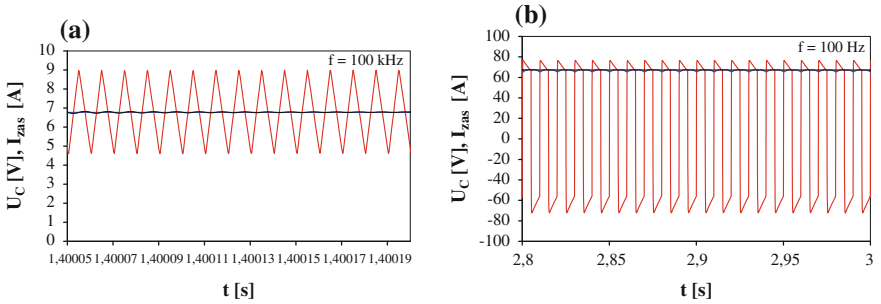

Fig. 5 Calculated waveforms of the voltage at the integrating circuit and of the current feeding the hydrogen generator at frequency equal to 100 kHz (**a**) and 100 Hz (**b**)

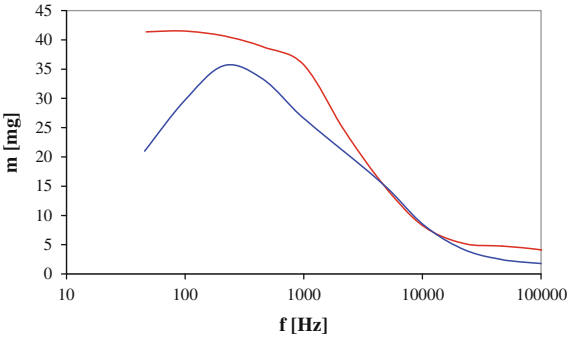

Fig. 6 Calculated dependences of hydrogen masses generated during 1 min on frequency

As it is visible, efficiency of the process of the hydrogen production depends on frequency of the feeding current and on concentration of the solution. The maximum efficiency of the process is observed at frequency below 100 Hz. The fall of solution concentration causes essential degradation of the process efficiency. This fall is the greatest at low frequency and for f ≈ 50 Hz it amounts even 50 %.

In order to verify the correctness of the project, the considered feeding circuit was constructed and tests of its operation at loading by the hydrogen generator and different values of the switching frequency in the range from 100 Hz to 200 kHz were performed. In all cases on the output of the power supply the measured values and the shapes of the voltage and the current were nearing the results of calculations.

5 Conclusions

In the paper the power supply of the hydrogen generator designed and constructed by the authors is presented. This circuit makes it possible to feed the considered generator with the voltage of the waveform nearing the rectangular pulses train of regulated frequency. Current efficiency of the circuit amounts theoretically to 70 A, but in practice it is relative to impedance of the load.

For the considered electrolyser, the highest efficiency of the process of the hydrogen production is obtained at frequency equal to about 200 Hz (at low concentration of KOH) and about 50 Hz (at high concentration of KOH). The maximum efficiency of the process amounts 30–40 mg/min.

The presented results of calculations of the considered circuit performed with the use of physical models of components prove correctness of the project. The results of measurement of the real circuit confirm reliability of the applied models of components of the circuit and the obtained results of calculations.

References

1. Górecki, K., Zarębski, J., Górecki, P., Halbryt, S.: Modelling and the analysis of the power supply system for the generator of hydrogen. In: Oral, A.Y., Bahsi Oral, Z.B., Ozer, M. (eds.) 2nd International Congress on Energy Efficiency and Energy Related Materials (ENEFM2014), pp. 451–457. Springer, Heidelberg (2015), doi:10.1007/978-3-319-16901-9_54
2. Mizeraczyk, J., Urashima, K., Jasiński, M., Dors, M.: Hydrogen production from gaseous fuels by plasmas—a review. Int. J. Plasma Environ. Sci. Technol. **8**(2), 89–97 (2014)
3. Mazloomi, K., Sulaiman, N., Ahmad, S.A., Yunus, N.A.: Analysis of the frequency response of a water electrolysis cell. Int. J. Electrochem. Sci. **8**(3), 3731–3739 (2013)
4. Mazloomi, K., Sulaiman, N., Moayedi, H.: An investigation into the electrical impedance of water electrolysis cells—with a view to saving energy. Int. J. Electrochem. Sci. **7**(4), 3466–3481 (2012)
5. Randolph, K.: Hydrogen production—session introduction. In: 2013 Annual Merit Review and Peer Evaluation Meeting, U.S. DOE, 16 May 2013
6. Górecki, P., Górecki, K.: The influence of a mounting manner of power MOS transistors on characteristics of the Totem-Pole circuit with RLC load. Microelectron. Int. **33**(3), 176–180 (2016)

The Use of Photo-Voltaic Panels to Charge Mobile Electronic Devices

Paweł Górecki, Krzysztof Górecki, Ewa Krac and Janusz Zarębski

Abstract In the paper the circuit to charge mobile electronic devices and the results of measurements of this circuit are presented. The construction of the presented circuit is analysed and the influence of the selection of the photovoltaic panel and optical power density on its surface on current efficiency of the considered circuit are discussed. The directions of the development of the worked out and constructed circuit are pointed.

Keywords Photo-voltaic panels · Charging system · Mobile electronic devices

1 Introduction

The development of electronic technology causes that more and more often photo-voltaic panels are used to power supply different kinds of devices [1, 2]. The well-known ones are, among other things, vehicles supplied with solar energy, systems of decorative and road lighting, and even cool boxes [3]. On the other hand, the development of tourism and general access to mobile electronic devices (laptops, mobile phones, smart-phones) cause problems with recharging the used energy in batteries of these devices. During high tourist season, when intensity of solar radiation is high, the necessary energy to charge these devices can be taken from photo-voltaic panels [3, 4].

Typically, the voltage obtained from the photo-voltaic panel is different from the value of the voltage required by the battery of a mobile device. So, in order to assure high watt-hour efficiency of the process of conversion of energy in the considered system, the use of the switch-mode power supply system is indispensable [5, 6]. Additionally, in order to be unaffected by temporary cut-offs of

P. Górecki · K. Górecki (✉) · E. Krac · J. Zarębski
Department of Marine Electronics, Gdynia Maritime University,
Morska 83, 81-225 Gdynia, Poland
e-mail: k.gorecki@we.am.gdynia.pl

A.Y. Oral and Z.B. Bahsi Oral (eds.), *3rd International Congress on Energy Efficiency and Energy Related Materials (ENEFM2015)*, Springer Proceedings in Energy, DOI 10.1007/978-3-319-45677-5_28

electrical energy (eg. during cloudiness), the power supply system should be equipped with the battery.

In the paper the project and the results of measurements of the power system supplying mobile devices with the use of photo-voltaic panels are presented. The structure of the worked out system and the construction of its block components are described. Furthermore, the analysis of its operation at different load and different conditions of lighting of the photo-voltaic panels is performed. The influence of parameters of the applied photo-voltaic panel on exploitive characteristics of the system is also analysed. The results of measurements of the constructed power supply system, operating at the selected conditions of lighting and load confirmed the correctness of theoretical considerations.

2 Structure of the Power Supply System

In the paper [4] the structure of the circuits charging laptops, shown in Figs. 1, was proposed.

As it is visible, this circuit contains 5 components: the photovoltaic panel, the battery, 2 switch-mode voltage regulators containing dc-dc converters—step-down the voltage and step-up the voltage and the linear voltage regulator. The load of the considered circuit is a laptop or some other mobile electronic equipment. The buck converter is used to step-down the voltage obtained from the photovoltaic panel (typically equal to about 30 V) to the value corresponding to the voltage on the battery. In turn, the boost converter makes it possible to step-up the value of the voltage obtained from the battery to the level indispensable to power supply the laptop (typically equal to about 19 V). The use of these converters makes it possible to obtain high watt-hour efficiency of the process of transformation of electrical energy between the photovoltaic panel and the laptop [3, 5, 7, 8]. The linear voltage regulator produces the voltage equal to 18 V to power supply controllers of switch-mode voltage regulators.

The battery is necessary in the station's structure to provide continuity of power supply for laptops, also at nights and on cloudy days. The lead-acid battery is used because of its high value of capacity (equal to 40 Ah) and a relatively high value of

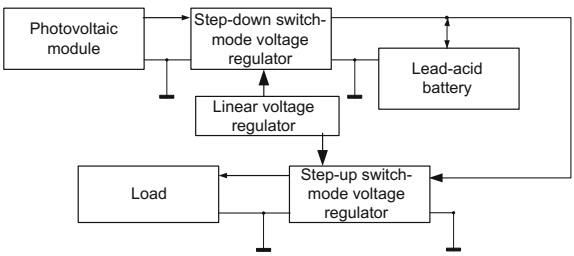

Fig. 1 Block diagram of the circuit charging laptops

the nominal voltage equal to 12 V. In the state of loading the voltage increases to about 13.9 V and in the state of discharge—decreases to about 10.8 V.

The assurance of the effective battery charge demands stabilisation of the output voltage of the buck converter equal to 13.9 V, and the output voltage of the boost converter—equal to 19 V. To this end, in each of the considered voltage regulators the PWM controller UC3842, described in the paper [9], is used.

The detailed description of both mentioned switch-mode voltage regulators is presented in the paper [4]. In the cited work the measured characteristics of the considered regulators supplied from the dc voltage source are also presented.

3 Investigations Results

Using the circuit described in the paper [4] the measurements of its characteristics are performed, using 2 kinds of photovoltaic panels operating at different values of power density of radiation on their surface. The results of these measurements are presented in Figs. 2, 3, 4 and 5.

Figure 2 presents the measured current-voltage characteristics of two panels of the area equal to about 1.5 m^2: monocrystalline panel SGM -250D and amorphous panel SG -HN-120GG. The measurements were performed at 3 values of power density of radiation on the panels surface equal to 354, 246 and 142 W/m^2, respectively by means of the measuring-set described in the paper [10].

As one can notice the amorphous panel has considerably smaller current efficiency than the monocrystalline panel, which results among other things in almost the near double difference between the nominal values of the power provided by these panels [11]. At the highest value of power density the occlusal current of the monocrystalline panel riches 4.8 A, and amorphous—only just 1 A.

In turn, a decrease in power density of radiation by about 30 % causes a decrease in the occlusal current of the monocrystalline panel by about 25 %. As a result of absorption of radiation, the temperature of the panel situated in the measuring-chamber described in the paper [10] and operating at the greatest power

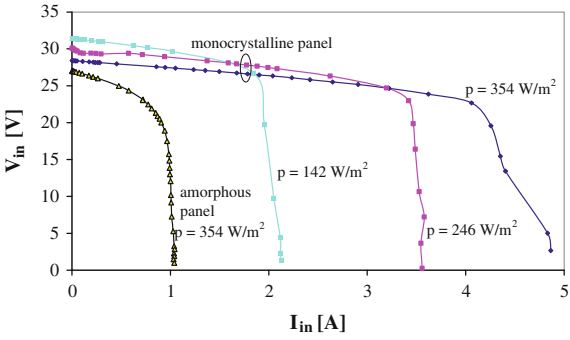

Fig. 2 Measured dc current-voltage characteristics of the considered panels

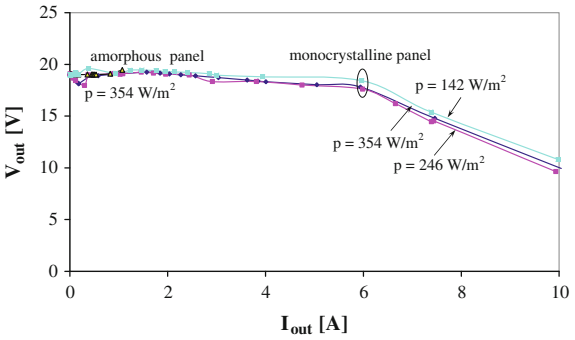

Fig. 3 Measured output characteristics of considered circuit

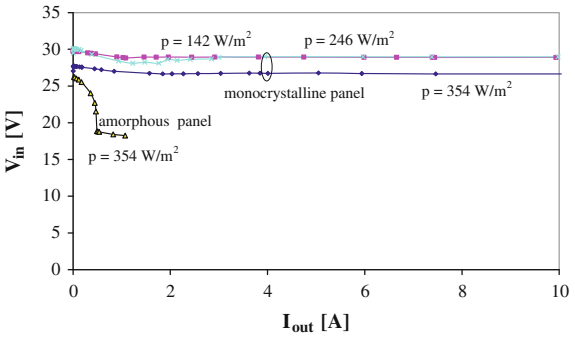

Fig. 4 Measured dependences of the input voltage of the considered circuit on its output current

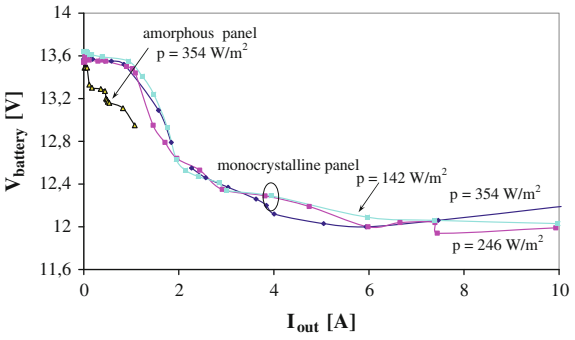

Fig. 5 Measured dependences of the battery voltage on the output current of the considered circuit

density grew up to 87 °C, and at smaller values of power density—accordingly to 72 and 53 °C. This difference of temperature also causes the differences in values of the voltage on the panel in the range of small currents.

In Fig. 3 the measured output characteristics of considered circuit, operating at the power supplying in turns both the considered panels at different values of power density of radiation are presented.

As one can notice, courses of the considered characteristics obtained at the power supply from the monocrystalline panel practically do not depend on power density of radiation on the surface of the panel. This results from the stabilising role of the battery assuring almost the constant value of the input voltage of the step-up voltage regulator. After exceeding by the output current the value equal to about 6 A a decrease in the circuit output voltage, resulting from energy losses in semiconductor devices of the boost converter (the MOS transistor and the diode) [7, 12] is observed. For the amorphous panel, the characteristic was measured only for the current $I_{out} < 1.2$ A, because at this value of the current I_{out} the input voltage V_{in} on the panel decreases to the value 16 V (Fig. 4). This value is too small to obtain the minimum value of the output voltage of the linear voltage regulator indispensable to power supply PWM controllers UC3842 contained in both switch-mode regulators. It results in obtaining at the output of the circuit the voltage of the value equal to the difference between the battery voltage and the voltage drop on the diode. This value is too small to power supply a mobile device (a laptop). From Fig. 4 it results also that the voltage on the monocrystalline panel, in the whole range of changes of the output current, is practically constant.

Dependences of the voltage on the battery on the output current presented in Fig. 5 show that at the output current exceeding 1 A, conducted losses in semiconductor devices are so large that it becomes impossible to deliver from the output of the step-down voltage regulator the current sufficient to load the battery and simultaneously to supply the step-up voltage regulator. The fall of the voltage on the battery at the height of the current I_{out}, observed in Fig. 5, shows that the considered circuit can charge laptops with time intervals. After the discharge of the battery, it is indispensable to switch-off the load in order to charge this element. Charging the battery lasts several minutes. Such a runtime mode is typical for this type of circuits to which only for a short time the load is joined, and for the most part of operation—the battery is loaded.

4 Conclusions

In the paper the circuit to charge mobile electronic equipment with the use of photovoltaic panels and the results of measurements of the constructed circuit are presented. Investigations were performed at the power supply of the circuit from two different photovoltaic panels operating at different values of light-power density on their surface.

From the obtained results of measurements it is easy to observe that the essential influence on the properties of the considered circuit has current efficiency of the applied photovoltaic panels. If this efficiency is too small a fall in the panel output voltage is so large that it makes it impossible to obtain the desirable value of the voltage supplying PWM controllers. Thereby, the output of the circuit decreases to the value equal to the difference between the battery voltage and the voltage drop on the forward biased diode in the boost converter.

For the panel of the required current efficiency the nominal value of the circuit output voltage can be obtain at the output current not exceeding 6 A. It is the sufficient value to charge the battery of the typical laptop. Increasing the output current of the considered circuit demands the use of photovoltaic panels of the greater current efficiency and semiconductor devices in switch-mode voltage regulators of smaller values of series resistance.

Acknowledgments The Authors thank DDS Poland for giving the photovoltaic panels.

References

1. Rashid, M.H. (ed.): Power Electronic Handbook. Academic Press, Elsevier, San Diego (2007)
2. Mulvaney, D.: Solar's green dilemma. IEEE Spectr. **51**(9), 26–29 (2014)
3. Castaner, L., Silvestre, S.: Modelling Photovoltaic Systems Using Pspice. John Wiley & Sons, Chichester (2002)
4. Górecki, P.: Voltage regulators for the laptop's power supply station with photovoltaic modules. In: Proceedings of 22nd International Conference, pp. 571–575. Mixdes, Toruń (2015)
5. Klugmann-Radziemska, E.: Fotowoltaika w teorii i praktyce. BTC, Legionowo (2010)
6. Piotrowicz, M., Marańda, M.: Sizing of photovotaic array for low feed-in tariffs. In: Proceedings of the 21th International Conference, pp. 405–408. Mixdes, Łódź (2014)
7. Ericson, R., Maksimovic, D.: Fundamentals of Power Electronics. Kluwer Academic Publisher, Norwell (2001)
8. Górecki, K., Górecki, P., Paduch, K.: Modelling solar cells with thermal phenomena taken into account. J. Phys.: Conf. Ser. **494** (2014). doi:10.1088/1742-6596/494/1/012007
9. Zarębski, J., Górecki, K.: SPICE-aided modelling of the UC3842 current mode PWM controller with self heating taken into account. Microelectron. Reliab. **47**(7), 1145–1152 (2007). doi:10.1016/j.microrel.2006.07.092
10. Górecki, K., Krac, E., Zarębski, J.: Photo-electro-thermal characteristics of photovoltaic panels. In: Oral, A.Y., Bahsi Oral, Z.B., Ozer, M. (eds.) 2nd International Congress on Energy Efficiency and Energy Related Materials (ENEFM2014), pp. 45–51. Springer, Heidelberg (2015). doi: 10.1007/978-3-319-16901-9_6
11. Górecki, K., Krac, E.: Measurements of thermal parameters of a solar module. J Phys.: Conf. Ser. **709** (2016). doi: 10.1088/1742-6596/709/1/012007
12. Górecki, K., Zarębski, J.: The method of a fast electrothermal transient analysis of single-inductance dc-dc converters. IEEE Trans. Power Electron. **27**(9), 4005–4012 (2012). doi:10.1109/TPEL.2012.2188546

Optimized Rapid Thermal Process for Selective Emitter Solar Cells

Abdelkader Djelloul, Abderrahmane Moussi, Linda Mahiou, Mourad Mebarki, Samir Meziani, Abdelkader Guenda, Kamel Bourai and Abdelkader Noukaz

Abstract In this paper we present an experimental approach for the realization of selective emitter by laser doping. Multi-crystalline Silicon wafers with thin layer of silicon nitride (SiN_x) are treated by laser after phosphorous diffusion and PSG removal. Rapid thermal annealing temperatures from 700 to 900 °C have been used for screen printed contacts. The surface of the selective emitter before and after annealing has been observed by scanning electron microscopy (SEM). Electrical characteristics show performance amelioration of the cell efficiency.

Keywords Selective emitter · Multi-crystalline · Annealing · SEM

1 Introduction

In the field of solar cells, cost and efficiency of the cell are critical points. Laser doping is a functional technique whose applications extend over a wide range of semiconductor technologies. The laser doping method is very simple and very fast. It is chosen for the development of the present work regarding to its versatility and easiness of implementation over most of the solar cells baseline production processes. This technique provides a way to boost local regions of the silicon beneath the contacts (Ag-front contact) to produce structures with selective emitters (Metal/n^{++}) [1–5]. In this paper, we used this technique for achieving selective emitter on multi-crystalline silicon (mc-Si) and to optimize rapid thermal annealing temperatures from 700 to 900 °C for screen printed contacts.

A. Djelloul (✉) · A. Moussi · L. Mahiou · M. Mebarki · S. Meziani · A. Guenda
Centre de Recherche En Technologie Des Semi-Conducteurs Pour L'Energétique 'CRTSE', 02 Bd Frantz Fanon. BP 140. 7 Merveilles, Alger, Algeria
e-mail: djelloulcrtse@gmail.com

K. Bourai · A. Noukaz
Centre de Développement Des Technologies Avancée (CDTA), Alger, Algeria

A.Y. Oral and Z.B. Bahsi Oral (eds.), *3rd International Congress on Energy Efficiency and Energy Related Materials (ENEFM2015)*, Springer Proceedings in Energy, DOI 10.1007/978-3-319-45677-5_29

2 Experimental

2.1 Cell Process

The substrate is boron doped p-type solar grade multi-crystalline silicon wafer with 0.5–1 Ω cm resistivity, square size of 50 mm × 50 mm and 300 µm thickness.

The process scheme of selective emitter formation by the laser doping technique is shown in Fig. 1.

Figure 1 shows process flow for the laser doping cell with $POCl_3$ diffusion [6] and anti-reflection layer (ARC) of silicon nitride (SiN_x) [7]. In this work we present an experimental approach for the realization of selective emitter by laser on mc-Si wafers. The phosphorous rich dead layer formed naturally after diffusion process is used as phosphorous source to perform the n++ region. Homogenous and lightly doped emitters were formed on p-type mc-Si wafers by thermal diffusion of $POCl_3$ using a Lydop furnace. The sheet resistance of the emitter, measured by 4-point probe is 60 Ω/□ [8]. The fabrication process is shown in Fig. 2.

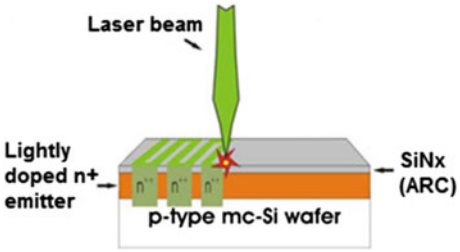

Fig. 1 Process scheme of selective emitter formation by the laser doping technique

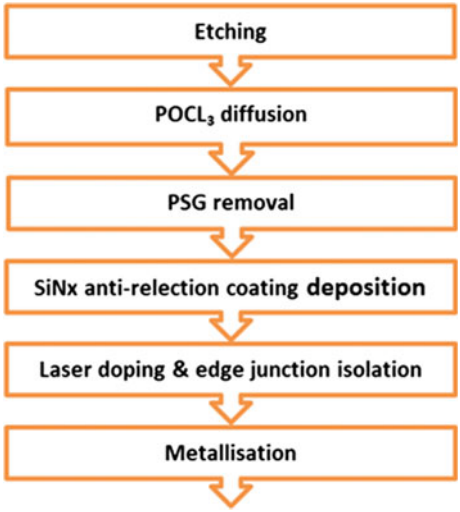

Fig. 2 Process sequence

The first step consists in the saw damage removing and surface etching of raw wafers. In the second step, $POCl_3$ furnace diffusion is performed using Lydop technique: during this step, a PSG layer with a thickness of approximately 40 nm grows. Emitter resistance of these cells was at round 65 Ω/□, which is typical for industrial standard cells. The third step (residual PSG removal) the PSG layer is immediately removed by a HF dip. The fourth step consists in the deposition of an anti-reflection layer (ARC) of silicon nitride (SiN_x) by Plasma-Enhanced Chemical Vapor Deposition (PECVD). The fifth step is the actual laser doping step, during which the n^{++} areas of the selective emitter are patterned according to the front side metallization grid [9]. The laser beam is circular with a radius of 40 μm and has a Gaussian energy density. Notice that this fifth step is the only additional step compared to standard cell processing. The following steps are then the same as those used for standard cell processing. The sixth is the screen-printing of metal contacts (Ag-front contact, Al-back contact) as well as their cofiring in a rapid thermal annealing at high temperature. The seventh and last step includes laser edge isolation.

Measurements of I (V) gave acceptable results with a 4.6 % efficiency and 47.7 % FF for selective emitter solar cell doped laser. This modest performance is possibly due to a problem in the RTP process that is not yet optimized with respect to this new concept device.

2.2 Rapid-Thermal Processes, RTP

Rapid Thermal Processing (RTP) can be used to reduce the thermal redistribution of impurities at high temperature. For small devices this is an important consideration and as a result most engineers make use of low temperature processes. RTP is thus a promising technology regarding to its short time treatment.

The surface of the front panel and rear panel for the selective emitter was annealed by RTP at different temperatures. This step is very important for the manufacture of a solar cell. The contacts are treated in RTP furnace at 700 °C for 05 min to realize the ohmic contact Ag/n^{++}.

3 Results and Discussions

3.1 Optimized RTP for Selective Emitter

In this study, a silver Ag-front contact and aluminum Al-back contact are deposited on a front and rear faces by screen printing process and annealed by rapid thermal processing (RTP) at different annealing temperatures in order to optimized rapid

thermal process for selective emitter solar cells. Additionally, the effects of RTP on film morphological properties are systematically investigated by scanning electron microscopy.

The cells have a size of 5×5 cm^2. For the rear part metallization, aluminum was used and was deposited by means of screen printing and dried out at 250 °C. For the front part metallization, silver contacts were used on the laser doped pattern with a good alignment.

After the metallization, samples with five different annealing conditions were elaborated. Rapid thermal annealing temperatures from 700 to 900 °C have been used (see Fig. 3).

From the RTP profile for samples with five different annealing temperatures, we note that there is separation and bursting metal for high temperature (900 °C). The best contacts are treated in RTP furnace at 750 °C to realize the ohmic contact Ag/n^{++}. Below, in Table 1, an example is presented with the test specifications.

Table 1 shows the four selective emitter solar cells (L1, L2, L3, and L4) obtained for multi-crystalline cells fabricated using laser doping method in comparison to the homogeneous emitter (C1).

3.2 *Surface Morphology*

The surfaces of the selective emitter before and after annealing have been observed by scanning electron microscopy (SEM). SEMs image of the surface of the front

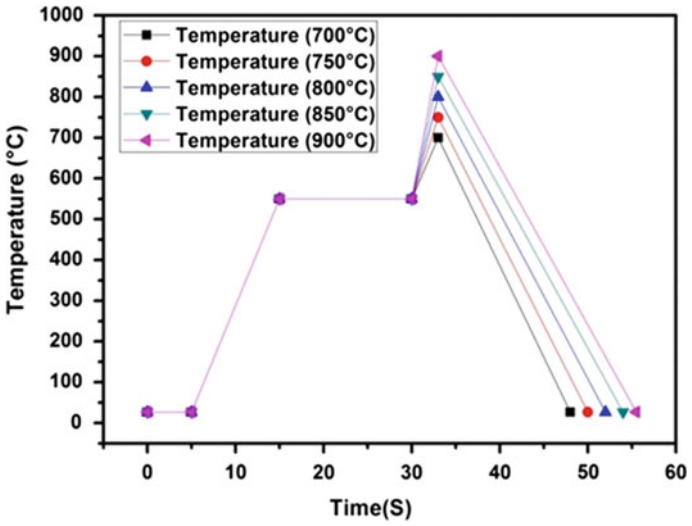

Fig. 3 Graph of RTP profile for samples with five different annealing temperatures from 700 to 900 °C

Table 1 Samples with four selective emitter solar cells (L1, L2, L3, L4) in comparison to the homogeneous emitter (C1)

Number of cells	Rsq Emitter	Laser treatment	RTP annealing (°C)
C1	60–65 Ω/□	No laser treated	750
L1	60–65 Ω/□	Laser treated (P = 6 W, V = 250 mm/s, F = 20 kHz)	700
L2	60–65 Ω/□		750
L3	60–65 Ω/□		800
L4	60–65 Ω/□		850

grid at two different magnifications: (a), (c) 100 μm; (b), (d) 10 μm are shown in Figs. 4 and 5 respectively.

Figures 4 and 5, SEM images, present the morphologies of the front grid (Ag films) for the selective emitter before and after annealing at 750 °C. The as-deposited Ag film show weakly bonded particles with voids and empty spaces on surface, as is evident from Figs. 4a, b and 5a, b.

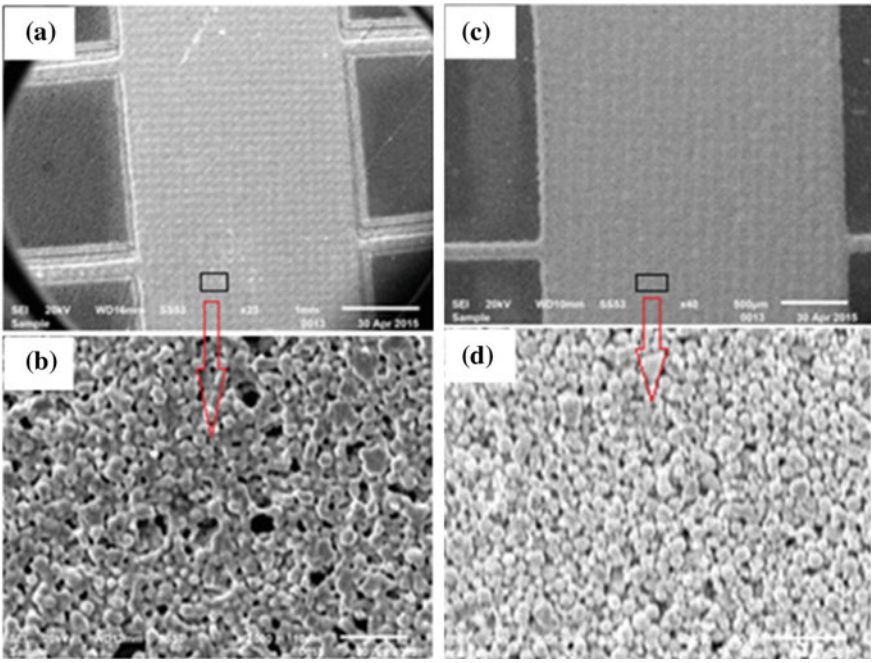

Fig. 4 Comparison of SEM micrograph of the surface of the front contact (busbar) for the selective emitter at different magnifications: **a**, **b** before annealing; and **c, d** after annealing at 750 °C

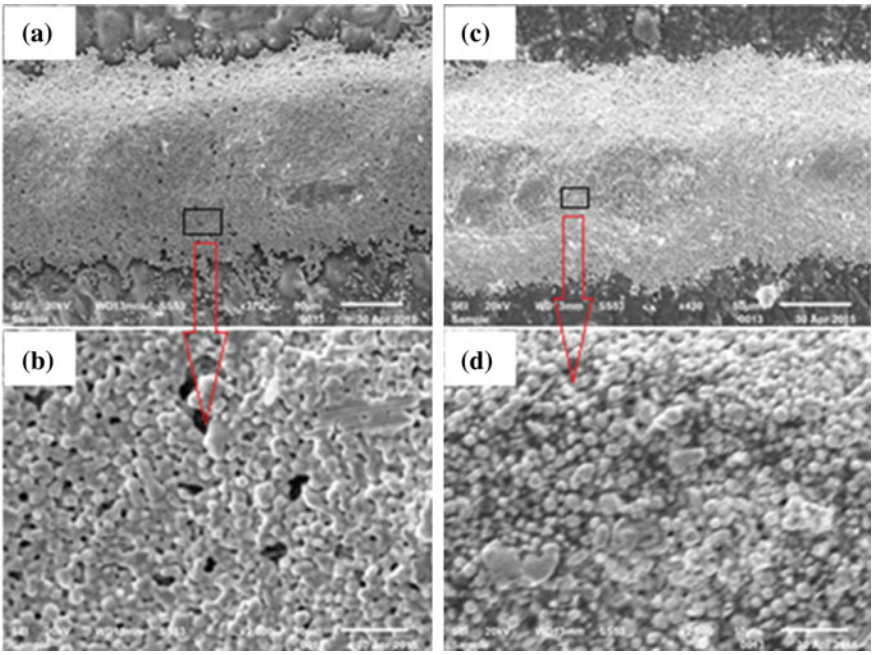

Fig. 5 Comparison of SEM micrograph of the surface of the front grid (finger) for the selective emitter at different magnifications: **a**, **b** before annealing; and **c, d** after annealing at 750 °C

Figures 4c, d and 5c, d, shows the surface morphology of Ag films for the selective emitter after annealing at 750 °C observed by SEM. From the micrographs, it is observed that the films are denser throughout all the regions and without any void, pinhole or cracks and they adequately cover the surfaces.

Figure 6 present the morphologies of the rear contact (Al films) before and after annealed at 750 °C. The as-deposited Al film demonstrates a poor with pinhole surface, as is evident from Fig. 6a. It can be clearly seen that the annealed Al films are dense and uniform with small grains (see Fig. 6b).

The SEM images indicated that the deposited films are sensitive to annealing temperature. It shows densification of deposited contact.

3.3 I-V Characteristics

In order to investigate the quality of the selective emitter cells, the electrical properties are measured for a 5 × 5 cm^2 test cell. The I-V characteristics of the multi-crystalline silicon solar cells are given in Table 2.

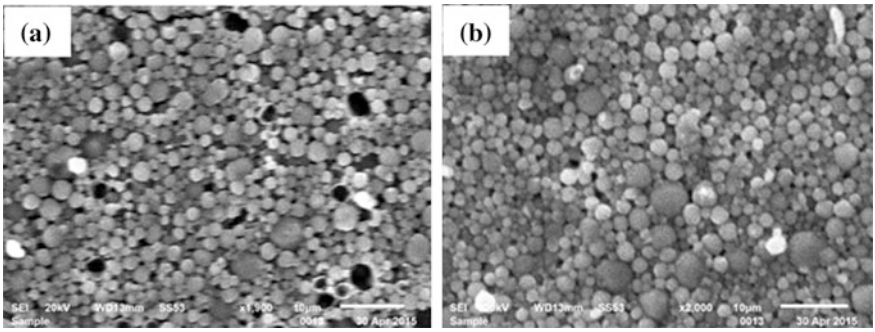

Fig. 6 Comparison of SEM micrograph of **a** the surface of the rear panel (Al) for the selective emitter before annealing and **b** the surface of the rear panel (Al) for the selective emitter after annealing

Table 2 I-V characteristics for a 25 cm^2 cell after annealing at 750 °C

Emitter type	J_{sc} (mA/cm^2)	V_{oc} (V)	FF (%)	η (%)
C1	15.164	0.585	28.9	2.6
L1	20.396	0.471	47.7	4.6
L2	21.516	0.504	59.6	6.5
L3	22.316	0.481	52.8	5.7
L4	22.056	0.500	57.6	6.4

Our results demonstrated the influence of the selective emitter formed by laser doping with annealing at 750 °C. The solar cell performances of the cells with and without the selective emitter are summarized in Table 2. V_{oc} was slightly decreased from 0.585 to 0.504 mV. This might be due to shunt resistance degradation by laser treatment on the edges. J_{sc} was increased considerably by the selective emitter formation from 15.164 to 21.516 mA/cm^2. This is due to the improvement of the current collection characteristic in the shallow pn junction by the deeply selective emitter formation. It will be investigated by spectral response measurement in the future. However, the fill factor was slightly increased by the selective emitter formation.

4 Conclusion

In conclusion, we tried to apply the laser doping method to form a selective emitter in phosphorous-doped p-type mc-Si solar cells using a laser at room temperature and in air ambient.

Rapid thermal annealing temperatures from 700 to 900 °C have been used. This step is very important for the manufacture of a solar cell. From the RTP profile for

samples with five different annealing temperatures, we note that there is rupture and bursting metal for high temperature (900 °C). The best contacts are treated in RTP furnace at 750 °C for 05 min to realize the ohmic contact Ag/n^{++}.

From SEM it is revealed that the as-deposited Ag film show a poor surface with voids and pinhole, and the films are not uniform throughout all the regions. But the surface morphology of Ag films after annealing at 750 °C are without any void, pinhole or cracks and that they cover uniformly the surface. From SEM images of Al film it can be clearly seen that the annealed Al films are dense and uniform with small grains.

Finally it was shown that despite the elaboration of a selective emitter solar cell by a laser doping, the technique present some optimization challenges. Therefore, the characteristics of the solar cell with the selective emitter are improved in this study. In particular, Jsc was considerably increased by the selective emitter formation, and eventually, the efficiency was also increased. Our results suggest that the laser doping technique is a promising alternative to form the selective emitter in p-type mc-Si solar cells. Moreover, it is possible that efficiency is increased by application of laser doping to the fabrication of mc-Si solar cell.

Acknowledgments This work has been developed under the National Research Fund, DGRSDT/MESRS (Algeria).

References

1. Hameiri, Z., Puzzer, T., Mai, L., Sproul, A.B., Wenham, S.R.: Laser induced defects in laser doped solar cells. Prog. Photovolt: Res. Appl. **19**, 391–405 (2010). doi:10.1002/pip.1043
2. Xu, G., Hallam, B., Hameiri, Z., Chan, C., Yao, Y., Chong, C., Wenham, S.: Over 700 mV implied V_{oc} on p-type CZ silicon solar cells with double-sided laser doping. Energy Procedia **33**, 33–40 (2013)
3. Gall, S., Paviet-Salomon, B., Lerat, J., Emeraud, T.: High quality passivation scheme combined with laser doping from SiN:P and SiN:B layer for silicon solar cell, Energy Procedia **27**, 467–473 (2012)
4. Ly, M., Hameiri, Z., Tjahjono, B.S., Wenham, S.R.: Rear junction laser doped solar cells on CZ n-type silicon. IEEE 34th PVSC conference, pp. 1811–1815 (2009). doi:10.1109/PVSC.2009.5411499
5. Sugianto, A., Bovatsek, J., Wenham, S., Tjahjono, B., Xu, G., Yao, Y., Hallam, B., Bai, X., Kuepper, N., Chong, C.M., Patel, R.: 18.5 % laser-doped solar cell on CZ p-type silicon. IEEE 35th PVSC conference (2010)
6. Fair, R.B.: Concentration profiles of diffused dopants in silicon. In: Wang, F.F.G. (ed.) Impurity Doping Processes in Silicon, pp. 315–442 (1981)
7. Hofstetter, J., del Canizo, C., Ponce-Alcantara, S., Luque, A.: Optimisation of SiNx:H anti-reflection coatings for silicon solar cells. In: 2007 Spanish conference on electron devices, pp. 131–134 (2007). doi:10.1109/SCED.2007.383961
8. Kuthi, E.B.: Crystalline silicon solar cells with selective emitter and the self-doping contact. LIX. **6**, 21–31 (2004)
9. Djelloul, A., Moussi, A., Meziani, S., Mebarki, M., Mahiou, L., Noukaz, A., Bourai, K.: Laser doping for selective emitter solar cells. Revue des Energies Renouvelables SIENR'14 Ghardaïa, pp. 129–134 (2014)

Integrating Superficially Treated 2024 Aluminum Alloy in Steel Drill String to Deal with Fatigue Problem in Crooked Trajectory for Vertical Deep Well

Lallia Belkacem, Noureddine Abdelbaki, Mohamed Gaceb, Elahmoun Bouali, Hedjaj Ahmed and Mourad Bettayeb

Abstract Drilling deep HPHT wells is the most compelling reason for drilling companies to look for alternative drill pipes that meet their requirements. Currently, with the emergence of drill pipes made of materials other than steel, a thorough study of superficially treated 2024 aluminum alloy combined with steel drill pipe in crooked well trajectory is presented in this study. Basically; this study is built on several parameters that affect fatigue resistance of a drill pipe such as fatigue endurance limit of the drill pipe material, drill pipe specification, torque and drag loads applied, dog leg severity, besides crooked trajectory. Chiefly, this paper shows a full study about 2024 aluminum alloy drill pipe and analyzes the prospect of using aluminum drill string for deep wells while the fatigue, torque and drag as well as drilling efficiency and drill string integrity stay acceptable. It also gives a better comprehension of the mechanical behavior of lightweight material for drill pipe, which can significantly improve well planning in order to drill wells with an increasing depth, length and complexity. Additionally, even though steel drill pipe has better mechanical properties in terms of density, Young's modulus, yield and tensile strength, than 2024 aluminum alloy drill pipe, the latter has a good fatigue resistance even in the simultaneous presence of high applied torque and axial load, and severe doglegs, which makes the use of other options (Steel Drill Pipe and Titanium Drill Pipe) impractical from the fatigue failure standpoint. Finally we can assume that, there is significant cost saving with the use of Aluminum Drill Pipe compared to steel drill pipes, because the ratio of the engine power needed to supply the drilling fluid at the required pressure for ADP versus steel drill pipe is lower, leading to a reduction in fuel consumption.

N. Abdelbaki (✉)
University Akli Mohand Oulhadj, 10000 Bouira, Algeria
e-mail: lallia.belkacem@gmail.com; abdelnor215@gmail.com

L. Belkacem · M. Gaceb · E. Bouali · H. Ahmed · M. Bettayeb
Faculty of Hydrocarbons and Chemistry Independence Street,
Laboratory of Petroleum Equipments Reliability and Materials,
University Mohamed Bougara, 35000 Boumerdes, Algeria

A.Y. Oral and Z.B. Bahsi Oral (eds.), *3rd International Congress on Energy Efficiency and Energy Related Materials (ENEFM2015)*, Springer Proceedings in Energy, DOI 10.1007/978-3-319-45677-5_30

Keywords HPHT wells · Steel drill pipe · 2024 aluminum alloy drill pipe · Fatigue resistance · Torque and drag · Dog leg severity · Crooked trajectory

1 Introduction

This paper outlines practically the benefit of using aluminum drill pipes which are characterized by higher strength-to-weight ratio than steel drill pipes due to a lighter specific weight despite reduced yield strength. This characteristic allows decreasing torque and drag loads while keeping a good resistance to axial, torsional and lateral loads. Lighter weight enables to reduce the contact side force between drill pipe and borehole, thus reducing friction between drill string and wellbore [1, 2].

Therefore, this article is based upon experiments on new drill string material which is integrated in drill string and analyses its behavior during the whole drilling period of 8.5 inch bore from 1905.2 to 5400 m to determine to what extent the aluminum drill pipe can drill without failures in this interval by using soft modeling Decision Space Well Engineering Software [1, 2].

Accordingly, a description is firstly given of the 2024 aluminum alloy which is treated superficially. This is followed by a synopsis on stress loads by using steel drill pipe during drilling operation using steel drill pipe. This will be compared to stress loads obtained using aluminum drill pipe. Results and interpretations are finally given [1, 2].

2 Superficially Treated 2024 Aluminum Alloy Technology

The proposal of the use of the 2024 aluminum alloy, treated superficially with "plasma electrolytic oxidation PEO" is thought to be profitable. Indeed to prove this, tensile micro-tests have been conducted on tubular specimens made of 2024

Table 1 Results of tests to traction (micro-tests) of test-tubes in 2024, carried out on the machine "ALA-TOO". E% = Error % $\sigma_{0,2}$ Proof stress, σ_r Ultimate tensile strength, σ_{pr} Elasticity limit, δ Relative extension to rupture, α [°] elastic range slope, E Young's modulus, E% = Error %

Test tube sections 2X30	σ_r (Mpa)	$\sigma_{0,2}$ (Mpa)			σ_{pr} (Mpa)		δ (%)		α (°)		E (Mpa)
	Before superficial treatment (OMA)										
	491	4.8 E%	381.6	2.9 E%	359.8	2.6 E%	12.2	14.0 E%	80.5	1.0 E%	71,805
	After superficial treatment (OMA)										
	467.5	6.0 E%	359.5	4.2 E%	337.0	4.5 E%	13.4	10.0 E%	80.8	1.2 E%	88,763

aluminum alloy in both treated and non-treated states [3]. The improvements in mechanical properties brought about by superficial treatment are shown in Table 1.

3 Stress Loads by Using Steel Drill Pipe

3.1 Engineering Overview of Drilling with Steel Drill Pipe

Based on the quick review conducted on the history of 8½″ hole of one well drilled in Algeria, it is imperative to point out that the severe wellbore instability, high torque peaks and stuck pipe problems encountered previously on this interval are still suspected to be one of the major challenges to encounter while drilling the 8½ hole section which is the longest one, approximately 2515 m. The basic possible causes for the various hole problems encountered on the 8½″ bore of this well may be attributed to the following major factors:

1. Hole Geometry (Spiraling—Wellbore Tortuosity 8½″)
2. No harmony in Drilling String and Parameters (WOB, RPM, BHA design, Bit selection). [4]

3.2 Load Summaries

From the load summary represented in Table 2, it is clearly seen that the drill-string is subjected to fatigue failure during rotating on/off bottom, tripping out and back-reaming operation. This is confirmed within the dog legs severity curve in Fig. 1 which revealed variation in wall trajectory via tortuosity [4, 5].

4 Stress Loads by Using Aluminum Drill Pipe

The solution proposed in this paper consists in simply replacing joints of standard steel drill pipe by lighter aluminum drill pipe while keeping the same bottom hole assembly (BHA). The tool-joints for aluminum drill pipe are manufactured from steel. Thus a torque and drag optimization study has been run to determine the optimum number of ADP joints along the drill string to minimize friction and reduce compression along the well trajectory and limit the maximum depth which aluminum drill pipe can reach without any failure. Table 3 represents details of each specific drilling string [5].

Based on weight applied on bit which is about 10t in addition to 130.6 t hook load with a safety factor of 1.33, the pipe reached its yield point at a depth of 4000 m. Therefore, 150 joints of standard steel DP have been replaced by

Table 2 Load summary for steel drill pipe

Load condition	Stress failure			Buckling limits			Torque failure (ft-lbf)	Torque at the rotary table (ft-lbf)	Measured weight (tonne)	Total stretch (m)
	Fatigue	90 % yield	100 % yield	Sinusoidal	Helical	Lockup				
Tripping out	X	–	–	–	–	–	–	16,859.1	160.95	7.63
Rotating on bottom	X	–	–	–	–	–	–	15,270.3	136.53	6.74
Back-reaming	X	–	–	–	–	–	–	18,804.2	148.52	7.36
Rotating off bottom	X	–	–	–	–	–	–	17,204.8	146.53	7.25

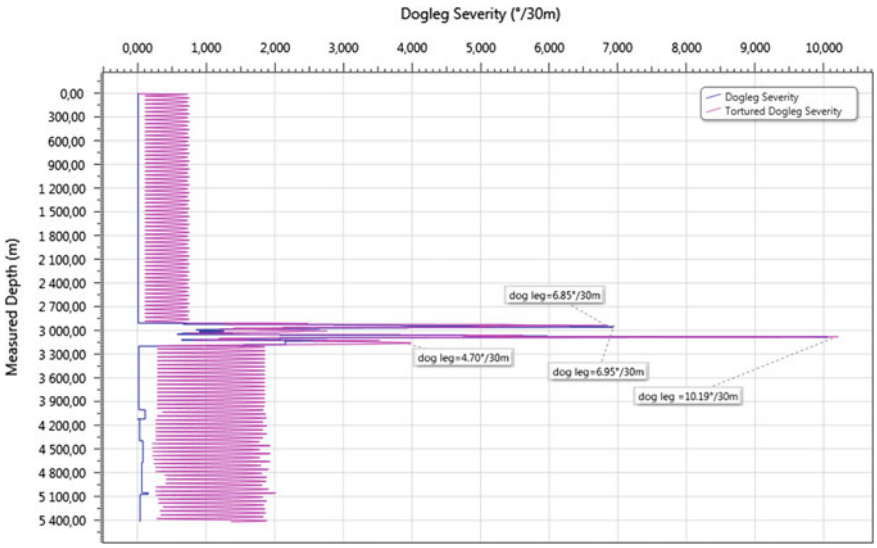

Fig. 1 Dog legs severity curve and related fatigue stress

Table 3 Details in each specific drilling string and section

Section	Steel/steel drill pipe		Aluminum/steel drill pipe	
8 1/2″ (in)	DP 5″-G105	DP 5″-S135	DP 5″-G105	DP5″-AL2024
Depth (m)	1350	2592.86	1350	2592.86
σ_e (psi)	10,500.00	135,000.00	10,500.00	52,127.5
σ_m (psi)	11,500.00	145,000	11,500.00	67,787.75
E (psi)	30,000,000	30,000,000	30,000,000	1,287,006.35
σ endurance limite (psi)	20,000.00	20,000.00	20,000.00	23,200.00

$\boldsymbol{\sigma_e}$ minimum yield strength; $\boldsymbol{\sigma_m}$ ultimate yield strength; **E** young's module

aluminum DP above the BHA. This gave good results compared to steel pipe as shown in Table 4 [5].

5 Results and Interpretation

It is obviously seen from effective tension curve in Fig. 2 below, that all drilling operations curves do not cross the tension limit curve at 4000 m. Consequently, there are no stresses exerted on aluminum drill pipe at that tortuous interval.

We can hence, assume that the 8½″ drilling phase benefited from ADP since there was a considerable reduction of the Surface Torque and Hook Load for the reason that there was a reduction in side force: as represented in Table 5.

Table 4 Load summary for aluminum drill pipe

Load condition	Stress failure			Buckling limits			Torque failure	Torque at the rotary table (ft-lbf)	Measured weight (tonne)	Total stretch (m)
	Fatigue	90 % yield	100 % yield	Sinusoidal	Helical	Lockup				
Tripping out	–	–	–	–	–	–	–	16,859.1	160.95	7.63
Rotating on bottom	–	–	–	–	–	–	–	15,270.3	136.53	6.74
Back-reaming	–	–	–	–	–	–	–	18,804.2	148.52	7.36
Rotating off bottom	–	–	–	–	–	–	–	17,204.8	146.53	7.25

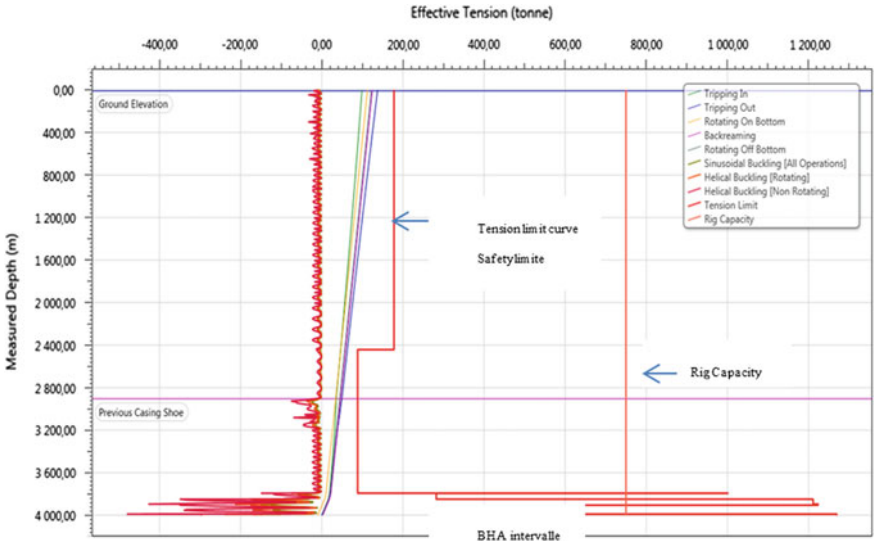

Fig. 2 Effective tension curves for mixed aluminum/steel drill pipe

Table 5 Side force for aluminum drill pipe and steel drill pipe

True vertical depth	Rotating on bottom ADP side force	Rotating on bottom SDP side force
(m)	(lbf/length)	(lbf/length)
290,788	700	713
291,700	1305	1328
292,611	2431	2475
293,523	2154	2192
294,434	1961	1995
295,344	1397	1422
296,253	714	726
297,160	569	578
298,066	615	626
298,972	845	859
299,876	878	892
300,778	787	800
301,679	455	463
302,579	436	444
303,479	516	525
304,380	1039	1058
305,282	1489	1515
306,186	994	1010
307,092	828	843
307,996	2172	2210

ADP Aluminum drill pipe, **SDP** Steel drill pipe

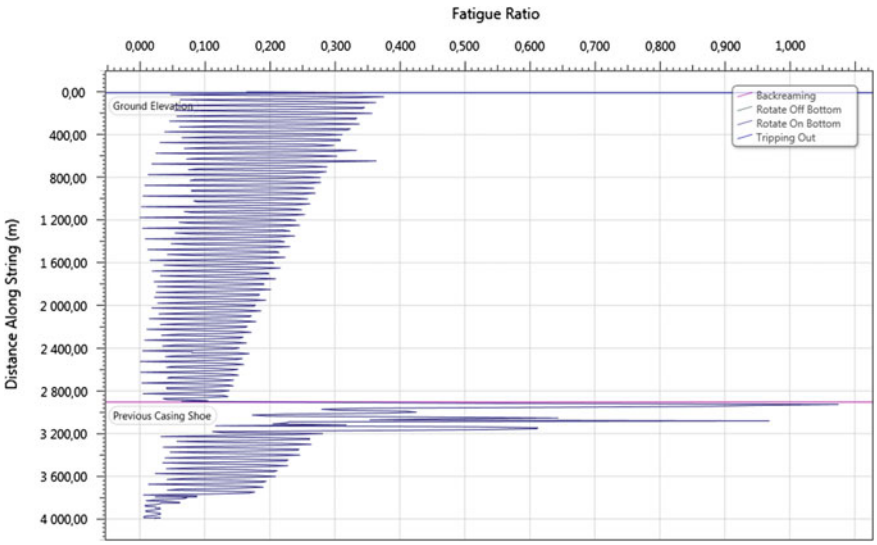

Fig. 3 Steele DP fatigue ratio curve

Accordingly Results can be explained as follows:

Initially; Aluminum drill pipe have a lower friction coefficient compared to steel drill pipe in open and cased hole, which resulted in decrease of both the torque and the side force.

Above and beyond; depending on well trajectory together with the friction coefficient and the higher flexibility of aluminum drill pipe, can be balanced by the reduced contact side forces with the wellbore and producing less compression along the drill string.

Moreover; steel drill pipe fatigue damage occurs under cyclic loading conditions due to rotation in a dogleg region. Therefore, the following dog leg makes high stress concentration areas susceptible to fatigue damage in drill pipe which led to increase in fatigue ratio up to 1.075 (minimum fatigue ratio is 1) as illustrated in Fig. 3.

Contrariwise, Aluminum drill pipe has significantly a good fatigue resistance even in the simultaneous presence of high torque and axial load in addition to severe doglegs; these were confirmed by the fatigue ratio value which is 0.642 less than 1 his makes the use of steel drill pipe impractical from the fatigue failure standpoint as revealed in Fig. 4.

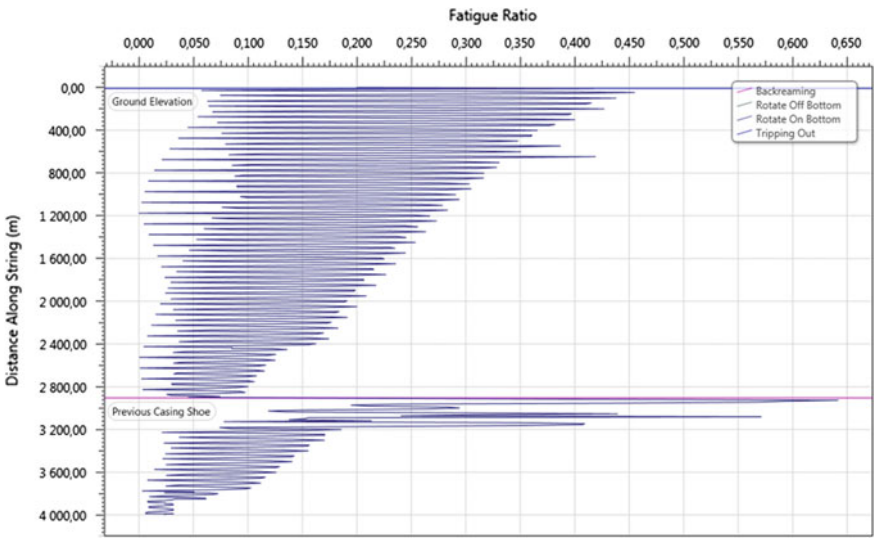

Fig. 4 Aluminium DP fatigue ratio curve

6 Conclusion

To sum up, the Aluminum drill pipe undergoes significantly less stress through the dogleg compared to steel drill pipe. This is due to their smaller elasticity modulus in addition to lighter density compared to steel drill pipe.

Furthermore Aluminum drill pipe has significantly a good fatigue resistance even in the simultaneous presence of high applied torque, axial load, and severe doglegs, which makes the use of other options like Steel drill pipe impractical from the fatigue failure standpoint. We can therefore see that the limiting factor for using Aluminum drill pipe in such severe conditions is not the fatigue resistance of the material from which the pipe is made of, but its high contact forces between the wellbore and the body of drill pipe. In view of that, we assume that the generated contact forces at the tool-joints and pipe body adds more complexity to the decision as to which type of drill pipe is more appropriate for drilling at severe dogleg.

However, large contact forces at the pipe body can make relatively major scratches on the surface of the pipe tube of Aluminum drill pipe and Steel drill pipe, which can render their corrosion resistance features insignificant. But the following 2024 Aluminum drill pipe has a good resistance to wear and corrosion even at high temperature, for the reason that the following material has been treated superficially with “plasma electrolytic oxidation PEO”, which enhanced their mechanical properties as cited in Table 1.

Finally, the ultimate goal of our research is to introduce a light-weight materials drill pipe such as aluminum in drilling of tortuous vertical deep wells, regarding

their ability to decrease torque and drag loads and improving fatigue resistance. Besides to significant cost saving compared to steel drill pipes.

References

1. Menand, S., Jeffry, Lehner, K.: Successful use of mixed aluminum-steel drill pipe string in complex horizontal wells. J. Pet. Sci. Eng. SPE-170255 (2014). doi:10.2118/170255-MS
2. Gelfgat, M.Y., Basovich, V.S., Tikhonov, V.S.: Drill string with aluminum alloy pipes design and practices. Paper SPE 79873 presented at the 2003 SPE/IADC Drilling Conference, 4, Amsterdam, The Netherlands, 19–21 Feb 2003
3. Abdelbaki, N., Atmani, D.: Test of an aluminium alloy treated superficially using oxidation by electrical micro-arc, to the fissures formation under tension. In: 15th International Congress of Chemical and Process Engineering, Prague, 25–29 Aug 2002
4. Daily drilling report of 8 ½″ hole section of well in Algeria field
5. Decision Space Well Engineering Software. EDT _5000.1. Software system.landmark products

Performance of Bi_2Te_3 Thermoelectric Element Improved by Means of Contact System Ni/Ta-W-N/Ni

Dmitry G. Gromov, Yury I. Shtern, Maxim S. Rogachev, Alexey S. Shulyat'ev, Alexey Yu. Trifonov and Elena P. Kirilenko

Abstract In this paper the materials with improved thermoelectric properties developed based on Bi_2Te_3 were used for the production of thermoelectric generator. It allowed to extend the operating temperature range of the material to 550 K. $Bi_{2.0}Te_{2.4}Se_{0.6}$ doped with 0.12 wt% CuBr (dimensionless coefficient ZT = 1.1 at a temperature of 450–550 K) was used as a material for manufacturing n-type branches. $Bi_{0.4}Sb_{1.6}Te_{3.0}$ doped with 0.12 wt% $PbCl_2$ and 1.5 wt% Te (dimensionless coefficient ZT = 1.2 at a temperature of 450–550 K) was used as a material for manufacturing p-type branches. The following materials were used as the contact system: 100 nm layer of nickel as the ohmic contact layer; 100 nm layer of amorphous alloy Ta-W-N as a diffusion barrier layer; and 400 nm layer of nickel as a wetting layer for soldering. Study of adhesion of this contact system demonstrated good quality. The breakout force was 12 MPa.

Keywords Adhesion · Ohmic contact · Thermoelectric element · Technology

1 Introduction

One of the problems of thermoelectric generators (TEG) for the conversion of energy is their low efficiency. To improve TEG efficiency it is necessary to solve two basic problems: the creation of effective thermoelectric materials and the development of an efficient design of TEG, including technology of its implementation.

D.G. Gromov (✉) · Y.I. Shtern · M.S. Rogachev · A.S. Shulyat'ev · E.P. Kirilenko
National Research University of Electronic Technology, Bld. 1, Shokin Square, 124498 Zelenograd, Moscow, Russia
e-mail: gromadima@gmail.com

A.Yu.Trifonov
Scientific Research Institute of Physical Problems Named After F.V.Lukin, Moscow, Russia

A.Y. Oral and Z.B. Bahsi Oral (eds.), *3rd International Congress on Energy Efficiency and Energy Related Materials (ENEFM2015)*, Springer Proceedings in Energy, DOI 10.1007/978-3-319-45677-5_31

Effective materials for thermoelectric cooling (Peltier effect) are solid solutions based on $(Bi,Sb)_2Te_3$, obtained by various methods of directional solidification and having a maximum thermoelectric figure of merit in the region of 300 K [1–3]. Among thermoelectric generators operating on the Seebeck effect, the materials having maximum *ZT* values (*Z*—thermoelectric figure of merit, *T*—temperature) in the range of 600–900 K, have maximum efficiency [4–7]. They are usually based on PbTe. Thus, the temperature range of 300–600 K is not covered for use in thermoelectric generators.

2 Thermoelectric Material

In this connection, we have developed materials with high thermoelectric efficiency based on bismuth telluride for use in thermoelectric generators, operating at temperatures from 300 to 600 K. These materials were obtained by vertical zone melting. As an n-type material $Bi_{2.0}Te_{2.4}Se_{0.6}$ doped with 0.18 wt% CuBr was synthesized. As a p-type material $Bi_{0.4}Sb_{1.6}Te_{3.0}$ doped with 0.12 wt% $PbCl_2$ and 1.5 wt% Te was synthesized. After synthesis, their thermal and electrical parameters have been studied: the temperature dependences of thermoelectric power, thermal conductivity and electrical conductivity, from which we calculated the temperature dependence of the parameter *ZT*, demonstrated in Fig. 1. As can be seen, these thermoelectric materials suitable for use in the temperature range from 350 to 650 K, in which they reach a maximum value of the dimensionless figure of merit coefficient ($ZT = 1.1$ at 550 K for $Bi_{2.0}Te_{2.4}Se_{0.6}$ + 0.18 wt% CuBr and $ZT = 1.2$ at 450–550 K for $Bi_{0.4}Sb_{1.6}Te_{3.0}$ + 0.12 wt% $PbCl_2$ + 1.50 wt% Te).

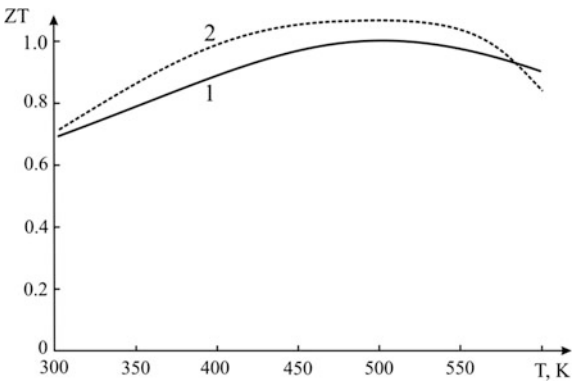

Fig. 1 Temperature dependences of the dimensionless parameter *ZT*: *1* for n-type material $Bi_{2.0}Te_{2.4}Se_{0.6}$ doped with 0.18 wt% CuBr; *2* for p-type material $Bi_{0.4}Sb_{1.6}Te_{3.0}$ doped with 0.12 wt% $PbCl_2$ and 1.50 wt% Te

3 Contact System

The most important problem in the manufacture of efficient thermoelectric generators is to provide quality heat-stable contact of the sections of the thermoelement branches among themselves and with commutation buses. To solve this problem the development of the contact system consisting of a set of layers with different functional purpose is required. These layers fulfil following functions: they perform the ohmic contact with the thermoelectric material; they are a diffusion barrier preventing interdiffusion of connected materials; they provide the necessary adhesion of the contact layers to thermoelectric materials and between the layers; they enable soldering to the switching bus. At the same time, these functions must be maintained at high operating temperatures of TEG.

We investigated two variants of contact systems. In the first case 500 nm layer of nickel was used as the contact material; in the second case, three-layer Ni/Ta-W-N/Ni contact system was used. It comprised a 100 nm Ni layer as the ohmic contact layer; 100 nm layer of amorphous alloy Ta-W-N as a diffusion barrier layer; and 400 nm Ni layer as a wetting layer for soldering.

To produce the samples we used the substrates of the aforementioned p- and n-type thermoelectric materials in with a diameter of 20 mm and a thickness of 4 mm. The substrates were prewashed in ultrasonic bath in deionized water, and then dried in isopropyl alcohol vapor. Immediately before application, the sample surface was subjected to in situ "dry" etching with argon ions. Layers of Ni and diffusion barrier Ta-W-N alloy were deposited onto unheated substrate by magnetron ion-plasma sputtering of a composite targets of Ni and Ta-W in vacuum by the plasma in argon or argon-nitrogen, respectively, at a residual pressure in the chamber 5×10^{-5} Torr and working gas pressure of 5×10^{-3} Torr.

The rate of diffusion processes in thin films are strongly influenced by a variety of structural imperfections. For example, it is well known that diffusion along grain boundaries in polycrystalline materials, although is slower than the diffusion along the interface, but in comparison with a bulk lattice diffusion proceeds by tens of times faster [8].

Amorphous alloys of transition metals are known as good barrier materials against diffusion. The amorphous state is characterized by a perfect atomic structural homogeneity. The lack of crystal structure defects (dislocations, vacancies, grain boundaries, etc.) determines the extremely high chemical inertness of amorphous films, their low diffusion permeability and high thermal stability. It was demonstrated that the thin film of Ta-W-N alloy, formed by magnetron sputtering is amorphous. Moreover, in the free state, the film remains amorphous even after 30 min of annealing at 970 K [9].

4 Adhesion

In order to measure the adhesion the contact system on these substrates of n- and p-type thermite materials was formed as an array of sites having 1 mm in diameter, and then the rod was soldered to these sites. The value of adhesion was measured by an avulsion using a dynamometer Force Gauge PCE-FM50. The obtained measurement results are shown in Table 1.

As can be seen, the value of adhesion is practically the same in both types of the thermoelectric material, and the incorporation of Ta-W-N into the contact system of the diffusion-barrier layer does not lead to any noticeable change of adhesion values. It should be noted that the values of adhesion are almost two times higher than the minimum allowed normative value of adhesion 4.9 MPa.

5 Thermal Stability

The obtained samples with two variants of contact systems were subjected to a 60-min annealing at a temperature of 570 K, which is the limit operating temperature for the investigated n- and p-type thermite materials. It has been found that after annealing of the sample with the pure nickel contact system the nickel surface becomes impossible to soldering.

Examination of this sample by Auger electron spectroscopy showed that the tellurium from the substrate diffuses through the nickel layer and accumulates on the surface, and obviously is a cause of impossibility to soldering surface (Fig. 2a).

At the same time, in the presence of the diffusion-barrier layer of amorphous Ta-W-N between nickel layers, the diffusion of tellurium is observed only into the nickel layer adjacent to the semiconductor thermoelectric materials. The diffusion of tellurium into the top layer of nickel is prevented, as demonstrated in Fig. 2b.

Table 1 Results of the study of adhesion of contact systems Ni and Ni/W-Ta-N/Ni to n- and p-type thermoelectric materials

Contact system	Type of thermoelectric material	Number of measurements	Average value of adhesion MPa	Standard deviation MPa
Ni	n	40	9.49	2.48
Ni	p	40	9.77	2.29
Ni/Ta-W-N/Ni	n	40	9.82	2.29
Ni/Ta-W-N/Ni	p	40	9.86	2.18

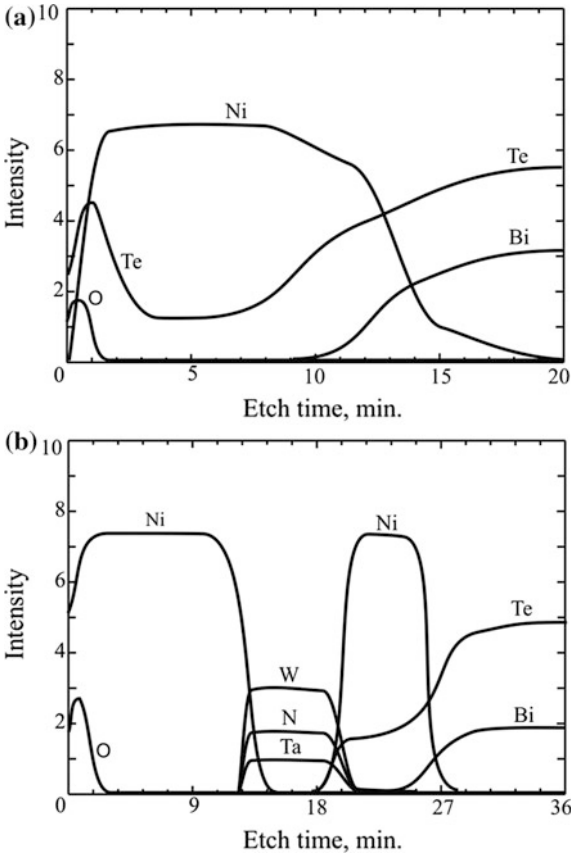

Fig. 2 Auger-electron spectroscopy depth profiles after heat treatment at 570 K for 60 min: **a** Ni/($Bi_{2.0}Te_{2.4}Se_{0.6}$ + 0.18 wt% CuBr), **b** Ni/Ta-W-N/Ni/($Bi_{2.0}Te_{2.4}Se_{0.6}$ + 0.18 wt% CuBr)

6 Conclusions

Efficient thermoelectric materials for the range 450–550 K are offered. The contact systems with high electrophysical and adhesion properties ensuring efficient operation of the thermoelectric generator in a specified temperature range have been developed.

Acknowledgments This work has been carried out under a sponsorship of the Ministry of Education and Science of the Russian Federation project number 14.578.21.0038 (RFMEFI57814X0038).

References

1. Snyder, G.J., Toberer, E.S.: Complex thermoelectric materials. Nat. Mater. **7**, 105–114 (2008). doi:10.1038/nmat2090
2. Zhao, L.D., Dravid, V.P., Kanatzidis, M.G.: The panoscopic approach to high performance thermoelectric. Energy Environ. Sci. **7**(1), 256–258 (2014). doi:10.1039/C3EE43099E
3. Minnich, A.J., Dresselhaus, M.S., Ren, Z.F., Chen, G.: Bulk nanostructured thermoelectric materials: current research and future prospects. Energy Environ. Sci. **2**(5), 466–479 (2009). doi:10.1039/B822664B
4. Baranowski, L.L., Snyder, G.J., Toberer, E.S.: Concentrated solar thermoelectric generators. Energy Environ. Sci. **5**, 9055–9067 (2012). doi:10.1039/C2EE22248E
5. LaLonde, A.D., Pei, Y.Z., Snyder, G.J.: Reevaluation of PbTe1 − *x*I*x* as high performance n-type thermoelectric material. Energy Environ. Sci. **4**(6), 2090–2096 (2011). doi:10.1039/C1EE01314A
6. He, J.Q., Kanatzidis, M.G., Dravid, V.P.: High performance bulk thermoelectrics via a panoscopic approach. Mater. Today **16**(5), 166–176 (2013). doi:10.1016/j.mattod.2013.05.004
7. Sherchenkov, A.A., Shtern, Y.I., Mironov, R.E., Shtern, M.Y., Rogachev, M.S.: Current state of thermoelectric material science and the search for new effective materials. **10**(11–12), 827–840 (2015). doi:10.1134/S1995078015060117
8. Poate, J.M., Tu, K.N., Mayer, J.W. (ed.): Thin films—interdiffusion and reaction. Wiley, New York (1978). doi:10.1002/pol.1979.130170107
9. Gromov, D.G., Mochalov, A.I., Klimovitskiy, A.G., Sulimin, A.D., Redichev, E.N.: Approaches to diffusion barrier creation and trench filling for copper interconnection formation. Appl. Phys. A **81**(7), 1337–1343 (2005). doi:10.1007/s00339-005-3259-4

Investigation of the Crystallization Kinetics in the Phase Change Memory Materials of Ge–Sb–Te System

A. Sherchenkov, S. Kozyukhin, A. Babich, P. Lazarenko, S. Timoshenkov, A. Shuliatyev and A. Baranchikov

Abstract In this work mechanism and kinetics of crystallization for thin films on the basis of Ge–Sb–Te–Bi and Ge–Sb–Te–In perspective for phase change memory application were investigated. Possible data processing and storage times of the PCM cell were estimated. It was shown that PCM cell based on $Ge_2Sb_2Te_5$ + 0.5 wt% Bi have minimum data processing and maximum data storage times in comparison with the other investigated materials.

Keywords Phase change memory · Crystallization kinetics · Ge–Sb–Te system

A. Sherchenkov (✉) · A. Babich · P. Lazarenko · S. Timoshenkov · A. Shuliatyev
National Research University of Electronic Technology, Bld. 1, Shokin Square, Zelenograd, Moscow, Russia
e-mail: aa_sherchenkov@rambler.ru

A. Babich
e-mail: drent@yandex.ru

P. Lazarenko
e-mail: aka.jum@gmail.com

S. Timoshenkov
e-mail: spt@miee.ru

A. Shuliatyev
e-mail: ashuliatyev@gmail.com

S. Kozyukhin · A. Baranchikov
Kurnakov Institute of General and Inorganic Chemistry of the Russian Academy of Sciences, 31 Leninsky Prospect, Moscow, Russia
e-mail: sergkoz@igic.ras.ru

A. Baranchikov
e-mail: baranchikov@gmail.com

A.Y. Oral and Z.B. Bahsi Oral (eds.), *3rd International Congress on Energy Efficiency and Energy Related Materials (ENEFM2015)*, Springer Proceedings in Energy, DOI 10.1007/978-3-319-45677-5_32

1 Introduction

Phase-change memory (PCM) devices are actively developed now. This type of memory has several advantages, one of which—low energy consumption. For recording of the information two phase states of material are used. The transition between these states does not require high energy budget. In this regard, low energy consumption is achieved. According to Samsung information, the transition from the use of NOR flash memory to PCM in mobile phones will enable a reduction of 30 % in energy consumption and 40 % of occupied space [1].

Two main types of PCM memory devices exist now—optical and electrical phase-change memories. The work of both types of devices is based on rapid reversible amorphous-to-crystalline phase transitions, which can be initiated by laser or electrical pulses, respectively. PCM materials in amorphous and crystalline states have very different optical and electrical properties, and are attributed as "zero" and "unit" logical states.

Chalcogenide materials of the of Ge–Sb–Te system are considered to be most promising for the phase-change memory application due to fast phase transition and high stability at room temperature. Most perspective among them is $Ge_2Sb_2Te_5$ (GST225) compound on the pseudobinary line GeTe-Sb_2Te_3. Yamada et al. [2] proposed to use GST225 in optical and electrical phase-change memories, which lead to commercial success of CD, DVD, Blu-ray discs.

Noticeable progress was achieved last years in the development of phase change memory. However, improvement of the PCM characteristics is still required. One of the problems is connected with the need of decreasing the data processing time of PCM to the level comparable with that of the random access memory ($\sim$10–50 ns). For this purpose increasing of crystallization rate and effective methods for controlling thermal properties of PCM materials are required. Isomorphic Bi and non-isomorphic In are considered to be promising dopants for the modification of thermal characteristics of $Ge_2Sb_2Te_5$. However, crystallization kinetics is needed to be elucidated.

So, the aim of this work was investigation of the crystallization kinetics in Ge–Sb–Te–Bi and Ge–Sb–Te–In thin films.

2 Experimental

The GST225 alloys with different amounts of Bi (from 0 to 7.7 wt%) and In (from 0 to 3 wt%) were synthesized with using quenching technique [3]. Thin films were prepared by thermal evaporation of synthesized materials. Substrate temperature during the deposition did not exceed 50 °C.

X-ray diffraction (Rigaku D/MAX, Cu Ka k = 0.15481 nm) showed that synthesized materials were polycrystalline and have trigonal modification of $Ge_2Sb_2Te_5$. Introduction of Bi leads to the appearance of trigonal modification of

Table 1 Results of composition analysis by RBS for GST 225 + Bi thin films

Initial compounds (bulk polycrystalline)	Thin film compositions, at. un., accuracy ±5 %				Bi content for thin film (calculation), wt %
	Ge	Sb + Te	Bi	Oxygen	
GST 225	2	7	–	–	–
GST225 + 0.5 wt% Bi	2	6.80 ± 0.20	0.024 ± 0.010	< (0.12 ± 0.04)	0.48
GST225 + 1 wt% Bi	2	6.86 ± 0.20	0.053 ± 0.010	< (0.20 ± 0.06)	1.07
GST225 + 3 wt% Bi	2	6.90 ± 0.20	0.14 ± 0.010	< (0.10 ± 0.04)	2.75

Table 2 Results of composition analysis by EDXRA for GST 225 + In thin films

Initial compounds (bulk polycrystalline)	Thin film compositions, at. un.				Bi content for thin film (calculation), wt%
	Ge	Sb	Te	In	
GST225 + 0.5 wt% In	0.224	0.222	0.547	0.00463	0.45
GST225 + 1 wt% In	0.197	0.263	0.527	0.00866	0.96
GST225 + 3 wt% In	0.191	0.268	0.505	0.0353	3.80

$Bi_2Ge_2Te_5$, which indicates on the replacement of Sb by Bi. As-deposited thin films were amorphous up to 3 % of Bi. Higher concentrations of Bi lead to the appearance of crystalline phases.

Rutherford backscattering (RBS, E_d = 1.0 and E_α = 2.7 meV at 135° scattering angle) and Energy Dispersive X-Ray Analysis (EDXRA, Inka-Sight) showed that the compositions of films were close to those of synthesized materials (Tables 1 and 2).

Differential scanning calorimetry (DSC-50, Shimadzu) was used for the investigation of thermal properties. Measurements were carried out at 8 different heating rates (from 1 to 90 °C/min) in a nitrogen flow (20 ml/min). Thin films were scraped off from c-Si wafers and pressed in Al pans.

3 Results and Discussions

Differential scanning calorimetry of the as-deposited amorphous films revealed a number of heat effects with crystallization peak for all compositions lays in the temperature range of 135–220 °C (Figs. 1 and 2).

Crystallization temperatures were estimated for all investigated materials, and concentration dependencies of crystallization temperatures are presented in Fig. 3.

As can be seen from the figure, crystallization temperatures increases with dopant concentration higher than 3 wt%. At lower concentrations dependencies are not monotonous with the largest deviation for GST225 + 0.5 wt% Bi.

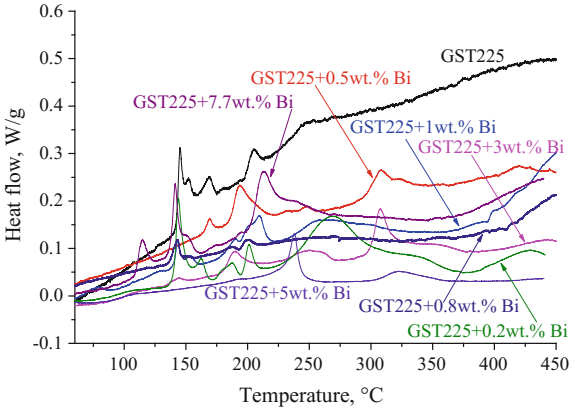

Fig. 1 DSC scans of as-deposited GST225+Bi thin films for heating rate of 10 °C/min

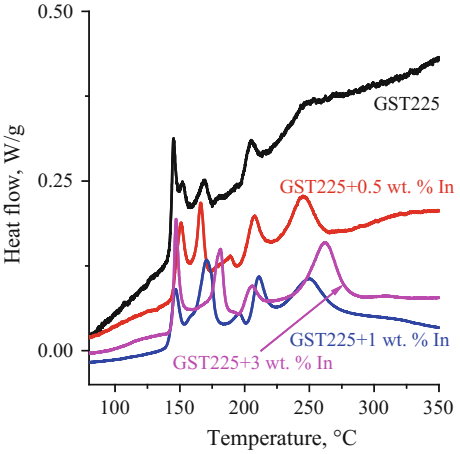

Fig. 2 DSC scans of as-deposited GST225+In thin films for heating rate of 10 °C/min

To determine kinetic triplet (effective activation energy of crystallization, pre-exponential factor, crystallization model) for crystallization process of GST thin films we used Isoconversional model-free method of Ozawa-Flynn-Wall (OFW) [4], and Coates-Redfern model-fitting method [4]. Such joint use of model-free and model-fitting methods allowed us to estimate activation energy and pre-exponential factor as functions of conversion, and determine reaction models.

It was found that crystallization process most adequately can be described by the second or third-order reactions, which are characteristic for spontaneous nucleation with further growth without overlapping [5].

Dependencies of the effective activation energy of crystallization on conversion for investigated materials are presented in Figs. 4 and 5.

As can be seen from the figures activation energy for undoped GST225 at the beginning of the crystallization is $\sim$2 eV, and gradually decreases with the

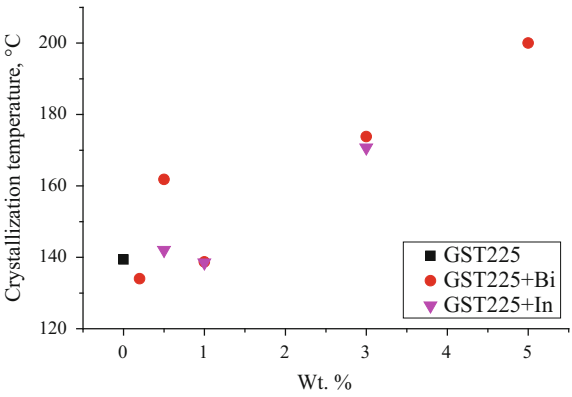

Fig. 3 Concentration dependencies of crystallization temperatures for investigated thin films

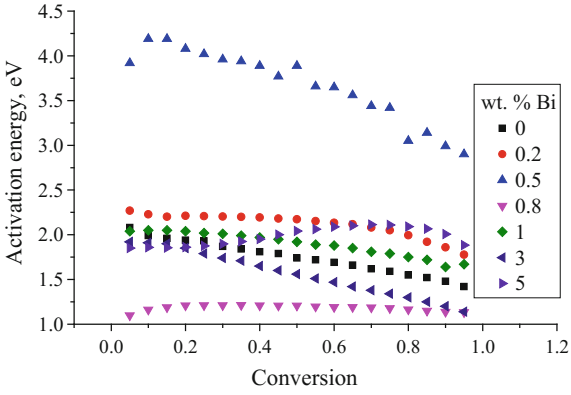

Fig. 4 Effective activation energy of crystallization for compositions with Bi

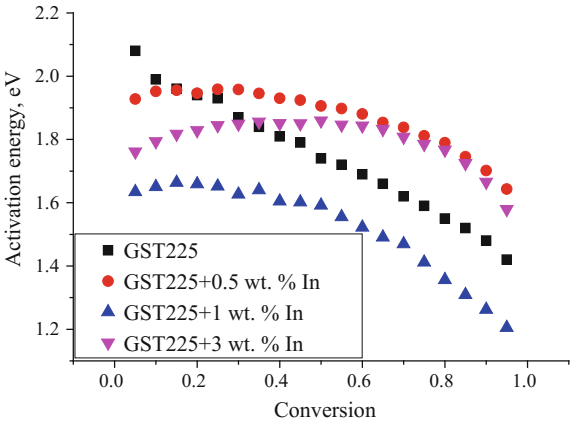

Fig. 5 Effective activation energy of crystallization for compositions with In

increase of conversion. This result indicates that crystallization of GST films is a complex process consisting at least of two stages. For crystallization process the most possible stages are nucleation and crystal growth. Contribution of the first process gradually decreases, while of the second increases. In this case, activation energy in the initial moment corresponds to the activation energy of nucleation, while in the end—to the activation energy of crystal growth. Similar tendency is observed for GST225 + Bi thin films. However, sufficiently higher values of the effective activation energy in comparison with other investigated materials were established for GST225 + 0.5 wt% Bi thin films.

For GST225+In slight change of the activation energy at the beginning of crystallization indicates on the enhanced influence of In doping on the nucleation in GST225, which leads to the elongation of the stage controlled by the nucleation.

After the kinetic triplet determination, we used it for the estimation of possible data processing and storage times of the PCM cells on the basis of investigated materials. We supposed that logical "zero" and "unit" states differs by the values of conductivity not less, than by 1–2 orders of magnitude. This allowed us to estimate conversion at which transition between "0" and "1" logical states of the PCM cell occurs by the equation [6]:

$$\alpha = (\ln \sigma - \ln \sigma_a)/(\ln \sigma_c - \ln \sigma_a), \tag{1}$$

where σ_a is the conductivity of a completely amorphous material, σ_c is the conductivity of a completely crystalline material, and σ is the conductivity of the material with the crystalline fraction α.

The calculations showed that the transition between "0" and "1" occurs at $\alpha = 0.45$. By using this value of conversion we estimated possible data processing and storage times of PCM cells as crystallization time of the films on the basis of investigated materials at different temperatures, which can be calculated by the equation [5]:

$$t = g(\alpha)/[A \exp(E_a/(RT))], \tag{2}$$

where g(α) is integral form of the found reaction model, A is the pre-exponential factor.

Calculated data processing and storage times for PCM cells on the basis of investigated materials are presented in Fig. 6.

As can be seen from the figure calculations predicts that PCM cells on the basis of $Ge_2Sb_2Te_5$ + 0.5 mass% Bi will have the best data processing and storage times in comparison with the rest compositions. At the crystallization temperature higher than 300 °C data processing time of the PCM cell on the basis of this material is lower than ~50 ns, which is comparable with the data processing time of the random access memory. In addition, PCM cells on the basis of $Ge_2Sb_2Te_5$ + 0.5 wt % Bi has extremely long storage time due to the longest crystallization time at room temperature among all investigated materials.

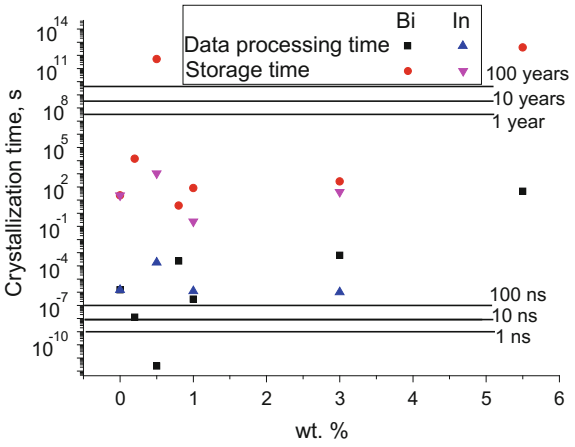

Fig. 6 Data processing and storage times for PCM cells on the basis of investigated materials

4 Conclusions

Thus, investigations showed that introduction of Bi and In in $Ge_2Sb_2Te_5$ can affects thermal properties of the material, in particular crystallization kinetics, which is important for the improvement of PCM technology.

It was found that $Ge_2Sb_2Te_5$ + 0.5 wt% Bi can provide data processing time of the PCM cell comparable with that of the random access memory. In addition, at room temperature this material has extremely long storage time.

Acknowledgments This study was supported by Ministry of Education and Science of RF (project ID: RFMEFI57514X0096).

References

1. Clarke, P.: Samsung moves phase-change memory to production. http://www.eetimes.com/document.asp?doc_id=1171737 (2009). Accessed 22 Sept 2009
2. Yamada, N., Ohno, E., Akahira, N., Nishiuchi, K., Nagata, K., Takao, M.: High-speed overwritable phase-change optical disc material. Jpn. J. Appl. Phys. **26**(Suppl. 26–4), 61 (1987). doi:10.1143/JJAP.26S4.61
3. Kozyukhin, S., Sherchenkov, A., Gorschkova, E., Kudoyarova, V., Vargunin, A.: Thermal effects in Ge–Sb–Te phase-change memory materials during multiple thermal cycling. Phys. Status Solidi C **7**, 848–851 (2010). doi:10.1002/pssc.200982703
4. Kozyukhin, S., Sherchenkov, A., Babich, A., Lazarenko, P., Nguyen, H.P., Prikhodko, O.: Peculiarities of Bi doping of Ge–Sb–Te thin films for PCM devices. Can. J. Phys. **92**(7/8), 684–689 (2014). doi:10.1139/cjp-2013-0607
5. Brown, M.E. (ed.): Handbook of Thermal Analysis and Calorimetry. Elsiever Science B.V, Amsterdam (1998)
6. Mehta, N., Kumar, A.: A study of thermal crystallization in glassy $Se_{80}Te_{20}$ and $Se_{80}In_{20}$ using DSC technique. J. Therm. Anal. Calorim. **83**, 669–673 (2006). doi:10.1007/s10973-004-6342-8

Fuel Cell for Standalone Application Using FPGA Based Controller

Kamalakanta Mahapatra and Kanhu Charan Bhuyan

Abstract Currently, escalation in consumption of energy, instability of crude oil price and global environment change has forced researchers to focus more on renewable energy sources. There are different new and renewable energy sources (such as photovoltaic and wind energy), however each possess some limitations or other. Fuel Cell is an important alternative that can be compared to other new and renewable sources of energy and proved to be better in certain terms and Solid oxide fuel cell (SOFC) is a more efficient, environmental friendly renewable energy source. This paper focuses on load/grid connected fuel cell power system (FCPS) which can be used as a backup power source for household and commercial units. This backup power source would be efficient and will provide clean energy at an affordable per unit cost. Load/grid connected fuel cell power system mainly comprises a fuel cell module, DC-DC converter and DC-AC inverter. This work primarily focuses on solid oxide fuel cell (SOFC) modelling, digital control of DC-DC converter and DC-AC inverter. Extensive simulation is conducted to validate our concepts and some experimental results confirm the same. Dynamic mathematical model of SOFC is developed to find out output voltage, efficiency, and losses in fuel cell stack. One output from fuel cell is DC voltage that is fed to a DC-DC converter for stepping up as usually this is a low voltage. Proportional-Integral (PI) controller and FPGA based PI controller are implemented and experimentally validated. The prototype of single phase system having fuel cell as input and delivering ac power is developed. FPGA (Field Programmable Gate Array) implementation of HCC is done using NI-cRIO-9014. FPGA implementation of three phase model of fuel cell power system is developed using adaptive-fuzzy-HCC using Xilinx/System Generator.

Keywords Fuel cell · Fuel cell power system · FPGA

K. Mahapatra (✉) · K.C. Bhuyan
ECE Department, National Institute of Technology, 769008 Rourkela, India
e-mail: kkm@nitrkl.ac.in

A.Y. Oral and Z.B. Bahsi Oral (eds.), *3rd International Congress on Energy Efficiency and Energy Related Materials (ENEFM2015)*, Springer Proceedings in Energy, DOI 10.1007/978-3-319-45677-5_33

1 Introduction

There is a loud rise in consumption of energy worldwide since last decade. Mostly energy is generated from fossil fuel that has a restricted supply. Generation of energy through conventional methods also reasons irretrievable damage to environment. In most parts of the world there is a substantial gap between demand and supply of energy that leads to the energy crisis scenario. The demand of electrical energy is increasing every day and is likely to rise by 75 % in the year 2030 compared to today's demand [1, 2]. Substantially energy crunch points to economic crisis. To meet the demand of energy, mankind has been using renewable energy sources like wind power, solar power, biomass power from past few decades. Steady progress in market deregulation and new legislations in terms of environmental constraints and greenhouse gas emissions has created a significant opportunity for distributed generation. Rising public awareness for ecological shield and continuously increasing energy consumption, coupled with the shortage of power generation due to constraints imposed on new construction have further resulted in a steady rise in interest in renewable and clean power generation. The switch to renewable energy has been proved beneficial for both mankind and environment. So researchers are working towards new ways to generate energy from renewable sources. The major part of the renewable energy comes from wind power. Solar power comes a distant second. One drawback of wind and solar energy sources is their variability. Wind is likely to flow irregularly and power from photovoltaic sources is only available during the daytime. If possible, additional energy generated during times when sufficient energy does exist; can be stored for periods when adequate electricity is not available. However, storage of this energy is usually a challenging task.

Due to the practical limitation of wind and solar energy, chemical energy is widely used for generation of electricity. A fuel cell is a device which transforms stored chemical energy (hydrogen, oxygen) to electrical energy. The conversion of the fuel to electricity takes place via an electrochemical process that is non-polluting and efficient. One of the major advantages of a fuel cell system is that it can be placed at any site in a distribution system without geographic limitations to provide optimal benefit, and they are not intermittent in nature whereas for solar and wind energy generation proper geographical survey has to be carried out to find the best possible place for their installation. Fuel cells offer numerous advantages over conventional power plants to achieve widespread adoption, such as:

- Great efficiency, even at part-load
- Few moving parts that results in quiet operation, upper reliability, lower maintenance and longer operating life
- Fuel diversity
- Zero or low emission of greenhouse gases
- Combined Heat and Power (CHP) capability, without the need for additional systems (i.e., low temperature fuel cells can provide district heating while high temperature fuel cells can provide high-quality industrial steam)

- Flexible, modular structure
- Increased energy security by reducing reliance on large central power plants and oil imports

In this paper we have made an attempt to use fuel cell as a power source. Fuel Cell output is connected to a DC-DC converter that in turn is connected to an inverter which provides us ac voltage at required voltage and frequency. We have experimentally verified our concept and we use an FPGA for reducing the size of control circuit.

2 Fuel Cell in Conjunction with DC-DC Boost Converter

A boost converter is a power converter with output dc voltage is greater than its input dc voltage. A boost converter steps up the output voltage by first storing energy by passing currents through an inductor and that energy is then delivered at intervals by a MOSFET regulated by PWM (Pulse width modulation) to a capacitor [3]. The charged capacitor will then supply a higher voltage at lower current to the load.

3 PWM-Current Control Techniques for Fuel Cell Inverter

DC-AC power converters are known as inverters. The function of an inverter is to change a dc input voltage to symmetric ac voltage that would appear at output with required amplitude and frequency. The output voltage of inverter could be fixed or variable frequency. The output waveforms of ideal inverters must be sinusoidal. However, the waveforms of practical inverters are non-sinusoidal and contain some harmonics.

This paper presents novel hierarchical control architecture that comprises battery and a Solid Oxide Fuel Cell. The objective is to improve power flow of this crossbreed generation system for various modes of operation while taking into an account component and system constraints. The inverter is controlled as a single phase power structure with resistor emulation at its output. The converter is reliable and exhibits a high efficiency over a wide input power range. Experimental results verify that the inverter exhibits a high power factor and low current total harmonics distortion (THD).

4 Experimental Validation and Analysis

This section describes the experimental validation of single-phase fuel cell power system. The fixed hysteresis current controller (HCC) technique is considered to provide accurate gate pulse for voltage source inverter. The prototype model of fuel cell power system consists of four IGBTs (SKM75GB063D), DC-link capacitor of 6800 μF and an inductor (5 mH). The single phase supply voltages, load currents and DC voltage signals are sensed and fed to the HCC. Figure 1 shows the schematic diagram of the fuel cell power system using hysteresis current controller technique. The design details and entire hardware development of fuel cell power system is represented below.

The prototype model of fuel cell power system consists of four-IGBT-SKM75GB063D, DC-link capacitor 6800 μF and an inductor (5 mH). The single phase supply voltages, load currents and DC voltage signals are sensed and computed, which are main inputs of the controller. Figure 1 shows the schematic diagram of the fuel cell power system using hysteresis current controller technique. The photograph of experimental set up is shown in Fig. 2. The HCC technique is used to generate the switching pulses of the voltage source inverter. The required switching pulses are provided to the IGBT inverter via compactRIO through the gate driver circuits. The performance of the fuel cell power system has been experimented under the linear load. Initially, voltage source inverter acts as rectifier to charge the DC-link capacitor voltage through anti parallel diodes. When

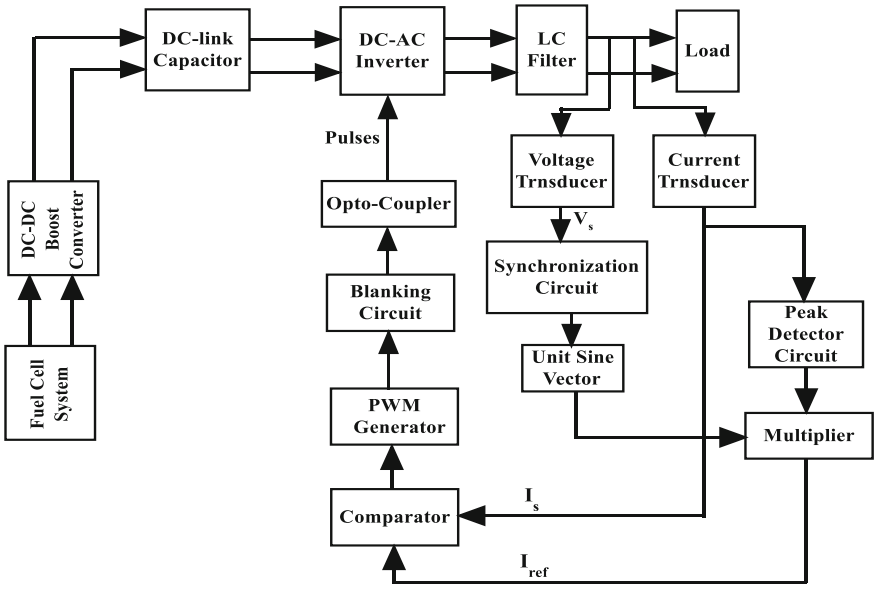

Fig. 1 Schematic diagram of fuel cell power system

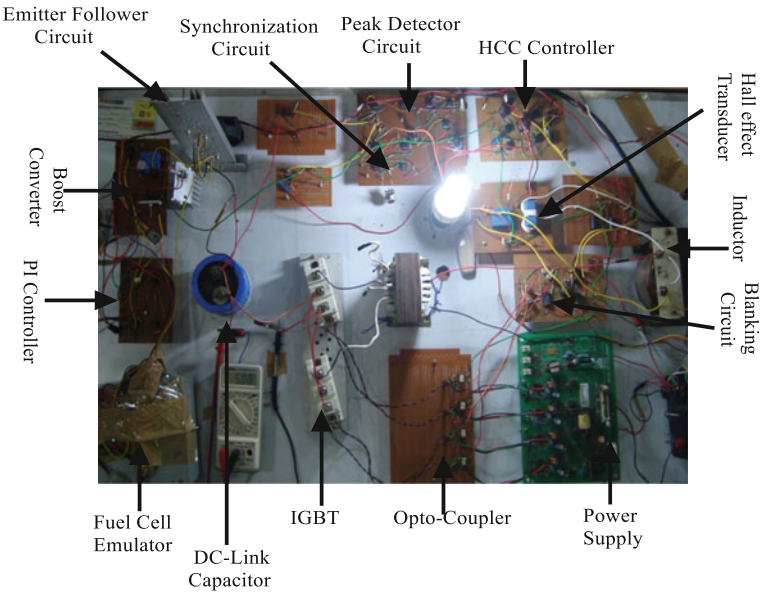

Fig. 2 Sketch of experimental set up

capacitor DC voltage reaches supply voltage level; it is considered to be in floating mode, the inverter will be ON in the sense that circuit now acts as an inverter with IGBTs being activated.

Figure 3 indicates experimental wave forms of a single-phase fuel cell system. These wave forms designate that the supply voltages (Vs = 150 V) are sinusoids. The inverter output waveform before filter is shown in Fig. 3b shows the source currents of fuel cell power system. The direct current control HCC technique is employed for generating gate control switching pulses to drive the fuel cell system. Figure 3a shows the experimental wave forms of single-phase fuel cell inverter system. The inverter output voltage waveform before filter is shown in Fig. 3b. Figure 3c shows the source currents of fuel cell power system. The direct current control HCC technique is employed for generating gate control switching pulses to drive the fuel cell inverter. The DC-link capacitor voltage is shown in Fig. 3d.

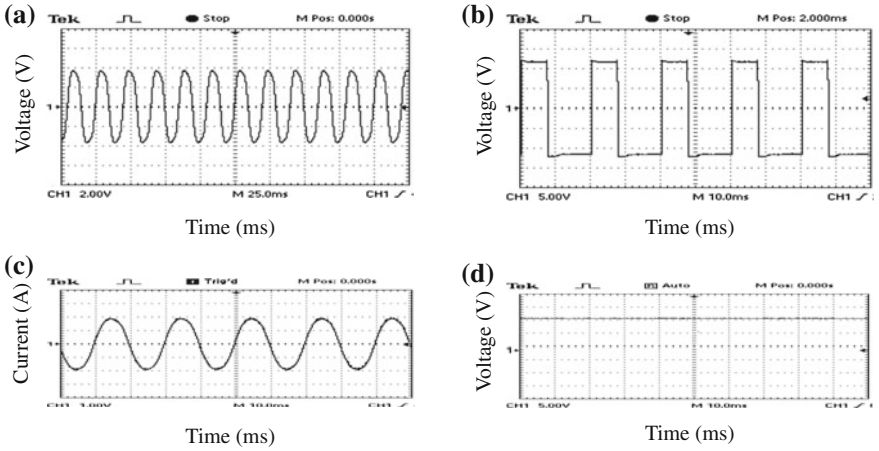

Fig. 3 **a** Supply voltage, **b** inverter output, **c** source current, **d** DC-link capacitor voltage

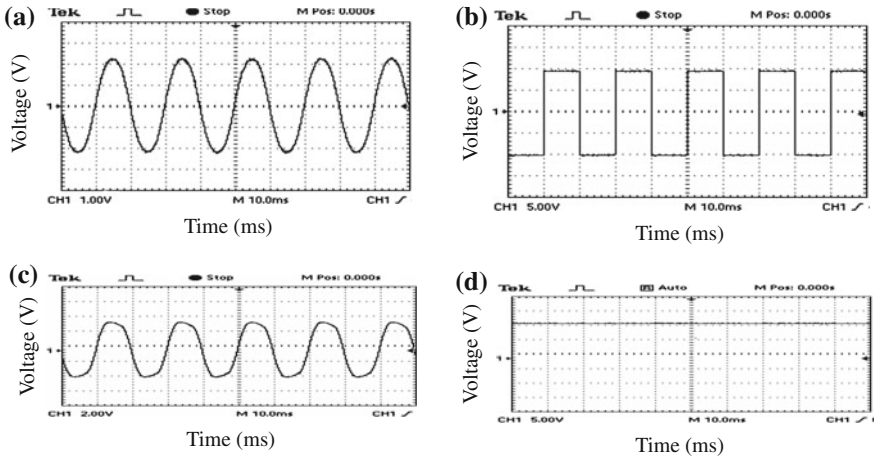

Fig. 4 **a** Supply voltage, **b** inverter output, **c** source current, **d** DC-link capacitor voltage

In this experimental set up, single phase load connected fuel cell power system is developed. FPGA implementation of HCC is carried out using NI CompactRIO-9014. The HCC provides accurate pulse width modulation signal to drive the DC/AC inverter. Figure 4 shows the experimental waveform of output voltage of a single-phase fuel cell system that uses NI-cRIO-9014 from National

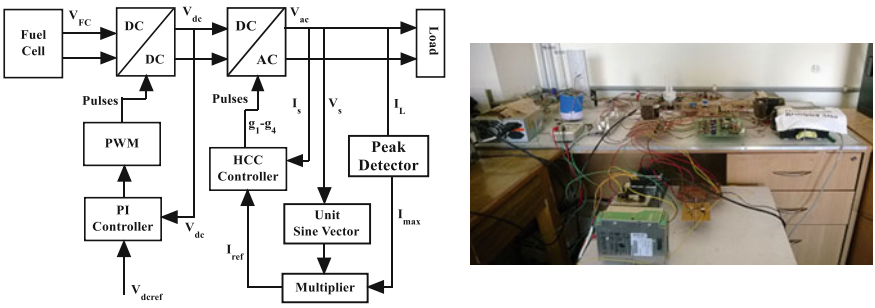

Fig. 5 Schematic diagram and experimental set-up using NI cRIO-9014 for fuel cell power system

Instruments. The direct current control HCC technique is designed in cRIO for generating gate control switching signals to drive the fuel cell power system. The inverter output voltage waveform is shown in Fig. 4. The PI controller is also designed in cRIO to control the DC-link capacitor voltage. The DC-link capacitor voltage is shown in Fig. 4d.

For simulation of the above system, following parameters are considered (Fig. 5).

1. Supply voltage 230 V
2. Frequency 50 Hz
3. Interfacing inductance 1.8 mH
4. Capacitance 2200 μF

The waveform of the instantaneous single-phase balance supply voltage is shown in Fig. 6a. Source Current and the output voltage waveforms are shown in Fig. 6b, c respectively.

The simulation results in Fig. 7 is obtained using adaptive-HCC technique to generate the switching pulses to drive the fuel cell inverter. In this simulation, 380 numbers of fuel cells are considered and these fuel cells are connected in series to make the fuel cell output voltage 400 V DC. The fuel cell output voltage is shown in Fig. 7a. To step up the fuel cell voltage up to approximately 500 V, a DC-DC boost converter is used. The boost converter output is shown in Fig. 7b. The inverter output is fed to LC filter to suppress the ripples. The LC filter is unable to suppress all the ripples of inverter output current. Figure 7c shows the inverter output current. Here some amount of ripples is present due to grid side interfacing

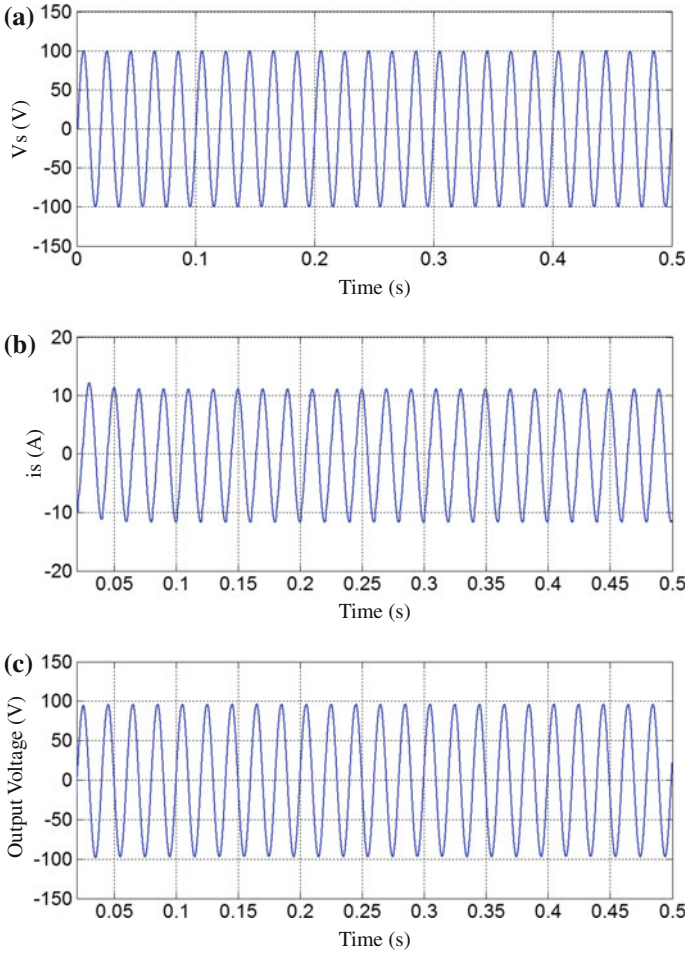

Fig. 6 Simulation results for single-phase fuel cell power system

inductance and LC filter. The interfacing inductance is also useful for isolation between inverter side and load/grid side. Figure 7d shows the output voltage of inverter after filter. These results are only presented to demonstrate that we can also use fuel cell in a three-phase system [4].

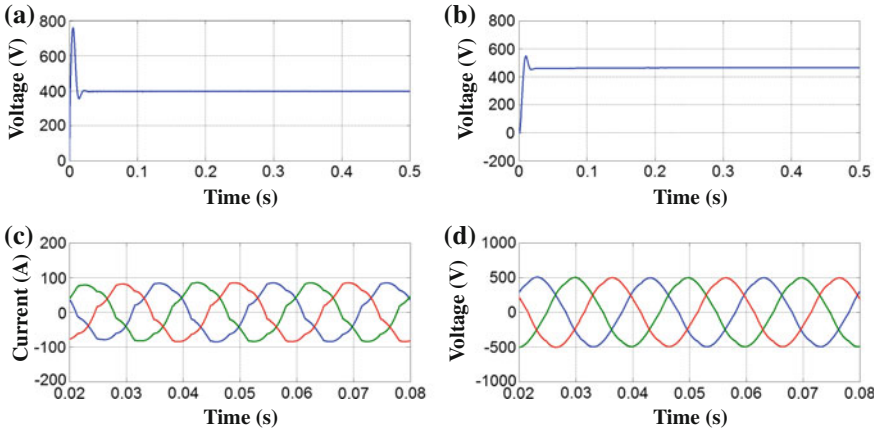

Fig. 7 Simulation waveform of **a** fuel cell output voltage, **b** DC-DC boost converter output voltage, **c** inverter output current, and **d** inverter output voltage (A-HCC)

5 Conclusions

The fuel cell power system (FCPS) is modeled and evaluated through MATLAB/SIMULINK tools. A complete dynamic model for SOFC fuel cell is developed. Fuel Cell in conjunction with DC-DC converter is used to develop DC voltage system. This system is developed using a novel FPGA based controller that simplifies the control circuit. Extensive simulation studies are conducted for both single-phase FCPS and the performance of the system are investigated. The single-phase fuel cell system with HCC controller is experimentally validated. HCC technique for single phase fuel cell power system is implemented using National Instruments compactRIO-9014 that includes an FPGA. FPGA based Adaptive-Fuzzy-HCC (AHCC) controller for three-phase fuel cell inverter is designed and is experimentally validated.

References

1. U.S. Department of Energy: International energy outlook 2009 (IEO 2009). http://www.eia.doe.gov/oiaf/ieo/index.html (2009)
2. World energy needs and nuclear power. http://www.worldnuclear.org/inf/inf16.html (2009)
3. Sahu, B., Rincon-Mora, G.: A high-efficiency, dual-mode, dynamic, buck-boost power supply IC for portable applications. Paper Presented at International Conference on Embedded System Design (VLSID), Kolkata, India, 3–7 Jan 2005
4. Bhuyan, K.C.: Development of controllers using FPGA for fuel cells in standalone and utility applications. Dissertation, National Institute of Technology, Rourkela, India (2014)

Al_2O_3 + TiO_2 Thin Film Deposited by Electrostatic Spray Deposition

Alicja K. Krella, Andrzej Krupa, Arkadiusz T. Sobczyk and Anatol Jaworek

Abstract In the paper are presented the morphology of Al_2O_3 + TiO_2 thin film produced by electrostatic spray deposition method and the results of investigations of its endurance when subjected to thermal cycles and slurry erosion. The film was produced in steam atmosphere by simultaneously spraying of colloidal suspension of Al_2O_3 nanoparticles in propanol-2 (as a solvent) with the addition of $C_{10}H_{20}O_5Si$ (to improve film adhesion) and 1 % solution of butoxy titanium Ti $(OCH_2CH_2CH_2CH_3)_4$ in propanol-2 as a precursor of TiO_2. Performed investigations showed that Al_2O_3 particles and TiO_2 particles are uniformly distributed within the film, and that the weight content of aluminum and titanium is nearly the same. The thermal tests did not cause any fracture of the film but decreased film adhesion. Decreased adhesion of the film intensified degradation during slurry test.

1 Introduction

Aluminum oxide Al_2O_3 is frequently used for heat-resistant coatings, which are applied in high-temperature industrial installations, for example, in electric power plants. Aluminum oxide has very good physical and chemical properties such as, high melting point, chemical inertness, good mechanical stability, low thermal expansion coefficient, and high hardness. However, pure Al_2O_3 coating possesses high porosity and low fracture toughness that limits its application in harmful conditions. In order to decrease coating porosity and/or to improve its fracture toughness, other elements or compounds are added to it, e.g., molybdenum, niobium, titanium oxide, titanium carbide, titanium diboride [1–6].

A.K. Krella (✉) · A. Krupa · A.T. Sobczyk · A. Jaworek
Centre of Hydrodynamics, Institute of Fluid-Flow
Machinery Polish Academy of Sciences, Fiszera 14, Gdańsk, Poland
e-mail: akr@imp.gda.pl

A.Y. Oral and Z.B. Bahsi Oral (eds.), *3rd International Congress on Energy Efficiency and Energy Related Materials (ENEFM2015)*, Springer Proceedings in Energy, DOI 10.1007/978-3-319-45677-5_34

Al_2O_3 based thin film or coating can be deposited by various techniques, e.g. plasma spraying [1, 2], aqueous tape casting with hot pressing process [3–6], sintering [7], chemical vapor deposition [7] or physical vapor deposition [7]. Electrostatic spray deposition technique is an alternative to the methods mentioned above. This is a method of liquid atomization by electrical forces and is used for the deposition of various materials from the aerosol phase of coating-material solution, colloidal suspension or from a precursor solution [8]. This method allows obtaining fine liquid droplets, whose size can vary between tens of nanometers to hundreds of micrometers, depending on the liquid physical properties, liquid flow rate and magnitude of voltage applied to capillary nozzle and its polarity [8]. Although electrostatic spray deposition method has been used for Al_2O_3 thin film deposition [9], the mechanical and thermal properties of those coatings have not been investigated and reported.

The aim of this paper is to presents the results of the investigations of the endurance of Al_2O_3 and TiO_2 thin film, produced by electrostatic spray deposition method onto stainless steel substrate, to withstand thermal-fatigue cycles and slurry erosion.

2 Experimental

Stainless steel X10CrAlSi18 (18 % Cr, 1 % Mn, 1 % Al, 1 % Si, Fe—rest) was used as the substrate in these experiments. All substrate samples were in the form of round-ended rectangular 40 mm long and 4 mm thick. The width of these samples was 10 mm, and the corners were rounded with a radius of 5 mm. Before coating, the substrates were thermally treated at 800 °C for 1 h in Nabertherm L3/11 furnace in order to obtain their optimal thermal and mechanical properties.

The Al_2O_3 + TiO_2 thin film was produced in the steam atmosphere by simultaneous spraying of a colloidal suspension and a precursor. The colloidal suspension consisted of 54 mg of Al_2O_3 powder of particles size in the range of 40–80 nm, 99.3 mg of $C_{10}H_{20}O_5Si$ (to improve film adhesion) and 19 g of propanol-2 (solvent). The precursor was a 1 % solution of butoxy titanium $Ti(OCH_2CH_2CH_2CH_3)_4$ in propanol-2 ($CH_3CHOHCH_3$).

The electrostatic spraying setup used for coating deposition consisted of stainless-steel capillary nozzle connected to high voltage supply SPELMANN SL600W/30kV/PN switched to positive polarity, and grounded metal collector on which a substrate was placed. The inner diameter of capillary nozzle used for precursor and colloidal suspension spraying was 0.5 and 0.8 mm, respectively. The distance between the nozzle tip and substrate was 40 mm. The flow rate of both liquids was set to 1.0 ml/h and deposition time was t = 1 h. The optimal distribution of spraying jets were obtained at a voltage U = 10 kV. The collector was designed as a turn-table to obtain more uniform deposition of the droplets onto the substrate. The collector was heated during the process of electrostatic spraying in order to obtain the substrate temperature of about 60 °C that facilitated solvent

evaporation. After deposition thin film was dried at 35 °C for 10 h. Next, some specimens were subjected to thermal test to investigate thermal resistance. Thermal test consisted of 35 thermal cycles. One thermal cycle comprised of: heating to a temperature of 1000 °C for 5 h, keeping specimens at this temperature for 4 h, and cooling in furnace to a temperature of 100 °C. One thermal cycle tested 24 h. Then, all specimens were tested against slurry erosion to investigate endurance against dynamic loading and an influence of thermal cycles on the film endurance.

Slurry test was performed in the slurry erosion test rig that was built based on the original rig presented in Ref. [10]. Because slurry tests belong to aggressive tests, the initial exposure time was chosen for 30 s, and the whole slurry tests lasted 300 s. A peripheral speed of the rotating specimens was 5 m s^{-1}. Rounded steel grit of 530 mm diameter and hardness of 51 HRC in the amount of 458 g per tank (6 l) was used as an erodent. To determine erosion curves, samples were weighted using an analytical balance of sensitivity of 0.1 mg.

Before and after all tests, specimens were investigated using scanning electron microscope EVO-40 (Zeiss). The elemental composition of thin film was studied by EDS (Energy Dispersive Spectroscopy) method using BRUKER AXS Quantax 200 spectrometer with detector SDD X-flash 5010, 10 mm^2, 125 eV, 20 kV (SEM accelerating voltage).

3 Results and Discussion

Microscopic observation of Al_2O_3 + TiO_2 thin film after deposition (Fig. 1a) showed that the thin film was deposited uniformly but roughness of this film was high. The thin film did not fracture during thermal cycles (Fig. 1b). Slurry test caused a removal of outer layer revealing a dense and continuous film (Fig. 1c, d).

Microscopic observations of thin film after thermal test and slurry erosion test (Fig. 1d) revealed the film was removed in many places. Also same cracks and coating undulation were observed. In the case of film that not was thermally tested, only coating undulation was observed. The coating undulation was likely caused by impacts of solid particles during slurry test. Increasing mass loss during slurry test (Fig. 2) and film removal in many spots indicated that thermal cycles decreased the endurance of the film against dynamic loading, likely due to a decrease of the film adhesion.

Elemental composition analysis (Tables 1 and 2) showed that thermal cycles caused the change in elements composition in the outer layer, especially an increase in content of aluminum. The content of aluminum in the Al_2O_3 + TiO_2 film increased from 3.67 to 24.62 % after 20 thermal cycles and to 27.53 % during the last 15 thermal cycles. In the case of uncoated substrate the content of aluminum increased from 1.01 to 24.79 % during 15 thermal cycles (Table 2). In both cases an increase of aluminum content was similar (23.8 %). The increase of aluminum was probably caused by two processes that occurred nearly simultaneously at high temperature: diffusion processes and oxidation-reduction reactions. At 1000 °C the diffusion process is highly probable, especially the grain boundary diffusion that is

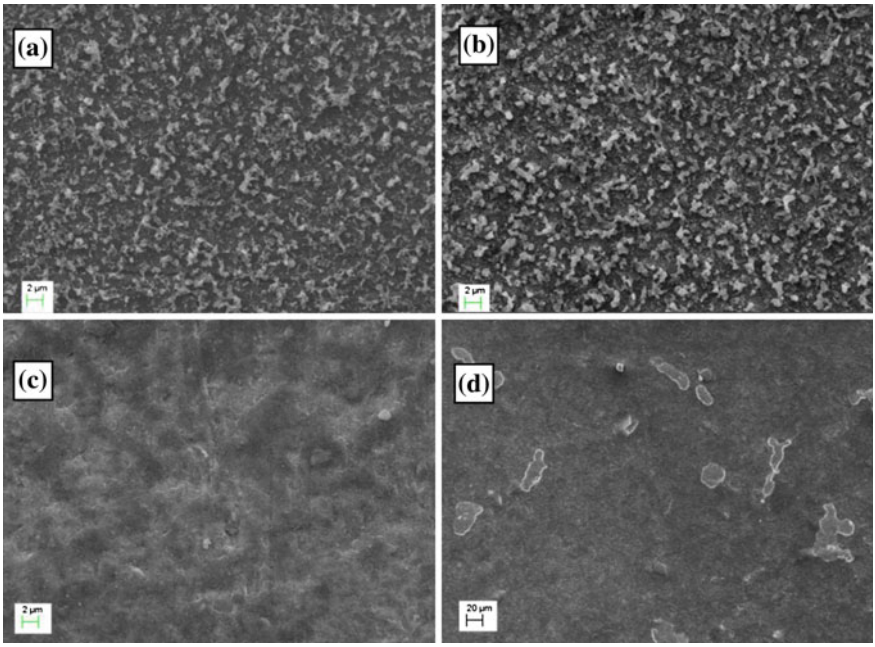

Fig. 1 Morphology of $Al_2O_3 + TiO_2$ thin film; **a** after deposition; **b** after 35 thermal cycles; **c** after slurry test, no thermally tested before; **d** after thermal cycles and slurry test

Fig. 2 Slurry erosion curves

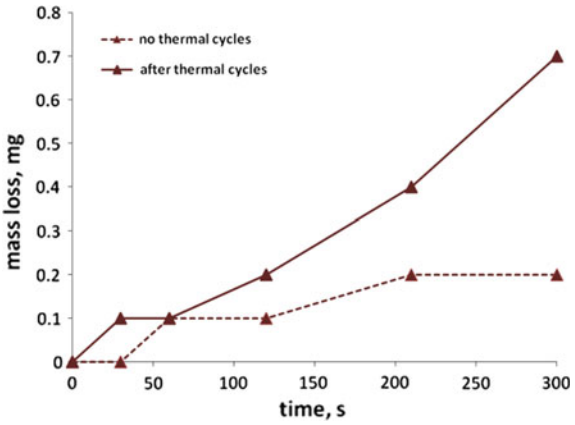

much faster than the lattice diffusion. Additionally, aluminum, whose enthalpy is less than the enthalpy of iron at 1000 °C, in accordance with the Ellingham diagram, reduces the iron oxide to aluminum oxide. This was the most probable process that caused such increase of aluminum content in the outer layer during thermal cycles. Because aluminum oxides very forms very quickly thin compact

Table 1 Elemental composition (wt%) of Al_2O_3 + TiO_2 thin film

Element	After deposition	After 35 thermal cycles	After slurry tests, no thermal cycles	After slurry test and thermal cycles
Aluminum	3.67 ± 0.21	27.53 ± 1.35	3.24 ± 0.19	26.18 ± 1.29
Silicon	0.94 ± 0.07	0.32 ± 0.04	1.14 ± 0.08	0.28 ± 0.04
Titanium	3.54 ± 0.13	4.05 ± 0.15	2.73 ± 0.11	2.42 ± 0.10
Chromium	15.29 ± 0.44	6.66 ± 0.22	14.53 ± 0.42	5.97 ± 0.20
Manganese	–	1.05 ± 0.07	0.43 ± 0.03	0.85 ± 0.06

Table 2 Elemental composition (wt%)

Element	Substrate as supplied	Substrate after 15 thermal cycles	Al_2O_3 + TiO_2 thin film after 20 thermal cycles
Aluminum	1.01 ± 0.08	24.79 ± 1.26	24.62 ± 1.22
Silicon	0.81 ± 0.06	0.19 ± 0.04	0.26 ± 0.04
Chromium	17.18 ± 0.47	11.23 ± 0.35	7.96 ± 0.25
Manganese	0.80 ± 0.07	1.30 ± 0.07	1.07 ± 0.07

layer that protects lower layers against further oxidation, the most intensive increase of aluminum content in the outer layer occurred during first few thermal cycles. Later, the rate of an increase of aluminum content decreased. After 35 thermal cycles the content of aluminum in the outer layer (Table 1) increased slightly comparing to that after 20 thermal cycles (Table 2).

After deposition, no manganese was detected in Al_2O_3 + TiO_2 thin film. The content of manganese in Al_2O_3 + TiO_2 thin film after thermal cycles was 1.05 wt%. It should be noted that the content of manganese did not change between 20 and 35 thermal cycles. On the other hand, the content of this element in a steel substrate was 0.8 % and after 15 thermal cycles increased to 1.30 % (Table 2). Thus, performed investigation showed that thermal cycles caused slightly larger increase of manganese content in uncoated steel substrate. The increase of manganese content in the outer layer was probably caused by grain boundary diffusion processes and oxidation-reduction reactions, similarly to the increase of aluminum. Similar to the case of aluminum, the enthalpy of manganese is less than the enthalpy of iron, so manganese can reduce iron oxide to manganese oxide. Thus, the deposition of Al_2O_3 + TiO_2 thin film on the substrate did not prevent substrate from manganese diffusion (Table 2). However, after initial increase of manganese content, an increase of the number of thermal cycles did not caused an increase in the content of manganese. Thus, this suggests that the diffusion process occurred mostly during first few thermal cycles.

Slurry erosion curves (Fig. 2) showed an influence of thermal cycles on the thin film endurance. In the case of specimen that was not thermally tested, the cumulative mass loss was only 0.2 mg after the whole test and during first 30 s of the test no mass loss occurred. The mass loss of 0.2 mg was probably correlated with the removal of the rugged top layer (Fig. 1c). This would mean that the rugged top

layer was very thin. In the case of specimen that was subjected to thermal cycles before, the mass loss began with the beginning of slurry test and the rate of mass loss increased with the duration of test. Cumulative mass loss of this specimen was 0.7 mg after whole test (Fig. 2). The mass loss of the thermally tested specimen was correlated with the removed thin film shown in Fig. 1d.

Slurry test caused a slight decrease in the content of elements. The decrease of aluminum and titanium content (Table 1) was probably correlated with the removal of top layer.

The decrease of the endurance of the Al_2O_3 + TiO_2 thin film caused by thermal cycles was probably the effect of the mismatch of thermal coefficients of elongation between substrate and the thin film leading to delamination and diffusion process of aluminum. Delamination of the Al_2O_3 + TiO_2 thin film facilitated oxidation-reduction reactions of aluminum that diffused from the substrate and formation of thin oxide layer on the substrate surface. On the other hand, formation of thin oxide layer increased the delamination of the film. Delaminated thin film was not able to resist dynamic loading and fractured easily.

4 Conclusions

Performed investigations showed that:

- Thermal cycles did not cause fracture of the Al_2O_3 + TiO_2 thin film deposited by electrostatic spraying.
- Deposition of Al_2O_3 + TiO_2 thin film did not prevent the substrate from diffusion processes and oxidation-reduction reactions of aluminum and manganese.
- Thermal cycles lessened the endurance of thin film against dynamic loading.
- Thermal cycles decreased the adhesion of the Al_2O_3 + TiO_2 thin film.

Acknowledgments The paper is supported by the Project No. 2011/03/B/ST8/05643 "The elaboration of coatings of heat resistant properties deposited by means of electrohydrodynamic method" financed by Polish National Science Centre.

References

1. Celik, E., Sengil, I.A., Avcı, E.: Effects of some parameters on corrosion behaviour of plasma-sprayed coatings. Surf. Coat. Tech. **97**, 355–360 (1997)
2. Gao, J., Suo, J.: Proposal of self-healing coatings for nuclear fusion applications. Surf. Coat. Tech. **204**, 3876–3881 (2010)
3. Deng, J., Can, T., Sun, J.: Microstructure and mechanical properties of hot-pressed Al_2O_3/TiC ceramic composites with the additions of solid lubricants. Ceram. Int. **31**, 249–256 (2005)

4. de Portu, G., Guicciardi, S., Melandri, C., Monteverde, F.: Wear behaviour of Al_2O_3–Mo and Al_2O_3–Nb composites. Wear **262**, 1346–1352 (2007)
5. Sbaizero, O., Pezzotti, G.: Influence of molybdenum particles on thermal shock resistance of alumina matrix ceramics. Mater. Sci. Eng., A **343**, 273–281 (2003)
6. Wang, Y., Tian, W., Yang, Y.: Thermal shock behavior of nanostructured and conventional Al_2O_3/13 wt% TiO_2 coatings fabricated by plasma spraying. Surf. Coat. Tech. **201**, 7746–7754 (2007)
7. Larsson, A., Ruppi, S.: Microstructure and properties of CVD γ-Al_2O_3 coatings. Int. J. Refract. Met. H. **19**, 515–522 (2001)
8. Jaworek, A.: Electrospray droplet sources for thin film deposition. A review. J. Mater. Sci. **42**, 266–297 (2007)
9. Jayasinghe, S.N., Edirisinghe, M.J.: Electrostatic atomisation of ceramic suspension. J. Europ. Ceramic Soc. **24**, 2203–2213 (2004)
10. Gandhi, B.K., Borse, S.V.: Nominal particle size of multi-sized particulate slurries for evaluation of erosion wear and effect of fine particles. Wear **257**, 73–79 (2004)

Mechanism of Breakdown and Plasma Evolution in Water Induced by Wide Pulse Widths of Laser Radiation: Numerical Study

Kholoud A. Hamam and Yosr E.E.D. Gamal

Abstract Numerical simulation is presented to investigate the experimental results that carried out to study the breakdown of distilled water as a good emulate of the ocular tissue of the eye. The experiment used a visible laser source (580 nm) operating with pulses of width 100 fs, 30 ps, and 6.0 ns. The model solves numerically a rate equation that describes the temporal evolution of the electron density in the focal volume under the collective effect of multi-photon and electron collision ionization processes. Besides diffusion of electrons from the interaction region and recombination are considered as removal mechanisms. The model is validated by carrying out the calculations to obtain first a comparison between the threshold intensity as a function of the pulse width and the experimentally measured ones. Secondly, a detailed investigation of the physical processes which contribute to water breakdown connected with each laser pulse width is performed. This study is fulfilled by the determination of; the temporal evolution of the electron density at the center of the focal volume and along its radial and axial distances. The results also presented the localized distribution of the electron density in the formed plasma and its surrounded ionization regions. Finally, the effect of laser power on the linearity of the medium at the interaction region is examined for the three laser pulses to clarify the role of the self-focusing phenomenon.

K.A. Hamam (✉)
Department of Physics, Faculty of Science, King Abdulaziz University, Jeddah, Saudi Arabia
e-mail: khamam@kau.edu.sa

Y.E.E.D. Gamal
National Institute of Laser Enhanced Sciences, Cairo University, El-Giza, Egypt

A.Y. Oral and Z.B. Bahsi Oral (eds.), *3rd International Congress on Energy Efficiency and Energy Related Materials (ENEFM2015)*, Springer Proceedings in Energy, DOI 10.1007/978-3-319-45677-5_35

1 Introduction

Laser-induced breakdown and plasma generation in distilled water have found keen interest in medical applications in particular in ophthalmic microsurgery [1, 2]. In this surgery different pulse widths of laser radiation are used. Therefore, this work is devoted to applying a numerical modeling technique to investigate results of the measurements which are carried out to study the breakdown of water as a good emulate of the ocular tissue of the eye. In this experiment, the plasma is generated by laser source of wavelength 580 nm with pulse width covering an extended range from femtosecond up to nanosecond scale [3]. The applied model based on a numerical solution of a rate equation that describes the temporal evolution of the electron density in the focal volume under the collective influence of multi-photon ionization and collisional ionization processes. The model also encountered the effect of electron removal mechanism namely diffusion out of the focal volume and recombination [4]. In this work an ionization potential of 6.5 eV is used for water as suggested and commonly used by others [5–8]. On this basis, the rate equation is solved numerically using the Runge-Kutta fourth order technique. This equation is incorporated into a computer program together with the relations that describe the cross-sections and rate constants corresponding to each of the physical processes considered in this model. Given that, calculations are performed to obtain the threshold intensity as a function of pulse width. Comparison between the calculated and measured thresholds is undertaken. Also, the analysis of the physical processes responsible for the variation of the electron density along the axial and radial distances enabled the determination of plasma size correlation with the laser pulse width. An interpretation of the effect of laser power on the linearity of the medium at the interaction region for the three laser pulses is performed to clarify the role of a self-focusing phenomenon.

2 Description of the Model

The model based on numerical solution of a rate equation that describes the electron density variation as a result of the joint effect of the electron cascade ionization (based on inverse Bremsstrahlung absorption) and photo-ionization mechanisms as well as the loss processes that might take place during the interaction, viz., electron diffusion and electron recombination.

2.1 Basic Equation

In this analysis the rate equation which represents the time evolution of the electron density during the laser pulse is given by [4]:

$$\frac{d\rho}{dt} = \frac{d\rho}{dt}|_{MPI} + \eta_{CAS}\rho - D\rho - R\rho^2 \quad (1)$$

The first two terms of Eq. (1) describe the time variation of electrons generated by the combined effect of multi-photon ionization ($\frac{d\rho}{dt}|_{MPI}$) and cascade ionization ($\eta_{CAS}\rho$) mechanisms. While, the last two terms account for the diffusion ($-D\rho$) and electron recombination ($-R\rho^2$) as electron loss processes. We adopted the same formulae for the cross sections and rates as the mentioned physical processes given in our previous publication [4]. In solving this equation, the reduction of water molecules due to ionization is taken into consideration.

2.2 Numerical Calculation Procedure

The rate equation is solved numerically using the Runge-Kutta fourth order technique. To account for the beam propagation of the ultrashort pulses in the focal volume (as a result of the beam diameter variation along the axial distance) the laser intensity is assumed to have a Gaussian shape in the form [7]:

$$I(t, r, z) = I_{\max}\left(\exp(-4\ln 2(t-\tau_p)^2/4\tau_p^2)\right) \times \exp\left(-2(r^2/d^2 + z^2/l^2)\right) \quad (2)$$

where I_{max} represents the peak laser power density, r is the distance along the beam radius and z is the distance along the focal volume axis. In our calculation z = 0 corresponds to the beam waist r_0, this represents the position of which the time t = 0 and the power has its maximum value $P_{max.}$ d is the focused beam diameter and l is the parameter which characterizes the axial distance. In this analysis, the breakdown criterion is taken as the attainments of electron density of the order of $10^{20}/cm^3$.

2.3 Self-focusing Effect

A study is conducted to justify the effect of self-focusing on the breakdown of water under the experimental conditions considered in this work. This investigation found an excessive interest in ophthalmologic microsurgery of a human eye [9] in particular when using ultrashort pulses. Accordingly, the calculations are devoted to adjusting the dimensions of the focal spot in such a way that to fit the human eye configuration. In the absence of plasma generation the critical power for self-focusing is calculated from the equation [10],

$$P_c = 3.77\lambda^2/8\pi n_0 n_2 \quad (3)$$

where λ is the laser wavelength, and n_0 and n_2 are the linear and nonlinear refractive indices, respectively [11]. Equation (3) is used to obtain the critical power for self-focusing corresponding to the experimental conditions examined in this work. We compared this predicted power and the breakdown threshold power related to each pulse width. So, we could determine the pulse width at which self-focusing effect is more probable.

3 Results and Discussion

The model is applied to the experimental conditions given in [3] to study the breakdown of water induced by visible laser radiation (wavelength 580 nm) from a Nd-YAG laser source at pulse widths 6.0 ns, 30 ps, and 100 fs. Therefore, calculations are carried to determine first the laser intensity as a function of laser pulse width. These are shown by curve (1) in Fig. (1). To facilitate the comparison, the experimentally measured thresholds [3] are represented as solid squares in the same figure. The effect of loss processes on the threshold intensity is tested by performing the calculation of the threshold intensity in the absence of; all loss processes (curve 2), electron recombination (curve 3), and electron diffusion (curve 4).

From this figure, it is noticed that reasonable agreement between the calculated thresholds and measured ones is obtained only when all electron removal processes are considered in the calculations, both undergo decrease as the laser pulse width increases as shown by curve (1) and the solid squares. This agreement gives a confidential validity of both the applied model in investigating the experimental measurements examined in this work as well as the assumption of treating the water as an amorphous semiconductor. On the other hand, a clear coincidence is shown between curves (2) and (3) for the omission of all loss processes and electron

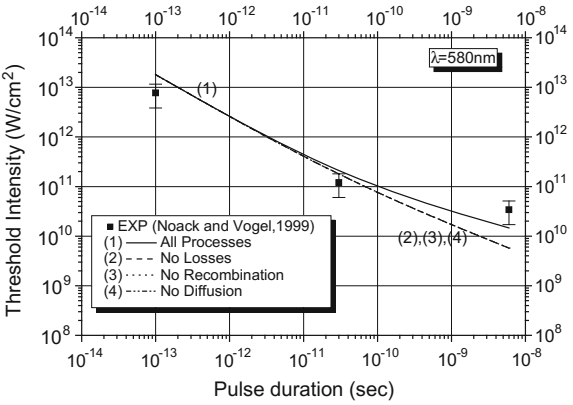

Fig. 1 Comparison between calculated and measured threshold intensities as a function of pulse width for distilled water

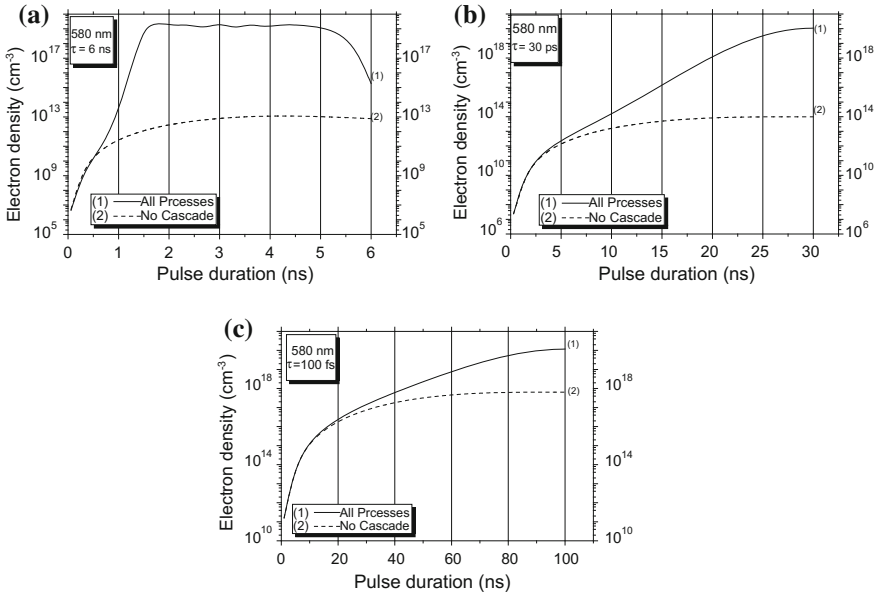

Fig. 2 Time evolution of the free electrons density calculated for the combined effect of MPI and CI (curve 1) and, for the sole contribution of MPI (curve 2) for the pulse widths. **a** 6 ns, **b** 30 ps and **c** 100 fs

recombination respectively both showed an observable deviation between the calculated and measured thresholds over the nanosecond pulse scale. This coincidence proves the unobservable effect of diffusion losses over the tested pulse width range ($\sim$ femtoseconds to nanoseconds scale). This is also clear from the coincidence of the calculated threshold intensities illustrated by curves (1) and curve (4). From this result it is shown that in relation to the experimentally examined laser pulse width, recombination losses have significant contribution only for the pulse width 6 ns. Moreover, the slow variation of the threshold intensity observed over pulse width ≤ 500 ps, indicates that breakdown is governed mainly by multiphoton ionization process. While the pronounced dependence of the threshold intensities at pulse widths ≥ 500 ps, assures the role played by electron collision ionization process in achieving breakdown and plasma generation. To confirm this result Fig. 2 represents the contribution of the ionization mechanisms to the calculated electron density growth. In doing so, the time evolution of the electron density is calculated for each pulse width (a) 6 ns, (b) 30 ps and (c) 100 fs, in the presence of all electron generation and loss mechanisms and in the absence of electron collision process (curve 2). These are shown in Fig. 2 as curves (1) and (2) respectively.

It is obvious from this figure that multiphoton ionization plays a crucial role in the breakdown of water at the femto and picosecond time scales (laser threshold intensities are 1.7×10^{13} and 1.4×10^{11} W/cm^2 respectively). At the long pulse

length (6 ns), however, where the laser threshold intensities are lower (1.6×10^{10} W/cm^2), ionization through collision processes is dominated. This process showed a noticeable contribution to the electron growth near the peak of the laser pulse where the intensity is higher. This, in turn, enhances the rate of energy absorption. It is also noticed in this figure that despite the observed decrease of the electron density shown near the end of the laser pulse for the 6.0 ns pulse which, is attributed to the effect of recombination loss process, the electron density undergoes a saturation behavior beyond the peak of the laser pulse.

To investigate the temporal and spatial variation of both laser intensity and electron density on the plasma size, computations are carried out to obtain the electron density evolution as well as the laser intensity variation as a function of time along different positions of both radial ($r_{(1)} = 2.5 \times 10^{-3}$ cm, $r_{(2)} = 1.5 \times 10^{-4}$ cm and $r_{(3)} = 2.5 \times 10^{-4}$ cm) and axial distances ($z_{(1)} = 3.5208 \times 10^{-4}$ cm, $z_{(2)} = 7.0416 \times 10^{-4}$ cm and $z_{(3)} = 1.1736 \times 10^{-3}$ cm). These are shown in Figs. (3, 4 and 5) represent these relations for the laser pulses (a) 6.0 ns, (b) 30 ps, and (c) 100 fs respectively.

Calculations showed also that the corresponding values of the threshold intensity obtained for the ultrashort pulse (100 fs) at the axial distance $z_{(1)}$ along the mentioned radial distances are found to vary as; at $r_{(1)}$: $I_{(th)} = 1.47 \times 10^{+13}$ W/cm^2, $r_{(2)}$: $I_{(th)} = 7.32 \times 10^{+12}$ W/cm^2 and $r_{(3)}$: $I_{(th)} = 2.04 \times 10^{+12}$ W/cm^2. This result reveals that the distribution of the electron density and the threshold intensity

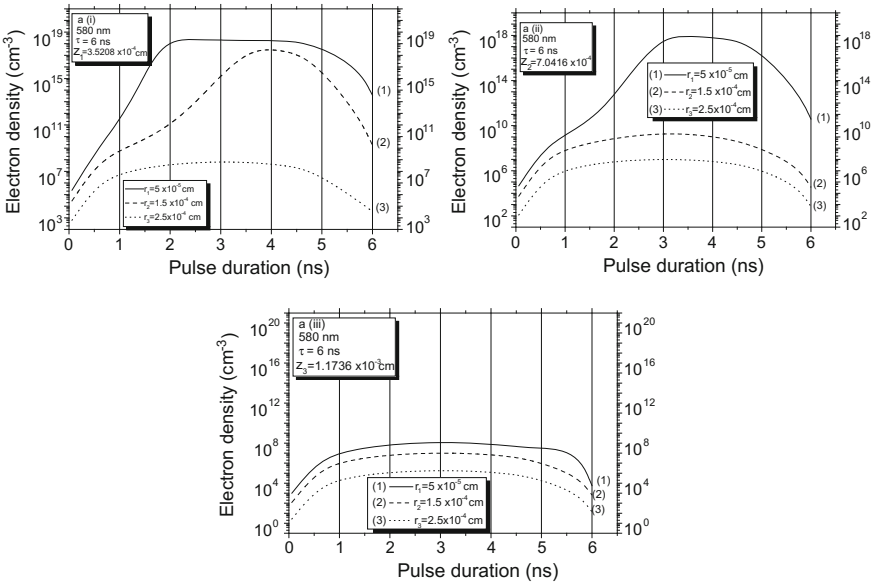

Fig. 3 Spatial distribution of the electrons density for the laser pulse. *a* 6 ns at three different positions along the axial distance, *i* z_1 cm, *ii* z_2 cm and *iii* z_3 cm

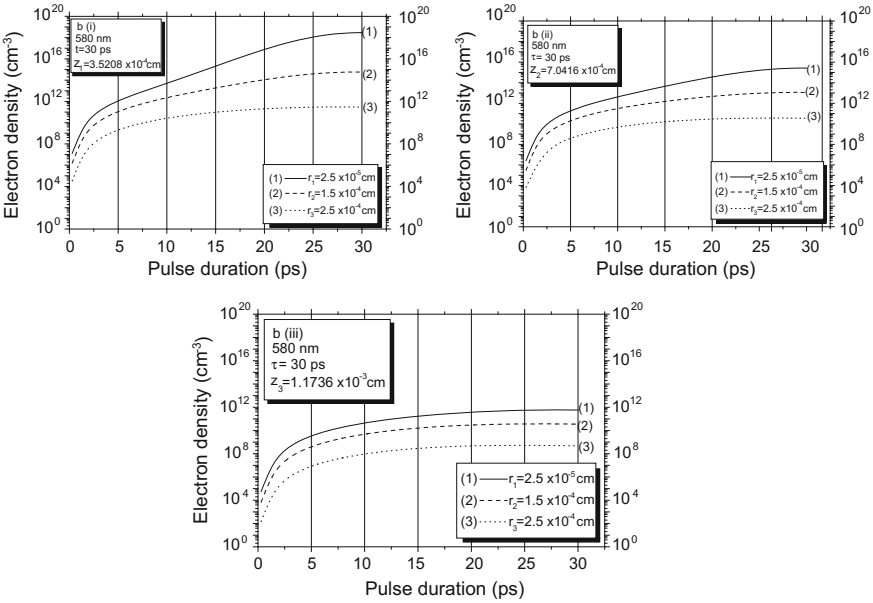

Fig. 4 The same relation as in Fig. 3, but for the laser pulse. *b* 30 ps

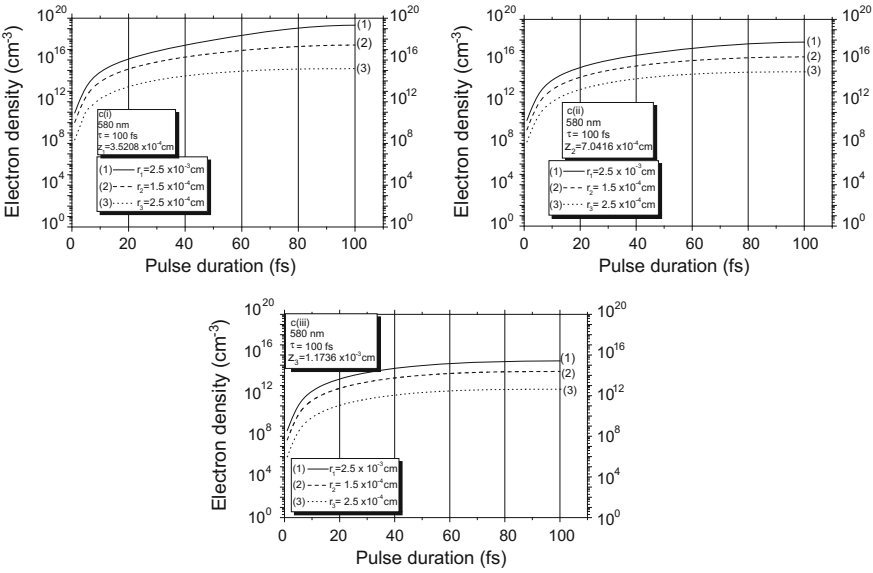

Fig. 5 The same relation as in Fig. 3, but for the laser pulse of *c* 100 fs

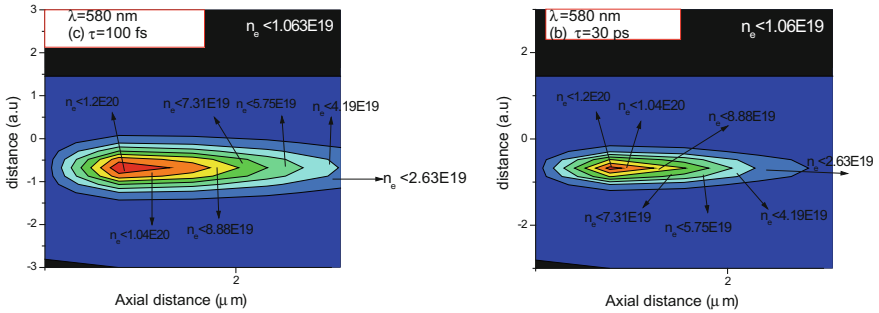

Fig. 6 Contour representation for the electron density along the axial and radial distances of the focal volume for *b* 30 ps and *c* 100 fs

decreases as the radial and axial distances increase away from the center of the focal volume. This decrease is more pronounced for the longer pulse width (6.0 ns).

The localized distribution of the electron density in the focal volume is understood by calculating the density of electrons at the end of the laser pulse at different points along the radial and axial distances. These calculations are signified for the ultrashort pulses (100 fs and 30 ps) as contour representation shown in Fig. 6. This figure illustrates the distribution of the electron density which decreases as the radial and axial distances directed away from the center of the focal volume.

The study of the effect of laser power on the linearity of the medium at the interaction region requires determination of the laser power for the tested laser pulses and comparing it with the critical power for self-focusing ($P_c = 0.88$ MW for the Wavelength 580 nm). These are shown in Fig. 7. This figure showed that self-focusing can occurs only when pulses of the order of femtoseconds and picoseconds are used where the determined powers are found to be greater than P_c (353.25 and 2.826 MW respectively). While for nanosecond scale pulses this phenomenon is hardly ever to occur.

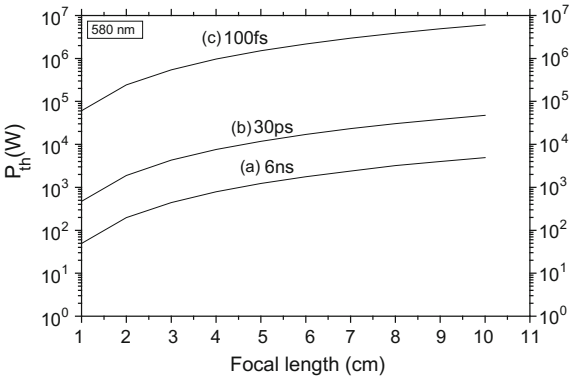

Fig. 7 Threshold power versus focal length for *a* 6 ns, *b* 30 ps, and *c* 100 fs

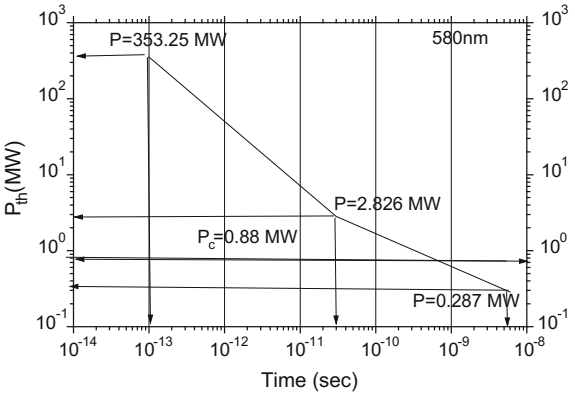

Fig. 8 Variation of the laser power with the focal length for the examined laser pulses

On the other hand, a study was performed to examine the relation between the focal length of the focusing lens and the laser power required to produce self-focusing in the interaction volume.

The results showed a gradual increase of the power for the three pulse widths over the whole range of the focal length considered in this analysis (1.0–10.0 cm) as shown in Fig. 8. Moreover, the value of the laser power decreases as increasing the laser pulse width. For the case of the human eye, the focal length of the lens is of the order of 1.7 cm (this value lies within the examined focal length range). Therefore, it is necessary to take into account the effect of self-focusing when lasers of pulses of the order of femtoseconds or picoseconds are used in ophthalmology microsurgery.

4 Conclusion

The applied model investigates the temporal and spatial evolution of electrons and laser intensity in water breakdown induced by wide range of laser pulses at wavelength 580 nm. The results are presented for pulse durations of 6 ns, 30 ps and 100 fs. The calculated threshold intensity as a function of the pulse width is compared with the experimentally measured ones [3], reasonable agreement is shown. Study of the role of ionization mechanisms in the breakdown of water revealed that multi-photon ionization is dominant for the pico and femto second time scales. Collisional ionization is found to be the main ionization mechanism at the nanosecond pulses. The obtained localized electron density in the breakdown region at different positions along the radial and axial distances envisaged that the size of the generated plasma increases as the pulse width decrease. This result is found to be strongly dependent on the temporal and spatial distribution of the laser intensity in the focal volume. For each pulse, the electron distribution within the breakdown region at end of the laser pulse is determined, and the growth of free

electrons with time at fixed positions within the focal region is predicted as well. Self-focusing is found to be important only for pulse width in the femtosecond scale when the focal length of the focusing lens of is ≥ 8.0. No evidence of this phenomenon is observed for the pulses 30 ps, and 6.0 ns. Therefore in ophthalmology microsurgery self-focusing effect should not be ignored when laser pulses of the order of femtoseconds are used.

References

1. Zhou, J., Chen, J.K., Zhang, Y.: Appl. Phys. B Lasers Opt. **90**(1), 141–148 (2008). doi:10.1007/s00340-007-2843-z
2. Takita, A., Hayasaki, Y.: Proceedings of SPIE, vol. 7201 (2009)
3. Noack, J., Vogel, A.: IEEE J. Q. Electron **35**(8), 1156–1167 (1999). doi:10.1109/3.777215
4. Gaabour, L.H., Gamal, Y.E.E.D., Abdellatif, G.: J. Mod. Phys. **3**, 1683–1691 (2012)
5. Williams, F., Varma, S.P., Hillenius, S.: J. Chem. Phys. **64**(4), 1549 (1976). doi:10.1063/1.432377
6. Sacchi, C.A.: J. Opt. Soc. Am. B **8**(2), 337 (1991)
7. Kennedy, P.K.: IEEE J. Q. Electron **31**(12), 2241 (1995)
8. Kennedy, P.K., Hammer, D.X., Rockwell, B.A.: Prog. Q. Electron **21**, 155–248 (1997)
9. Powell, J.A., Moloney, J.V., Newell, A.C., Albanese, R.A.: Beam collapse as an explanation for anomalous ocular damage. J. Opt. Soc. Am. B **10**(7), 1230–1241 (1993). doi:10.1364/JOSAB.10.001230
10. Shen, Y.R.: The Principle of Nonlinear Optics. Wiley, New York (1984)
11. Couairon, A., Mysyrowicz, A.: Phys. Rep. **441**, 47 (2007)

Research Towards Energy-Efficient Substation Connectors

F. Capelli, J.-R. Riba, A. Rodriguez and S. Lalaouna

Abstract The contact resistance is the main variable that defines the energy efficiency of an electrical connection, its stable performance and long term service. It is worth noting that according to the measurements performed in this work, the contact resistance in substation connectors can be several times that of the connector's resistance. To reduce connection losses and thus increase connector's efficiency, it is important to minimize contact resistance, to ensure an efficient connection. The aim of this work is to find out, by means of experimental measurements, the relationship between the different components of contact resistance in substation connectors and the main related variables such as material properties, applied bolts torque, true contact area, or surface's conditions among others. Furthermore, this study proposes a novel surface treatment for substation connectors, which allows reducing the contact resistance. Experimental measurements demonstrate the effectiveness of the novel chemical treatment in improving energy efficiency in substation connectors.

Keywords Contact resistance · Energy-efficiency · Substation connectors · Surface preparation · Chemical cleaning

F. Capelli (✉) · J.-R. Riba
Department of Electrical Engineering, Universitat Politècnica de Catalunya, 08222 Terrassa, Spain
e-mail: francesca.capelli@mcia.upc.edu

J.-R. Riba
e-mail: riba@ee.upc.edu

F. Capelli · A. Rodriguez · S. Lalaouna
SBI Connectors Spain SLU, 08635 Sant Esteve Sesrovires, Spain

A.Y. Oral and Z.B. Bahsi Oral (eds.), *3rd International Congress on Energy Efficiency and Energy Related Materials (ENEFM2015)*, Springer Proceedings in Energy, DOI 10.1007/978-3-319-45677-5_36

1 Introduction

Substation connectors are the joints that physically link the power transmission lines and the substation conductors and bus bars. They are usually divided into different categories, depending on the physical junction between the connector and the conductor, that are mechanical, welded, and compression type. In substation the most common ones are mechanical type connectors, which employ bolts by applying a given torque to create contact points, maintain the connection integrity and ensure adequate contact resistance [1]. The contact resistance defines the energy-efficiency, the stable performance and the long term service of an electrical connection. If contact resistance is low and stable in time, a good electrical connection and a long life of substation connector is guaranteed; whereas, if it is high and unstable, it could cause overheating of the connector and, consequently, a reduced operating life [2]. Connector's long term performance is directly related to the contact points established during installation [1]. The restriction of current flow to these few contact points, also known as "a-spots," constitutes a first contribution to the total contact resistance; this component is usually called constriction resistance [3].

Constriction resistance depends on some properties of conductor materials, such as hardness and electrical resistivity, applied bolts torque, true contact area, or surface's conditions among others. Many authors have studied constriction resistance and have found out different expressions to model it [4, 5].

Moreover, it is necessary to take into account the presence on contact interface of thin oxide film. The common used material to manufacture substation connectors is A356.0 aluminum cast alloy. It is well known that aluminum and its alloys reacts quickly with atmospheric oxygen, and a passivation layer of few nanometers of aluminum oxide, usually known as alumina, grows on atmospheric exposed aluminum surfaces [6]. Due to aluminum oxide is very insulating, current can transfer across the alumina only thanks to tunneling and fritting mechanisms [7]. As consequence, the film resistance is the second component of the total contact resistance of a joint. However, a good electrical contact between two conductors can be established only if the contact spots can be created by means of the mechanical rupture of the oxide insulating film [7].

The aim of this paper is to find out, by means of experimental measurements, the relationship between contact resistance in substation connectors and the main related variables such as material physical and mechanical properties, applied bolts torque, contact area or surface's conditions among others.

Moreover, this study aims to propose a surface treatment for substation connector's and associated conductors, which allows reducing the contact resistance. This treatment consists on a chemical cleaning before conventional substation connector's installation. Contact surface preparation is essential to guarantee proper contact between connector and conductor since the contact resistance can notably degrade substation connectors' performance.

2 The Contact Resistance Model

The total contact resistance consists of constriction resistance and oxide film resistance:

$$R_{contact} = R_c + R_{film} \tag{1}$$

The estimation of R_{film} is difficult, as consequence of the impossibility to model how the film is mechanically disrupted to allow the establishment of contact points [3, 7]. On the other hand, there are several analytic relations to model constriction resistance. The evaluation of constriction resistance generally considers circular a-spots. In practice, an electrical junction is composed by a large amount of a-spots. Grenwood showed that, in a simple case of large number (n) of circular a-spots within a single cluster, contact resistance can be expressed by the following relation [8].

$$R_c = \rho\left(\frac{1}{2na} + \frac{1}{2\alpha}\right) \tag{2}$$

where a is the a-spot radius and α cluster's radius, usually known as Holm's radius. However, Nakamura and Minowa demonstrated that the resistance of a junction with fixed electrical area was not affected by the number and the distribution of the a-spots [9]. Thus, it is sufficient to know only Holm's Radius (α) to estimate contact resistance. Holm's radius is related with the true area of contact Ac, by relation (3), and the true area of contact can be calculated as function of the applied load F and the plastic flow stress H (Eq. 4).

$$\alpha = \sqrt{\frac{A_c}{\pi}} \tag{3}$$

$$F = A_c \cdot H \tag{4}$$

Thus, the constriction resistance can be expressed as follows:

$$R_c = \frac{\rho}{2\alpha} = \sqrt{\frac{\rho^2 \pi H}{4F}} \tag{5}$$

3 Analyzed Substation Connectors and Installation Procedures

Resistance measurements of contact resistance at room temperature has been conducted on a junction composed by different typologies of substation connectors from SBI Connectors catalogue and 32 mm diameter AAAC conductors. Specifically, analyzed connectors are listed below:

Table 1 Installation procedures applied to substation connectors

Installation procedure	Conductor's surface treatment	Connector's surface treatment
1	Not treated	Not treated
2	Brushed Oxide inhibiting compound application	Brushed Oxide inhibiting compound application
3	Brushed Oxide inhibiting compound application	Chemical cleaning Oxide inhibiting compound application

- T-connector S330TLS (I);
- Coupler with two caps S330SLS (II);
- Coupler with three caps S330SNS (III)

Different assembling procedures and surface treatments, summarized in Table 1, are studied.

The conventional assembling procedure consists in brushing both conductor and connector's surfaces just before assembling, with the aim to remove the aluminum oxide film (alumina). After brushing it is generally a recommended practice to paint both contact surfaces with an oxide inhibiting compound. These compounds ensure good contact and enhance the expected life of the connection [1].

Chemical cleaning treatment involves the application of a chemical solution on the contact surfaces between the connector and the conductor during about 25 min, after which the components were assembled according to the standard procedure.

4 Experimental Results

The Kelvin or 4-wire method was employed to perform resistance measurements, as shown in Fig. 1. To this end a Raytech Micro-Centurion II digital micro-ohm meter (max. current 200 A_{DC}, accuracy ±0.1 % Rdg ±0.01 μΩ) was used. Resistance measurement was performed between points A and B as shown in Fig. 1. The theoretical resistance of the connectors was calculated through electromagnetic FEM-simulation, which was subtracted from the measured resistance, thus obtaining the contact resistance.

Resistance measurements shown in Table 2 indicate that when no surface treatment is applied (procedure 1), the contact resistance is very high, since the rupture of the alumina film caused by the axial force due to the bolts assembly is not enough and, therefore, few contact points have been established between the contact surfaces of the conductor and connector. The conventional installing

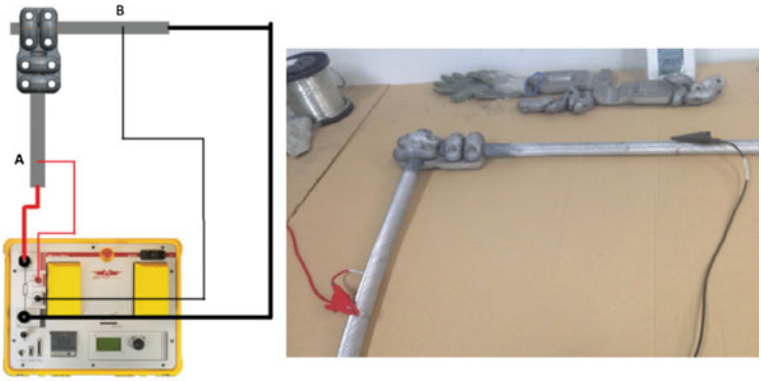

Fig. 1 Resistance measurement with the Kelvin 4-wire method

Table 2 Measured values of contact resistance a total connector's resistance

	S330TLS		S330SLS		S330SNS	
Installation procedure	Contact resistance (μΩ)	Total resistance (μΩ)	Contact resistance (μΩ)	Total resistance (μΩ)	Contact resistance (μΩ)	Total resistance (μΩ)
1	32.16	36.37	51.42	55.28	52.33	57.13
2	8.74	12.95	11.01	14.87	9.89	14.69
3	**4.88**	**9.09**	**4.54**	**8.40**	**5.87**	**10.58**

The values in **bold** are the lower value between the three installation procedure

procedure (2) results in an important decrease of the contact resistance compared to procedure 1, due to the mechanical rupture of the oxide insulating film by brushing surfaces.

With procedure 3 a significant decrease of the contact resistance is obtained compared to the conventional procedure, through the complete elimination of the oxide layer from the surface of the connector.

Experimental resistance measurements clearly demonstrate that oxides and contaminants difficult the establishment of a good electrical connection.

5 Components of Connector's Resistance

In Fig. 2 the different components of S330SNS connector's resistance with the three installation methods are shown. Thanks to estimated value of constriction resistance, calculated by means of Eq. 5, it is possible to note that, with the novel chemical cleaning proposed by the authors (procedure 3), the contact resistance component due to the oxide film is practically eliminated.

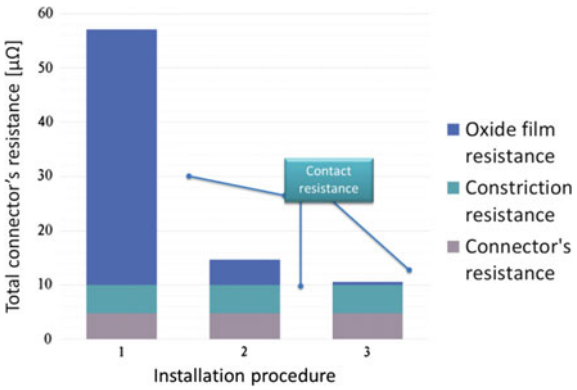

Fig. 2 S330SNS connector. Components of connector's resistance

6 Conclusions

The contact resistance defines the energy-efficiency of an electrical connection, its stable performance and long term service. In this paper a new a chemical cleaning for substation connectors to minimize contact resistance has been presented. By means of experimental measurements and an analytical model, it has been shown that the decrease of connector's resistance is related to the almost complete elimination of the aluminum oxide film from connector's surface. The object of this study has been different typologies of substation connectors which join two AAAC conductors, with rated diameter d = 32 mm.

Experimental resistance measurements by applying the 4-wires Kelvin method have been conducted on the connectors, assembled with different installing procedures. By this way, and by means of analytical models, the different components of the connectors' resistance have been calculated.

Results presented show that the installation procedure proposed in this work allows minimizing the contact resistance of substation connectors, and thus to improve energy efficiency of the electrical connection, its performance and increasing the operating life.

Acknowledgments The authors would like to thank SBI Connectors Spain that supported this study by provisioning the equipment for experimental test. They also thank Spanish Ministry of Economy and Competitiveness for the financial support received under project RTC-2014-2862-3 and Generalitat de Catalunya under Doctorat Industrial program 2013 DI 024.

References

1. Burndy: Electrical Contacts: Principles and Applications (1999)
2. Dzekster, N.N., Izmailov, V.V.: Some methods for improving aluminium contacts. In: Thirty-Sixth IEEE Conference on Electrical Contacts, and the Fifteenth International Conference on Electrical Contacts, pp. 518–520. IEEE (1990)

3. Braunovic, M., Myshkin, N.K., Konchits, V. V.: Electrical Contacts: Fundamentals, Applications and Technology (2006)
4. Holm, R.: Electric Contacts. Springer, Berlin (1967)
5. Greenwood, J.A., Williamson, J.B.P.: Contact of nominally flat surfaces. Proc. R. Soc. A Math. Phys Eng. Sci. **295**, 300–319 (1966)
6. Campbell, T., Kalia, R.K., Nakano, A., Vashishta, P., Ogata, S., Rodgers, S.: Dynamics of oxidation of aluminum nanoclusters using variable charge molecular-dynamics simulations on parallel computers. Phys. Rev. Lett. **82**, 4866–4869 (1999)
7. Slade, P.G.: Front matter. In: Electrical Contacts, pp. FM1–xliv. CRC Press (2014)
8. Greenwood, J.A.: Constriction resistance and the real area of contact. Br. J. Appl. Phys. **17**, 1621–1632 (1966)
9. Nakamura, M., Minowa, I.: Computer simulation for the conductance of a contact interface. IEEE Trans. Compon. Hybrids Manuf. Technol. **9**, 150–155 (1986)